

## THÈSE DE DOCTORAT

# **Monofilament entangled materials: relationship between microstructural properties and macroscopic behaviour**

Présentée devant  
**l'Institut National des Sciences Appliquées de Lyon**

pour obtenir  
**le grade de Docteur**

École doctorale :  
**Matériaux de Lyon**

Spécialité :  
**Science des Matériaux**

par  
**Loïc Courtois**  
**Ingénieur INSA**

Thèse soutenue le 13 décembre 2012 devant la Commission d'examen

### **Jury**

John Hutchinson	Professor (Harvard University)	(President)
Olivier Bouaziz	(Arcellor Mittal)	(Rapporteur)
Patrick Onck	Professor (University of Groningen)	(Rapporteur)
Laurent Orgeas	Chargé de recherche CNRS (INP Grenoble)	
Michel Perez	Professeur (INSA de Lyon)	
Eric Maire	Directeur de recherche CNRS (INSA de Lyon)	

Université de Lyon  
MATEIS - UMR CNRS 5510 - INSA de Lyon  
25, avenue Jean Capelle, 69621 Villeurbanne Cedex, France





## INSA Direction de la Recherche - Ecoles Doctorales – Quinquennal 2011-2015

SIGLE	ECOLE DOCTORALE	NOM ET COORDONNEES DU RESPONSABLE
<b>CHIMIE</b>	<b>CHIMIE DE LYON</b> <a href="http://www.edchimie-lyon.fr">http://www.edchimie-lyon.fr</a>  Insa : R. GOURDON	<b>M. Jean Marc LANCELIN</b> Université de Lyon – Collège Doctoral Bât ESCPE 43 bd du 11 novembre 1918 69622 VILLEURBANNE Cedex Tél : 04.72.43 13 95 <a href="mailto:directeur@edchimie-lyon.fr">directeur@edchimie-lyon.fr</a>
<b>E.E.A.</b>	<b>ELECTRONIQUE, ELECTROTECHNIQUE, AUTOMATIQUE</b> <a href="http://edeea.ec-lyon.fr">http://edeea.ec-lyon.fr</a>  Secrétariat : M.C. HAVGOUDOUKIAN eea@ec-lyon.fr	<b>M. Gérard SCORLETTI</b> Ecole Centrale de Lyon 36 avenue Guy de Collongue 69134 ECULLY Tél : 04.72.18 60 97 Fax : 04 78 43 37 17 <a href="mailto:Gerard.scorletti@ec-lyon.fr">Gerard.scorletti@ec-lyon.fr</a>
<b>E2M2</b>	<b>EVOLUTION, ECOSYSTEME, MICROBIOLOGIE, MODELISATION</b> <a href="http://e2m2.universite-lyon.fr">http://e2m2.universite-lyon.fr</a>  Insa : H. CHARLES	<b>Mme Gudrun BORNETTE</b> CNRS UMR 5023 LEHNA Université Claude Bernard Lyon 1 Bât Forel 43 bd du 11 novembre 1918 69622 VILLEURBANNE Cédex Tél : 04.72.43.12.94 <a href="mailto:e2m2@biomserv.univ-lyon1.fr">e2m2@biomserv.univ-lyon1.fr</a>
<b>EDISS</b>	<b>INTERDISCIPLINAIRE SCIENCES-SANTE</b> <a href="http://ww2.ibcp.fr/ediss">http://ww2.ibcp.fr/ediss</a>  Sec : Safia AIT CHALAL Insa : M. LAGARDE	<b>M. Didier REVEL</b> Hôpital Louis Pradel Bâtiment Central 28 Avenue Doyen Lépine 69677 BRON Tél : 04.72.68 49 09 Fax :04 72 35 49 16 <a href="mailto:Didier.revel@creatis.uni-lyon1.fr">Didier.revel@creatis.uni-lyon1.fr</a>
<b>INFOMATHS</b>	<b>INFORMATIQUE ET MATHEMATIQUES</b> <a href="http://infomaths.univ-lyon1.fr">http://infomaths.univ-lyon1.fr</a>	<b>M. Johannes KELLENDONK</b> Université Claude Bernard Lyon 1 INFOMATHS Bâtiment Braconnier 43 bd du 11 novembre 1918 69622 VILLEURBANNE Cedex Tél : 04.72. 44.82.94 Fax 04 72 43 16 87 <a href="mailto:infomaths@univ-lyon1.fr">infomaths@univ-lyon1.fr</a>
<b>Matériaux</b>	<b>MATERIAUX DE LYON</b>  Secrétariat : M. LABOUNE PM : 71.70 –Fax : 87.12 Bat. Saint Exupéry <a href="mailto:Ed.materiaux@insa-lyon.fr">Ed.materiaux@insa-lyon.fr</a>	<b>M. Jean-Yves BUFFIERE</b> INSA de Lyon MATEIS Bâtiment Saint Exupéry 7 avenue Jean Capelle 69621 VILLEURBANNE Cédex Tél : 04.72.43 83 18 Fax 04 72 43 85 28 <a href="mailto:Jean-yves.buffiere@insa-lyon.fr">Jean-yves.buffiere@insa-lyon.fr</a>
<b>MEGA</b>	<b>MECANIQUE, ENERGETIQUE, GENIE CIVIL, ACOUSTIQUE</b>  Secrétariat : M. LABOUNE PM : 71.70 –Fax : 87.12 Bat. Saint Exupéry <a href="mailto:mega@insa-lyon.fr">mega@insa-lyon.fr</a>	<b>M. Philippe BOISSE</b> INSA de Lyon Laboratoire LAMCOS Bâtiment Jacquard 25 bis avenue Jean Capelle 69621 VILLEURBANNE Cedex Tél :04.72.43.71.70 Fax : 04 72 43 72 37 <a href="mailto:Philippe.boisse@insa-lyon.fr">Philippe.boisse@insa-lyon.fr</a>
<b>ScSo</b>	<b>ScSo*</b>  <b>M. OBADIA Lionel</b>  Sec : Viviane POLSINELLI Insa : J.Y. TOUSSAINT	<b>M. OBADIA Lionel</b> Université Lyon 2 86 rue Pasteur 69365 LYON Cedex 07 Tél : 04.78.69.72.76 Fax : 04.37.28.04.48 <a href="mailto:Lionel.Obadia@univ-lyon2.fr">Lionel.Obadia@univ-lyon2.fr</a>

\*ScSo : Histoire, Géographie, Aménagement, Urbanisme, Archéologie, Science politique, Sociologie, Anthropologie



---

# **Monofilament Entangled Materials : relationships between microstructural properties and macroscopic behaviour**

---

## **Abstract**

---

Playing with the architecture of a material is a clever way of tailoring its properties for multi-functional applications. A lot of research have been made, in the past few years, on what is now referred to as “architected materials” (metal foams, entangled materials, steel wool, etc), mostly for their capacity to be engineered in order to present specific properties, inherent to their architecture. In this context, some studies have been carried out concerning entangled materials but only a few on monofilament entangled materials. Such a material, with no filament ends, could exhibit interesting properties for shock absorption, vibration damping and ductility. In this study, entanglements were manually produced, using different types of wire, and submitted to constrained (inside a PTFE die) in-situ compressive tests within the laboratory tomograph. This technique enabled a 3D, non destructive, microstructural characterization of the complex architecture of these materials, along with the analysis of their macroscopic mechanical properties.

The stiffness of this material was found to be in a 20-200 MPa range and homogeneous samples could be obtained, while lowering their stiffness, by pre-deforming the initial wire as a spring. Damping measurements were performed using different types of entanglements (constitutive materials, volume fraction, wire diameter, wire shape) under both monotonic and dynamic loadings and directly linked to the measurements of the number of contacts. The Dynamic Mechanical Analysis underlined the great capacity of this material to absorb energy with a loss factor of about 0.25 and damping was found to decrease with the stiffness of the entanglement.

The mechanical properties of this material were first modeled using an analytical “beam” model based on the experimental evolution of the mean distance between contacts and a good agreement was found with the experimental results.

In parallel, a Discrete Element Method was used in order to model the compressive behaviour of Monofilament Entangled Materials. Although purely elastic properties were taken into account in the model, a very good agreement with the experimental results was obtained by adjusting the friction coefficients of the model. This tends to prove that the plasticity of these entangled materials is rather due to the structure (friction) than to the constitutive material itself.

**Keywords :** entangled, monofilament, X-ray tomography, microstructure, mechanical properties, damping, shear, sintering, Discrete Element Method

---

## **Materiaux monofilamentaires enchevêtrés : étude des relations microstructure - propriétés mécaniques**

---

### Résumé

---

Les matériaux architecturés attirent de plus en plus d'attentions de par leur capacité à combiner différentes propriétés ciblées. Dans ce contexte, les matériaux enchevêtrés, et plus particulièrement les matériaux monofilamentaires enchevêtrés, présentent des propriétés intéressantes en terme de légèreté, de ductilité, et de facteur de perte. En raison de l'architecture interne complexe de ces matériaux, leur caractérisation et la compréhension des mécanismes de déformation nécessitent une méthodologie adaptée. Dans cette étude, l'enchevêtrement est réalisé manuellement pour différents fils d'acier et soumis à une compression oedométrique. De manière à étudier le comportement sous charge de ce type de matériaux, un dispositif de compression uniaxiale guidée a été mis en place dans le tomographe. Il est ainsi possible de suivre, à l'aide de mesures quantitatives, la déformation de l'échantillon et l'évolution du nombre de contacts pour différentes fraction volumiques. L'utilisation de ces données microstructurales a permis une meilleure compréhension du comportement mécanique de tels enchevêtrements.

Une rigidité pouvant varier de 20 à 200 MPa en fonction des paramètres de mise en forme (diamètre et forme du fil, fraction volumique, matériau constitutif) a été déterminée. Un matériau homogène de rigidité plus faible a pu être obtenu en pré-déformant le fil sous forme de ressort avant enchevêtrement. Le facteur de perte du matériau a ensuite été mesuré à la fois sous chargement statique et dynamique. L'analyse mécanique dynamique a mis en évidence la capacité de ce matériau à absorber de l'énergie avec une valeur de facteur de perte d'environ 0.25.

Les propriétés mécaniques du matériau ont tout d'abord été modélisées analytiquement par un modèle de poutres et un bon accord avec les résultats expérimentaux a pu être obtenu en définissant un paramètre d'orientation équivalent, spécifique à la compression oedométrique de matériaux enchevêtrés. En parallèle, un modèle éléments discrets a été développé afin de simuler le comportement en compression de matériaux monofilamentaires enchevêtrés. Ce modèle s'appuie sur une discrétisation du fil en éléments sphériques, acquise à partir de données de tomographie. Bien que seul le comportement élastique du fil constitutif ait été pris en compte, une bonne adéquation entre résultats numériques et expérimentaux a été obtenue en ajustant les coefficients de frottement du modèle.

**Mots-clés :** enchevêtrement, monofilamentaire, tomographie aux rayons X, microstructure, propriétés mécaniques, amortissement vibratoire, cisaillement, frittage, modélisation éléments discrets

# Contents

<b>Contents</b>	<b>v</b>
<b>0 Introduction</b>	<b>1</b>
0.1 Problematics . . . . .	2
0.2 MANSART Project . . . . .	2
0.2.1 A new strategy for materials development . . . . .	2
0.2.2 Advanced case study . . . . .	4
<b>1 Literature review</b>	<b>7</b>
1.1 Introduction to hybrid and sandwich structures . . . . .	8
1.2 Entangled materials : state of the art . . . . .	12
1.2.1 Fiber network with no permanent link . . . . .	12
1.2.1.1 Experimental work . . . . .	12
1.2.1.2 Analytical models . . . . .	19
1.2.1.3 Numerical models . . . . .	22
1.2.2 Sintered wire mesh . . . . .	27
1.3 Conclusion . . . . .	28
<b>2 Monofilament Entangled Materials under compressive loading</b>	<b>31</b>
2.1 Manufacturing samples . . . . .	33
2.1.1 Raw materials . . . . .	33
2.1.2 Sample preparation . . . . .	33
2.2 In-situ oedometric testing in X-ray tomography . . . . .	35
2.2.1 X-ray tomography's principle . . . . .	35
2.2.2 Processing raw data . . . . .	37
2.2.2.1 Sticking . . . . .	38
2.2.2.2 Useful image processing . . . . .	38
2.2.2.3 Segmentation . . . . .	39
2.2.2.4 Skeletonization . . . . .	41
2.2.3 In-situ device . . . . .	42
2.3 Microstructural analysis . . . . .	44
2.3.1 Radial density distribution . . . . .	44
2.3.2 Number of contacts . . . . .	45
2.3.3 Mean distance between contacts . . . . .	48
2.4 Mechanical Characterization . . . . .	49
2.4.1 Generalities on the experiment . . . . .	49
2.4.2 Influence of the wire diameter . . . . .	51
2.4.3 Analytical model . . . . .	52
2.5 Conclusion . . . . .	57

<b>3</b>	<b>Tailoring the properties</b>	<b>59</b>
3.1	Experimental procedures . . . . .	60
3.1.1	High yield strength of the wire . . . . .	60
3.1.2	Modification of the initial wire shape . . . . .	61
3.1.2.1	Spring pre-forming . . . . .	61
3.1.2.2	Short fibers . . . . .	62
3.1.2.3	Cables . . . . .	62
3.1.3	“Sintered” materials . . . . .	63
3.1.3.1	Conventional sintering . . . . .	63
3.1.3.2	Spark Plasma Sintering . . . . .	64
3.2	Microstructural characterization . . . . .	68
3.2.1	Distribution of density and orientation along the compression axis . . . . .	68
3.2.2	Radial density profiles . . . . .	70
3.2.3	Number of contacts . . . . .	75
3.3	Monotonic mechanical analysis . . . . .	77
3.3.1	Compressive oedometer testing . . . . .	77
3.3.2	Damping . . . . .	80
3.3.3	Shear testing . . . . .	84
3.3.4	Tensile test . . . . .	86
3.3.5	Characterization of sintered materials . . . . .	87
3.4	Dynamic Mechanical Analysis . . . . .	92
3.5	Conclusion . . . . .	97
<b>4</b>	<b>Discrete Element Method applied to the simulation monofilament entangled materials</b>	<b>99</b>
4.1	Numerical model . . . . .	101
4.1.1	Principle . . . . .	101
4.1.2	Generation of discrete numerical samples . . . . .	107
4.1.3	Solicitation : oedometric compression . . . . .	110
4.1.4	”Quench“ relaxation . . . . .	111
4.1.5	Measurements . . . . .	112
4.2	Microstructural analysis . . . . .	113
4.2.1	Investigation of the random generation . . . . .	113
4.2.2	Comparison to the experimental data . . . . .	114
4.2.3	Influence of the volume fraction . . . . .	115
4.2.4	Deformation mechanisms and reorientation . . . . .	116
4.2.5	Number of contacts . . . . .	118
4.3	Mechanical analysis . . . . .	120
4.3.1	Random/experimental comparison . . . . .	120
4.3.2	Influence of the wire/wire friction coefficient . . . . .	121
4.3.3	Influence of the wire/wall friction coefficient . . . . .	123
4.3.4	Comparison to the experiment . . . . .	124
4.4	Conclusion . . . . .	124
<b>A</b>	<b>Industrial specifications</b>	<b>129</b>
<b>B</b>	<b>Materials selection and process : “materials selection” project</b>	<b>143</b>
	<b>Bibliography</b>	<b>159</b>

# Glossaire

ATECA : Applications des TEchnologies Avancées  
CIRIMAT : Centre Interuniversitaire de Recherche Ingénierie MATériaux, laboratoire basé à Toulouse  
CT scan : Computed Tomography scan  
DEM : Discrete Element Method  
DMA : Dynamic Mechanical Analysis  
EADS : European Aeronautic Defence and Space company  
ENSMP : Ecole Nationale Supérieure des Mines de Paris  
FE : Finite Element  
ICA : Institut Clément Ader  
LAMMPS : Large-scale Atomic/Molecular Massively Parallel Simulator  
MATEIS : MATÉriaux : Ingénierie et Sciences  
MD : Molecular Dynamics  
MEM : Monofilament Entangled Material  
ONERA : Office national d'études et de recherches aérospatiales  
PTFE : PolyTetraFluoroEthylene  
SEM : Scanning Electron Microscopy  
SMCI : Sainte-Marie Constructions Isothermes  
SME : Small And Medium Enterprises  
SPS : Spark Plasma Sintering  
Voxel : Volumetric pixel, extension of a pixel in 3D





# Chapter 0

## Introduction

*This introduction aims at presenting the problematics and goals of the study of monofilament entangled materials, as well as the context and objectives of the project in which it was included.*

### Chapter's content

0.1	Problematics . . . . .	2
0.2	MANSART Project . . . . .	2
0.2.1	A new strategy for materials development . . . . .	2
0.2.2	Advanced case study . . . . .	4

### 0.1 Problematics

In many industrial fields such as the aeronautic industry, structural materials remain a limiting step in the increase of performance. New requirements for multifunctional design lead to more and more stringent requests on materials properties. In cases where structural functions, thermal and damping properties are simultaneously required, bulk materials are often unable to fulfil those conflicting requirements.

On the one hand, the standard microstructural optimisation strategy currently implemented by metallurgists and ceramists can improve materials properties, but only give a limited degree of freedom. On the other hand, the shape optimisation routes, used in the mechanics of structures, take advantage of the geometry of the system. The aim of this PhD project was to explore, based on practical industrial requirements, the potentialities offered by the combination of both those strategies when designing a material.

Playing with the architecture of a material is a promising way of tailoring its properties for multifunctional applications. What is now referred to as “architected materials” (metal foams, entangled materials, steel wool, etc), has triggered numerous research in recent years, mostly for their ability to be engineered in order to exhibit specific combinations of properties, which “classical materials” could not offer. These materials have been proposed as ideal candidates for a top-down approach of “materials by design”.

Some studies have been carried out concerning entangled materials, but only a few on monofilament entangled materials. Such a material, with no filament ends, sliding contacts and a high relative porosity (80-95%), could exhibit interesting properties for shock absorption, vibration damping and ductility. The simplicity of the manufacturing process as well as the large permeability and the resistance to high and low temperatures, are also of interest for high technology applications, such as high strength reinforcements or vibration damping materials.

### 0.2 MANSART Project

#### 0.2.1 A new strategy for materials development

Materials are usually classified in two distinct categories, depending on their main use: structural materials and functional materials. The first ones are mechanically optimized whereas the later ones are used in order to answer to a specific functional need such as vibration damping, electrical conductivity or ionic conductivity. In more recent years, much attention has been placed into combining both of those characteristics in order to reduce the price, weight or size a specific part. In some cases, the structured material can present better properties than the combination of several materials. This led to the investigation of “architected materials” for which the spatial arrangement matters as much as the constitutive material.

In this context, the MANSART (MAtériaux Sandwich et ARchiTecturé) project, funded by the french National Research Agency, aims at studying sandwich structures, composed of architected materials, using a “materials by design” approach for multifunctional requirements. In order to develop this approach and to evaluate its ability to generate innovative solutions, a specific choice of multifunctional requirements has been made: combining mechanical properties such as shear modulus or damping, thermal properties and acoustical properties, but the procedures and methods

studied here, in the case of sandwich structures, are expected to be adaptable to other multifunctional specifications. In this research consortium, constituted of 11 partners, applications were chosen in two extreme fields : aeronautics and thermal management.

The partners gathered in this project are both industrial and academic, thus creating collaborations between complementary expertises. The industrial partners are either big companies (EADS, Airbus) or SME (ATECA, SMCI). On the academic side, a group of laboratories was assembled in which partners possesses complementary skills :

- MATEIS : Tomography characterization
- SIMAP : Materials design and mechanical metallurgy
- ENSMP : mathematical morphology and continuum mechanics
- CIRIMAT : High temperature materials and oxidation
- ICA : Impact and sandwich structures
- ENSAIT/GEMTEX : Advanced fibrous materials.

In addition, ONERA will contribute to the processing of new materials, their implementation in sandwich structures, their characterization for structural and acoustic properties.

The consortium was mainly organized around 5 PhD, each localized at academic partners. Each PhD was aimed at studying either a new type of “core material” the effective properties of a structure or a modeling approach (continuum mechanics). Here is a list of subjects as well as their respective laboratories (the subject of the current PhD is highlighted) :

- SIMAP : Interlocked materials
- **MATEIS : Monofilament entangled materials**
- ICA : Impact tests and residual properties after impact (characterization and mechanical modeling)
- GEMTEX : Fibrous structures for innovative sandwich panels (nonwoven, knitted structures)
- ENSMP : Generalized continuum mechanics of structured materials (Auxetic materials)
- ONERA : Optimization of structured materials (genetic algorithm).

Collaborations between academic partners, as well as industrial ones, were encouraged. In the case of the monofilament entangled materials study, close interactions were held with the SIMAP group who had developed a discrete element method approach for the modeling of entangled materials. Interactions with industrial partners happened through the definition of a set of requirements, the creation of innovative materials and the characterization of the implemented structures. Those requirements will be presented in the following section.

This project was anticipated to be a new way of studying multifunctional design. It aimed at developing and implementing, on specific cases, a new approach for materials optimization. It mainly focussed on studying one specific type of multi-material : sandwich structures. In this context, new, innovative core materials were prepared and studied.

### 0.2.2 Advanced case study

The developpement and implementation of new materials in sandwich structures was approached using concrete industrial applications, submitted by the industrial partners of the project. They provided us, as a part of the collaborations among the project, with a list of specifications with regards to a few particular functions, such as :

- Impact resistance with a 1J/13kJ energy range
- Vibroacoustic damping on a 0 to 20kHz range
- Stress transmission in static and fatigue
- High temperature behavior.

A list of all the specifications is shown in Appendix A. More specifically, in accordance with the goals of the project, each studied material was linked with one of these applications. In the case of monofilament entangled materials, the subject concerning the connecting rod was chosen for its vibroacoustic damping requirements, along with the high service temperature.

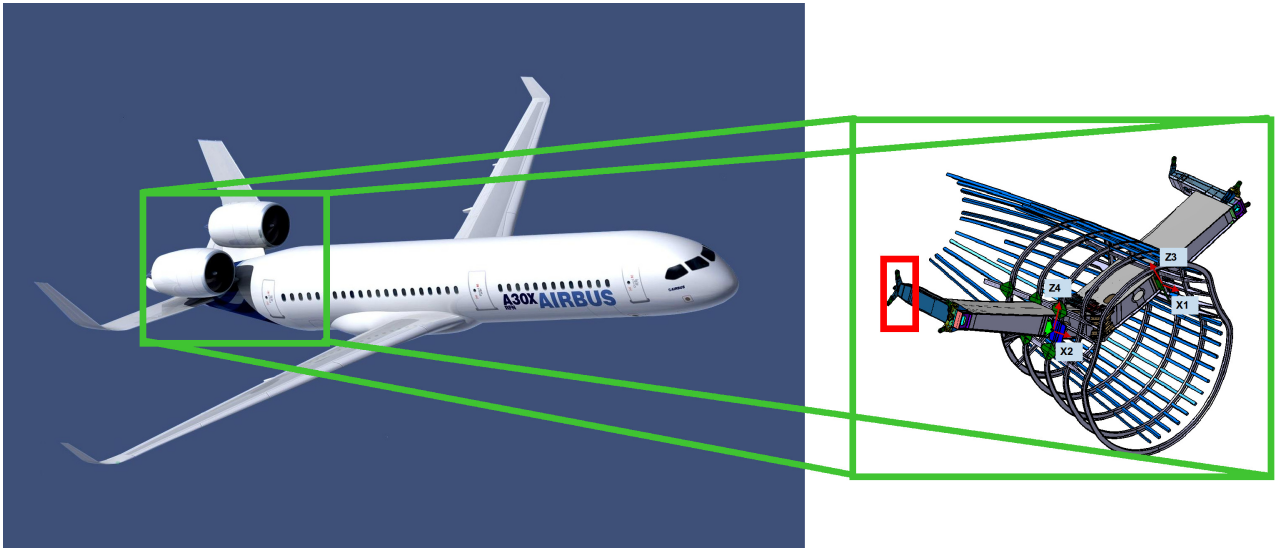


Figure 0.1: Location of the connecting rod (in red) at the tail of an airbus plane.

Figure 0.1 shows a schematic of the location of the connecting rod in the back part of a A30X plane. This connecting rod links the motor to the fuselage of the plane. When in operation, the rotor produces both heat (250 to 450°C, depending on the cooling state) and vibrations thus creating an extreme environment. The current existing piece, already being used at Airbus, is an Inconel 718

tube (700 mm long with a 100 mm diameter) with a thickness of 3-4 mm. The properties of Inconel 718 are shown in table 1. It was designed in order to be able to stand the mechanical load imposed on the rod, but from the rotation of the blades in the rotor, vibrations, that appeared from changes applied to the motor or the dimensions of the wing, are transmitted to the plane. Those vibrations have frequencies of around 20 and 50 Hz, which is susceptible to cause physical pain to passengers.

Density ( $\text{kg.m}^{-3}$ )	8220
Melting range	1210-1344 °C
Modulus of elasticity (GPa) at 20 °C	208
Modulus of elasticity (GPa) at 430 °C	186
Yield strength (MPa) at 430 °C	1076

Tableau 1: Inconel 718 technical data.

For this specific application, the idea is to add specific functions to an existing part. While preserving the mechanical strength of the structure, a vibratory damping function needs to be added. The inconel tube does not meet the damping requirements and this new function would thus have to be implemented to the already existing piece.

To solve this problem, the structure presented in Figure 0.2 was proposed, which integrates a mass/spring system inside the Inconel tube in order to act as a damper. In this type of arrangement, the different components have specific roles and materials need to be chosen adequately.

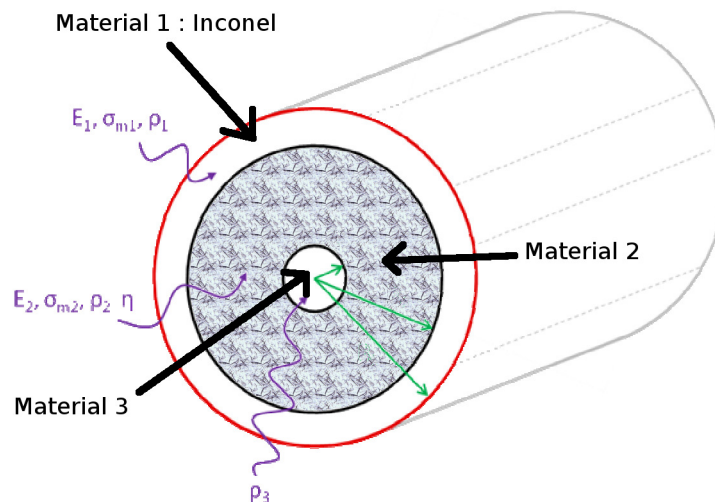


Figure 0.2: Damping solution : mass/spring damper.

The material 1 corresponds to the Inconel tube. It ensures the mechanical strength necessary to bear the weight of the jet engine. Inside this hollow cylindrical volume, a damper is inserted, composed of two different parts:

- Material 3 corresponds to the “mass” which oscillates when submitted to vibrations. It has to be selected in order to resonate at the given frequencies that are specifically targeted.

- Material 2 is chosen to transmit the oscillations to the “mass” while absorbing as much energy as possible.

A “material selection” approach was used in order to determine the materials as well as their dimensions that could allow to absorb the right frequency. The report on this analysis is presented in Appendix B. Taking into account most of the requirements, a set of materials was determined, but the high temperature resistance(450°) was not included as no solutions could answer to every specifications.

The analysis showed that, in order to fulfill the set of requirements, the material 2 had to be chosen with a shear modulus as low as possible and that the material 3 should possess a high density. It was shown that many polymers could be used as a material 2, but only few of those could resist at 250°C and none at 450°C. As a “mass”, tungsten or lead alloys would be suitable.

While the “spring-mass” system does satisfy the damping requirement once the dimensions have been defined, it can not, in this configuration, operate at high temperature. Architected materials can, in this type of situations, become very interesting as they can be tailored to specific needs. Entangled materials will thus be investigated in order to evaluate their capacity to replace the polymers as material 2. Considering that metallic fibers can be used, it will then be possible to use the assembly at high temperature, but the material will need to be optimized and characterized from the mechanical and microstructural point of view. This is the goal of this PhD project.

In the end, it was finally concluded that no bulk materials could answer to every requirements as the high temperature resistance was found to be incompatible with the required damping properties. For demanding multi-functionnal applications, bulk materials are often unable to combine all specifications and in this context, “architected” materials recently appeared as a good, adjustable, solution to this type of problems.

# Chapter 1

## Litterature review

*In this litterature review, the design of hybrid and sandwich structures will first be presented before focusing on entangled materials. A state of the art of “entangled materials” will regroup the data of the litterature and its limitations in order to identify the main influential parameters. To conclude, the strategy of this PhD work will be defined, as well as the outline of this manuscript.*

### Chapter’s content

1.1	Introduction to hybrid and sandwich structures . . . . .	8
1.2	Entangled materials : state of the art . . . . .	12
1.2.1	Fiber network with no permanent link . . . . .	12
1.2.2	Sintered wire mesh . . . . .	27
1.3	Conclusion . . . . .	28

Designing “architected” or hybrid materials for multi-functionnal applications enables the combination of conflicting properties which bulk materials could not possess. In this context, sandwich structures have been widely investigated and will first be reviewed before describing in more details a state of the art of “entangled materials” in order to highlight the decisive parameters of such a structure. Finally, the methodology used in this study, which includes manufacturing, characterizing and modeling the material of interest, will be introduced.

## 1.1 Introduction to hybrid and sandwich structures

This project being mainly centered around sandwich structures, the specificity of this material, and of hybrid materials in general, will first be introduced in order to better identify the ins and outs of its development.

Hybrid materials are defined ([1]) as the combination of two or more materials and of an architecture. The aim of this type of materials is to fill the empty areas of some important Ashby maps. Figure 1.1 shows the loss factor as a function of the stiffness. This shows the typical incompatibility between stiffness and damping but using hybrid materials is a way of obtaining a good compromise between the properties (example : equivalent to an elastomer) while, for example, including a high temperature resistance. In order to be able to fill the holes in the material’s space, the effective properties of the hybrid structures need to be measured, and this study will be an example of how we could add “new” materials to the existing database.

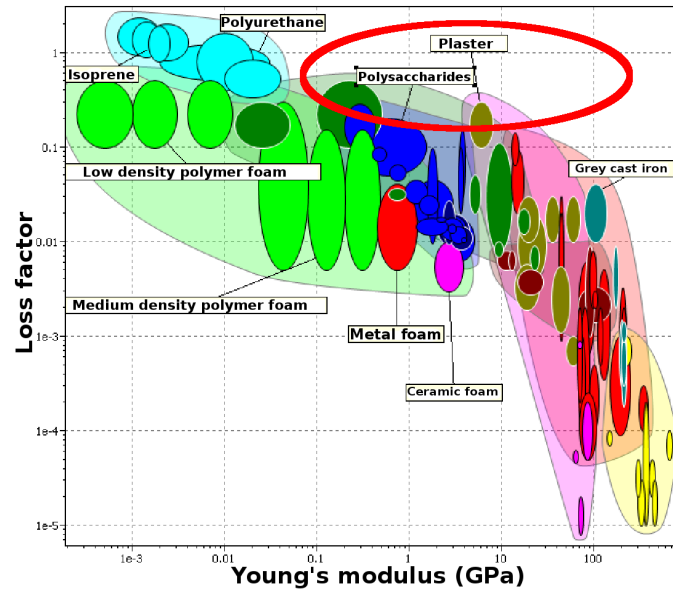


Figure 1.1: Ashby map of the loss factor as a function of the materials stiffness, taken from the CES software [2].

Figure 1.2 shows a schematic representation [1], on a map for two given properties, of the combination that can be made using any two material’s family : M1 and M2 (shown in gray). A few typical results of the hybridation are specified here :



- A : it correspond to the ideal solution. The hybrid materials then presents the best property of both materials. Fore example, applying a protective zinc coating to steel will combine the high stiffness of steel to the anti-corrosive properties of zinc, thus preventing rusting.
- B : it results in a rule of mixtures of materials M1 and M2. Often, when combining bulk properties in an hybrid, the best achievable result is the arithmetic average of the properties of the components, weighted by their volume fractions. Unidirectional fiber composites, in terms of axial modulus, are a good example of that.
- C : it is a scenario where “the weaker link dominates”, in which the hybrid properties fall below those of a rule of mixtures, lying closer to the harmonic than the arithmetic mean of the properties.
- D : This is the worst case scenario. It can never be an objective if the goal is to maximize the properties P1 and P2.

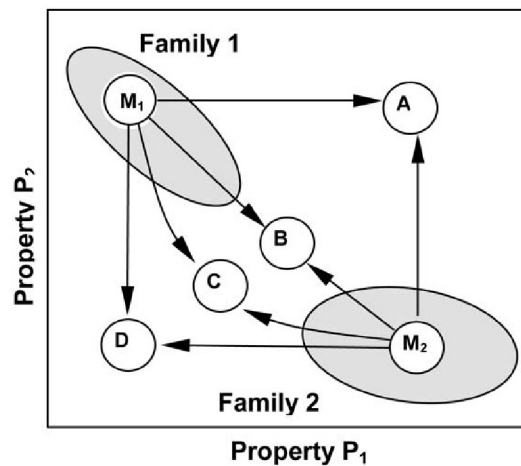


Figure 1.2: The possibilities of hybridization between two materials : M1 and M2. A few combinations of their properties are presented here (A,B,C and D) [1].

There is, on this topic, a duality about the way hybrid materials are perceived. On one side, materials like wood or composites, made of different components, are seen as stand-alone materials with their own sets of properties, whereas some, like galvanized steels, are defined as a combination of materials and of their properties, even though it could be seen as a whole new material. Sandwich panels, which will be presented in more details later, illustrate this duality as they are sometimes viewed as a combination of layers and sometimes as a material on its own, with a set of specific macroscopic properties : density, flexural strength and stiffness. Although sandwich structures are one of the most studied components in mechanical design, it is only recently that the possibility of systematic investigations of multifunctionnal applications was considered.

In this context, sandwich structures are one of the simplest and more common hybrid material. They correspond to the assembly of two thin, but stiff, skins to a thicker low-density core material (Figure 1.3). This core aims at separating the two skins, using a light material, in order to increase the moment of inertia and thus, the stiffness of the assembly, without increasing its mass significantly.

This layered structure allows for the combination of an infinity of materials and proportions. Sandwich structures are hybrid materials in which functions can be combined and specifically chosen

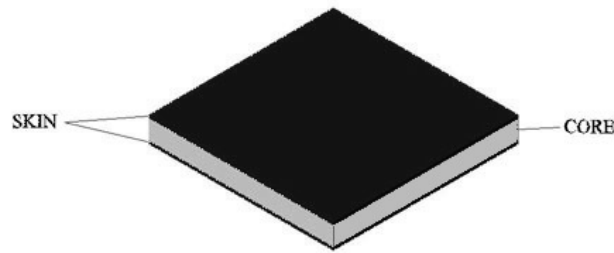


Figure 1.3: Schematic representation of a sandwich structure.

by carefully selecting the constitutive materials of each layer. In the following section, the properties of those materials will be presented.

### **Skin materials**

The materials used as skins need to possess good mechanical properties in both compression and tension. This will give the structure a strong flexural strength. Both metallic and non-metallic materials can be used. Flat panels are often used and, in the case of applications submitted to an external environment, they need to have a good surface finish and be able to resist to external stimuli and shocks.

The most common non-metallic materials that can be used are composites (carbon or glass fibers...). Their high modulus (20-200 GPa) combined to a low density make them suitable to act as skin material. They are often used in aeronautics or for high-end sport equipments as they can be very expensive.

For metallic materials, light materials such as aluminum are preferentially used as it allows to lighten the structure. For light enough sandwich structures, steel can be used and thus strengthen the resulting material. We can already notice that by combining one of these “dense” materials with a very light, and possibly porous, material (elastomer, honeycomb,...), metal manufacturers, such as Alcan or ArcelorMittal, can easily obtain lighter solutions with a high rigidity and energy absorption.

### **Core materials**

Core materials are usually materials with low densities which will act as a separator of both skins. It thus needs to exhibit a sufficient rigidity in the direction perpendicular to the skins. It is mostly submitted to shear loadings and thus needs to have a high shear strength to ensure the rigidity of the structure. Most of the functions (thermal insulation, energy absorption) that can be added depend on the choice of the core material. In this context, many different types of core materials can be used.

- Bulk materials can be used as core materials. They are easily obtainable and the manufacturing process is relatively simple and straightforward. Moreover, their intrinsic properties are well known and modeled.
- Cellular materials : historically, wood (balsa) was used as a core material. This cellular material was used in the very first project that included sandwich structures, the manufacturing of the British combat aircraft “De Havilland Mosquito”. Its low density (0.1 to 0.25) as well as its high mechanical properties in the longitudinal direction (parallel to the fibers) were particularly interesting for this application.

But processed materials such as foams ([3]) are now widely used in sandwich structures. Foams correspond to highly porous materials that can be made of either ceramics, polymers or metals. More recently, hollow spheres stackings have been investigated as a core material ([4]). They present the specificity to possess both closed and open porosities and are thus very interesting in terms of acoustic properties.

Finally, entangled fibers (carbon, glass, aramid...) networks have been investigated ([5–7]) for the simplicity of the manufacturing process, the freedom in terms of shape and constitutive materials and their high porosity.

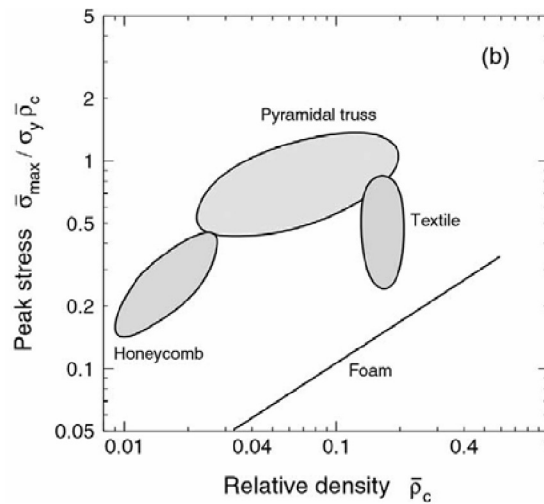


Figure 1.4: Comparison of the peak stress as a function of the relative density for textiles, foams, honeycomb and truss structures [8].

- Honeycomb structures are natural or man made structures that have the geometry of a honeycomb to allow the minimization of the amount of used material and thus the materials' cost and weight. The shape of the 2D pattern can vary (square, hexagon, triangle,...) and provide specific properties, depending on its proportions. It can be composed of either metal, paper or polymers.
- Engineered structures can be developed and optimized in order to add specific properties while minimizing the weight. Their 3D, regular, geometry is particularly interesting to control the local properties of the structure (it is for example possible to obtain, locally, a higher tensile strength).

Figure 1.4 shows a comparison of the mechanical strength of the different materials presented here.

## Adhesives

The core is bonded to the skins with an adhesive (epoxy or polyurethane glues, ...) or, for metal components, by brazing them together. The strength of the final structure greatly depends on the interface between core and skins. Shear stresses are indeed transmitted through the adhesive and if the bond is too weak, it will most probably result in delamination.

To conclude, the possibilities of developments are endless and materials can be tailored in order to answer to particular specifications. In a way, the structure presented in section 0.2.2 can be seen as a sandwich structure with a cylindrical symmetry and any new material needs to be thoroughly investigated in order to be able to estimate the potential of any given assembly.

### 1.2 Entangled materials : state of the art

In this context of hybrid, or architected materials, entangled materials appear as an obvious solution as they can be easily processed and allow for many manufacturing parameters to be modified. Although many studies were carried out on fiber entanglements as reinforcements for composite materials [9–11], only a few were performed on the entangled media itself [12, 13].

This section aims at presenting a review of the literature on entangled media from both an experimental and numerical point of view. The properties of entanglements with either sliding or fixed contacts will be introduced and their benefits for different types of application will be highlighted.

#### 1.2.1 Fiber network with no permanent link

Generally, entangled materials are defined as a network of elongated objects (high shape ratio: one dimension much higher than the others). Many parameters then influence the behavior of this type of material such as the state of the contacts (permanent or sliding), the rigidity of the fibers, their initial shape, the orientation distribution.

##### 1.2.1.1 Experimental work

The study of the compressive behavior of entangled media started over 70 years ago but the microstructural evolution (number of contacts, reorganisation) of the structures has not yet been fully investigated because of the complexity of the internal architecture of this type of material. The first studied materials were natural materials ([14]) such as sheep wools [12]. Van Wyk [15] used it as well to compare experimental results to his first analytical model on the compressibility of fibrous materials. More recently, synthetic materials such as glass wools [16], steel wools [17], or aluminum wools [13], were investigated. The analysis of the behavior of fiber bundles also attracted a lot of attentions for its use in the analysis of fiber reinforced composites [18–22].

In 2005, Poquillon et al. [13], tested comparatively the behavior of many different types of entangled materials, from carbon nanotubes to glass wool and human hair. In this study, materials were loaded in guided uniaxial compression (inside a cylindrical die) as shown in Figure 1.5. The results of this analysis are shown in Figure 1.6.

A strong non-linearity was observed for all materials. This can not be explained by the behavior of singles fibers alone since fibers showed a linear elastic behavior at the beginning of tensile tests. A remaining plastic deformation was observed as well for every material but it was more or less pronounced depending on the properties of the fiber. For elastic fibers, the residual strain appeared to be quite constant for increasing load levels (Figure 1.6) whereas it is load-dependent for fibers with an important plastic domain. This indicates that the general compressive behavior is due to the

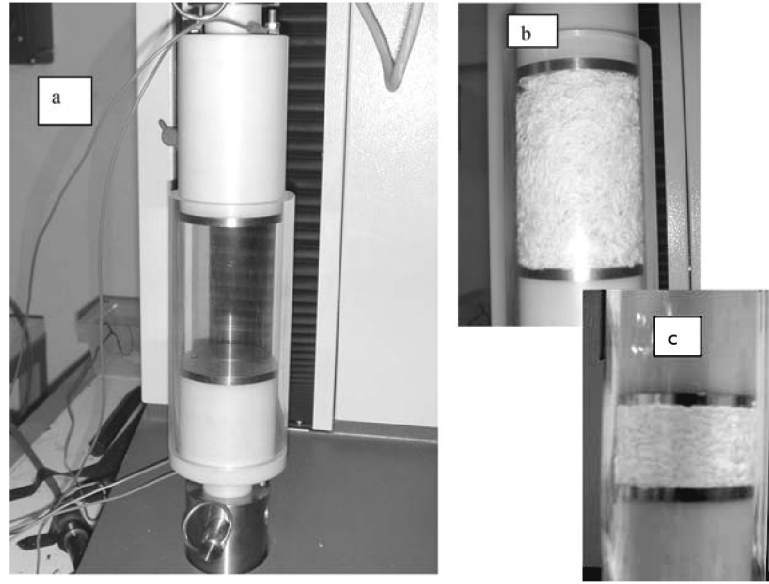


Figure 1.5: Experimental device (a) used by Poquillon et al. for guided uniaxial compression tests. Sample at the beginning (b) and end (c) of the test [13].

architecture of the material and to rearrangement and friction of fibers.

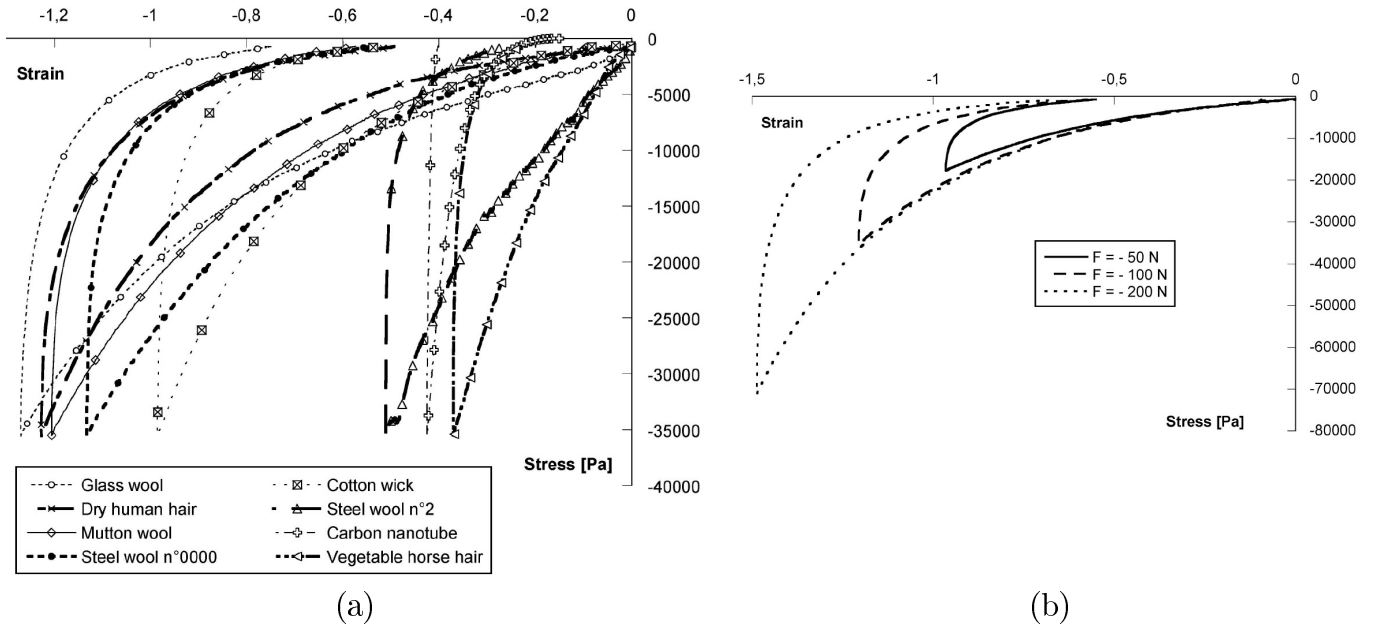


Figure 1.6: (a) : Stress-strain curves for all materials tested in [13] and (b) : Load-unload cycles for increasing loads [13]

The authors also observed a different behavior when loading and unloading all samples. During cyclic deformation, the hysteresis was shown to reach a stable state after 2 or 3 cycles (Figure 1.7). The internal architecture of the material is thus modified by the first compression before reaching a stable geometry. Once obtained, it would not be affected by the cycles anymore and one can suppose that the fibers would bend while staying relatively still. Bending was thus supposed to be the common

deformation mechanism to all those different materials. This hysteresis phenomenon was previously pointed out by other studies [17,23–27].

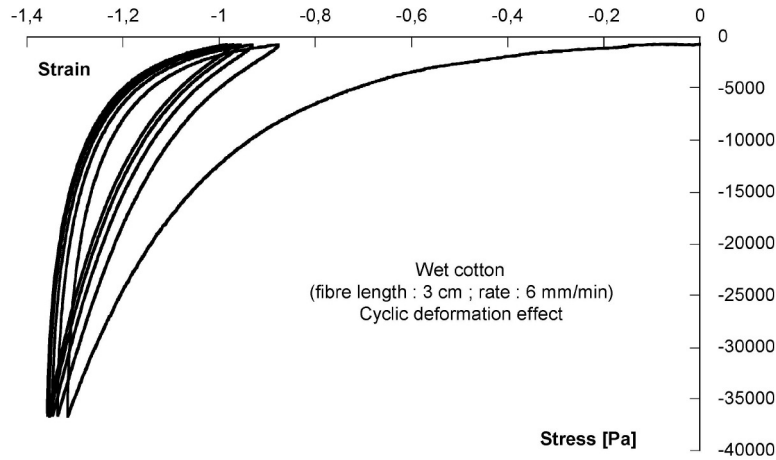


Figure 1.7: Cycling of a sample made of humid raw cotton fibers.

A systematic approach of entangled materials was developed in this study and a few typical behaviour, such as the remaining plastic deformation and the hysteresis cycles, were highlighted. In parallel to the mechanical analysis, a study of the evolution of the internal microstructure is missing in order to identify the mechanisms controlling the deformation.

Following this study, some more work was done by Masse et al. on the compressive behavior of steel wools [17]. Masse’s PhD aimed at linking the microstructural properties of the network of fibers to the macroscopic properties of the wool. X-ray tomography analysis were performed in order to achieve quantitative measurements of structural parameters. Both the number of contacts and the orientation of fibers were followed during compression. On the mechanical point of view, unloading sequences were performed in order to measure the stiffness of the structure and to observe the usual hysteresis phenomenon characteristic of entangled media.

Figure 1.8 presents the 3D volumes acquired in tomography for different volume fractions of steel wools. It was noticed that the fibers were oriented preferentially in the  $x_2$  direction and that this tendency seemed to increase with the relative density.

The number of contacts between fibers was measured by either computing the local curvature of the interface between the steel fiber and the air. The interface of a single fiber will indeed be convex whereas the one of a contact between two fibers will be concave. So by measuring, for each point of the interface, the local curvature, and by then segmenting the resulting image, the position of the contact points can be determined. Another way to measure the number of contacts (which will be described in more details in section 3.2.3) is to use the skeleton of the binary 3D image. In this skeleton, a contact will indeed be defined by a short segment with a length lower than the fiber diameter.

So for each 3D volume, the number of contacts can be measured and Figure 1.9 shows the evolution of the number of contacts per unit volume (in  $\text{mm}^{-3}$ ), with the relative density for non-loaded samples, measured experimentally and compared with a calculation using the tube model ([28])

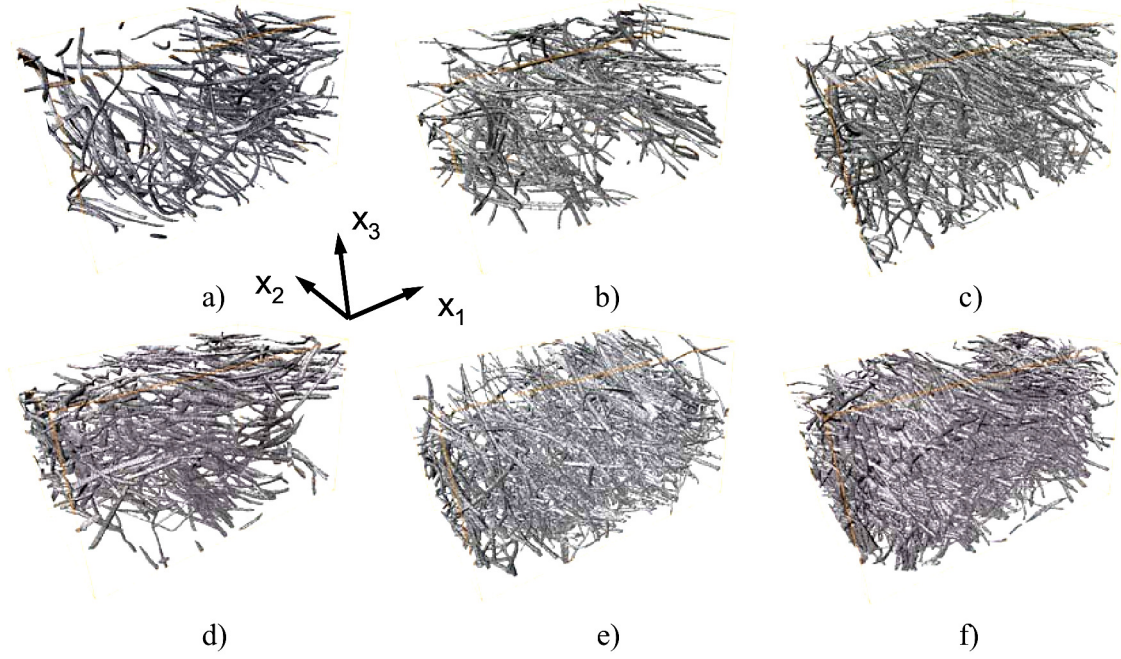


Figure 1.8: 3D visualization 6 steel wool samples with volume fractions of : (a) 1.64%, (b) 2.1%, (c) 2.59%, (d) 3.4%, (e) 3.93% and (f) 5.43%.

which defines the number of contacts per unit volume as :

$$N_{cv} = \frac{16f}{\pi^2 d_f^3} \rho^2 \quad (1.1)$$

where  $d_f$  is the diameter of the fibers,  $\rho$  the relative density and  $f$  is a parameter describing the orientation distribution of the entanglement.

Fibers show a mean diameter of around  $80 \mu\text{m}$  and the error bars correspond to measurements made for a diameter of  $70$  and  $90 \mu\text{m}$ .

The agreement between experimental values and the tube model was shown (figure 1.9) to be not very good for low relative densities (inferior to 3%) but quite good for higher relative densities (the relative error was found to be below 10%). By fitting the experimental points with a power law, an exponent of 1.87 was found. In the case of the model, an exponent of 2 is expected. This discrepancy can be explained qualitatively if we consider that the “rigid fibers” hypothesis will tend to be more and more valid with the relative density since the distance between contacts will tend to decrease.

The behavior of the fiber network was then studied under compressive loading. The evolution of a sample (2.9% initial relative density) with the compression was followed thanks to the in-situ acquisition of 3D volumes in tomography.

Figure 1.10(a) shows the evolution of the compressive stress as a function of the relative density for fiber networks with different initial volume fractions. It was shown that, for the same relative density, higher stress values are observed for wools with a lower densities until a volume fraction of around 10% for which curves come together. On this log-log plot, it was also noticed that, after a

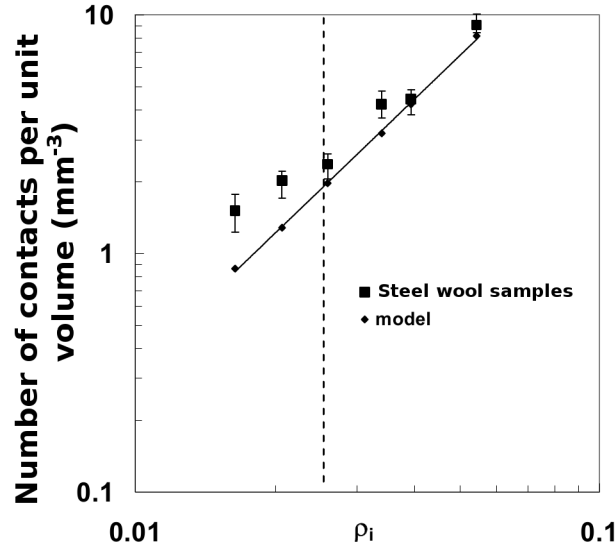


Figure 1.9: Evolution of the number of contacts per unit volume measured experimentally and by using the tube model [28] in steel wools [29].

brief transitional state, the stress evolution is linear, thus indicating that it follows a power law with the relative density ( $\sigma \propto \rho^n$ ).

Many different samples were compressed and Figure 1.10(b) shows the evolution of the exponent  $n$  as a function of the threshold relative density, which corresponds to the relative density from which a force is detected on the compressive device. This exponent varies between 3.2 and 4.5 and seems to reach a limit above 2.6%. These values are in good agreement with theoretical ones that were found in [28] and that will be presented in more details in the following section. This model predicts a value of 3 for a 3D arrangement and 5 for a 2D network. Experimental values are thus very close to the literature and it would appear that the wool tends to become 2D-arranged with the volume fraction.

Using in-situ X-ray tomography, a microstructural and a mechanical analysis of a steel wool could be combined and parameters, descriptive of the structure's behaviour, were defined. However, the complex shape of the fibers (irregular cross-section) made the discretization process difficult and individual fibers could not be separated. In order to be able to model the mechanical properties of experimental samples using a Discrete Element Method (presented in the following section) and thus be able to compare it to the experimental results, a model material, composed of regular fibers with a circular cross-section, facilitate the task.

In terms of in-situ microstructural characterization, Latil *et al.* [18] studied the evolution of the microstructure of a bundle of fibres under uniaxial compression. A dedicated micro-compression rheometer, which can be mounted on a synchrotron X-ray tomograph, was developed. Consequently, 3D volumes of the evolving fibrous microstructure could be obtained.

Following a standard thresholding operation, a 2D watershed allowed to define, slice by slice, the center of mass of each cross section and subsequently, to obtain the complete skeleton of each fiber.

In this study, the entanglements were prepared manually from a fluorocarbon fishing wire with a 150  $\mu\text{m}$  diameter. Volumes were acquired for different strains and the position, orientation, dis-



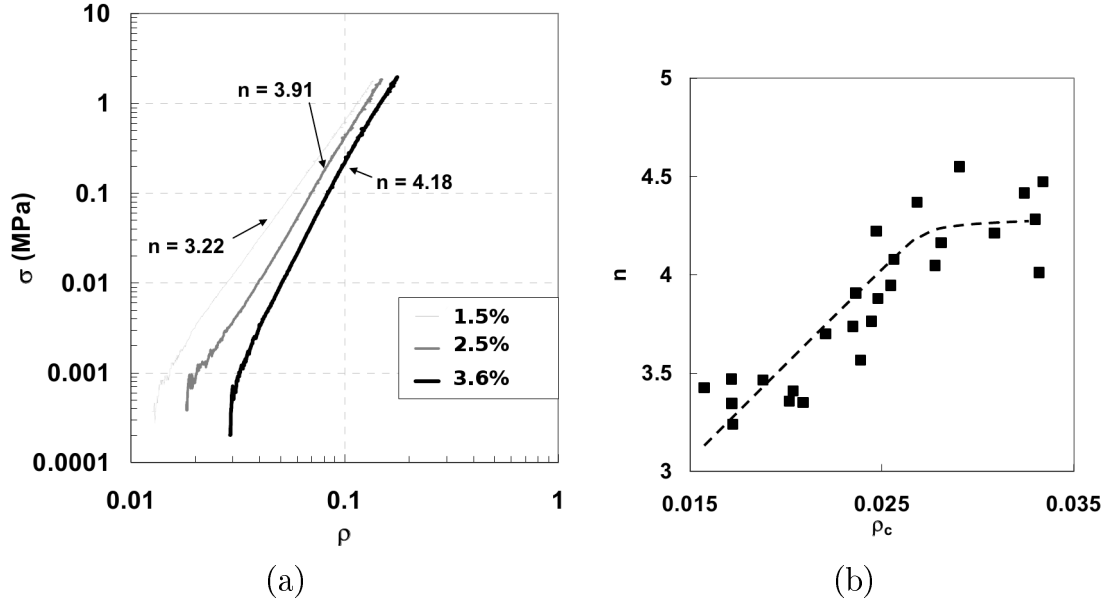


Figure 1.10: (a) : Log-log representation of the stress as a function of the relative density and (b) : Evolution of the power law exponent ( $\sigma \propto \rho^n$ ) as a function of the threshold relative density [29]

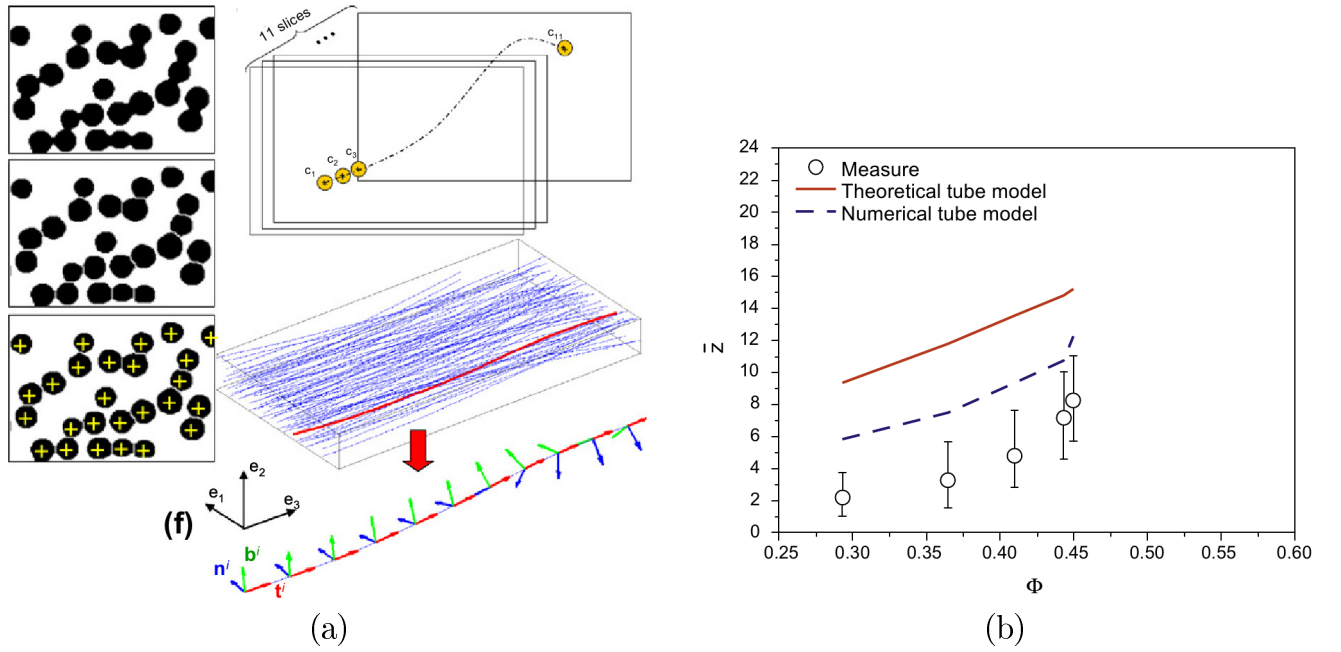


Figure 1.11: (a) : Method used to detect and characterize the centerlines of the fibers and (b) : Evolution of the number of contacts per fiber (coordination number) as a function of the volume fraction [18]

placement and deformation of each fiber, together with the position and evolution of each fiber-fiber contacts were followed. Figure 1.11(a) describes the method that was used in order to detect and characterize the fiber centerlines.

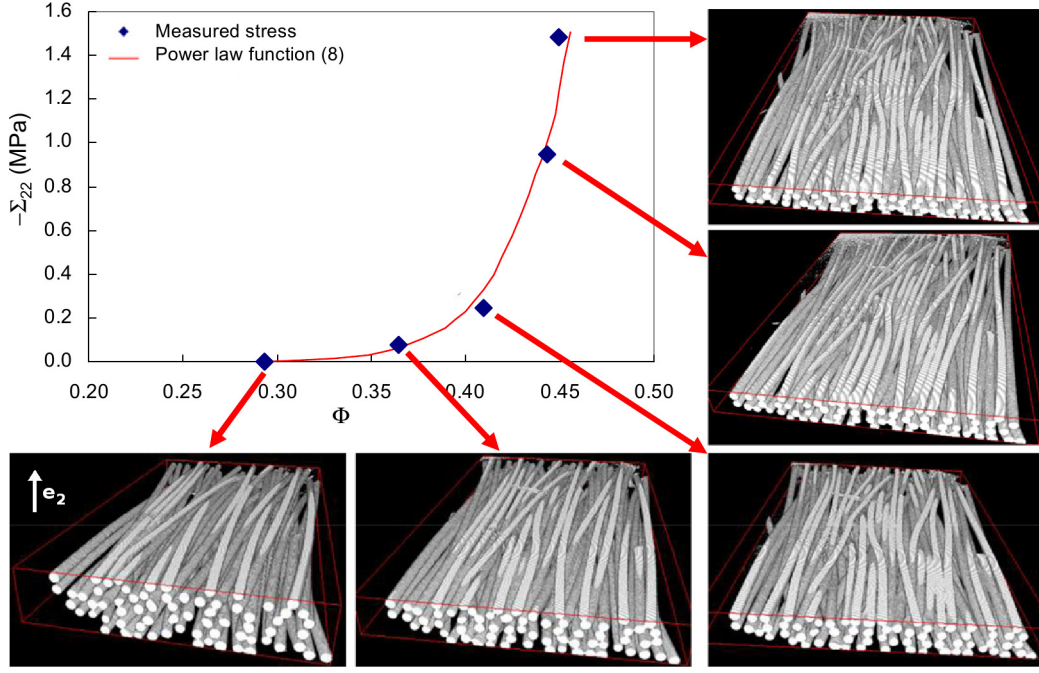


Figure 1.12: Evolution of the compressive stress as a function of the volume fraction, along with 3D segmented volumes for five compression steps [18].

Figure 1.12 shows the evolution of the mean compression stress  $\Sigma_{22}$  as a function of the volume fraction, along with 3D representations of the entanglement. The mesoscopic mechanical response of the studied bundle is characterized by strong consolidation and hardening effects, typical of the compressive behaviour of entangled media. This behaviour is closely linked to the actual microstructure of the bundle and its evolution. The evolution of the number of contact per fiber was thus studied and Figure 1.11(b) shows its evolution as a function of the volume fraction, compared to a calculation using the “tube” model [28]. Although the experimental trend is more or less reproduced, the analytical tube model largely overestimates the experimental coordination number, mostly because the tested material does not fulfil the hypothesis of the model as fibers are not homogeneously distributed (in particular along the  $e_3$  direction).

Accordingly, the stress levels were shown to depend on microstructural parameters such as the number of contacts. However, the strong heterogeneity of the entanglement prevented the experimental results from validating microstructural models from the literature.

To conclude, the relations between microstructure and mechanical properties ([30]) are, in this type of entangled materials, very important. Thanks to X-ray tomography, structural parameters could be measured and linked to the macroscopic mechanical response of the fiber network.

Finally, a few studies were performed regarding the influence of a “closed matrix” configuration on the microstructural properties of entangled materials. It was first shown that entanglements, prepared inside a cylindrical die, exhibited a strong radial heterogeneity [31], which was successfully lowered by using pre-coiled wires [32]. This technique will be described in more details in the next chapter.

### 1.2.1.2 Analytical models

The historical model the compressive behavior of fiber entanglements was developed by Van Wyk in 1946 [15]. It involved random 3D arrangement of fibers. It was later completed and refined by Toll in 1998 for random 2D structures. Both those models are mainly dimensional analyses and are based on the same assumption that fibers are deformed by bending between contact points. Figure 1.13 shows the schematic representation of this specific deformation mechanism.

The model for estimating the number of contacts as a function of the density will be detailed first,

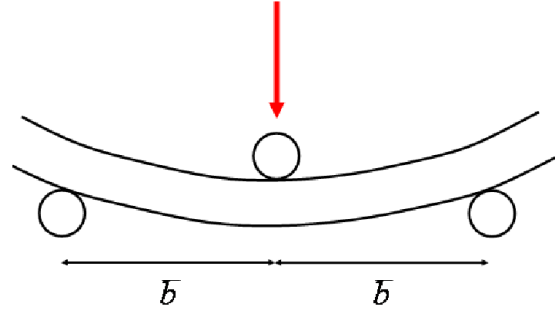


Figure 1.13: Schematic representation of the bending mechanism.

before presenting the micromechanical approach of Toll's model [28]

#### Number of contacts

The “tube model” is based on the hypothesis that fibers are straight, infinitely rigid and spread homogeneously in the material. In many studies done on the number of contacts in fibrous materials, the common fact was the determination of an excluded volume. It is defined as the volume around a fiber in which the center of a similar object can not penetrate. This volume depends on the geometry of the fibers and their orientation distribution in the material. This type of model developed in [33–35] and are presented in more details in [36].

In the model developed by Toll [28, 37], the initial fiber assembly, constituted of straight fibers with a circular cross-section, is created by adding “phantom” fibers successively, which can interpenetrate each other, and by then adjusting their position such that they no longer interpenetrate but are just in contact. The volume surrounding each cylindrical fiber, in which the center of fibers intersecting it can be present, is studied and when inserting a new fiber, the number of contact points in the network is estimated as the number of volume intersections in this random network of interpenetrating fibers. This volume depends on the geometry of the fiber and on the orientation distribution of fibers which can be described by the following scalar invariants :

$$f = \frac{1}{N_f^2} \sum_{\alpha} \sum_{\beta} \|p_{\alpha} \times p_{\beta}\| \quad (1.2)$$

$$\text{and } g = \frac{1}{N_f^2} \sum_{\alpha} \sum_{\beta} \|p_{\alpha} \cdot p_{\beta}\| \quad (1.3)$$

where  $N$  is the total number of fibers and  $p_{\alpha}$  and  $p_{\beta}$  are the direction vector of fibers.

Thereby,  $f$  is proportional to the mean cosine of the angle between two fibers whereas  $g$  is proportional to the sine. In the case of a few particular cases,  $f$  and  $g$  take the following values :

- $f=\pi/4$  and  $g=0.5$  for a 3D random orientation
- $f=g=2/\pi$  for a 2D random orientation
- $f=0$  and  $g=1$  for aligned fibers.

The average number of contacts per fiber was then demonstrated to be equal to :

$$\bar{N}_{cf} = 8\frac{r}{\pi}\rho f + 4\rho(g + 1) \quad (1.4)$$

where  $\rho$  is the relative density and  $r$  is the average fiber aspect ratio (length of the fiber/diameter of the fiber).

We can notice that for non-aligned slender fibers ( $f, g \sim 1$  and  $r \gg 1$ ), Equation 1.4 reduces to :

$$\bar{N}_{cf} = 8\rho\frac{r}{\pi}f \quad (1.5)$$

The average spacing  $\lambda$  between contact points along a fiber can thus be written as :

$$\bar{\lambda} = \frac{l}{\bar{N}_{cf}} \quad (1.6)$$

or for non-aligned slender fibers, using Equation 1.5 :

$$\bar{\lambda} = \frac{\pi d}{8\rho f} \quad (1.7)$$

Since the material is described by a relative density, it can be said that the number of fibers per unit volume,  $N_{fv}$ , corresponds to the relative density divided by the volume of one fiber :

$$N_{fv} = \frac{4}{\pi d_f^2 l_f} \rho \quad (1.8)$$

It was then showed that multiplying the number of fiber per unit volume by  $\bar{N}_{cf}/2$  yields the number of contact points per unit volume, thus giving :

$$N_{cv} = \frac{16f}{\pi^2 d_f^3} \rho^2 \quad (1.9)$$

From this model, it is then possible to link the number of contacts per unit volume and the mean length between contacts to the relative density through relatively simple equations. Considering the pivotal role of contact points in the mechanical behavior of entangled material, the knowledge of this relations is necessary in order to have a good understanding of the microstructural evolution of a fibrous material under compressive loadings.

### Modeling of the mechanical stress under loading

The micromechanical approach defining the stress during compression was developed by Toll ([28]). It considers that the total pressure on the entanglement, in the case of uniaxial compression,

can be written as :

$$\sigma = \eta \bar{h} f \quad (1.10)$$

where  $\eta$  is the number of deformation units (shown in Figure 1.14 per unit volume,  $h$  is the height of the deformation unit and  $f$  is the force exerted on it.

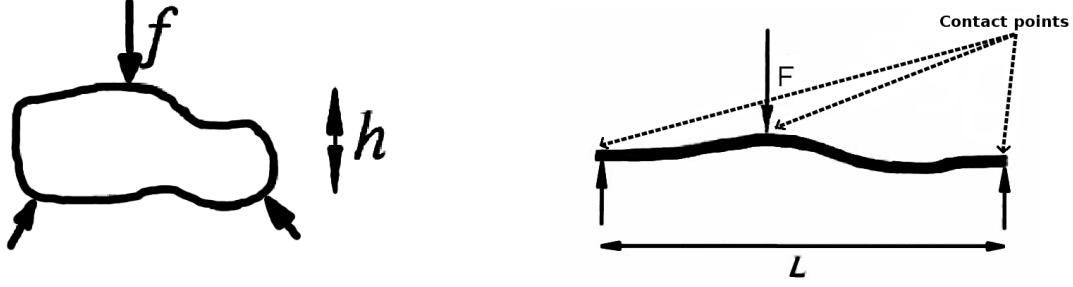


Figure 1.14: Schematic representation of the deformation unit considered for the mechanical analytical model. Fiber segments are loaded in 3-point bending between contact points [28].

By considering that the total pressure only depends on the relative density, it can be written as an integral of the relative density. And if one considers bending as the deformation mechanism of fibers,  $\sigma$  writes :

$$\sigma \propto \int_0^{\rho} \frac{N_{cv} h^2}{\rho \frac{L^3}{E_f d^4}} d\rho \quad (1.11)$$

As each parameter depends on the relative density, it was shown, by rearrangement of Equation 1.11, that the stress can finally be written as :

$$\sigma = k E_f (\rho^n - \rho_0^n) \quad (1.12)$$

where  $\rho_0$  is the fiber volume fraction where the compressive force is different than zero,  $E_f$  is the Young Modulus of the fibers and  $k$  is a multiplicative factor that depends on the loading direction. Two extreme cases can be considered : fiber networks with either a random 3D or 2D distribution. The corresponding elementary cells are shown in figure 1.15.

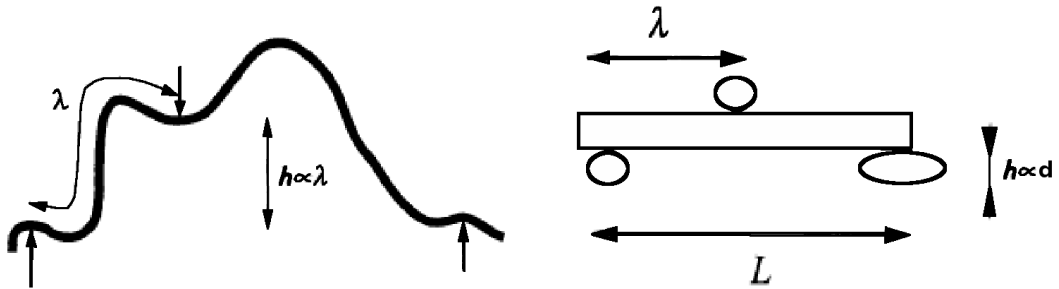


Figure 1.15: Deformation unit cell for a 3D (a) and 2D random distribution [28].

In both cases, the orientation is supposed to be constant while compressing the network and the length of the beams is taken as the distance between contacts. As for the height of the deformation cell, it was set to the length between contacts in the “3D random” case and will thus evolve with the compression, and to the diameter of the fibers in the “2D random” case (it is thus constant). The relationship, as a function of the relative density, deduced from this analysis, are shown in table 1.1.

	2D random	3D random
$N_{cv}$	$\propto \rho^2$	$\propto \rho^2$
$L$	$\propto \lambda \propto \rho^{-1}$	$\propto \lambda \propto \rho^{-1}$
$h$	$\propto d$	$\propto \lambda \propto \rho^{-1}$
$n$	5	3

Tableau 1.1: Parameters dependence on the relative density [28].

Although well established for many entangled materials, this model was developed for straight, rigid fibers and does not account for any “boundary conditions” such as for an oedometric compression. By comparing it to experimental results, correlations could be defined in order to adapt it to new experimental materials.

#### 1.2.1.3 Numerical models

A few methods were developed in the past few years in order to model the behavior of entangled fibers. Those models were able to provide data in terms of rearrangement of fibers and hysteresis. Two main models will be presented in more details here. The first uses a Finite Element Method whereas the second one is based on Discrete Element.

#### Finite Element

Durville [38, 39] considered, in the reference configuration, a collection of straight cylindrical fibers. Those long, infinite fibers were inserted in a cubic cell with periodic boundary conditions. Each fiber was identified by a succession of curvilinear segments defined by an abscissa and two vectors characterizing its cross-section. The author described the kinematics of each cross-section by means of three vectors : one for the translation of the center of the section, and two for the variation of the cross-section directors. The global problem was set in the form of a principle of virtual work, which includes the virtual works of all beams of the collection, and the virtual work of contact-friction interactions between fibers. The detection of contacts between fibers turned out to be one of the main difficulties of the problem. In the media considered, since the geometry and arrangement of fibers evolve, contact appeared and disappeared continuously. The number of contacts did indeed increase as the medium was getting more dense and friction was introduced into the model through a regularized Coulomb’s law, which allows a small reversible displacement before the pure sliding to occur. The tangential reaction was expressed as a function of the tangential relative displacement :

$$if \ \Delta \mathbf{U}_T \leq u_T, \ \mathbf{F}_F = \frac{\mu ||\mathbf{F}_I||}{u_T} \Delta \mathbf{U}_T \ else \ \mathbf{F}_F = \frac{\mu ||\mathbf{F}_I||}{||\Delta \mathbf{U}_T||} \Delta \mathbf{U}_T \quad (1.13)$$

where  $\Delta \mathbf{U}_T$  is the tangential relative displacement,  $\mathbf{F}_F$  is the tangential friction component,  $\mathbf{F}_I$  is the normal friction component,  $\mu$  is the friction coefficient and  $u_T$  is the adjustable reversible tangential displacement.

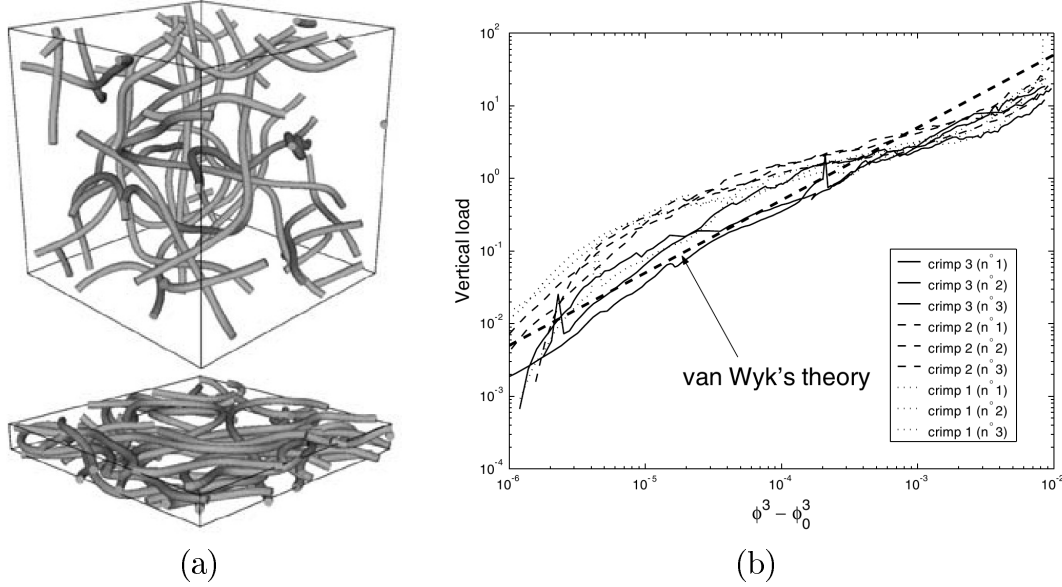


Figure 1.16: (a) : 3D representation of the initial and final compression state of a sample and (b) : Superposition of the simulated loading curves with the theoretical measurements of Van Wyk [38]

Samples with different tortuosities were generated and compressed up to high strains ( $\sim 90\%$ ). Figure 1.16(a) shows the 3D representation of the fiber network before and after compression. It was observed from Figure 1.16 that, for low deformations, the simulation was in good agreement with Van Wyk's theory [15] as the stress, on a log-log scale, increases as a function of the difference  $\phi^3 - \phi_0^3$  with the same exponent : 3.

Although friction is taken into account in this model, it is very time consuming and simulations are limited to relatively small volumes. Large strains can however be applied and the friction behaviour and contact detection are well described.

### Discrete Element Method

The behavior of entangled materials under compressive loadings was modeled using a Discrete Element Method in [40, 41], where semiflexible fibers were modeled using molecular dynamics techniques developed for the simulation of polymers [42]. Fibers were discretized as a succession of spherical elements whose positions are the degrees of freedom of the model. The behavior of the fibers was modeled by means of a potential energy (Equation 1.14 which takes traction, bending stiffness, as well as nonpenetrability between fibers into account.

$$\begin{aligned}
E = & \sum_{\substack{(i,i+1) \\ \text{consecutive}}} \frac{K_S}{2} \left(1 - \frac{r_{i,i+1}^2}{D}\right) + \sum_{\substack{(i-1,i,i+1) \\ \text{consecutive}}} \frac{K_B}{2} (\theta_i - \pi)^2 \\
& + \sum_{\substack{(i,j) \text{ non} \\ \text{consecutive}}} \frac{K_I}{2} H(D - r_{i,j}) \left(1 - \frac{r_{i,j}}{D}\right)^{5/2}
\end{aligned} \tag{1.14}$$

The traction stiffness of the wire was modeled by linear springs between consecutive nodes which could be fitted to the material's properties (Young's modulus) by controlling the  $K_S$  value. The second part of Equation 1.14 corresponds to the bending stiffness of the fiber which was introduced by means of angular springs between consecutive pairs of nodes. Since the fibers were considered as initially straight, the equilibrium angle for this spring was  $\theta = \pi$ . Interactions between fibers was modeled by a repulsive pair potential (third part of Equation 1.14) which only contributed to the total potential energy when the distance between nonconsecutive nodes became less than the fiber diameter  $D$ . A Hertz contact potential for elastic indentation between spheres was chosen which means that the fibers could be seen as a "pearl necklace" constituted of beads with a diameter  $D$ .

Fibers were initially straight and oriented at random in a cubic cell with periodic boundary conditions. Isostatic compressions were performed by decreasing incrementally the cell size. Fibers were thus translated affinely at the beginning of each increment and the system was then relaxed until an equilibrium state was reached by running a "quench" algorithm (variation of the VERLET algorithm where the nodal inertial term was set to zero whenever the scalar product of the force on a node by its velocity was negative) for a few hundred thousand timesteps. This allowed for very low oscillations around the minimum energy and thus, a faster convergence.

Using this model, the authors aimed at studying, as a function of the fiber's aspect ratio ( $\alpha = \frac{\text{Length}}{\text{Diameter}}$ ), the mechanical percolation of the entanglement and the following deformation stages, since the fibers could be deformed elastically. Figure 1.17(a) shows the evolution of the number of contacts per fiber and of the corresponding potential energy with the relative density of the entanglement, for different aspect ratios.

A clear transition region could be noticed between two equilibrium states : one where fibers are not touching and one where they interact with each other. In this second region, the number of contacts per fiber and the total potential energy were increasing. At the transition, some configurations were not reaching an equilibrium and are shown by smaller symbols. It was observed that fibers with a relatively low shape ratio ( $\alpha < 100$ ) showed up to around 8 contacts per fiber at the mechanical transition. This number appeared to decrease for increasing value of  $\alpha$ . From this, a percolation relative density was defined for each aspect ratio and Figure 1.18(a) shows its evolution. On this graph, the values presented by Williams et al. [43] were reported (small circles) alongside the numerical results from the simulations (big symbols). Rodney *et al.* used the following relation for aspect ratios between 20 and 50 :  $\rho_C = \frac{4.6}{\alpha}$  which presents a 4.6 value where the excluded volume's theory presents a slightly higher value for a perfect fit : 5.1.

Authors also investigated the relationship between the potential energy per fiber and the difference between the relative density in compression and the percolation relative density. They



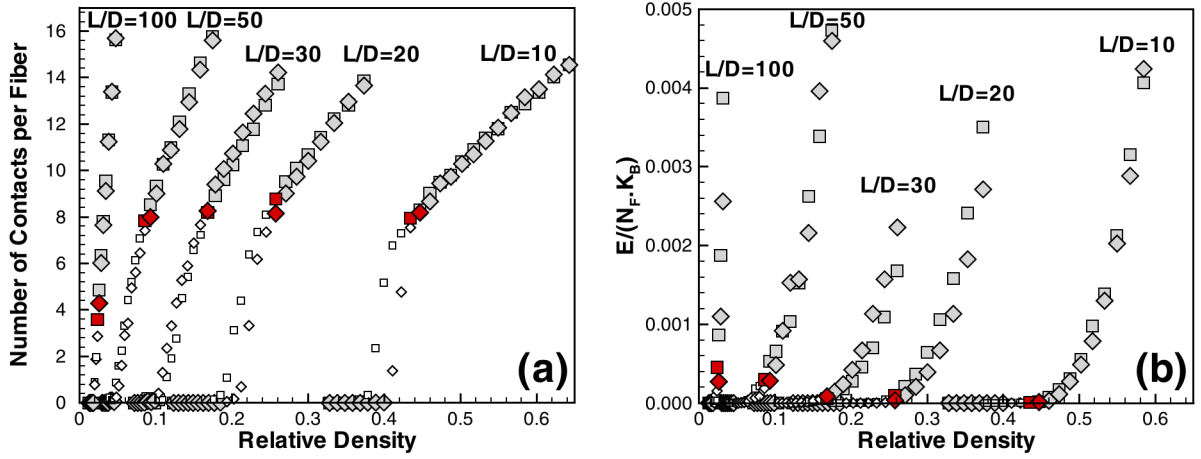


Figure 1.17: Evolution of the number of contacts per fiber (a) and of the potential energy per fiber (b) as a function of the relative density and aspect ratio (simulations by Rodney et al. [40]).

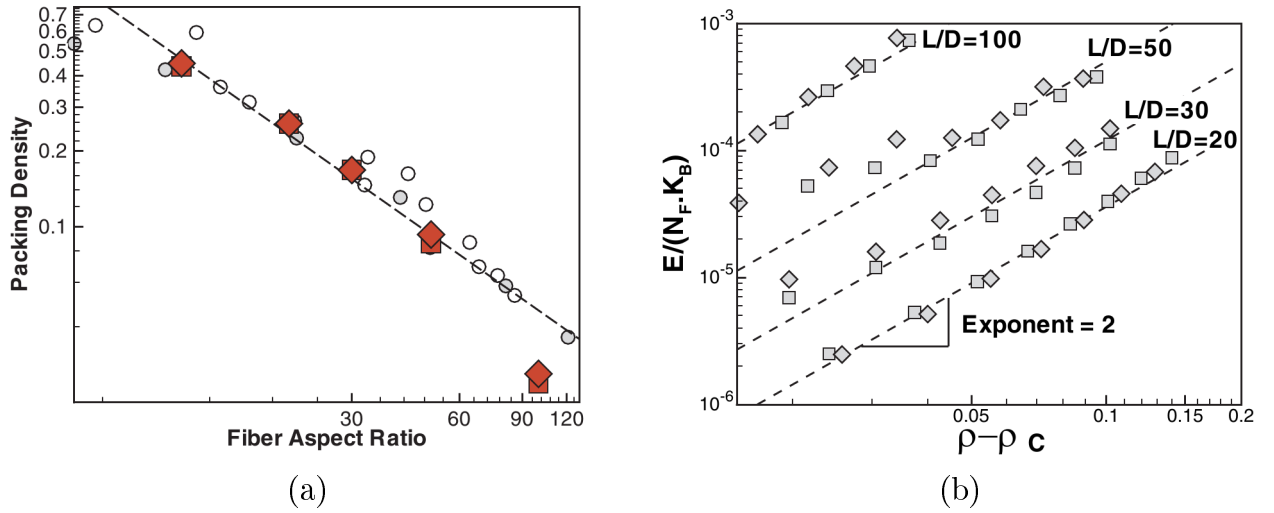


Figure 1.18: (a) : Evolution of the percolation relative density with the aspect ratio and (b) : Log-log representation of the potential energy per fiber as a function of the difference between the relative density in compression and the percolation relative density (simulations by Rodney et al. [40])

observed a behavior where  $E/N_F \approx (\rho - \rho_c)^\gamma$  with  $\gamma=2$ . This allowed them to determine an exponent of 3 between compressive pressure and relative density. This results differed from the literature as pressure was shown to depend on  $(\rho - \rho_c)^3$  and not on  $(\rho^3 - \rho_c^3)$ , as predicted in Toll's model [28].

This work was continued by Barbier's PhD study ([36]) which aimed at decreasing the simulation time by using cylindrical elements instead of spheres. A sufficient number of element was still necessary in order to well describe the mechanical behavior of fibers. In a very similar way to [40], the system was described by a potential energy containing three components : one for the tensile behavior, another for the flexural stiffness and the last one for the inter-fiber interactions. In this model, forces were still computed at the nodes (segments ends) but the potential energy is computed from segment lengths and orientations. The one important addition to the previous simulation was

the friction behavior between fibers.

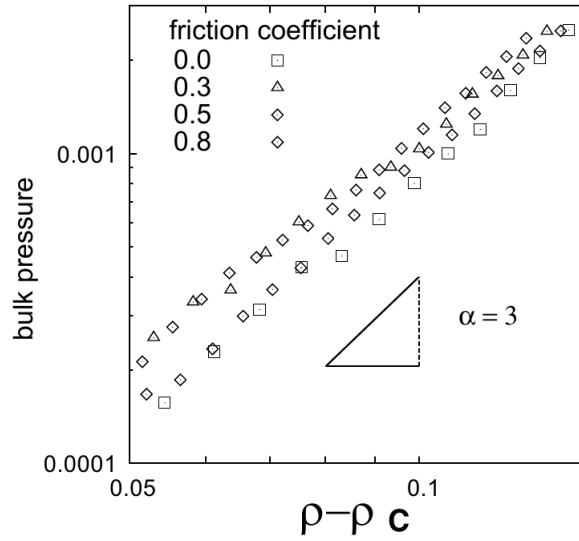


Figure 1.19: Log-log plot of the pressure as a function of the difference between relative density and packing density for fibers with an aspect ratio of 20 (4 segments per fiber) and for increasing values of the friction coefficient (simulations by Barbier et al. [44]).

Fiber arrangements with different aspect ratio ranging from 20 to 200 were compressed in a similar way to [40] and the results were shown to be very close to what was presented in Figure 1.17(a). This indicates that the number of nodes per fiber could be reduced while still obtaining consistent results. It was thus not surprising to find the same power law relation between the pressure and the relative density. Figure 1.19 shows a log-log representation of the pressure as a function of  $(\rho - \rho_c)$ . The data without friction, that were thus comparable to the results of Rodney et al., are shown as squares and follow a linear evolution with a slope of 3, confirming the exponent appearing in Van Wyk relation ([15]).

A coulomb-like static friction at contact points was implemented in order to study the influence of friction between fibers. The friction behavior was modeled by creating a “spring” whenever a contact was detected between the fiber surface of two elements. In the case of sliding contacts, the spring was then stretched from its equilibrium position thus generating a tangential friction force.

Cycles were performed with different amounts of friction (0 : no friction, to 0.8) and Figure 1.20(a) shows the corresponding pressure-density plots. It was noticed that the packing density decreases when the friction coefficient increases, due to the stabilization of some contacts that, without friction, would have slipped and led to fiber rearrangement. A lower density was thus required for the fibers to start interacting and for the entanglement to respond mechanically. Figure 1.20(a) also illustrates an hysteresis between loading and unloading sequences that increased with the friction coefficient. This indicated that the entanglement tended to dissipate energy through friction when cycled.

Figure 1.20(b) represents the evolution of the energy contributions of bending and stretching as a function of both relative density and friction coefficient. It was noticed that for all amounts of friction, the bending energy was higher than the stretching one. This was expected and confirms the

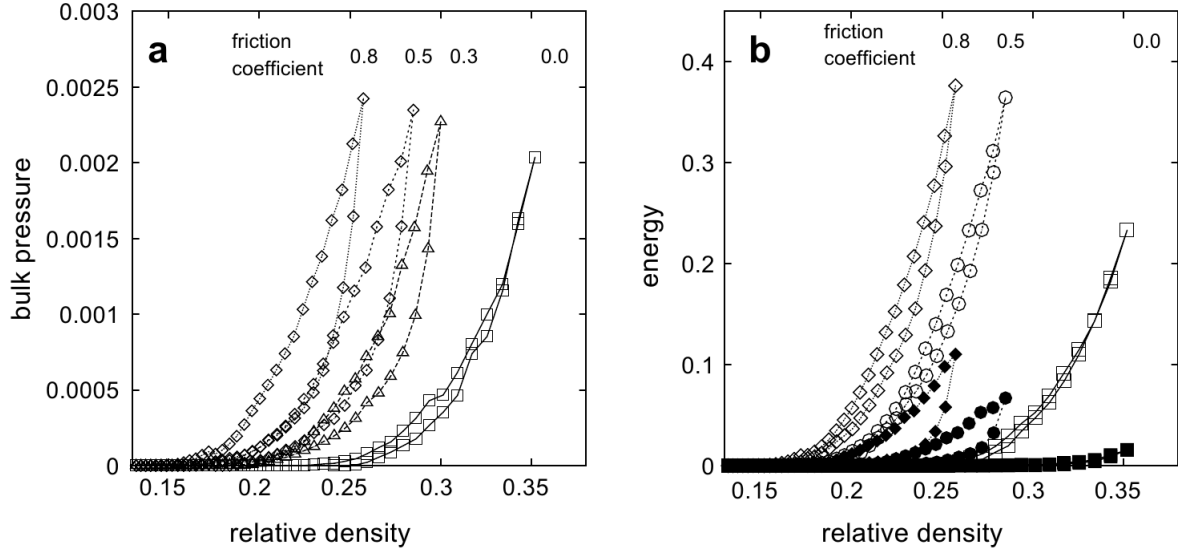


Figure 1.20: Evolution of the pressure (a), bending (open symbols) and stretching (filled symbols) energies (b) as a function of the relative density and friction coefficient for fibers with an aspect ratio of 20 [44].

assumption previously made that the main deformation mode for entangled systems was bending between contact points. However, Figure 1.20(b) also underlines the increasing role of stretching with the amount of friction. Indeed, for higher friction coefficient, frictional contacts were more resistant and could lead to fiber stretching between contact points. Finally, Figure 1.19 shows that the exponent of the power law, equals to 3, that relates the pressure to the difference between relative density and packing density was not influenced by friction [45].

Although the simulation time was quite long and the flexural stiffness had to be set to high values (not fitted to actual constitutive materials), the compressive behaviour of entangled media was well described in this study and some observations were made on the comparison of numerical and experimental results. This combined experimental/numerical analysis can however be pushed even further by simulating the behaviour of a sample acquired from tomography data. Moreover, the numerical behaviour of entangled materials under oedometric compression was not found in the literature.

## 1.2.2 Sintered wire mesh

Porous metals have been widely used in various industrial fields for their high porosity combined to a relatively high mechanical strength. They were historically prepared by metal powder sintering or metallurgical casting, but many processes were recently developed such as replication methods, space holder methods or fiber sintering. The latter has shown advantages in terms of porosity control and pore distribution.

Liu et al. ([31, 46–48]) studied the mechanical behavior of sintered steel wire meshes. Entanglements were prepared using a single steel wire (monofilament) with a 0.3 mm diameter and were placed in a specially designed cylinder-piston device with a 20 mm diameter. Cylindrical samples were formed by applying a pressure on the piston-rod for a period of time. The porosity of the

material was controlled through the applied pressure. The compacted cylindrical samples were then placed inside a furnace under vacuum at either 1373 or 1473 K for 3 to 5 hours.

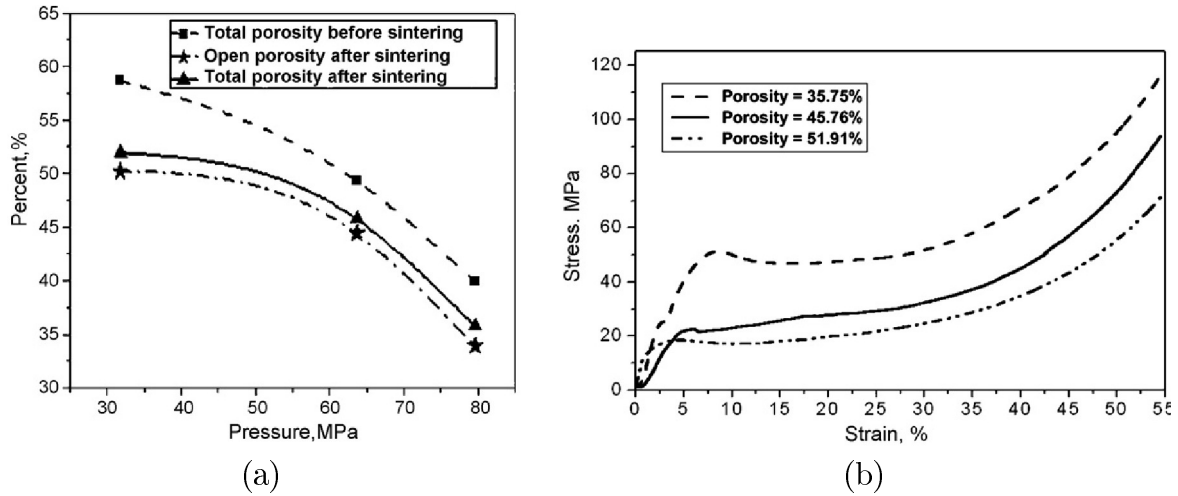


Figure 1.21: (a) : Evolution of the total and open porosities as a function of the forming pressure and (b) : Compressive stress-strain curves as a function of the forming pressure [31]

The total and open porosities were found to be closely related to the forming pressure as shown in Figure 1.21(a). With the increase of the pressure, the total porosity decreases rapidly. It was shown that the sintering parameters (time and temperature) had little influence on the porosity. However, the strength of the physical bridges created through sintering was shown to increase with both temperature and time.

Figure 1.21(b) shows the compressive stress-strain curves of the steel wire mesh with different porosities. The compressive mechanical behavior of this material was found to be very close to the one of other cellular materials such as metallic foams. Three stages were observed : a linear elastic stage, a plastic plateau and a densification stage.

Under uniaxial tensile loading (see figure1.22(a)), the material was first deformed elastically before reaching a yielding stage accompanied by local wire failure. The maximal stress was then reached and a sudden drop of the stress occurs, due to wire rupture and joints breaking. It was then followed by the final rupture of the sample where each single wire in the entangled structure deforms and fails in a ductile necking manner. It was shown that the Young's modulus of the material decreases with the porosity (see figure1.22(b)).

Similar studies were performed on sintered fiber networks composed of austenitic stainless steel fibre [49], titanium [50], copper [51] or aluminum [32] and the same typical behaviour could be observed. However, these studies mainly used conventionnal sintering techniques and only a few alternatives could be found ([29]).

## 1.3 Conclusion

This work comes within the scope of a “material by design” approach and aims at being able to develop materials that can answer to specific requirements such as the ones presented within the

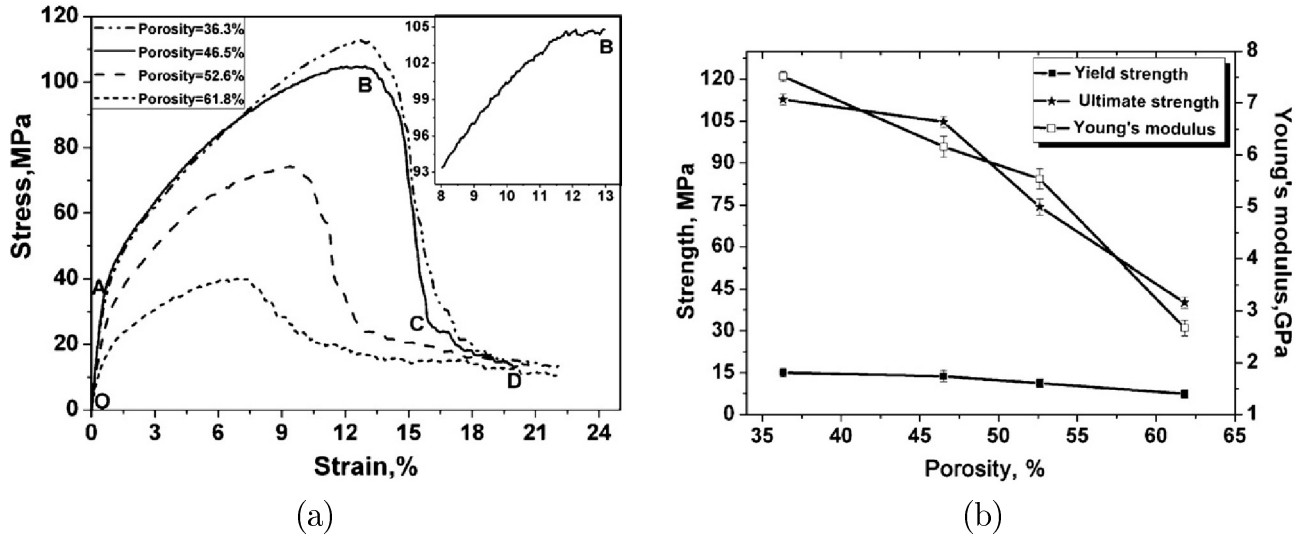


Figure 1.22: (a) : Stress-strain curve under uniaxial tensile loading and (b) : Evolution of the material's properties with the porosity [46]

framework of the MANSART project. “Architected” or hybrid materials were developed in order to combine conflicting properties that any bulk materials could not possess.

Previous studies showed, from the analysis of the compressive and hysteretic behaviour of entangled materials, the strong relationship between a few microstructural parameters such as the number of contacts, and thus friction, and their mechanical response for both experimental and numerical analysis. It then appears critical to be able to follow the evolution of the complex internal architecture of this entanglement in order to fully comprehend its compressive behavior. Tomography appears to be, in the case of an assembly of regularly shaped fibers, the perfect way to characterize it.

A validation of the numerical models can also be made by combining experimental tomography data to the discrete element method, thus allowing to model the behaviour of actual experimental samples.

It was also showed that by adding a sintering step, a network which has normally low mechanical properties can be strengthened by creating physical bridges at contact points. By using metallic fibers, and as it was presented in [29], resistive sintering methods can be used and new metallic porous materials can be developed.

MEM could be a promising way of reaching different objectives of the design constraints of sandwich cores and especially the filling of the connecting rod described in the introduction, but the relation between the microstructure and the mechanical properties of this new class of materials has yet to be studied further. This is the main objective of this PhD.



## Chapter 2

# Mechanical and microstructural properties of Monofilament Entangled Materials under compressive loading

*In this chapter, the manufacturing process developed in this PhD in order to obtain monofilament entangled materials will be presented in the case of stainless steel wires. We will focus on the influence of the wire diameter.*

*Given the complex internal architecture of this entanglement, X-ray tomography will be used as an imaging tool, allowing to perform quantitative measurements of the network's parameters. After giving a few details on both tomography and image analysis, the in-situ setup will be described.*

*The relationship between the macroscopic mechanical behaviour and the microstructural evolution of the material will then be investigated by studying the compressive behaviour of monofilament entangled materials. From the in-situ mechanical experiment, a first initial mechanical analysis leading to a simple analytical model will be proposed based on the experimental microstructural evolution of the entanglement.*

### Chapter's content

2.1	Manufacturing samples . . . . .	33
2.1.1	Raw materials . . . . .	33
2.1.2	Sample preparation . . . . .	33
2.2	In-situ oedometric testing in X-ray tomography . . . . .	35
2.2.1	X-ray tomography's principle . . . . .	35
2.2.2	Processing raw data . . . . .	37
2.2.3	In-situ device . . . . .	42
2.3	Microstructural analysis . . . . .	44
2.3.1	Radial density distribution . . . . .	44
2.3.2	Number of contacts . . . . .	45
2.3.3	Mean distance between contacts . . . . .	48
2.4	Mechanical Characterization . . . . .	49
2.4.1	Generalities on the experiment . . . . .	49

2.4.2	Influence of the wire diameter . . . . .	51
2.4.3	Analytical model . . . . .	52
2.5	Conclusion . . . . .	57

---



This chapter will focus on studying the compressive properties of monofilament entangled materials in a “closed matrix” configuration. In the case of entangled media, the mechanical properties is closely linked to the microstructural evolution. It is thus necessary, in parallel to a macroscopic mechanical characterization, to study the evolution of a few key internal parameters such as the number of contacts.

Although the mechanical properties of entangled materials has been widely investigated from both an experimental [6, 13, 29, 32] and a numerical [28] point of view, only few experimental studies [17, 18] were performed on the microstructural characterization of their complex internal architecture. Much attention will thus be put into linking the macroscopic mechanical behaviour of an entanglement to its microstructural evolution, using an in-situ oedometric approach in X-ray tomography.

In this chapter, the manufacturing process is first introduced before presenting the experimental testing procedures for in-situ oedometric compression in X-ray tomography. Finally, results from both the mechanical and microstructural investigations are presented and an analytical model of the mechanical response of the entanglement is then developed and compared to experimental results.

## 2.1 Manufacturing samples

In this PhD, the studied material was specifically manufactured from single stainless steel wires and a procedure was developed in order to obtain Monofilament Entangled samples, in a relatively reproducible manner.

### 2.1.1 Raw materials

One of the general specification mentionned in the Introduction being to resist at high temperature, steel wires were used as a raw material in this study. A 304L stainless steel was chosen, mostly for its anticorrosive properties and its low price (10 euros/kg).

Three different diameters were selected in order to be able to study the influence of the wire diameter on the materials properties. Table 2.1 shows the chemical compositions of the raw material and table 2.2 shows a summary of the dimensions and mechanical properties of all the wires used.

In terms of surface finish, wires presented a relatively low surface roughness (see figure 2.1). This plays a role in the friction behavior at the contact points. The static friction coefficient for a steel-steel contact was taken as 0.5 whereas the value for a steel-PTFE contact dropped to 0.1.

Given the relatively small diameter of the wires, they are easily deformable and can thus be simply shaped in order to fit inside the mould, which gives the sample its final dimensions.

### 2.1.2 Sample preparation

Monofilament entangled materials can be, by nature, easily processed since they are made of a single wire. It is a clean process and, considering the typical size of the constitutive wire, it is of no danger for either health or the environment (no solvent and no micro fibers). It also presents a lot of degrees

	304L (wt%)
Carbon	0.03
Manganese	2.00
Phosphorus	0.045
Sulfur	0.030
Silicon	0.75
Chromium	18.0-20.0
Nickel	8.0-12.0
Nitrogen	0.10
Iron	Balance

Tableau 2.1: Chemical composition of a stainless steel 304L.

Material	Diameters ( $\mu\text{m}$ )	Yield strength (MPa)
Stainless steel 304L	127, 200 and 280	200

Tableau 2.2: Properties of used wires.

of freedom for the process. The present study was limited in terms of adjustable parameters but a lot more could be eventually varied.

In this study, a sample was characterized by its volume fraction which appeared to be the most relevant parameter. The control of the volume fraction was achieved through the measurement of the total length of the wire. For a given sample volume, this indeed assured a precise control of the volume fraction for the initial geometry of the sample (height = 35 mm, diameter = 15 mm, volume fraction = 5%).

$$\text{Volume fraction} = \frac{\text{Volume}_{\text{wire}}}{\text{Volume}_{\text{sample}}} = \frac{L_w D_w^2}{h * D_{\text{sample}}^2} \quad (2.1)$$

where  $\text{Volume}_{\text{wire}}$  is the volume occupied by the stainless steel wire with a  $D_w$  diameter and a  $L_w$  length,  $\text{Volume}_{\text{sample}}$  is the total volume of the sample (height  $h$  and diameter  $D_{\text{sample}}$ ).

The sample could then either be tested in “closed matrix” conditions (oedometer test) or taken out of the mold for additional testing.

The wire was first entangled manually to form a precursory wire-bundle. Care was taken here to try to be as consistent as possible in this part of the process. Every sample in this study was prepared using the exact same procedure and by the same person in order to be consistent in the manufacturing process. The influence of this step on the reproducibility of the microstructure will be tested later in this chapter.

At this point, a random entanglement was obtained but it did not present the targetted final shape required to start an experiment. In order to start with a known volume fraction and shape, the so-formed precursory wire-bundle was then placed into a specific PTFE cylindrical die with a typical diameter  $D_{\text{sample}}$  of 15 mm and it was brought to a given height  $h$ , which, in accordance with the wire length measurement (Table 2.3 presents a few examples of the measured length of the wire for

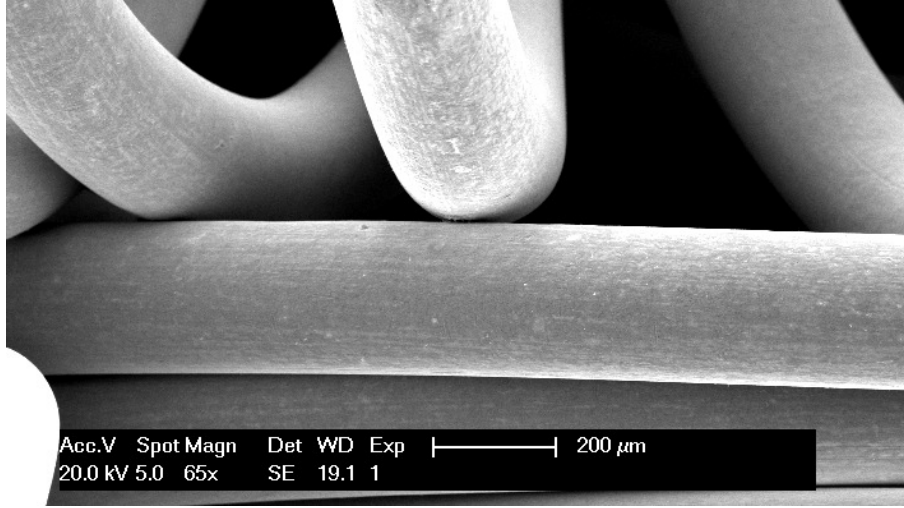


Figure 2.1: Visualization of a wire's surface using a Scanning Electron Microscope (SEM).

different wire diameters), resulted in a cylindrical sample with an exact volume fraction.

Wire diameter ( $\mu$ m)	Volume fraction (%)	Wire length (m)
127	5	24.413
200	5	9.844
280	5	5.022

Tableau 2.3: Example of wire length required to achieve a 5% volume fraction for different wire diameters.

The next section presents the experimental testing techniques and procedures for in-situ oedometric compression in X-ray tomography.

## 2.2 In-situ oedometric testing in X-ray tomography

### 2.2.1 X-ray tomography's principle

X-ray tomography is a non-destructive, three dimensional, imaging technique based on the difference in X-ray absorption of the phases constituting a material. It uses simple radiography techniques, where a projection of the local absorbance through the thickness of the sample is obtained, to which a rotation of the sample is added. It is comparable to a medical CT-scan, with the only exception that unlike the latter, the sample is rotating and both the X-ray source and the X-ray detector, are fixed.

X-ray radiography is based on Beer-Lambert's law which gives, for a given path  $\Delta_x$  across a sample, the ratio of the number of transmitted photon  $N$  over the number of incident photon  $N_0$  (see Equation 2.2).

$$\frac{N}{N_0} = \exp \left[ - \int_{\Delta_x} \mu(x_i, y_i, z_i) dx \right] \quad (2.2)$$

where  $\mu(x_i, y_i, z_i)$  is the local absorption coefficient in any position in the material.

A radiography thus represents the integral of the absorption coefficient along a trajectory through the sample. This projection varies with the composition and width of the crossed path. Each point of a detector, situated behind an irradiated object, receives a different number of photons depending on this path. Therefore, each pixel corresponds to the sum of all the information gathered along the beam's trajectory. By acquiring a set of radiographies (a few hundreds) for different angles of the sample with respect to the X-ray beam, a 3D map of the local X-ray absorption coefficient can be reconstructed, thanks to a filtered back-projection algorithm (see Figure 2.2).

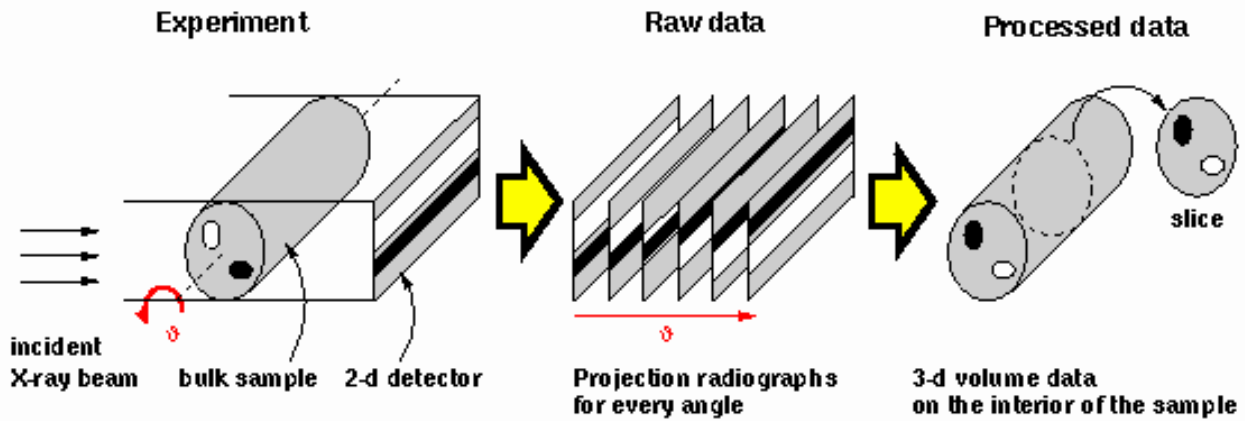


Figure 2.2: Overview of the principle of X-ray computed tomography

A few parameters can affect the quality of the resulting image, such as the number of projections, the pixel size of the detector, and the exposure time. Some of those will consequently influence the scan-time which can range from a few seconds to an hour [36]

The one last decisive parameter is the X-ray beam geometry. It can either be conical or parallel. A parallel beam can be obtained at a synchrotron facility. In the case of the laboratory tomograph at our disposal in the MATEIS laboratory (Figure 2.3), a conical beam is used. But, taking into account the strong porosity of our materials, the typical spacial resolution needed (the smaller wire's diameter being around  $120\text{ }\mu\text{m}$ , no resolution below  $20\text{ }\mu\text{m}$  is needed) as well as the good contrast between the two phases (air and steel), a cone beam configuration is very well suited to this specific study.

In a conical beam setup, the voxel size can be set by changing the relative distance between the sample and the beam source. It can go down to slightly less than a micron. Unlike synchrotron beam line, the intensity of the beam on a laboratory tomograph is rather low and thus, the exposure time needs to be longer. The X-ray tube's voltage can range from 40 to 160keV and can be focused to less than a few microns, depending on the intended spatial resolution. In order to make the acquisition faster, a binning technique can be used were pixels are regrouped four by four. The resolution will double, and images will be smaller, but less memory will be needed.

In this study, CT-scans were performed using the following parameters :

- detector size : 1920 pixels x 1536 pixels (with binning).  
 $\Rightarrow$  Radiography size : 960 pixels x 768 pixels.

- X-ray beam :  $V = 120 \text{ keV}$ ,  $A = 188 \mu\text{A}$ .
- Exposure time for one projection : 100 ms (Pratically, the first projection was skipped and the final radiography was calculated from the mean value of 4 projections).
- Number of projections : 720.
- Spatial resolution :  $24 \mu\text{m}$ .
- Total scan time : 15 minutes.

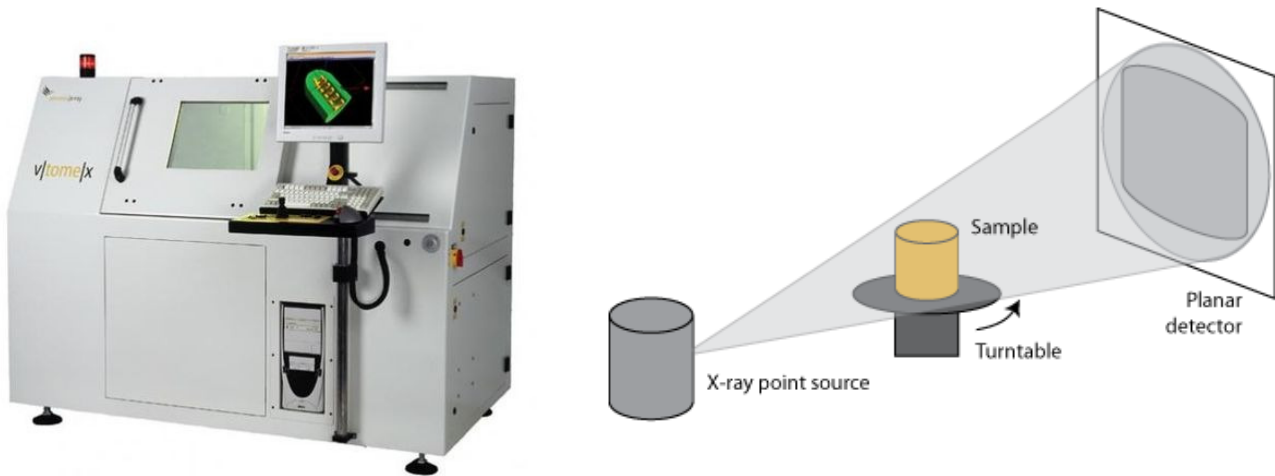


Figure 2.3: Cone beam configuration

### Limitations

For materials with a high absorption coefficient, the voltage of the beam needs to be increased in order to be able to cross the sample while still detecting a high enough intensity, thus increasing the background noise and creating a blur. Moreover, the sample needs to stay perfectly still during the whole scan (which is often not the case for entangled materials as contacts can eventually slide during the acquisition). Indeed, radiographies at  $0^\circ$  and  $360^\circ$  have to be identical. Although a correction can be applied if the sample happens to slightly move during the acquisition, the quality of the image can be heavily affected, thus making the segmentation of the phases more difficult.

Consequently, much care was taken when acquiring images in order to get the best reconstruction quality possible and thus enable precise and reliable measurements.

### 2.2.2 Processing raw data

From the reconstruction, a 3D gray level image of the material is obtained. However, without any post-treatment, these images can only allow qualitative observations. A few treatments are necessary in order to be able to first, create a 3D representation of the sample, and then mostly to be able to perform measurements of some key parameters on the structure (e.g. contact density). In-situ tests

will allow to follow the evolution of mean parameters as well as local ones such as the number of contacts or the orientation.

The post-processing step was realized using ImageJ [52, 53], an open-source image-processing program, its FIJI package [54], and the Avizo commercial software.

### 2.2.2.1 Sticking

Since the sample can often be higher than the field of view, for a given spatial resolution, multiple volumes need to be acquired for the sample at different height in order to obtain a full image (Figure 2.4 on the left). Those volumes then need to be stitched in order to obtain one big volume for a given sample. The most reliable way to do that is by finding the overlapping zones by hand and then to concatenate all the stacks together once the redundant zones have been removed (Figure 2.4 on the right). The final volume can be as big as 1.5 GB.

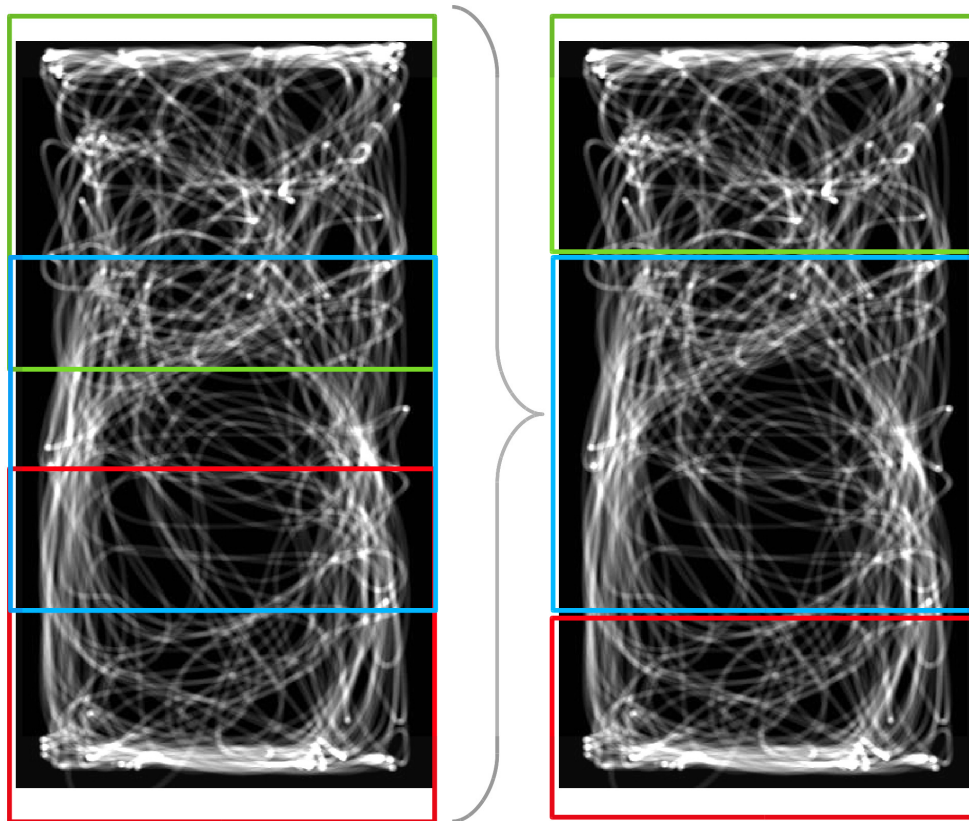


Figure 2.4: Presentation of the stitching process for 3 scans of one sample (on the initial image, each colored rectangle corresponds to one 3D volume)

### 2.2.2.2 Useful image processing

When treating a 3D image, there is a few important methods that lead to an improvement of the image quality. It is critical to work on having the best quality possible before performing any quantitative measurement.

#### **Filter**

Depending on the final quality of the image, a filtering step might be necessary in order to decrease the noise induced by the experimental acquisition especially at the boundaries between two phases. A median filter is commonly used. It averages the grey level value over a neighborhood of each pixel thus smoothing the different shapes inside a volume.

### Erosion/Dilation

When working on the 3D volumes, some unwanted features can appear, due to the ring artifact (one or many “rings” appear within the image due to a detector fault) or the background noise for example. In order to get rid of those, morphological operations can be used. A structural element is first defined, which can be, in 3D, a sphere. It is then moved all across the image and will interact with the image by either enlarging (dilation) or shrinking (erosion) any existing set of pixel. For example, an erosion of a cylindrical tube with a diameter of 10, using a structural element of 1 pixel, will result in the same cylindrical tube but with a diameter of 8. This function will later be used in Chapter 4.

### Scale

In the case of a volume with more data than needed, or if a good precision is not needed, the image can be down-sized. Each dimension can be resized to a given length by using a bilinear interpolation. For example, if a 2D image is scaled with a 0.5 scale factor, a group of 4 pixels would be grouped to take an average value of those initial pixels. This leads to a significant decrease of the image size, as well as, for example, the number of white pixels. This will again be used later in Chapter 4.

#### 2.2.2.3 Segmentation

In the case of entangled materials, it was soon noticed that since the samples were shaped randomly, there were density fluctuations inside a sample (see Figure 2.5). A classical segmentation, where a threshold value is simply defined between 0 and 255, would not work as some segment, like the one shown in Figure 2.5(b), of the wire would be over or under-estimated. An adaptive threshold was then used in this study in order to obtain binary images (only black for void and white for steel).

The Robust Automatic Threshold Selection, which is part of the FIJI distribution, computes a threshold map for a 2D image, based on the value of a pixel, as well as their gradients. This analysis is only performed in two dimensions as the elliptical cross-section of the wire leads to high gradients and that the area of interest is limited to the contact surface between both phases. The gradient is defined using the Sobel kernels which is commonly computed using Equation 2.3.

$$G_{x,y} = \sqrt{\nabla_x^2 + \nabla_y^2} \quad (2.3)$$

where  $\nabla_x$  is the gradient in the x direction and  $\nabla_y$  the gradient in the y direction.

However, it was showed in [55] that, by eliminating the square root, much computing time can be saved while the results stay consistent. In this algorithm, the gradient is thus simply equal to:

$$g_{x,y} = G_{x,y}^2 = \nabla_x^2 + \nabla_y^2 \quad (2.4)$$

Pixels with a gradient lower than a certain value, estimated from the noise in the image, are

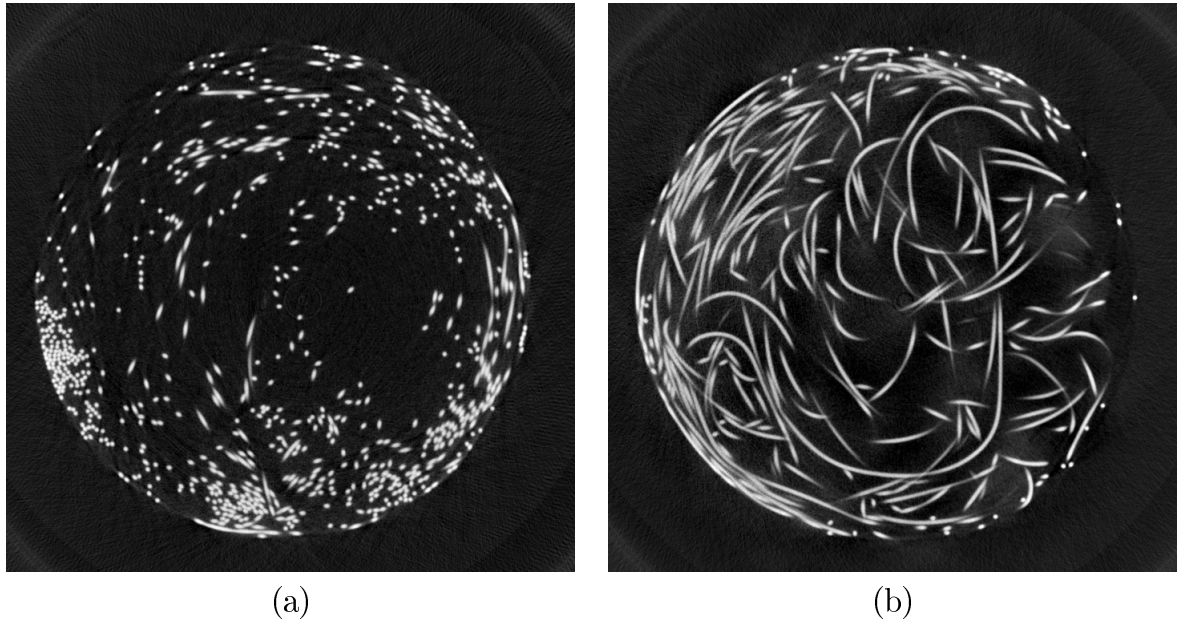


Figure 2.5: Grey level image of the cross sections of the same stainless steel wire mesh at two different height : (a) center of the sample and (b) near the top of the sample.

rejected. The image is then divided into small regions (quadtree) for which a local threshold  $T_R$  is measured as the gradient weighted sum of the pixels  $P$  (Equation 2.5). According to that regional value, each region is then turned into a binary image by giving a pixel the value of 255 (white) if their value is greater than the threshold and 0 (black) otherwise. As a result, the final image is constituted of only black and white voxels. The wire appears as a set of white voxels and the air black.

$$T_R = \frac{\Sigma(g_{x,y} \cdot P_{x,y})}{\Sigma(g_{x,y})} \quad (2.5)$$

Image segmentation is key in performing quantitative measurement on a 3D volume. Indeed, the chosen threshold to obtain a binary image impacts a lot of meaningful parameters such as the volume fraction, the number of contacts or the connectivity. In order to validate the segmentation method used here, the specific surface of the binary image was measured and compared to the real value, which can be calculated since the length of wire that was placed inside a finite volume is known.

The measurement was performed by first going through the whole image and recording each group of touching white voxels. In this specific case, since the sample was made of a single wire, the whole white phase, which corresponds to the steel phase, is continuous, thus resulting in only one cluster of white voxels. It was then analyzed and the contact surface between white and black voxels was measured. Considering the discrete nature of voxels, a marching cube algorithm [56] was first applied in order to allow a more meaningful result in terms of surface. The ratio of this surface over the total volume of the sample then provided a value of the specific surface in  $\text{m}^2 \cdot \text{m}^{-3}$ . Table 2.4 gives the resulting contact surface obtained for different compression state of the same  $200 \mu\text{m}$  stainless steel sample. This surface was supposed to be constant as a finite length of wire was placed inside the sample but as the volume fraction increases, the number of contacts, and thus the area of wire-wire



contacts increases.

Volume fraction (%)	Contact surface (m <sup>2</sup> )	Experimental specific surface (m <sup>2</sup> .m <sup>-3</sup> )	Real specific surface (m <sup>2</sup> .m <sup>-3</sup> )	Relative error (%)
5	0.00569	920.3	934.6	1.5
6	0.00567	1068.8	1090.4	2.0
7	0.00560	1268.4	1308.4	3.1
8.7	0.00554	1567.1	1635.6	4.2
11.7	0.00549	2071.5	2180.7	5.0
17.5	0.00545	3084.1	3271.1	5.7

Tableau 2.4: Comparison of the experimental and real specific surface.

First of all, the experimental specific surface is consistently lower (relative error between 1 and 6%) than the theoretical value. This might come from the fact that when measuring the wire's surface from the tomography data, the contact surface at each contact points is not taken into account. As the number of contacts increases with the volume fraction, the surface value decreases and the relative error thus tends to be higher when the relative density goes up. However, the result seems consistent throughout the compression test and the error stays relatively low. This confirms that the segmentation method is well fitted to this type of material and that the final image faithfully represents the experimental sample. The surface measurement also confirms the continuity of the samples (they are made of a single wire) as only one continuous set of white voxels was found for every compression state.

#### 2.2.2.4 Skeletonization

In shape analysis, the skeleton of a volume corresponds to a thinner (one pixel in diameter), geometrically faithful, version of that shape. The skeleton locus is equidistant to the surface of the object (Figure 2.6). The aim of this treatment is to extract a corresponding shape feature representing the general form of an object and it is particularly interesting when we are focusing, not on the size of a pattern but rather on its relative position.

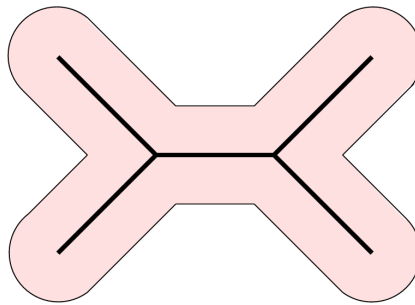


Figure 2.6: Example of a shape and its skeleton (black lines).

Skeletons can, in the literature, have different mathematical definitions and there are many different algorithms for computing them. In the case of the Avizo software that was used, they are, however, comparable to a sequence of “thinning” operations down to a point where the shape has a size of one pixel. The final skeleton then consists in a list of nodes and segments (two nodes being supposed to be linked by a straight line).

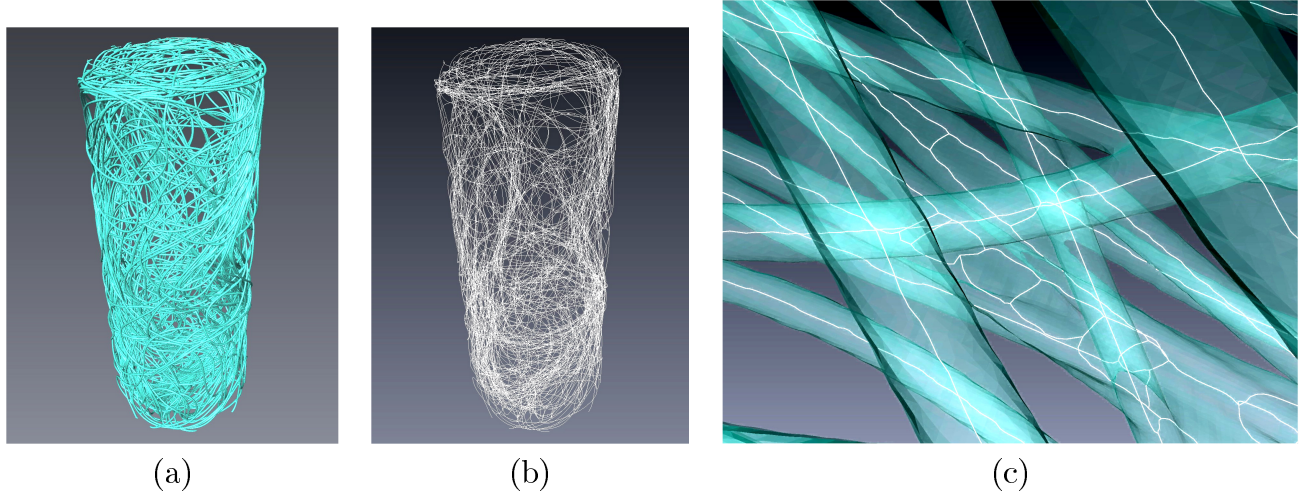


Figure 2.7: (a) 3D representation of the binary volume and (b) Skeleton extracted from the sample image and (c) Representation of a network inside the sample with both the skeleton and the volume in transparency.

From the acquired 3D volumes, it is possible, by using the Avizo software, to obtain a 3D representation of the experimental sample. The binary image is first treated in order to assign a “material” to the “solid” phase (here, the wire, in blue in figure 2.7(a)). The skeleton algorithm is then applied to the same binary image and the corresponding network of segments and nodes is obtained (see Figure 2.7(b)). In the particular case of a monofilament entangled material, the wire is reduced to its center-line, as it can be seen in figure 2.7(c). Contact points are also observed to be represented by many short segments in the skeleton. This will be discussed further in a subsequent section.

### 2.2.3 In-situ device

A dedicated in-situ device, described in [57], was designed in the MATEIS group for uni-axial tensile and compressive tests. It can be mounted on the rotation stage of either the lab tomograph or a synchrotron beamline. A specific oedometer compressive device is then introduced inside this machine, as shown in Figure 2.8. This allows a follow-up of the deformation of an entanglement through the whole compression.

In order to obtain a good quality scan, the component of the machine that are outside of the field of view and that are crossed by the X-ray beam have to be invariant by rotation and with a negligible attenuation coefficient (it is then almost transparent to X-rays). If this is fulfilled, the attenuation of the machine is constant for any angle of the sample and it behaves simply as a filter. For materials with a low mechanical response, a perspex or polycarbonate tube can be used, as shown in Figure 2.8. For stronger materials, it can be replaced by aluminium tubes to enhance the rigidity of the device

and because polymers do not resist to high energy X-rays (see Figure 2.8).

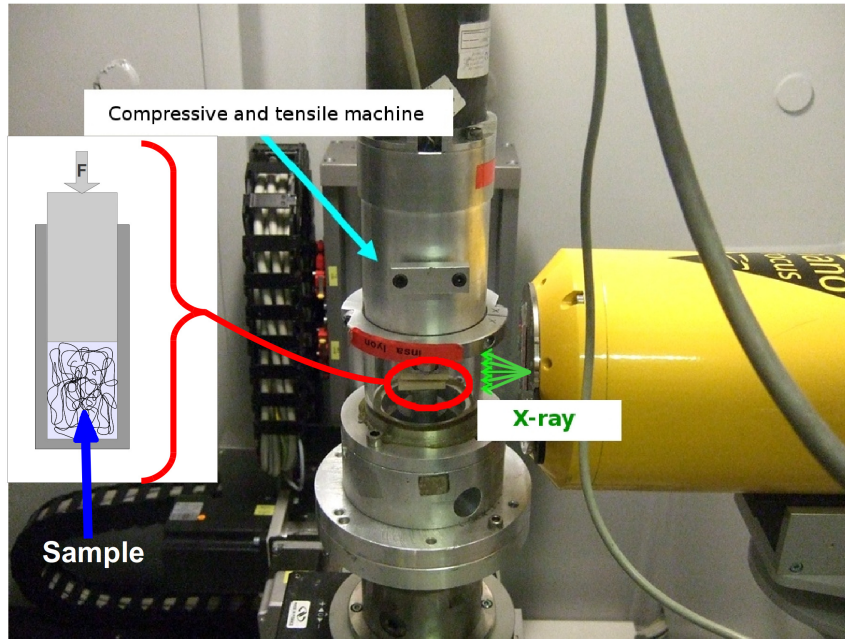


Figure 2.8: In-situ experimental oedometric device inside the PHOENIX laboratory tomograph

The initial configuration of the sample was a 35 mm high cylinder with a 15 mm diameter and a 5% volume fraction. This was defined in order to be able to fit the sample entirely inside the field of view, for the higher spatial resolution possible, which is limited to  $13\ \mu\text{m}$ . This limitation stemmed from the fact that the tube of the machine could not come closer than 40 mm from the X-ray tube.

The sample was then compressed, step by step, and for each step, unloaded. From the displacement of the grip and the initial length and diameter of the wires, it was possible to calculate the “theoretical” volume fraction of the sample during the compression test. A 3D volume was acquired and reconstructed from a set of X-rays. During the compression test, both the displacement and the resulting force along the compression axis were acquired.

In parallel to the in-situ characterization and for easier access, compressive tests were also performed on a traditional mechanical device. A Instron 3365 machine was used as well as a PTFE mold/piston device (see Figure 2.9(b)) comparable to the one used in situ.

By combining a compressive mechanical characterization to the acquisition of 3D volumes of the sample, the relationship between microstructure and mechanical properties of the entanglement could be investigated. The following section presents results on the compressive behaviour of Monofilament Entangled Materials made of stainless steel wires with three different diameters.

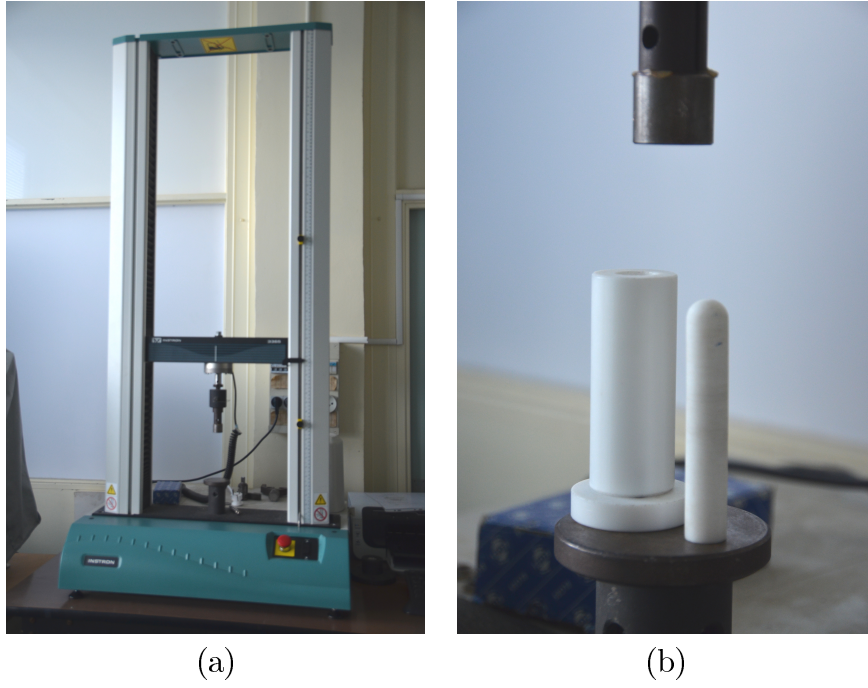


Figure 2.9: (a) : Compressive testing device INSTRON 3365 and (b) : PTFE mold/piston system

## 2.3 Microstructural analysis

### 2.3.1 Radial density distribution

Given the random and constrained nature of the entanglement, the tomography data were first used in order to study the radial distribution inside the material. From the binary 3D volumes, a local density, at a given  $r$  distance from the axis of the cylindrical sample, can be measured using the following equation :

$$Local\ density(r) = \sum_{k=0}^{N_v} \frac{(255 * \delta_i)}{N_v} \quad (2.6)$$

where  $N_v$  is the number of voxels situated at a distance  $r$  from the sample's axis and

$$\delta_i = \begin{cases} 0 & \text{if black voxel} \\ 1 & \text{if white voxel} \end{cases}$$

By applying this equation from the center of the sample up to its external boundary, a radial density profile can be measured. Taking into account the discrete nature of the image, the size of the classes in  $r$  will obviously affect the results. Every measurements were made using the same class size, chosen in order to have a good description of the profile's shape while limiting the noise on the measurements.

By using the three available diameters for stainless steel wires, the influence of the wire diameter on the radial distribution inside a sample could be studied. Experiments were performed on samples with a 5% volume fraction. Figure 2.10 shows the influence of the diameter of the initial stainless steel wire on the radial density profile. A heterogeneous distribution of the wire, with a higher local density close to the contact with the mould, could be observed.

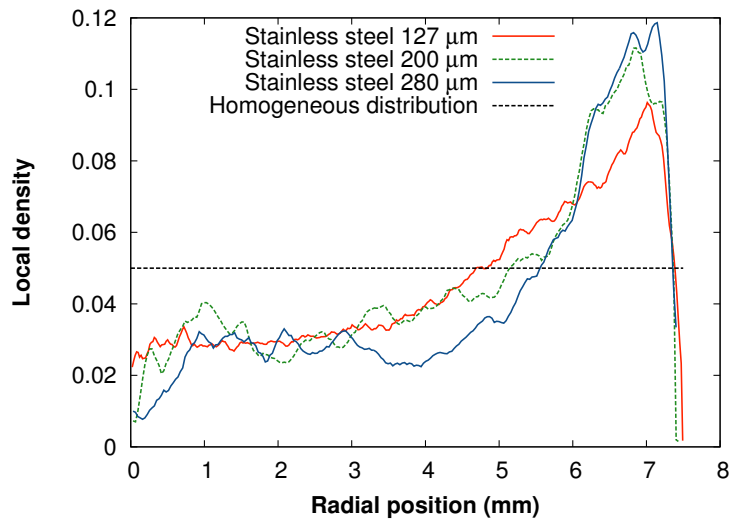


Figure 2.10: Influence of the wire diameter on the radial density profiles (same 5% volume fraction).

This “wall effect” is typical of confined entangled media and seems to be less important for a smaller diameter of the wire. This was expected since a smaller wire diameter means a smaller bending modulus and thus more flexibility of the wire and easier arrangements for the same mould radius.

### 2.3.2 Number of contacts

In the specific architected structure of this type of material, the mechanical strength mostly comes from the creation of contact points through the compression. Thus, from the tomography data, the evolution of the number of contacts was studied.

From the acquisition of 3D volumes for different volume fractions, it was possible, as previously introduced, to obtain skeletons of the actual shape of the sample. It was then possible to measure the experimental number of contacts for the whole sample. Considering that the skeleton was acquired by a succession of “thinning” operations, it results in a network of lines of 1 pixel in diameter. Consequently, two types of lines could be differentiated : wires parts and contact links. One contact would ideally be defined by a segment shorter than the actual diameter of the wire (Figure 2.11(a)). By going through the list of nodes and segments for a given sample, a count of the number of contacts could be obtained and normalized to the volume of the sample, thus resulting in a number of contacts per unit volume.

Although, the ideal representation of a contact inside a skeleton corresponds to a single short segment, depending on the surface area of the contact, it could turn into a much more complicated structure for real materials. For longitudinal contacts, it would for example be represented by a network like the one showed in Figure 2.11(b).

So the initial count can be refined by taking the extra assumption that, if the distance between two short segments is smaller than the diameter of the wire, those two segments belong to the same contact point.



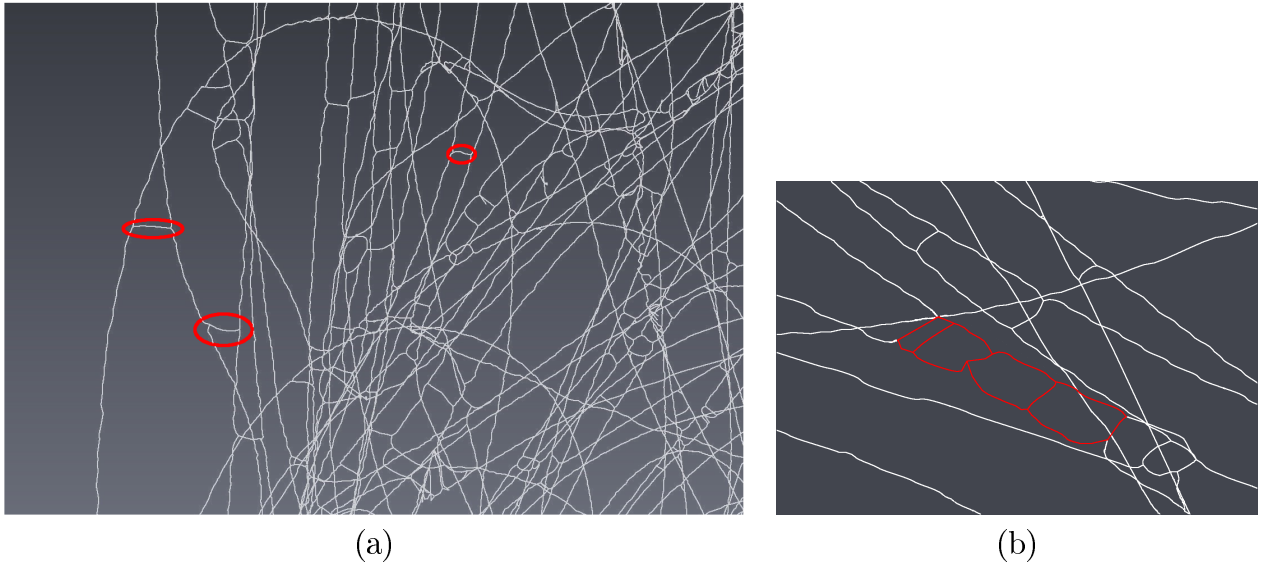


Figure 2.11: (a) Selection of a few contacts (in red) in the 3D skeleton of a sample and (b) representation of a more complex linear contact.

The evolution of the number of contacts was followed thanks to the in-situ setup and measurements were performed on samples with different volume fraction and wire diameter. The influence of those parameters will here be investigated in more details.

### Comparison to the “tube” model

The “tube model”, developed by Toll and studied in more details in section 1.2.1.2 yields the following relationship between number of contacts per unit volume and relative density [28] :

$$N_{cv} = \frac{16f}{\pi^2 d_f^3} \rho^2 \quad (2.7)$$

where  $d_f$  is the diameter of the fiber and  $f$  is a parameter describing the orientation distribution.

A sample made of a 200  $\mu\text{m}$  stainless steel wire was compressed and the number of contacts was followed in-situ. Fig 2.12 shows the evolution of the experimental number of contacts per unit volume as well as values measured from the model. As presented in more details in section 1.2.1.2, it was showed that in the specific case of a 3D random distribution, the parameter  $f$  describing the fiber orientation distribution takes a theoretical value of 0.8.

Since the experimental measurement of the number of contacts was based on the determination of a threshold value for the length of the contact, error bars could then be estimated (shown in Fig 2.12). For a given wire diameter, we first measured the diameter in voxels. A 200  $\mu\text{m}$  diameter corresponds to 8.4 voxels (the voxel size in the tomographic reconstruction was 24  $\mu\text{m}$ ). The error bar was thus measured by averaging the number of contacts for values of the size threshold equal to 8 and 9.

First of all, the scattering of the measurements is relatively low and the evolution of the number of contacts per unit volume then exhibits a typical increase with the volume fraction. When compressing the sample, contact points are created, thus increasing the mechanical strength of the material. Finally, and just as the model predicts, the number of contacts roughly evolves as a function

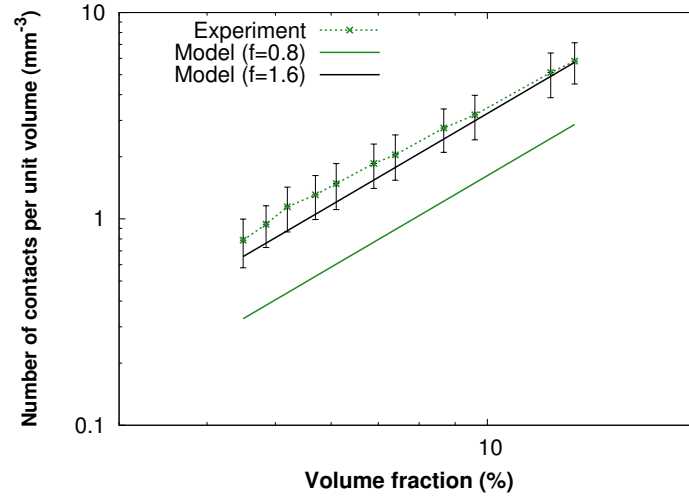


Figure 2.12: Evolution of the experimental number of contacts for a 200  $\mu\text{m}$  stainless steel wire as well as the values measured using the “tube” model [28] for two values of the orientation parameter  $f$  : 0.8 and a fit of the experimental data with  $f = 1.6$ .

of the square root of the volume fraction. Indeed, the slopes of the experimental plot is almost identical to the one of the model in this log-log plot.

Although the general slope of the experimental plot does fit the model, the model using the theoretical value of  $f = 0.8$  largely under-estimates the experimental results in terms of absolute values. In order to fit the model to the experimental results, the orientation parameter  $f$  of the equation for the number of contacts per unit volume was set to a value of 1.6. For this value, a good agreement is obtained. Considering the very specific loading conditions (oedometric compression) and that the experimental material did not entirely verify the hypothesis of the model (wire segments are not straight and not infinitely rigid), it is not surprising to obtain a value of  $f$  which does not fit in the hypothesis of the model. This value can however be taken as an equivalent orientation parameter for the oedometric compression of entangled media and will be used in the following section in order to fit experimental measurements of the number of contacts per unit volume.

Using the experimental measurement of the contact density, an equivalent orientation parameter was defined for the calculation of the theoretical number of contact per unit volume in the specific case of the oedometric compression of entangled media.

### Influence of the wire's diameter

The same experiment was performed for all three diameters of the stainless steel wire, thus allowing to study the influence of the fiber diameter on the number of contacts. Figure 2.13 shows the evolution of the number of contacts per unit volume for all wire diameters as well as the corresponding models (in the conditions that were just determined).

Firstly, the contact density decreases with the diameter of the wire. This was expected since, for a smaller diameter, the length of the wire gets longer, for a given volume fraction. As a result, more contacts are created.

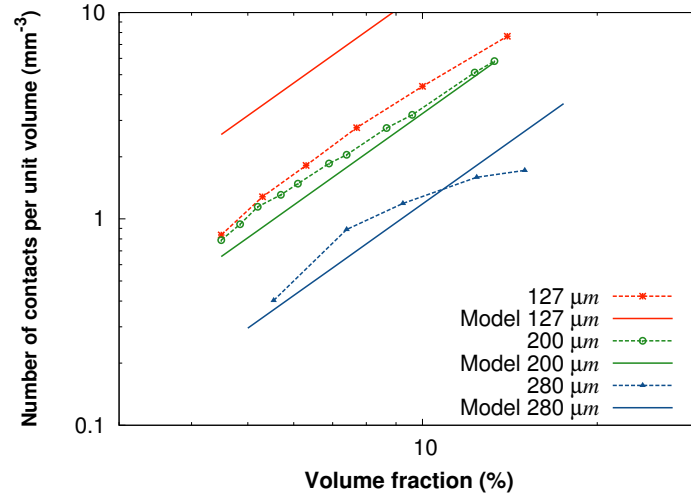


Figure 2.13: Evolution of the experimental number of contacts for stainless steel wires as well as the values measured using the “tube” model [28] for  $f=1.6$ .

Although the model seems to fit quite well the experimental values for the two larger diameters (200 and 280  $\mu\text{m}$ ), it is not the case for the smaller one. Even though the general slope of the experimental plot does still fit the model, the absolute values are not in agreement with the model. One reason might be that, since we are using the same spatial resolution (24  $\mu\text{m}$  when acquiring the 3D data for all diameters, the contacts might not be as well defined for thin wires as for thicker ones since they are defined by less pixels across the diameter. Moreover, for small diameter, the bending modulus of the wire is smaller and it is deformed even more. The “straight fibers” assumption of the model thus tends to be less valid.

### 2.3.3 Mean distance between contacts

From the same skeleton used for the number of contacts measurements, another parameter can be extracted : the mean distance between contacts. The contacts were defined like neighbourhoods where the constitutive segments of the skeleton are shorter than the typical diameter of the wire. So by definition, the parts of the wire located between two contacts will correspond to segments longer than that threshold length. By averaging their length over the whole skeleton, the mean distance between contacts along the wire could be obtained and from the set of skeletons acquired from tomography data, it could be studied as a function of the volume fraction or the wire shape for example.

For a given sample, the mean distance between contacts is directly linked to the density of contacts. In order to validate the observations made from the number of contacts measurements, an equivalent analysis was performed for the mean distance between contacts. Samples with an initial 5% volume fraction were analysed for the three stainless steel wires and results are shown in figure 2.14.

First, for any given volume fraction, an increase of the mean length between contacts with the wire diameter was observed, in agreement with the decrease of the contact’s density. Moreover, as expected from the increase of the contact’s density with the volume fraction, the mean distance between contacts was shown to decrease significantly over this volume fraction range (Figure 2.14).



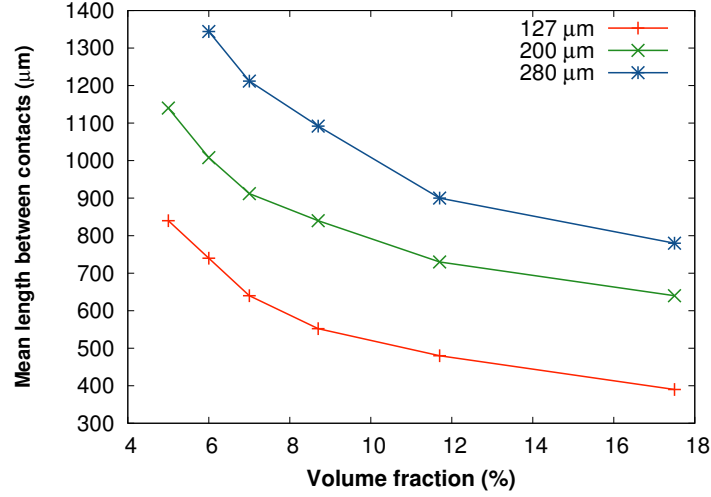


Figure 2.14: Evolution of the mean distance between contacts as a function of the volume fraction for all three stainless steel wires.

As a conclusion, the influence of all parameters, deduced from the analysis of the number of contacts per unit volume, were confirmed by the measurements of the mean distance between contacts. The knowledge of this microstructural parameter could then be used as input in an analytical model to be able to fit it properly to the experiments.

## 2.4 Mechanical Characterization

Using either the in-situ device or the traditional mechanical equipment previously introduced, the properties of Monofilament Entangled Materials were characterized under oedometric compression. In parallel to the experimental mechanical results, an analytical model was developed, taking into account the microstructural evolution of a regular entanglement. Experimental and numerical data could thus be compared from the mechanical and microstructural points of view.

The oedometer conditions being very specific, it appeared interesting to first look at the representativity of the results that it could produce. Samples made of different types of wires were then characterized in order to have a better understanding of the mechanical properties of monofilament entangled materials.

### 2.4.1 Generalities on the experiment

#### Representativity of the engineering stress

During the compressive oedometer test, the resulting force  $F$  along the vertical direction was recorded as a function of the displacement. This type of data is usually treated by plotting the engineering stress  $\sigma = F/(\pi R^2)$  (where  $R$  is the radius of the compression mould) as a function of the strain. However, for this specific type of porous materials, using the engineering stress could be questionable.

In order to ensure a good representativity of this measurement, experiments were made for two

different values of the diameter of the compression mold for the same  $280\text{ }\mu\text{m}$  stainless steel wire. In theory, the result should not be affected since the stress is expressed in  $\text{N.mm}^{-2}$

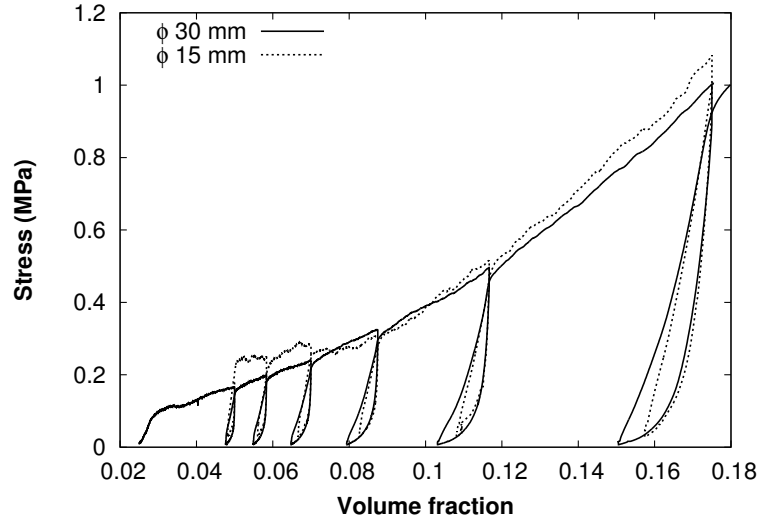


Figure 2.15: Evolution of the axial stress as a function of the volume fraction for two different diameters of the compression mould (15 and 30 mm).

Figure 2.15 shows the evolution of the stress as a function of the volume fraction for two diameters of the compression die : 15 mm and 30 mm. In both cases, a typical non-linear behaviour is observed and the mechanical responses are consistent. In a way, it also shows the reproducibility of the manual sample preparation.

### Influence of the shear component at the contact with the mold

In this study, the material was mostly characterized under compressive loading in a “closed matrix” configuration. This implied a very specific solicitation of the material. Generally, the stress in the compression direction can be written as :

$$\frac{F}{\pi R^2} = \frac{2}{R^2} \int_0^R \sigma_z|_{z=0} \cdot r \cdot dr + 2\pi R \int_0^h \sigma_{rz}|_{r=R} \cdot dz \quad (2.8)$$

where  $F$  is the force along the compression direction,  $R$  the radius of the compression mold,  $h$  the height of the sample,  $\sigma_z|_{z=0}$  the axial stress and  $\sigma_{rz}|_{r=R}$  the shear component at the contact with the mold.

Two specific experiments were performed in order to analyze the influence of the shear component on the resulting axial stress. First, two samples with the same initial volume fraction (2,5%), but different height (35 mm and 70mm), were prepared and studied over the same volume fraction range, thus allowing to study the influence of the contact surface between the wire and the PTFE mold. Figure 2.16(a) shows the evolution of the stress as a function of the volume fraction for both those samples. A lower mechanical response can clearly be observed for the sample with the smallest surface contact. But except from that, the behaviour is globally the same (hysteresis and non-linearity). This seems to indicate that, although PTFE was used to limit the friction with the mold, the contribution of the shear component is not negligible and plays an important role in the

measurements performed in a “closed matrix” configuration.

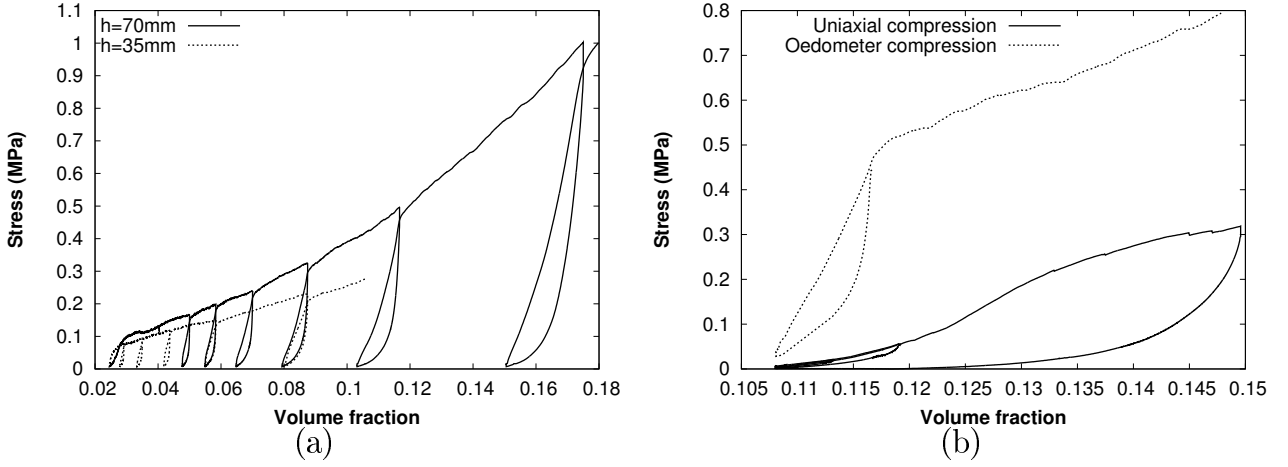


Figure 2.16: Influence of the contact surface with the cylindrical die : (a) same volume fraction with different height and (b) Uniaxial vs Oedometer.

A second experiment was carried out. It consisted in comparing the behaviour of the same sample (height = 15 mm and volume fraction  $\approx 11.75\%$ ) in uniaxial compression and in oedometric compression, with the same  $5.10^{-4} \text{ s}^{-1}$  strain rate. It can first be noticed that, when under uniaxial compression, the sample presents a residual strain after unloading, which is in accordance with the study by Poquillon *et al* [13] in which a remaining plastic deformation was observed for steel wools. Figure 2.16(b) also shows that the mechanical strength of the material is also considerably lower when tested under uniaxial compression. In conclusion, the effect of the friction of the wire with the PTFE mold was shown to be quite noticeable and these experiments showed the specificity of the oedometer test, for a given initial sample geometry. In the rest of the study, the geometry of the mould will then be kept constant (initial volume fraction : 5%, height : 35 mm, diameter : 15 mm) and the behaviour will not be regarded as absolutely representative of a given material but it will rather be used for relative comparison of the different materials.

#### 2.4.2 Influence of the wire diameter

For the oedometer compressive tests, the samples were compressed with a strain rate of  $5.10^{-4} \text{ s}^{-1}$ . As it was shown, it was then possible to plot the evolution of the stress as a function of the volume fraction, which is, in this case, the most relevant parameter to characterize the entanglement, as opposed to a classical stress-strain curve, from recording the evolution of the force as a function of the displacement of the moving piston.

For given volume fractions (6%, 7%, 8.7%, 11.7% and 17.5%), the samples were unloaded until a 0 N force and the stiffness of the entanglement was characterized by discharge modulus measurements (slope of the stress-strain curve at the first instant of the discharge). After unloading, the sample was reloaded in order to observe the hysteresis phenomenon. In order to first capture the influence of the diameter of the wire on the typical behavior of the studied monofilament entangled material, results will be presented for all stainless steel wires. Moreover, for a clearer representation, unloading cycles will only be shown for one of the three wire diameter tested.

As samples were manufactured manually, the reproducibility of the process was first investigated. Figure 2.17(a) shows the evolution of the stress as a function of the volume fraction for three identical samples made of a 280  $\mu\text{m}$  stainless steel wire. It can be noticed that, even if the curves are not perfectly identical, which would be surprising with this type of entangled structures, results are rather consistent and the mechanical response of the samples, whether submitted to unloading cycles or not, are relatively close.

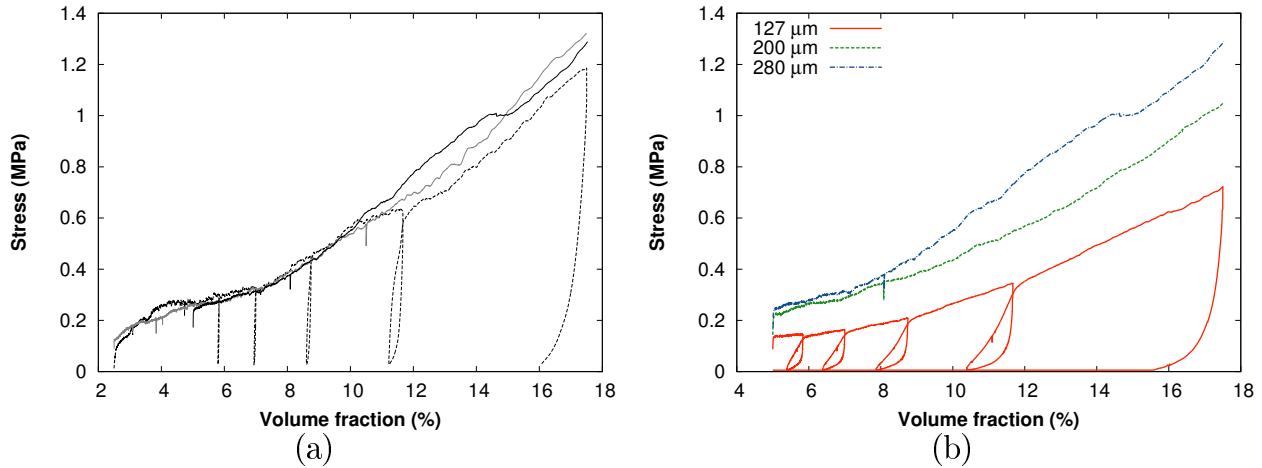


Figure 2.17: Evolution of the stress as a function of the volume fraction for three identical 280  $\mu\text{m}$  stainless steel wire (a) and for stainless steel wire samples with 3 different wire diameters.

As commonly observed in entangled materials ([13]), the compressive mechanical behavior of the entanglement shows a non-linear evolution (Figure 2.17). There is no regime in which a purely linear elastic deformation could be observed. The material gets denser and denser as the number of contacts per unit volume increases and the wire is deformed by bending between two contact points. Note also that, as it was presented in Chapter 1, a very strong hysteresis phenomenon is observed when a cyclic load is applied (unloading/reloading). This means that this material does exhibit good damping abilities. Loss factor measurements will be presented in Chapter 3.

The stiffness of the material was assessed by measurements of the slope of the stress-strain curve at the very beginning of the unloading sequence. The stiffness of these materials ranges from 20 to 200 MPa over the studied volume fraction range. Figure 2.18 shows that the entanglement tends to become stiffer as the volume fraction increases. Even though it was shown that the contact density is higher for a smaller wire diameter, the samples tend to be less stiff when the diameter decreases. The effect of the increase of the stiffness of the wire due to the increase of its diameter seems to over pass the effect of the decrease of its number of contacts.

### 2.4.3 Analytical model

As presented in Chapter 1 and from the numerical model developed in [36], it was showed that the entanglement can be seen as a network of beams being deformed mostly by bending between two contacts points (Figure 1.13). So, in the case of a stainless steel wire sample, the deformation of a sample can be viewed as an increase of the number of contacts along with deformation of the wire by bending and the entanglement can then be represented as the regular arrangement shown in

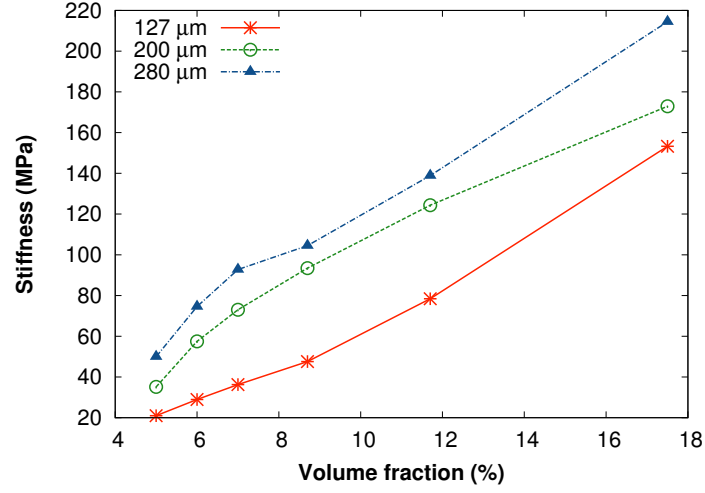


Figure 2.18: Evolution of the stiffness as a function of the volume fraction for stainless steel wire samples with 3 different diameters.

Figure 2.19(a) which assumes a homogeneous orientation distribution and contact density throughout the sample. One unit cell, which can be replicated in every direction, is here represented.

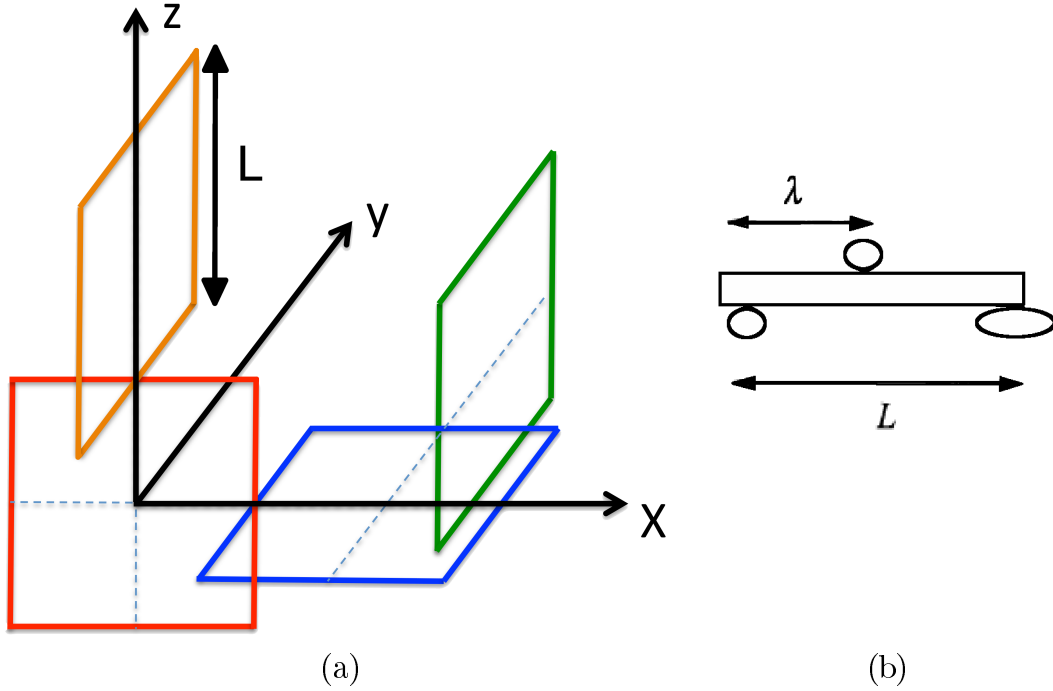


Figure 2.19: Representation of one unit cell of size  $2L$  (a) as a network of bending beams (b).

For a given volume fraction  $p$ , the characteristic length  $L$  of the bending beam was obtained by considering that, as illustrated in Figure 2.19(b),  $L = 2\lambda$ , where  $\lambda$  is the experimental mean length between contacts previously acquired from the tomography data.

Considering that  $h = h_0 \exp(-\epsilon)$  (where  $h_0$  is the initial height of the unit cell and  $h$  its final height under load), the resulting strain  $\epsilon$  on a unit cell of size  $2L$  can be written as:

$$|\epsilon| = \ln \left( \frac{2L - 4\delta}{2L} \right) \quad (2.9)$$

where  $\delta$  is the deflection of the bending beam.

Accordingly, the curvature radius  $\rho$  of the bending beam can then be defined as :

$$\rho = \frac{\left(\frac{L}{2}\right)^2 + \delta^2}{2\delta} \quad (2.10)$$

Finally, the local strain of the wire, in bending between two contact points, can be determined using equation 2.11.

$$\epsilon_w = \ln \left( 1 + \frac{r}{\rho} \right) \quad (2.11)$$

where  $r$  is the radius of the wire.

The characteristic length  $L$  of the structure was shown to decrease with the volume fraction and as far as the plastic behaviour of the resulting beam is concerned, a low diameter of the wire and a relatively low yield strength induced an important deformation. In order to take that into account, an equivalent elasto-plastic modulus can be defined (Equation 2.12) as :

$$E_{ep} = \frac{\sigma_y E}{\sigma_y + E \epsilon_w} \quad (2.12)$$

where  $E$  is the Young's modulus of the constitutive material,  $\sigma_y$  the yield strength of the material and  $\epsilon_w$  the strain of the beam in bending.

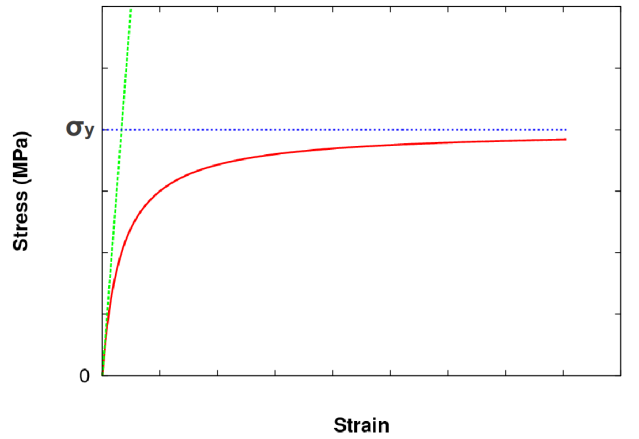


Figure 2.20: Presentation of the stress-strain behaviour as the sum of two limit behaviors.

This modulus takes into account the plastic behavior of these stainless steel wires. It corresponds to a rule of mixtures of two limit behaviors : the perfectly elastic relation given by  $\sigma = E \epsilon_w$  (see green curve in figure 2.20) and the perfectly plastic limit where  $\sigma = \sigma_y$  (see blue curve in figure 2.20).

As  $L$  was shown to decrease with the volume fraction, it resulted in a decrease of the apparent modulus during the compression.

The resulting force of a beam (length =  $L$ ) to a deflection  $\delta$  can be written as :

$$F = \frac{48E_{ep}I}{L^3}\delta = K\delta \quad (2.13)$$

where  $E_{ep}$  is the elasto-plastic modulus and  $I$  the area moment of inertia equal to  $(\pi d_f^4)/64$  (where  $d_f$  is the wire's diameter).

Consequently, in the case of a compression along the  $z$  direction, each deformed segment, perpendicular to the compression direction, can be regarded as a spring with a stiffness  $K = \frac{48EI}{L^3}$  and the resulting force  $F_z$  on a unit cell can thus be calculated as :

$$F_z = K\delta = \frac{KL}{2}(1 - \exp(-\varepsilon)) \quad (2.14)$$

where  $\varepsilon$  is the macroscopic strain on the unit cell.

Finally, the resulting stress  $\sigma_z$  on the unit cell was calculated by adding the contribution of the bending beams to an initial stress value  $\sigma_0$  taken from the experiment (see Equation 2.15). The evolution of the stress with the volume fraction could then be plotted and compared to experimental results. Figure 2.21 shows the results of this analytical model in parallel to the results previously presented for different diameters of a stainless steel wire.

$$\sigma_z = \sigma_0 + \frac{F_z}{(2L)^2} \quad (2.15)$$

A very good agreement between the experimental and model behaviour was obtained for all three wire diameters. Consequently, this model provides an analytical prediction of the mechanical response of an entanglement based on experimental data of the mean length between contacts.

In parallel, another method, based on the theoretical increase of the number of contacts was defined. In a cubic unit cell of size  $L$ , similar to the one shown in Figure 2.19, 6 contacts are considered and the characteristic length  $L$  of the entanglement can thus be calculated according to equation 2.16.

$$L = \left( \frac{6}{N_{cv}} \right)^{\frac{1}{3}} \quad (2.16)$$

where  $N_{cv}$  is the number of contacts per unit volume, calculated from the “tube” model using the experimental orientation parameter  $f$  defined experimentally ( $f = 1.6$ ).

Consequently, the resulting stress on the unit cell can be obtained and its evolution as a function of the volume fraction can be studied. Figure 2.22 shows the model behaviour of both analytical methods, along with the corresponding experimental plot (wire diameter : 200  $\mu m$ ).

A good agreement could be obtained using both methods for the calculation of the characteristic length  $L$ , thus validating the hypothesis of 6 contacts per unit cell of size  $L$ . However, it appears that, for higher volume fractions, the measurement performed using the “tube” model (with  $f = 1.6$ , green curve in Figure 2.22) for the increase of the number of contacts remains closer to the experimental results. This indicates that the experimental measurement of the mean length between contacts

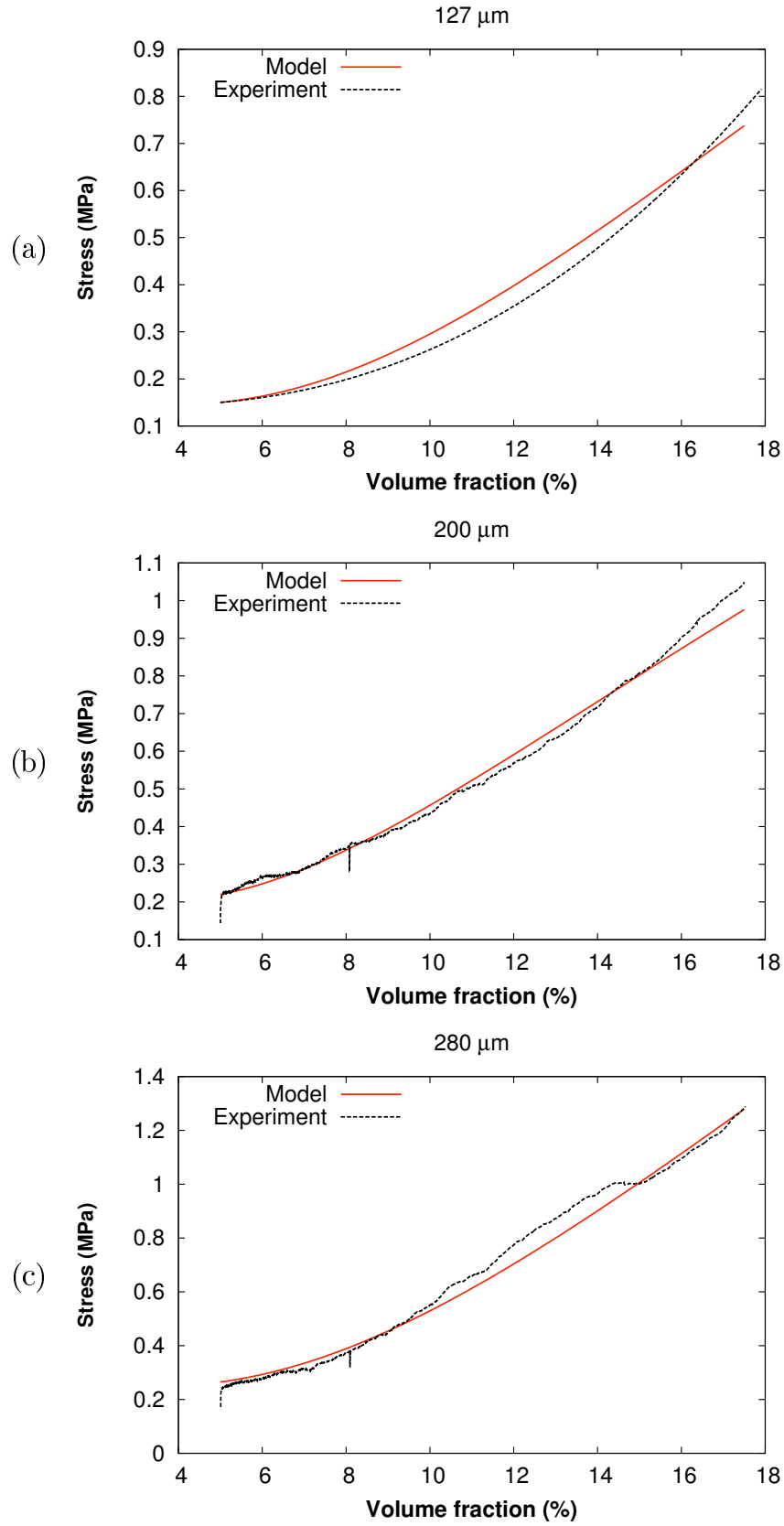


Figure 2.21: Fit of the analytical model to the experimental results for a stainless steel wire with a 127  $\mu\text{m}$  (a), 200  $\mu\text{m}$  (b) and 280  $\mu\text{m}$  (c) diameter.



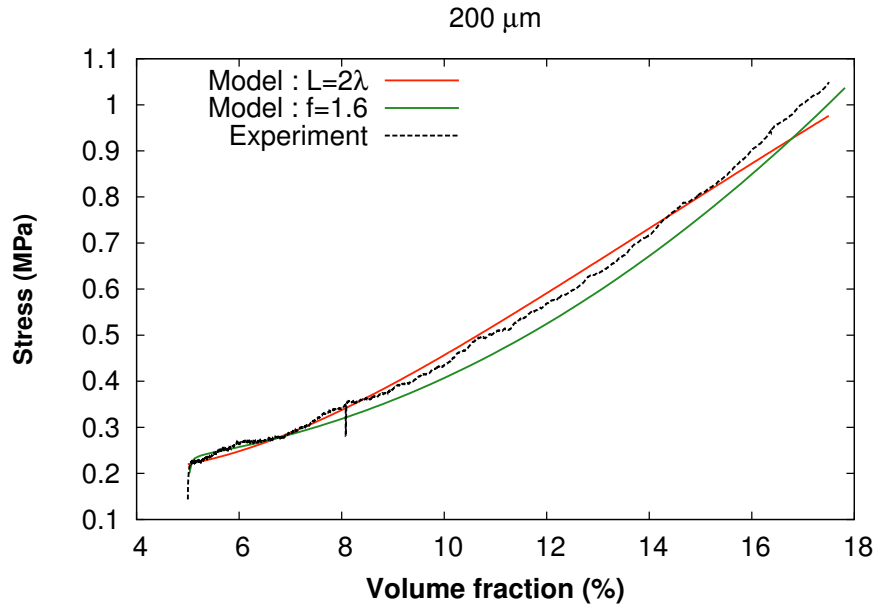


Figure 2.22: Comparison of the model behaviour for both analytical methods (red : experimental length between contacts and green : “tube” model for the increase of the number of contacts per unit volume, with  $f = 1.6$ ) to the experimental stress/volume fraction plot for a  $200\mu\text{m}$  stainless steel wire.

(red curve in Figure 2.22) diverges from a “theoretical value” for higher densities. This was to be expected as quantitative measurements from tomography data might become less precise for high volume fractions (more contacts).

## 2.5 Conclusion

In this chapter, methods used to manufacture samples were presented. Samples were all prepared in the laboratory and analyzed using an in-situ approach in order to study the evolution of microstructural parameters under compressive loadings. The treatment of the 3D volume was introduced and will be described in more details in the following chapter.

From the microstructural analysis, Monofilament Entangled Materials were shown to be very heterogeneous with a strong “wall effect” that could be reduced by using smaller wire diameters. It was also shown that the evolution of an internal parameter such as the number of contacts is directly linked to the global mechanical response of the material. As the entanglement gets denser and denser, the number of contacts increases as a function of the square of the volume fraction, thus leading to a higher and non-linear mechanical response. Finally, an equivalent orientation parameter  $f$ , specific to the oedometric compression of entangled media was defined.

The stiffness of monofilament entangled materials was shown to be conditioned by the shear component at the contact with the mould and to be in a 20-200 MPa range, which is relatively high for a highly porous entangled material. It is also worth noticing that the entangled structure, under compressive loading, exhibits a stiffness evolution, with the volume fraction, opposite to many usual cellular materials (foams, for example, tend to get weaker when compressed). A strong hysteresis phenomenon was noticed when under a cyclic load, which conveys the damping ability of this

material. Loss factor measurements will be shown in the upcoming section.

The mechanical properties of this material were modeled analytically by taking into account the experimental evolution of the mean distance between contacts, as well as the plastification of the stainless steel wire. A good agreement between the experiments and modelling was finally obtained.

# Chapter 3

## Tailoring the properties

*This chapter aims at studying the influence of manufacturing parameters on both the microstructural and the macroscopic mechanical behaviour of Monofilament Entangled Materials. From the tomography data, the complex internal architecture of this material was first characterized in order to have a better understanding of the deformation mechanisms and of the evolution of some key parameters such as the density distribution and number of contacts. The mechanical behaviour was then investigated under different types of loadings. The damping properties of the entanglement was defined in order to estimate its energy absorption ability. Finally, the mechanical properties of sintered wire meshes were tested for two different sintering techniques (conventional and Spark Plasma Sintering).*

### Chapter's content

3.1	Experimental procedures . . . . .	60
3.1.1	High yield strength of the wire . . . . .	60
3.1.2	Modification of the initial wire shape . . . . .	61
3.1.3	“Sintered” materials . . . . .	63
3.2	Microstructural characterization . . . . .	68
3.2.1	Distribution of density and orientation along the compression axis . . . . .	68
3.2.2	Radial density profiles . . . . .	70
3.2.3	Number of contacts . . . . .	75
3.3	Monotonic mechanical analysis . . . . .	77
3.3.1	Compressive oedometer testing . . . . .	77
3.3.2	Damping . . . . .	80
3.3.3	Shear testing . . . . .	84
3.3.4	Tensile test . . . . .	86
3.3.5	Characterization of sintered materials . . . . .	87
3.4	Dynamic Mechanical Analysis . . . . .	92
3.5	Conclusion . . . . .	97

Given the large number of parameters that can be modified when manufacturing Monofilament Entangled samples, the material can be tailored to specific requirements by adjusting them.

Using the in-situ experimental procedures previously presented, this chapter aims at studying the influence of those different adjustable parameters (constitutive material, initial shape of the wire and state of the contacts : fixed or sliding) in order to have a better understanding of the properties of Monofilament Entangled Materials.

At first, additional manufacturing procedures, such as wire pre-deformation and sintering steps, will be presented. Microstructural results will then be shown and links with the precedently presented mechanical behaviour will be investigated. Samples will then be tested under different solicitations (monotonic and dynamic) and both stiffness and loss factor measurements will be presented.

## 3.1 Experimental procedures

Following the same procedure that was presented in Chapter2, samples can be prepared while changing a few manufacturing parameters such as the yield strength or the initial wire shape.

### 3.1.1 High yield strength of the wire

In addition to the stainless steel wires, a pearlitic steel wire was obtained, thanks to O. Bouaziz and his collaborators. This wire was chosen here because of its high yield strength (4000 Mpa) compared to a 304L. Table 3.1 shows the chemical composition of the raw material and table 3.2 shows a summary of the dimensions and mechanical properties of the wire.

	Pearlitic steel (wt%)
Carbon	0.91
Manganese	0.69
Phosphorus	0.012
Sulfur	0.0009
Silicon	0.23
Chromium	0.2

Tableau 3.1: Chemical composition of a pearlitic steel.

Material	Diameters ( $\mu$ m)	Yield strength (MPa)
Pearlitic steel	120	4000

Tableau 3.2: Properties of used wires.

Unlike samples made of stainless steel wires, pearlitic samples can only be characterized under oedometric compression as the deformation induced during the precedently described manufacturing

steps is purely elastic.

### 3.1.2 Modification of the initial wire shape

Given the low diameters of the stainless steel wires that were chosen, they are easily deformable and can be pre-formed to given shapes. While preserving an “entangled media” arrangement, this allows us to study the influence of the wire initial shape on the macroscopic properties of the material.

#### 3.1.2.1 Spring pre-forming

In the simplest case, the wire is entangled as received, with no pre-deformation. But as it was first introduced in [32] and as suggested by informal discussions with D. Embury at the beginning of the project, an entanglement made of a pre-coiled wire was also produced. It presents a more homogeneous distribution and thus, more isotropic properties. In the case of the stainless steel wires (again the pearlitic wire could not be plastically deformed), some samples were then prepared using the process shown in Figure 3.1.

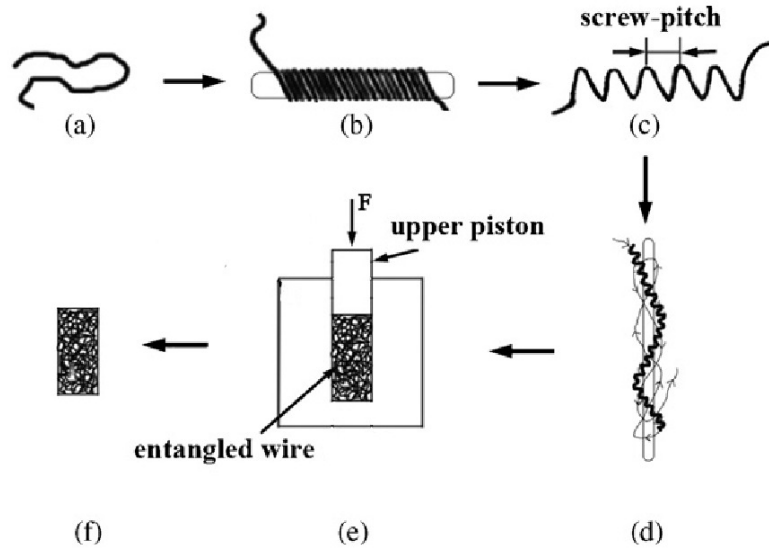


Figure 3.1: Schematic diagram of the preparation process of the spring pre-deformed entangled stainless steel wires [32]

The wire was first coiled around a rod having a diameter of 3 mm. This spring was then stretched to the point where the distance between two consecutive turns was of the order of magnitude of the diameter of the spring ( $\approx 3$  mm). This pre-coiled wire was subsequently wound around the rod in order to obtain a precursory entanglement that was then placed inside a cylindrical die. Figure 3.2 shows the as-prepared spring as well as the final entanglement before shaping in the mould.

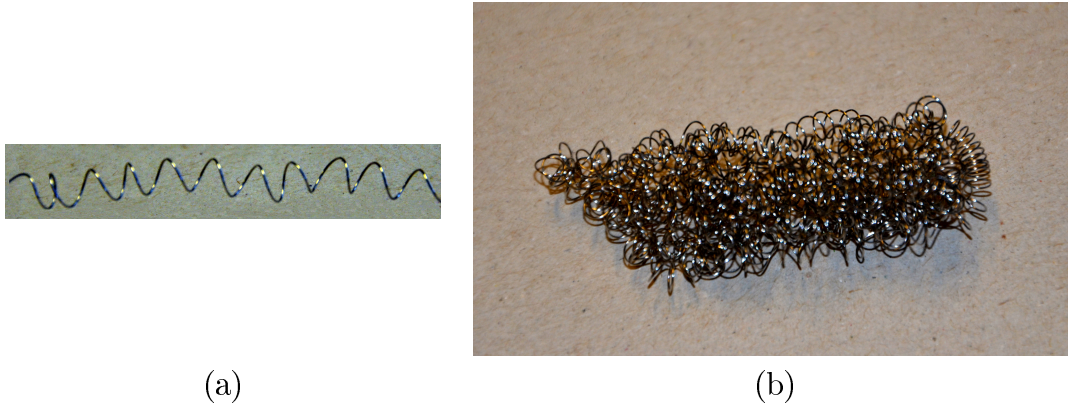


Figure 3.2: (a) : Pre-coiled stainless steel wire with a  $200\mu\text{m}$  diameter and (b), the entanglement made out of it

#### 3.1.2.2 Short fibers

In order to compare all these entanglement methods to a better known structure, samples were prepared using short fibers. The wire was cut in pieces with a length of the order of magnitude of the final size of the sample ( $\approx 30\text{ mm}$ ). This aimed at helping us to study the influence of the “monofilament” characteristic of our specific material.

#### 3.1.2.3 Cables

As suggested during informal discussions with O. Bouaziz at the beginning of the project, a given section of wire can be split into several smaller wires wound together to form a cable. A cable has the same tensile properties but is much less stiff in bending than an equivalent monofilament. Cables were thus prepared using the smallest stainless steel wire ( $127\mu\text{m}$ ). Three wires were weaved using a rotating drill so as to obtain a cable with a cross section roughly equivalent to the one of a  $200\mu\text{m}$  stainless steel wire. Table 3.3 shows the cross section’s value for both those cases. Since the equivalent surface of the cable is not exactly the same as the simple  $200\mu\text{m}$  stainless steel wire, this will have to be taken into account when shaping up a sample with a given volume fraction. For the same final volume fraction, the cable will indeed have to be 80% shorter in order to be comparable to the  $200\mu\text{m}$  monofilament.

Initial shape	Cross section ( $\mu\text{m}^2$ )
Straight $200\mu\text{m}$ wire	31415.9
Cable (3x127 $\mu\text{m}$ wire)	38003.1

Tableau 3.3: Equivalent cross section in ( $\mu\text{m}^2$ ) of the cable in parallel to the straight  $200\mu\text{m}$  wire.

The above mentioned modifications of a few manufacturing parameters leads to a large number of combinations and then lead to different macroscopic and microstructural properties. The next section will focus on developing a sintering step for monofilament entangled materials, in order to be able to modify the stiffness and damping properties of the material.

### 3.1.3 “Sintered” materials

Entangled materials present, by definition, relatively low mechanical properties. If the sliding of the contacts is the reason why they might be interesting in terms of damping, this is also responsible for a strong reduction of the rigidity. In order to stiffen an entanglement of metallic fibers, fixed permanent contacts need to be created, thus forming a “sintered” entanglement. A few different approaches can be considered to sinter entangled media.

#### 3.1.3.1 Conventional sintering

Conventional sintering of wires uses the same principle as powder metallurgy. The entanglement is heated up to a temperature close to the melting point of the material under vacuum. A pressure can be applied on the sample during the process as shown in [31, 46]. In these studies, porous cylindrical-shaped samples with a volume fraction between 40% and 70% were manufactured from a stainless steel wire with a 0.3 mm diameter. It was shown that the applied pressure is strongly linked to the final porosity whereas the temperature and sintering time had a minor impact. With this method, the sintering quality is excellent as contacts are well bonded. It is however a very long process and it requires, in this specific case, to place the sample under pressure inside the vacuum oven.

In this study, for Monofilament Entangled materials, once the sample was formed inside the PTFE cylindrical mold, it was taken out and placed inside a quartz tube. The tube was then sealed on one side using a blowtorch (Figure 3.3 (a)) before being put under a secondary vacuum (Figure 3.3 (b)). While still under vacuum, the tube was closed by melting down the remaining “neck” (Figure 3.3 (c)). This way, a tightly vacuum-sealed capsule was obtained which could then be placed inside a simple high temperature oven. Once brought back to room temperature after sintering, the capsule was simply broken and the “sintered” sample taken out for characterization.

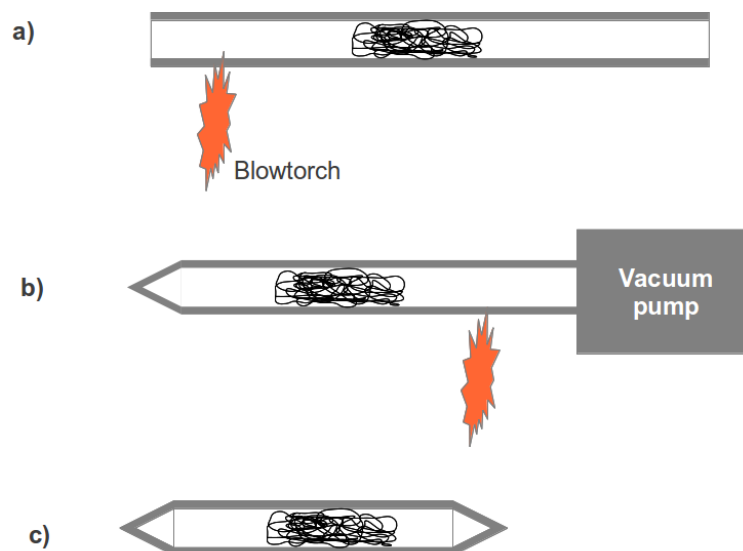


Figure 3.3: Overview of the vacuum-sealing method of a sample

In this study, samples were not submitted to any pressure (except the axial one due to the containing tube, which is relatively small considering that the samples were previously formed) since they were placed inside quartz tubes. The heat treatment was performed in a regulated Nabertherm furnace with a 5°C/min heating rate. The vacuum-sealed tubes were placed on an aluminum oxide plate. Previous studies on steel wire mesh sintering indicated a sintering temperature of around 1200-1300°C [31, 46]. Taking that into consideration, Table 3.4 shows a summary of the different parameter that were studied, for a given volume fraction (7.5%).

Temperature (°C)	Sintering time (h)	Wire shape
1250	2	straigth
	3	straigth
	2	spring
1350	2	straigth

Tableau 3.4: List of the conditions for the conventionnally sintered samples.

The effect of the temperature, initial wire shape, as well as the sintering time, was studied. And in parallel to that conventional sintering method, resistive sintering approaches were tested using first a GLEEBLE thermo-mechanical simulator. Results were not conclusive due to the heterogeneity of the samples (more or less short current path) and to the temperature control method of the machine. This, indeed, had to be controlled through a set temperature that was read through a thermocouple welded on the side of the sample. This very local reading was subject to high fluctuations, considering the heterogeneity of the material. At times, the intensity was set at a very high voltage because of a low temperature reading from the thermocouple when parts of the sample were already at higher temperature and thus started to melt.

Given the difficulties with the GLEEBLE machine, this investigation was then rather pursued using another high current and high temperature device, the Spark Plasma Sintering.

#### 3.1.3.2 Spark Plasma Sintering

Considering that the studied material is metallic and is constituted of a singled continuous wire, a resistive sintering method can be applied. Consequently, a device was designed in order to be able to create fixed nodes at the contact points inside the entangled material by applying a strong current through it.

##### **Principle**

Spark Plasma Sintering, also known as Field Assisted Sintering Technique (FAST) is a high speed sintering technique using pulsed DC current (high amperage : about 5 V and 2000 A) in order to heat and activate the consolidation of materials. This pulsed DC current passes directly through the graphite die, as well as the sample (or powder), in case of conductive materials. Unlike conventional sintering methods, where the heat is provided by external heating elements, it is here generated internally, and as shown in Figure 3.4, the samples are usually placed inside a graphite die, under high pressure.



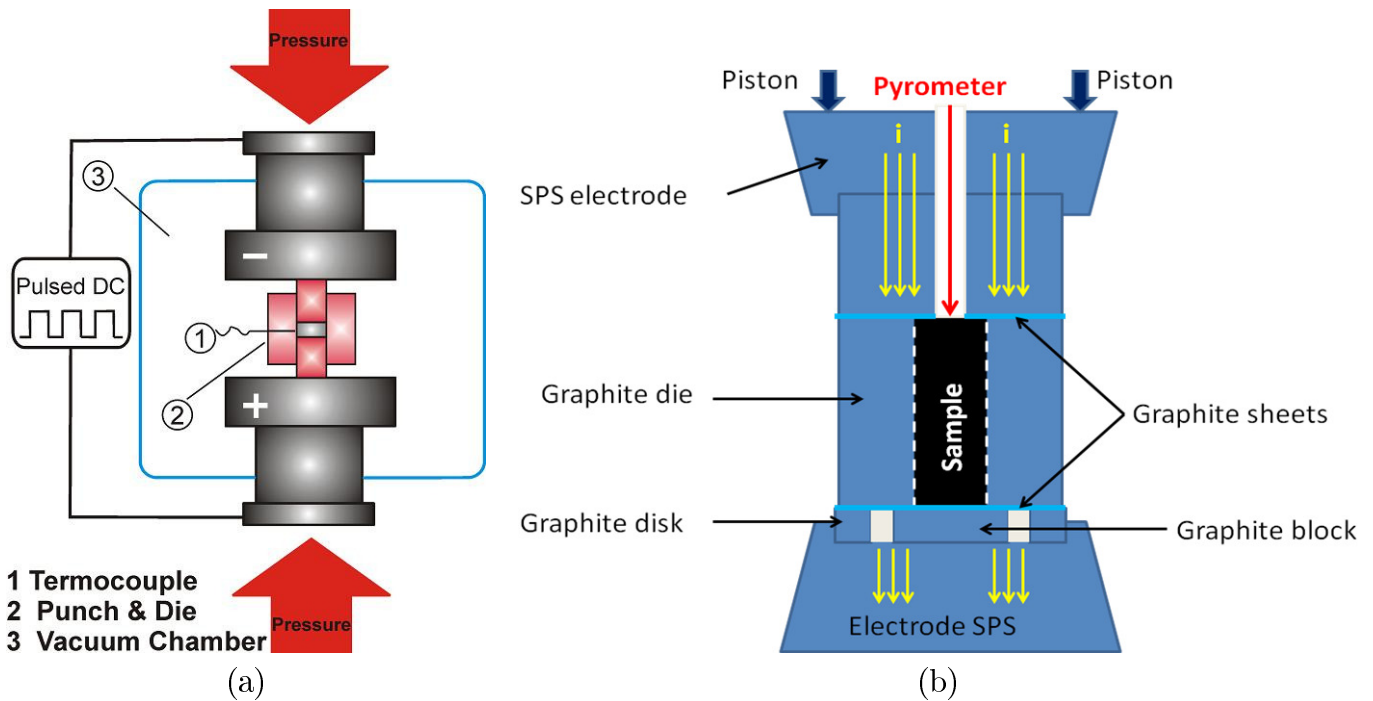


Figure 3.4: (a) : Schematic of a basic SPS configuration and (b) : SPS device for sintering entangled materials

Therefore, high heating or cooling rates can be achieved (up to 1000K/min) and both the sintering time and temperature can be lowered. Whether plasma is generated has not really been confirmed yet [58], especially when non-conductive materials are compacted, but an accelerated sintering is clearly observed and no other clear explanation has been proposed.

### Sintering device for entangled materials

SPS is now a widely used way of sintering materials, but it normally aims at obtaining fully dense materials, or at least for the densification of powders. This study was thus first intended at testing the feasibility of a resistive sintering method for fibrous materials aiming at keeping the amount of open porosity.

In the case of entangled materials, the “classical” SPS process has to be modified in order to obtain the desired reinforced architecture. Generally, in order to be able to sinter a non fully dense material, the minimal pressure applicable in the SPS (5kN) has to be sustained by the graphite die so that the entanglement, which present low mechanical properties (compared to the 5 kN pressure applied in the machine), does not get crushed. With this aim in view, the device presented in Figure 3.4 was designed.

Using this setup, all the load was sustained by the graphite die and graphite sheets were placed to ensure a good electrical contact between all the different components. The monofilament sample was firstly prepared just slightly higher than the height of the die in order to get it slightly compressed once placed inside the device. This ensured a good electrical contact. Unlike in the standard setup where a thermocouple is rather used to read the sample’s temperature, a pyrometer was used here at the top of the sample, through a pierced top-electrode. For an accurate measurement, the pyrometer had to be first calibrated to the materials emissivity. For stainless steels, this thermophysical property

was set to 0.32. Considering that in reality, the emissivity also depends on the temperature and that it is only a local measurement, the temperature given by the pyrometer could be slightly different than the actual temperature of the sample.

Taking that into account, a set of experiments was performed in order to calibrate the temperature on the machine. A batch of samples were sintered at different “machine temperatures”. Just like for a conventional sintering, a temperature of around 1200°C should be reached in order to obtain a sintering of the entanglement. But since, as mentioned, the actual temperature of the sample is hard to determine using SPS sintering, we started by trying out lower temperatures in order not to melt samples inside the SPS’s chamber. Table 3.5 shows a summary of the samples used to calibrate the device.

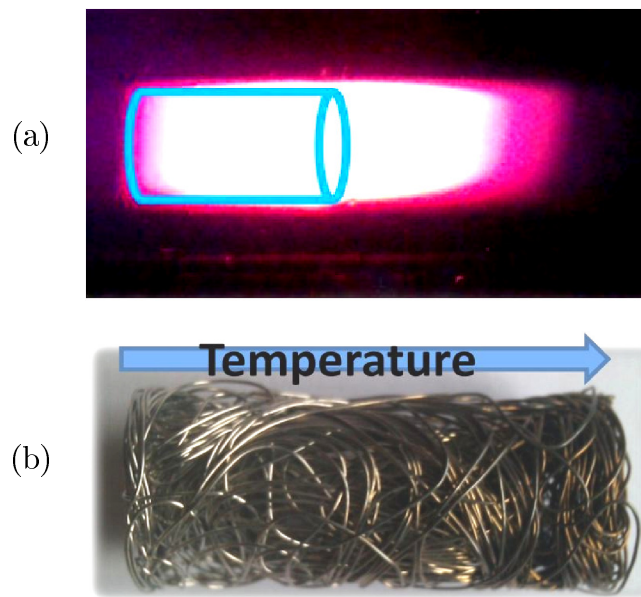


Figure 3.5: (a) : Picture of the sample inside the graphite die during sintering and (b) : sample once sintered

This sample’s batch showed that for temperatures above 1050°C, the stainless steel wire started to partially melt, thus defining the optimal sintering temperature as being equal to 1000°C. Those samples were only analyzed qualitatively and an important thermal gradient was noticed on the sample, as shown in Figure 3.5(a) which corresponds to the view of the sample inside the chamber, while operating.

Temperature (°C)	Sintering time (min)	Wire’s diameter ( $\mu\text{m}$ )	Sample’s height mm	Volume fraction %
850, 900, 950, 1000, 1050 and 1100	1	127	35	10

Tableau 3.5: SPS sintering conditions used to calibrate the “machine temperature”.

In order to limit this gradient, the graphite die was reduced to contain 10 mm high samples, the sintering time was increased and samples with a higher volume fraction were used. Moreover, the graphite sheets that were meant to ensure a good electrical conduction between the different parts of the device were replaced by tungsten sheets. Tungsten being less conductive, we intended to redirect the current through the sample at its exit side. Lastly, “spring” samples, using a stainless steel wire with a  $280\text{ }\mu\text{m}$  diameter, were used in order to limit the heterogeneity of the sample and thus of the current field. Figure 3.6 shows the interior of the chamber while operating with the new setup. The temperature is clearly more homogeneous and no thermal gradient can be observed on the sample once sintered.

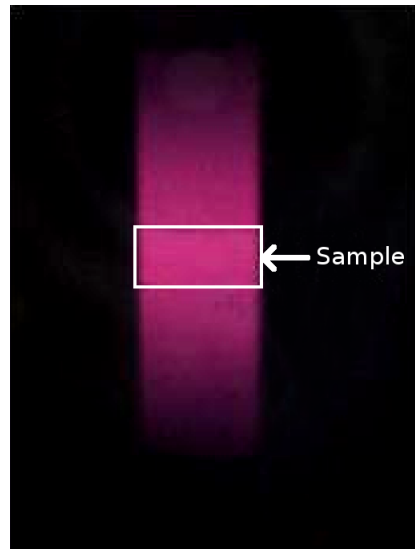


Figure 3.6: Picture of the sample inside the graphite die during a 10 minutes long sintering.

Sintering time (min)	Temperature (°C)	Volume fraction %
10	950	10
	1000	10
	950	20
	1050	20

Tableau 3.6: List of samples sintered using the SPS.

Table 3.6 shows the list of the second batch of samples that were sintered. Those samples were characterized by uniaxial compression and results will be presented below. The samples were compressed with a  $1.10^{-4}$  compression rate using a Instron 3365 testing device which will be presented later in more details.

Manufacturing methods were presented in this section which allow for a control of the properties of the material. The following section will focus on characterizing the influence of those parameters on both the microstructural and mechanical behaviour of the materials under different loading conditions.

## 3.2 Microstructural characterization

As it was introduced in Chapter 1, the mechanical properties of entangled materials are closely linked to their internal microstructure. The preliminary results presented in Chapter 2 tend to confirm it as a non-linear stress evolution was observed, as well as a strong hysteresis when cycling the sample, thus indicating that contact points play an important role on both the compressive and hysteretic behaviour of the entanglement.

In the following sections, a thorough characterization of the complex internal architecture of the material will first be performed using in-situ X-ray experiments in order to follow the evolution of some key parameters such as the number of contacts while compressing (as introduced in Chapter 2, multiple volumes were acquired for a given sample during the deformation). This entangled material is, by definition, constituted of a complex network of wire segments, which would be very difficult to characterize without 3D imaging techniques. The density distribution inside the material will thus be studied in order to identify the deformation mechanisms as well as to permit a prediction of the homogeneity of a sample as a function of its manufacturing characteristics (yield strength and shape of the wire, volume fraction,...).

### 3.2.1 Distribution of density and orientation along the compression axis

Similarly to what can be done when studying the oedometric compression of granular media, the evolution of the density distribution along the compression axis (z-axis) was monitored, based on the 3D images. Once processed, these consist in a pile of 2D images. The third dimension is given by the number of slides in a stack. Therefore, by measuring, for each cross-section of the sample (perpendicular to the z direction), the ratio of the number of white pixels over the total number of pixels constitutive of the sample (a circle since the sample corresponds to a cylinder), a local density value (0 to 1) can be obtained for a given z position (from top to bottom).

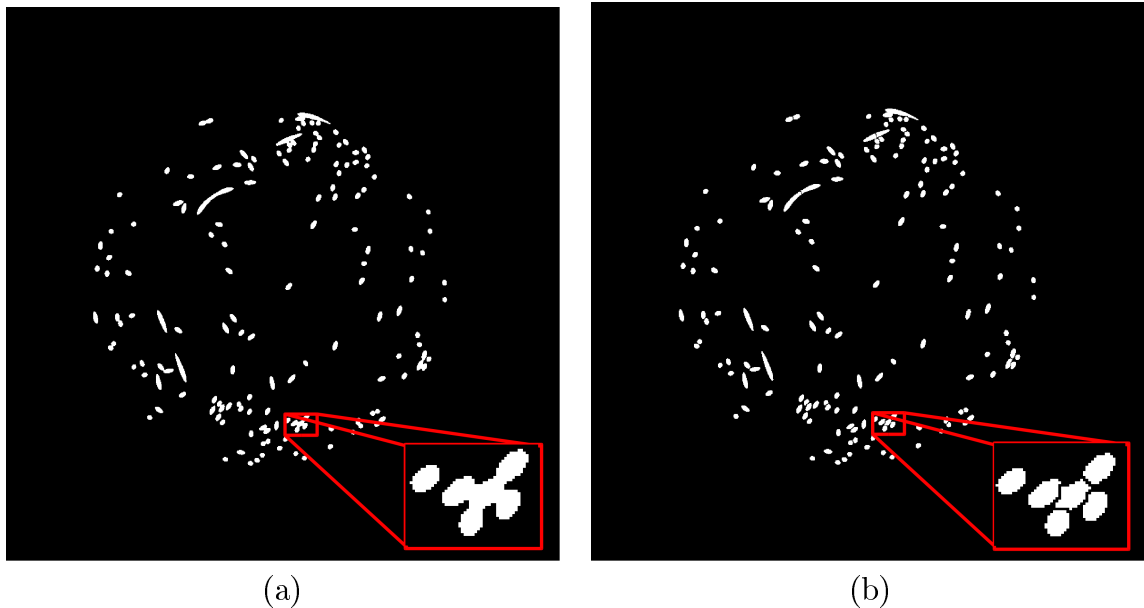


Figure 3.7: Cross section of a cylindrical sample before (a) and after watershed (b).

In parallel and in order to better understand the deformation mechanisms when compressing the sample, it is important to follow the mean local orientation of the wire as well. The local orientation was measured by studying the elliptical cross-section of the wire. The intersection of each bit of wire with an X-Y slice is an ellipse, the aspect ratio of which being related to the local orientation of the wire.

For each slice of the stack and for each cross-section of the wire (example shown in Figure 3.8), the orientation can then be deduced from the parameters of the fitting ellipse. Since each individual cross-section of the wire needs to be fitted, a first step was needed in order to separate the connected ellipses. A “watershed” algorithm [59] was applied to each 2D slices of a 3D volume (the slices being perpendicular to the compression axis) thus providing usable ellipses for the orientation measurement (see Figure 3.7).

The major axis will be referred to as  $a$  and the minor one as  $b$  (Figure 3.8). The angle  $\theta$  to the normal of the cross-section plane is defined as  $\theta = \arccos(\frac{b}{a})$  ([60]). By averaging the as-measured orientation over a whole section of the sample (perpendicular to the compression axis), a single local orientation value is obtained for a given  $z$  position. By doing so from top to bottom of the sample, an orientation distribution along the compression direction can be measured.

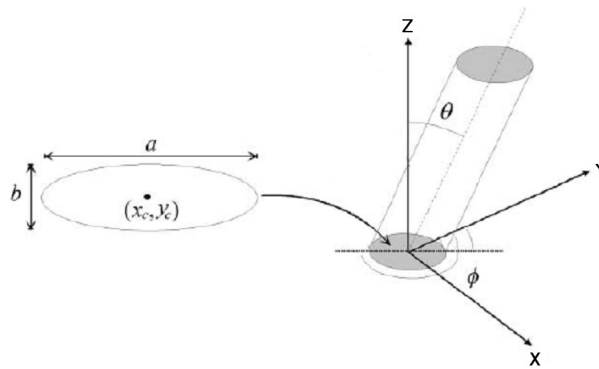


Figure 3.8: Representation of a fiber in 3D along with the description of its elliptical cross-section

A compressed sample (200  $\mu\text{m}$  stainless steel wire and initial volume fraction : 5%) was analyzed during its compression and data were gathered in Figures 3.9 and 3.10. Figure 3.9 shows the evolution of the density with the volume fraction while figure 3.10 presents the evolution of the corresponding mean orientation angle to the compression axis. A relatively homogeneous profile could be observed in the initial state (5%, figure 3.9), except for the denser parts at the top and bottom of the sample (this “wall effect” will be discussed in more details later). In terms of orientation, the internal part of the sample seems to be composed of wire sections oriented at an average angle of  $35^\circ$  whereas close to both ends the wire tends to be oriented, in average, parallel to the horizontal faces of the mold ( $70^\circ$ ).

With the increase of the volume fraction, densification peaks start to appear and grow (Figure 3.9). From the orientation distribution, it was shown that densification is accompanied by a reorientation of the wire in the direction perpendicular to the compression axis (highest angle between the  $z$ -axis and the wire). This structuring in the  $z$ -direction shows that the deformation of this material is not homogeneous and that localized deformation is accompanied by local densification and fiber reorientation.

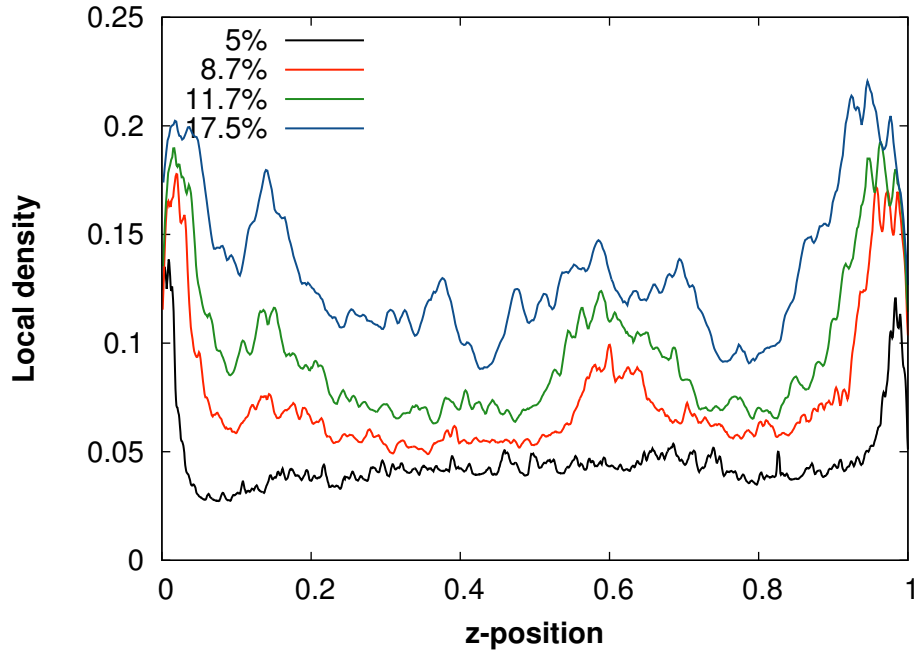


Figure 3.9: Representation of a fiber in 3D along with the description of its elliptical cross-section

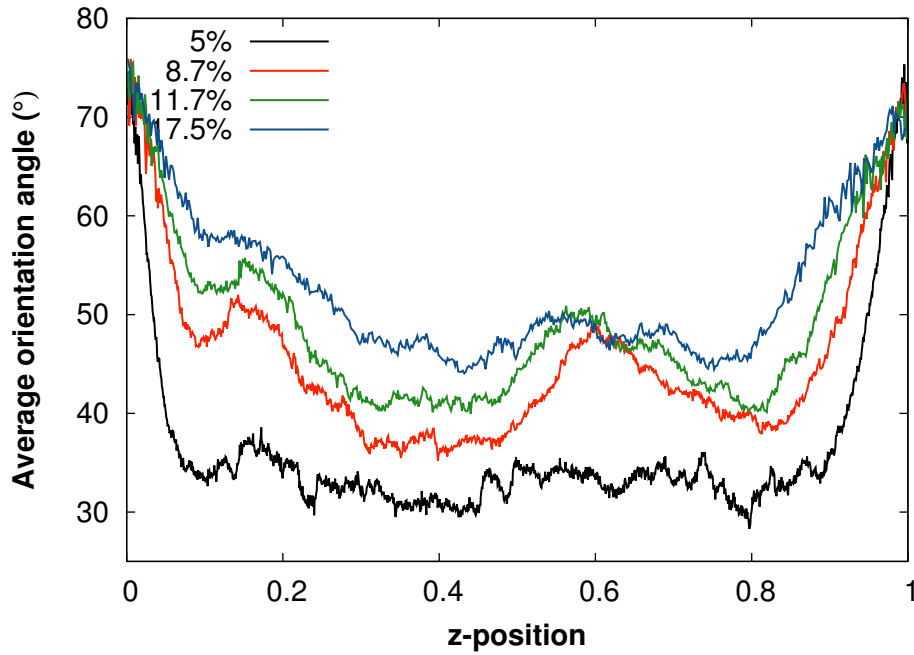


Figure 3.10: Representation of a fiber in 3D along with the description of its elliptical cross-section

### 3.2.2 Radial density profiles

After characterizing the density distribution along the compression axis and as it was shown in Chapter 2 that random Monofilament Entangled Materials exhibit a strong “wall effect”, the influence of the manufacturing parameters on the radial density distribution was then investigated. By playing with the yield strength, initial shape of the wire or volume fraction of the sample, more or less homogeneous materials could be obtained.

### Influence of the yield strength of the wire

From the experiments with the pearlitic steel, we could study the influence of the yield strength of the wire on the density distribution. Samples with a 5% volume fraction and straight wires were shaped and placed inside the 15 mm PTFE mold. From the radial density profiles shown in Figure 3.11, it can clearly be seen that the density gradient in the case of a high yield strength (pearlitic steel) is much more important than for low yield strength (stainless steel). This strong heterogeneity might also play a role in the mechanical response of this materials since we have, locally, a very dense material and thus a higher contact surface with the mold, which will tend to rigidify the structure.

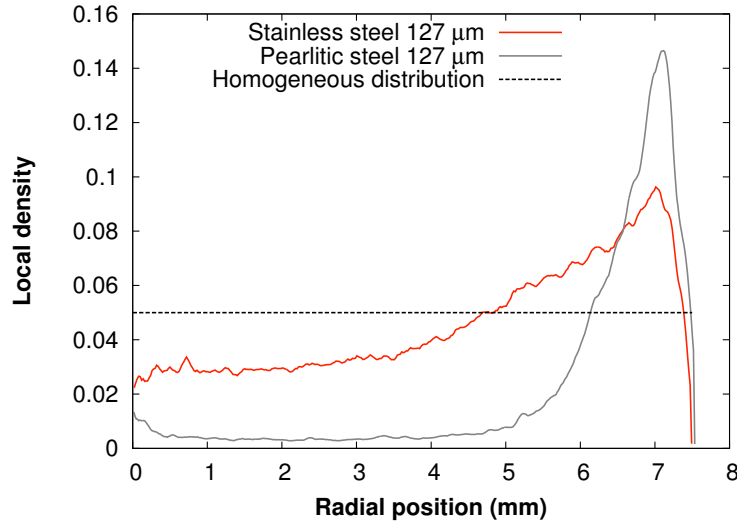


Figure 3.11: Influence of the yield strength on the radial density profiles (same volume fraction 5%).

For two materials with the same modulus of elasticity, the arrangement of the wire in a given volume is radically different. The very heterogeneous structure that can be noticed for pearlitic steel wires could indicate that the deformation of the wire is, in this particular case, mostly elastic and that the average curvature of the wire is equivalent to the radius of the compression mold.

### Influence of the volume fraction

By normalizing the local density, measured for a given radial position, by the height of the sample, profiles could be compared for different volume fractions of a same sample. Figure 3.12 shows the evolution of the normalized radial density profile ( $= \frac{\text{local density}}{\text{height of the sample}}$ ) with the volume fraction. The analysis was made for a sample made of a 200  $\mu\text{m}$  stainless steel wire with an initial volume fraction of 5% (initial height : 35 mm).

It appears that, although the material does get denser, the general shape of the profile does not evolve much. For all other types of material, no significant modification of the radial density profile was observed. This would indicate that there is no re-arrangement of the wire in the radial direction when compressing the entanglement. The material is compressed along the compression axis with no evolution of the radial distribution. This, of course, is valid over the studied volume fraction range (5-17.5 %). For much higher volume fraction, the density will of course tend to be more and more homogeneous.

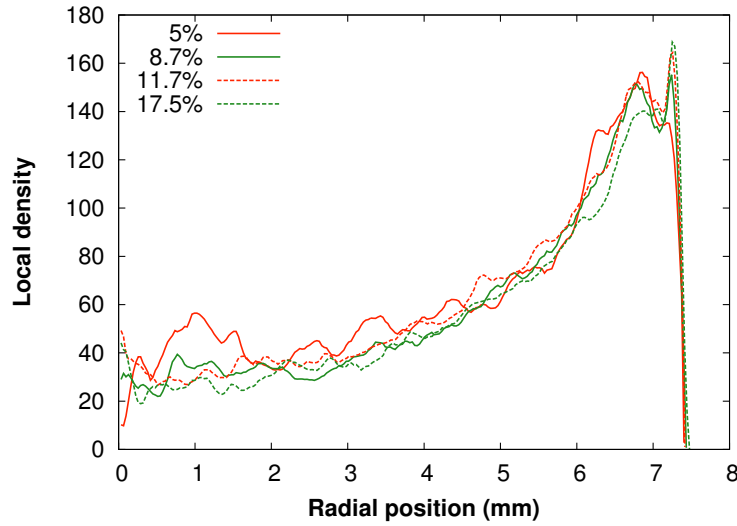


Figure 3.12: Influence of the volume fraction on the radial density profiles (wire :  $200\ \mu\text{m}$  Stainless steel).

### Influence of the wire's shape

As it was mentioned in section 3.1.2, studies such as [32] have shown that pre-deforming the wire as a spring had a tendency to improve the homogeneity of entangled materials. In order to verify this statement, an analysis of the density distribution was performed for all the wire shapes presented in section 3.1.2. Samples were prepared for each initial shape with a 5% volume fraction and 3D volumes were acquired.

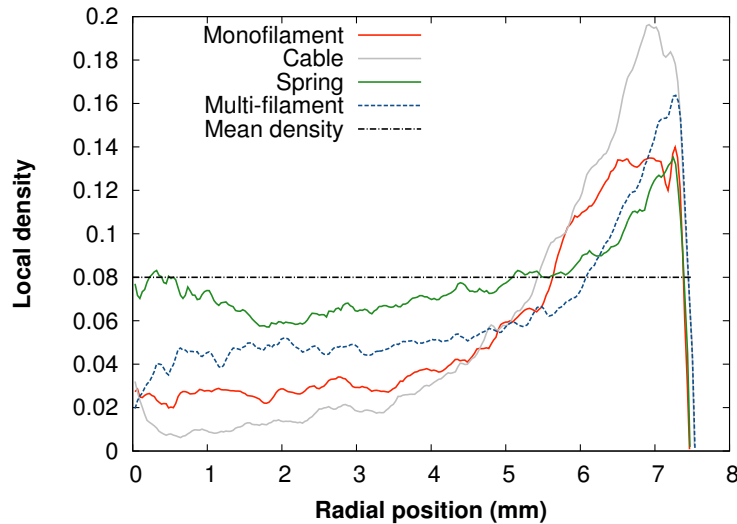


Figure 3.13: Influence of the initial shape of the wire on the radial density profiles (same volume fraction 5%, same diameter of the wire  $200\ \mu\text{m}$ , cable :  $3 \times 127\ \mu\text{m}$ ).

By using shorter fibers, the structure tends to be slightly more homogeneous and this tendency is even more noticeable when using spring pre-deformed samples. Although a small wall effect is still present, the heterogeneity of the material is far less pronounced. So as it was noticed when preparing the samples, entangling pre-coiled wires is easier for the same given volume. It seems like



the turns in the spring help create more evenly distributed contacts. The behaviour observed for the cable is a little bit more difficult to apprehend. It can be seen that the heterogeneity tends to increase when using a cable. Considering the lower bending stiffness of the cable, a more homogeneous structure could be expected. The experiment could not be pushed much further but one reason for this behaviour could be the plastification of the wires inside the cable when preparing it, which could affect the properties of the material, and thus make it behave differently.

### Phenomenological approach

Experimental microstructural analysis showed the heterogeneous nature of this type of material. Having a phenomenological index to predict this heterogeneity would thus be very interesting, taking into account the geometry of a sample and the intrinsic properties of the wire.

Intuitively, this index basically corresponds to the equivalent bending modulus of the wire constituting the entanglement. The heterogeneity parameter  $H$  can thus be written as :

$$H = (E_{ep}I)_{equ} \quad (3.1)$$

where  $E_{ep}$  corresponds to the elasto-plastic modulus of the material presented in Chapter 2.4.3 and  $I$  is the moment of inertia of the wire's section.

If we consider a beam, with a diameter  $d$ , in a bending loading condition, and with a curvature radius  $R_c$ , we can write that :

$$\epsilon = \frac{d}{R_c} \quad (3.2)$$

We can here write that  $d < R_c < R$ , where  $R$  is the diameter of the cylindrical mold. The perfectly homogeneous case does indeed correspond to a “chain” or “pearl necklace” with no bending modulus and for which  $R_c$  is equal to  $d$ . On the other hand, in the extreme heterogeneous (see Figure 3.14) case where the wire would be constrained against the side of the mould, we would have  $R_c = R$  or  $h$  (height of the sample), depending on the slenderness of the sample. It can thus be said that :

$$\frac{1}{R_c} = \frac{1}{R} + \frac{1}{h} \quad (3.3)$$

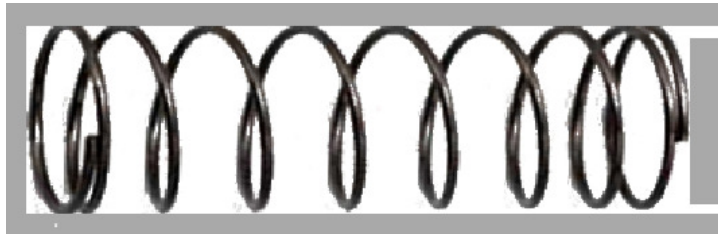


Figure 3.14: Schematic representation of the extreme heterogeneous case where the wire is packed against the mold.

In the heterogeneous case pictured in figure 3.14, we then obtain :

$$H_{max} \propto \frac{\sigma_y E}{\sigma_y + Ed(\frac{1}{R} + \frac{1}{h})} d^4 \propto \frac{E}{1 + \frac{Ed}{\sigma_y}(\frac{1}{R} + \frac{1}{h})} d^4 \quad (3.4)$$

Now in the perfectly homogeneous case, it can be said that, by making an analogy with a dislocation density, the mean distance between contacts can be written as :

$$\lambda_c = \sqrt{\frac{R^2 h}{L}} \quad (3.5)$$

Indeed, we have for dislocations, a density  $\rho = \frac{L}{V}$  and a mean distance  $d = \frac{1}{\sqrt{\rho}}$ . In this specific case, the curvature radius is then equal to the distance between contacts, as shown schematically in figure 3.15.

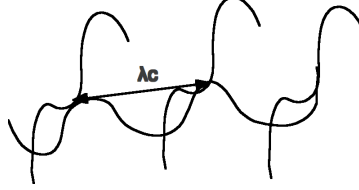


Figure 3.15: Schematic of the homogeneously distributed wire. Analogy with dislocations density.

It can also be said that :

$$\rho_0 \propto \frac{L d^2}{R^2 h} \quad (3.6)$$

From this, the heterogeneity parameter in the homogeneous case comes down to :

$$H \propto \frac{\sigma_y E}{\sigma_y + E \sqrt{\rho_0}} d^4 \propto \frac{E}{1 + \frac{E}{\sigma_y} \sqrt{\rho_0}} d^4 \quad (3.7)$$

An heterogeneity index  $i_h$  between 0 and 1 was then defined such as :

$$i_h = \frac{H}{H_{max}} \propto \frac{1 + \frac{E d}{\sigma_y} (\frac{1}{R} + \frac{1}{h})}{1 + \frac{E}{\sigma_y} \sqrt{\rho_0}} \quad (3.8)$$

Finally, the experimental radial density profiles could be described through the following equation :  $\rho(r) \propto r^n$ , characterized by the  $n$  exponent. An heterogeneity index was then measured for each diameter of the wire (for the same sample's geometry :  $R=7.5$  mm and  $h=35$  mm) as well as the corresponding  $n$  values. Figure 3.16 shows an example of the “power fit” of the radial density profile as well as the relationship between the exponent of the power law and the measured index. Based on this small set of data (more diameters and yield strengths would be needed), the relationship seems to be close to linear which is in good agreement with the experiments as a high  $n$  value stands for a highly heterogeneous structure, and thus a high heterogeneity index.

## Conclusions

In this experimental study of the morphology of the structure of monofilament materials, a description of the influence of the different manufacturing parameters on the density distribution was performed. It was shown that by pre-deforming the wire as a spring, more homogeneous structures could be obtained and that by combining the “spring effect” to a low wire diameter, homogeneous samples could be prepared. It was also showed that no rearrangement was observed over the studied

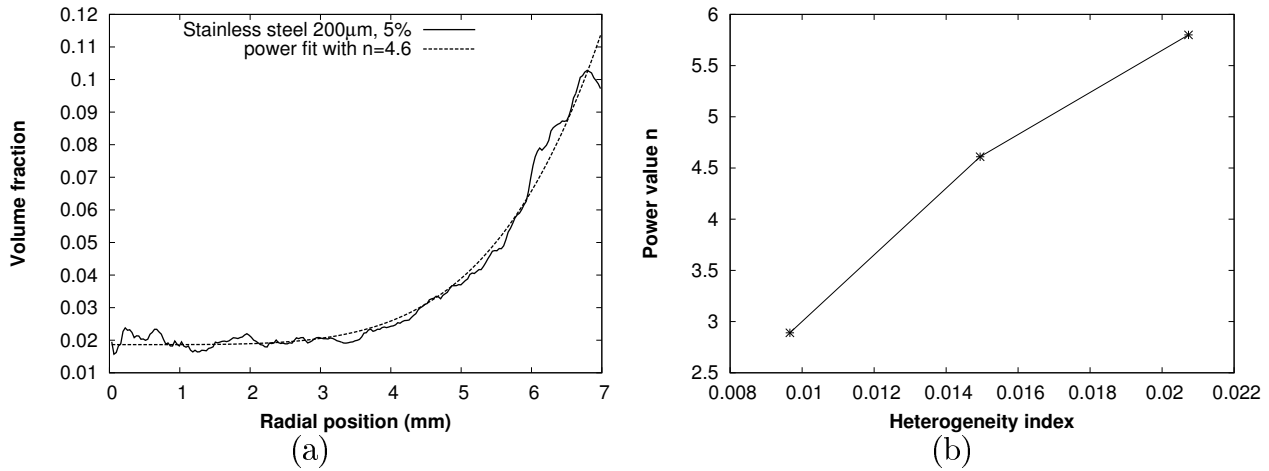


Figure 3.16: (a) “power fit” of a radial density profile and (b) evolution of the  $n$  exponent as a function of the heterogeneity index for stainless steel samples with 3 different diameters.

volume fraction range when compressing entanglements. Contacts are surely created but no clear evolution of the density distribution was observed (except the one along the compression axis, that was presented earlier).

### 3.2.3 Number of contacts

Just like for the study of the density distribution, samples with the same initial volume fraction were prepared for all wire shapes presented in section 3.1.2 in order to study its influence on the number of contacts. Samples with a 5% relative density were compressed inside a PTFE mold, and 3D volumes were acquired during the compression. Figure 3.17(a) shows the evolution of the number of contacts per unit volume with the volume fraction for a “monofilament”, a “multi-filament”, a “spring” sample as well as for a “cable” sample. In the latter case, the 3D volume was first submitted to a succession of dilatation and erosion (closings) in order to “fill” the cable and to only take into account the contacts between two cables and not the ones between two wires constitutive of the cable.

Values measured from the “tube” model are shown as well, using a value of 0.8 for the orientation parameter  $f$ , since the value previously defined is only valid for the specific case of the monofilament sample. The pre-deformation of the wire as a spring seems to increase the contact’s density while the number of contacts per unit volume still increases as a function of the square of the volume fraction. The slope of the experimental curve is indeed equivalent while the experimental values are higher. This could become important when looking at damping properties, considering that energy is dissipated through friction at each contact point.

In the case of cables, a high contact density can be observed, compared to a regular entanglement, due to the lower flexural strength of the cable structure. Considering the complex topological definition of a contact between two cables in the skeleton, the measurement of the length between contacts would here be more precise. However, the contacts inside the cable would play a very important part in the damping properties of the material (as it will be discussed later).

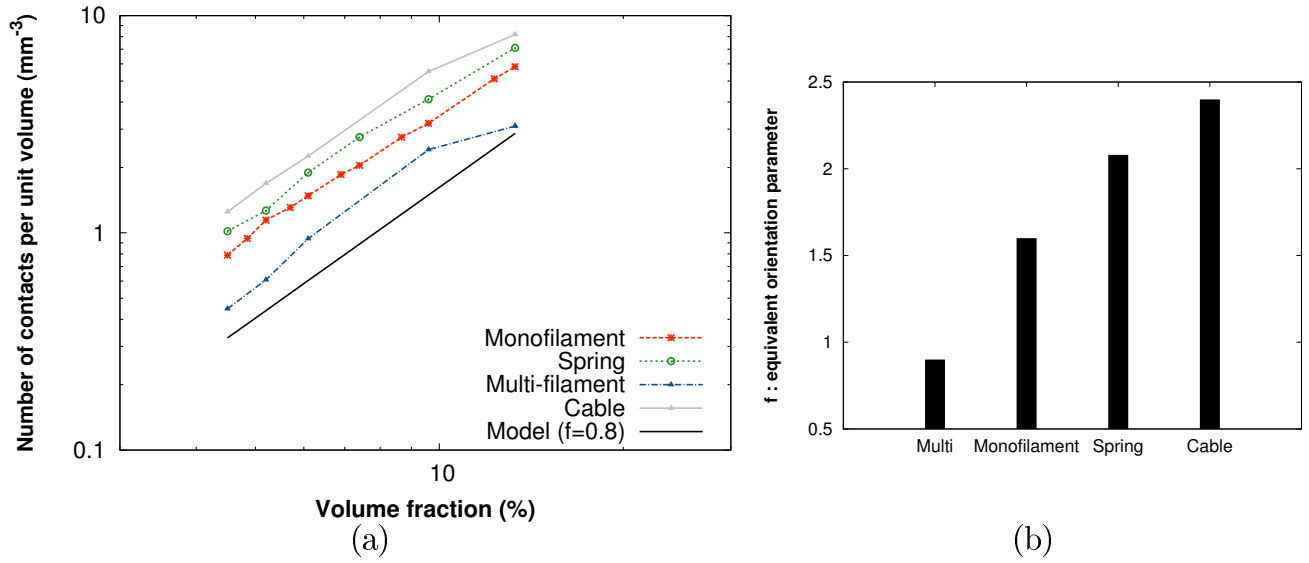


Figure 3.17: (a) Evolution of the experimental number of contacts for different shapes of a 200  $\mu\text{m}$  stainless steel wire as well as the values predicted using the “tube” model [28] for  $f=0.8$ . and (b) equivalent orientation parameter  $f$  for each specific shape.

On the other hand, using shorter fibers seems to decrease the number of contact per unit volume and the experimental results fall closer to the model with the value of  $f$  corresponding to a random 3D distribution of straight, rigid fibers. This would indicate that this network of fibers is closer to the hypothesis of the model, in particular in terms of the curvatures of the fibers, which is not surprising. Shorter wire segments will indeed be less deformed in the initial configuration of the wire.

Figure 3.17(b) regroups the equivalent  $f$  values required to fit the “tube model” to each specific shape. A value close to the theoretical 0.8 value was obtained for the multi-filament sample whereas higher values (up to 2.4) could be reached for other structures.

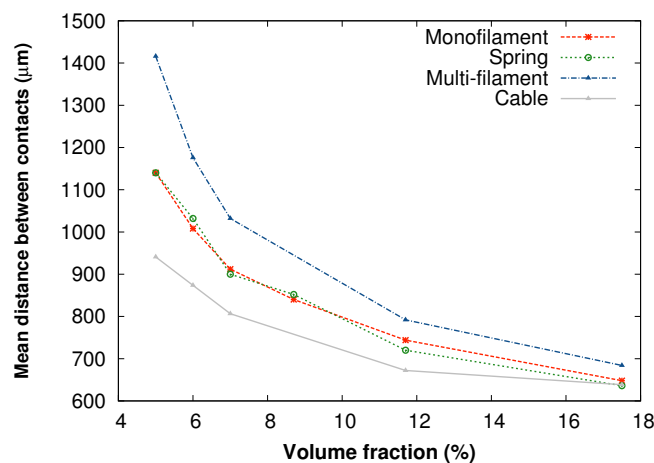


Figure 3.18: Evolution of the distance between contacts as a function of the volume fraction for 200  $\mu\text{m}$  stainless steel wire samples.

Figure 3.18, showing the evolution of the mean distance between contacts as a function of the volume fraction and wire shape, confirms the influence that was deduced from the previous analysis of the number of contacts. However, even though the contact density was shown to be higher in the case of the “spring” sample, the distance between contacts evolves similarly to the “monofilament” case, due to the strong heterogeneity of this material. Contacts are indeed closer together in high density parts of the material.

For shorter fiber, a higher distance between contacts is observed, but this could come from the fact that they are more homogeneously spread since the distribution was shown to be more homogeneous for this type of samples. The very heterogeneous density distribution of monofilament samples could indeed introduce a high dispersion of the distance between contacts.

The cable structure here presents the shortest distance between contacts, which in correlation with the high contact density, indicates an increased ability to create contacts in this type structure.

These measurements should then be combined with the analytical model defined in Chapter 2 in order to predict the mechanical response of an entanglement based on the experimental decrease of the mean distance between contacts with the volume fraction.

### 3.3 Monotonic mechanical analysis

By performing a microstructural analysis on different types of monofilament entangled materials, several key local parameters were determined. Our goal in this section is to link those internal parameters to the macroscopic mechanical behaviour of this material under different types of monotonic loading : uniaxial and oedometric compression, cyclic load, shear and tensile load. The analysis of sintered materials will be presented as well in order to study the effect of the sintering step on the contacts and thus, on the mechanical properties of the structure.

#### 3.3.1 Compressive oedometer testing

Following the preliminary results on the straight stainless steel wires, oedometric compressive tests were performed on samples with different initial wire shapes and different wire yield strengths. Samples with a 5% initial relative density were compressed with a  $5 \cdot 10^{-4} \text{ s}^{-1}$  strain rate until a 17.5% volume fraction.

##### **Influence of the yield strength**

First of all, samples were prepared using both the pearlitic steel wire ( $120 \mu\text{m}$ ) and a stainless steel wire with an equivalent diameter ( $127 \mu\text{m}$ ) in order to be able to study the influence of the materials' yield strength on the mechanical behaviour of the entanglement. As a reference, the curve corresponding to a  $280 \mu\text{m}$  stainless steel wire is also plotted. Figure 3.19(a) shows that a higher yield strength of the wire seems to increase the rigidity of the material. Indeed, the mechanical behaviour of the sample made of a pearlitic steel wire is very close to the one made of a stainless steel wire with a diameter more than twice larger. Although the elastic moduli of both constitutive materials are very similar, the macroscopic behaviour of the corresponding entanglements are significantly different and furthermore, the deformation, in the case of the pearlitic steel is almost entirely elastic (when unloading, the sample comes back to its initial shape almost exactly) whereas it is mostly plastic for

stainless steel wires.

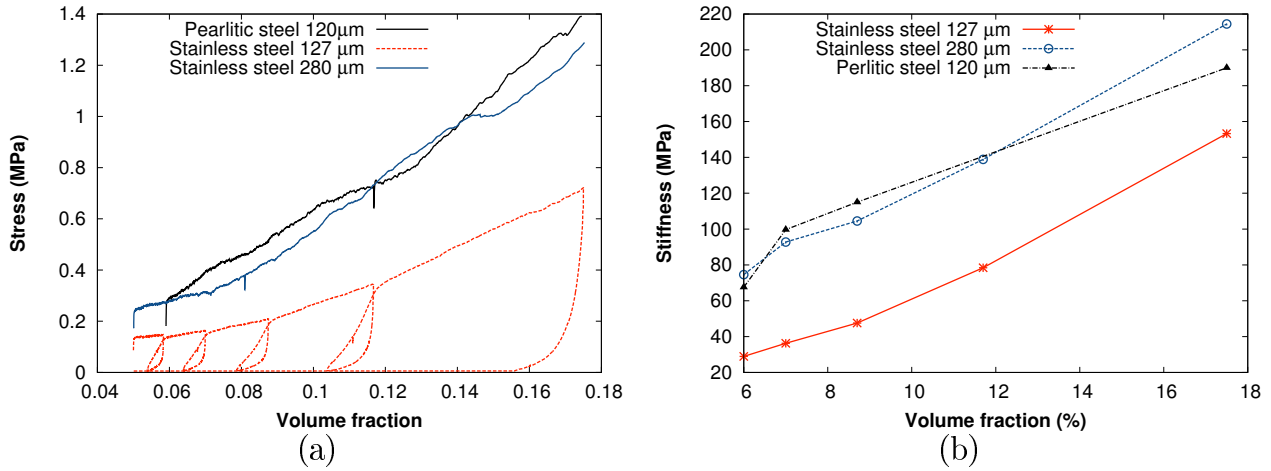


Figure 3.19: (a) Evolution of the axial stress as a function of the volume fraction for wires with different yield strengths and (b) evolution of the stiffness, measured during unloading, as a function of the volume fraction.

In a similar way to what was presented in Chapter 2, the stiffness of the structure was assessed by “discharge modulus” measurements (slope of the stress-strain curve at the very first beginning of the unloading sequence). Figure 3.19(b) shows the evolution of the stiffness as a function of the volume fraction. It appears clearly, that for an equivalent wire diameter, the stiffness increases greatly with the yield strength. The dependence on the volume fraction is however roughly the same in both cases.

The stiffer mechanical behaviour of entanglements made of high yield strength wires can also be linked to their highly heterogeneous density distribution (as shown in section 3.2.2). A higher density at the contact with the containing mould does indeed imply a higher contact surface

#### Influence of the initial wire shape

Oedometric compressive tests were performed on samples with a 5% volume fraction using monofilament, multi-filament and spring pre-deformed wires (diameter 200  $\mu\text{m}$ ). Figure 3.20 shows the evolution of the stress as a function of the volume fraction for all sample types as well as the evolution of the stiffness.

Although multi-filament samples are slightly less heterogeneous (as shown previously), their macroscopic mechanical behaviour is very similar to the one of a monofilament. Since the length of the fibers were approximately equal to the initial height of the sample, it is quite clear that the “single wire” characteristic is only of consequence for entanglements where the length of the fibers is smaller than its shortest dimension. For lengths above this threshold, while the general behaviour is the same, the major benefit of using a single wire is the freedom and simplicity of the manufacturing process.

For the “spring” sample, the mechanical response is clearly lower than for the straight monofilament. The stress values are approximately cut down in half. The stiffness measurements confirm that the pre-deformation of the wire leads to a much lower rigidity. However, the evolution of the

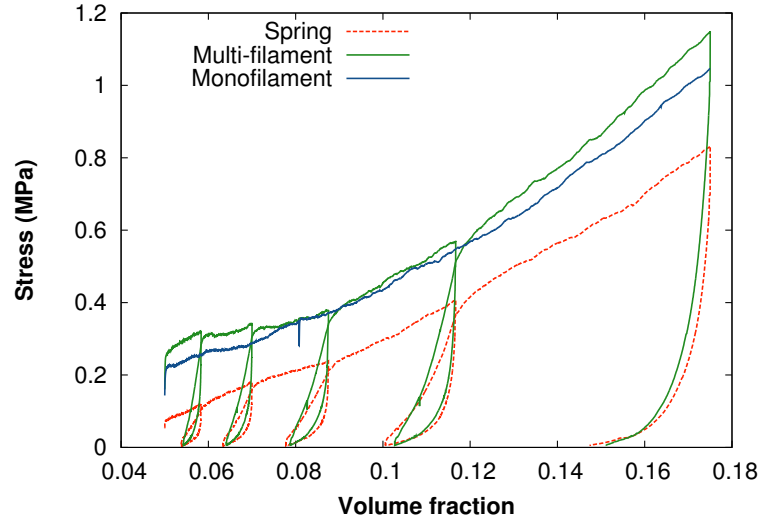


Figure 3.20: Evolution of the axial stress as a function of the volume fraction for 200  $\mu\text{m}$  stainless steel samples with different initial shape of the wire.

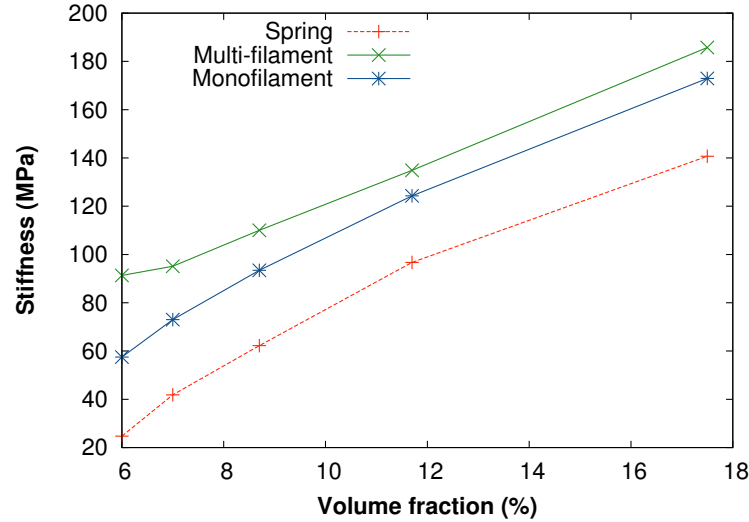


Figure 3.21: Evolution of the stiffness as a function of the volume fraction for 200  $\mu\text{m}$  stainless steel samples.

stiffness with the volume fraction is very similar to what was previously observed.

The lower mechanical properties of “spring” samples can be due to both the less heterogeneous distribution and the pre-deformation of the wire. The more homogeneous distribution of the wire implies that the density at the contact with the cylindrical die is lower and thus the wire/mold contact surface is lower. Since it was previously showed that the shear component, corresponding to the friction with the mold, influences greatly the mechanical response of the material, this would partly account for the decrease of the stiffness. Moreover, the pre-deformation of the wire as a spring results in a network of pre-buckled beams whose mechanical properties have been lowered by the plastic deformation, thus resulting in a lower stiffness of the entanglement.

To conclude, it was shown that the stiffness of the entanglement can be increased by modifying a few different parameters (diameter and initial shape of the wire, volume fraction, yield strength) and

that some of those changes in the mechanical response can be linked to the microstructural evolution of the entanglement.

### 3.3.2 Damping

From this mechanical analysis and especially from the unloading sequences, it was shown that this material exhibits a very strong hysteresis phenomenon when under cyclic loads. Loss factor measurements were thus performed using first a static approach.

In order to investigate the energy absorption capacities of monofilament entangled materials, the hysteresis cycles can be used in order to measure a loss factor, corresponding to the capacity of the material to absorb energy (here, mostly through friction). In the case of the oedometric test, the loss factor of the sample/mold system, and not of the sample alone, is measured. As the contact surface evolves during the compression test, values could not directly be compared for increasing volume fractions. However, it was possible to investigate the influence of different manufacturing parameters such as the diameter or shape of the wire.

From the hysteresis cycles, the dissipated energy per cycle  $\Delta W$  is studied. It corresponds, on a stress-strain plot, to the internal area of the hysteresis and can be written as :

$$\Delta W = \int_0^\epsilon \sigma d\epsilon \quad (3.9)$$

where  $\sigma$  denotes the stress and  $\epsilon$ , the strain.

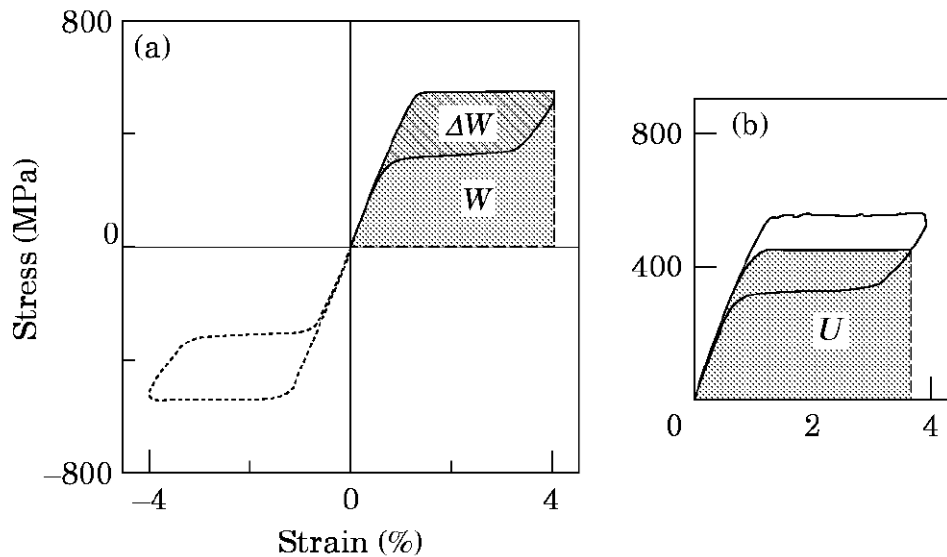


Figure 3.22: (a) Superelastic stress-strain curve of a Shape Memory Alloy.  $\Delta W$  and  $W$  are respectively the dissipated energy and the maximum strain energy. (b)  $U$  is the maximum dissipated energy in a cyclic solicitation [61].

Loss factors are defined for a full cyclic deformation in tension-compression and can be written as :



$$\eta = \frac{1}{2\pi} \frac{2\Delta W}{U} \quad (3.10)$$

where  $U$  is the maximum dissipated energy [62].

For a linear viscoelastic material with low damping, the maximum dissipated energy  $U$  is equal to  $\frac{1}{2}\epsilon_{max}\sigma_{max}$  and corresponds to the total elastic energy at stake, but in the case of a non-linear material, a more precise definition is  $U = W - \frac{1}{2}\Delta W$  [61], where  $W$  is the maximum strain energy at  $\epsilon_{max}$  as shown in Figure 3.22 and  $\frac{1}{2}\Delta W$  is the energy dissipated up to this point. From the stress-strain curves, these values can be determined by numerical integration.

### Influence of the friction with the mould

As friction with the PTFE mould plays an important role in the damping behaviour of the system, measurements were first compared between oedometric and uniaxial compression. Loss factors were measured for both cases from the stress strain curves presented in Figure 3.23. More details on this experiment can be found in section 2.4.1. A cyclic deformation was applied in both cases while remaining in the “elastic” domain, thus allowing to come back to the initial strain when unloading.

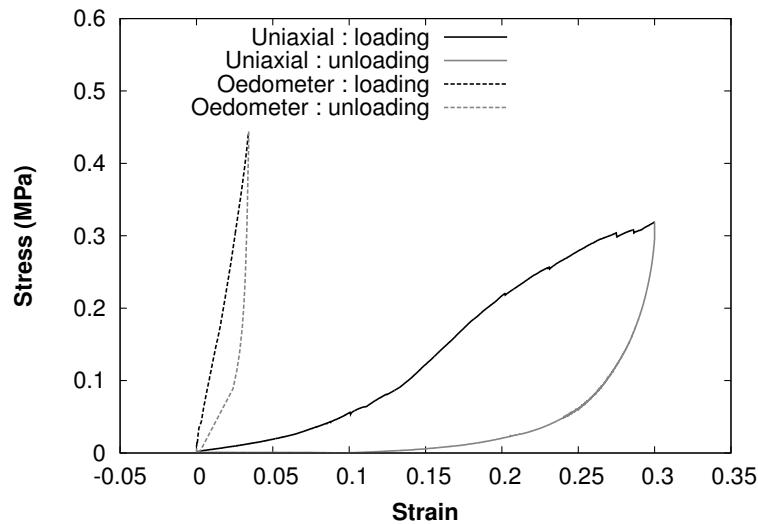


Figure 3.23: Hysteretic stress-strain curves for uniaxial and oedometer compression.

As a result, it was shown that the loss factor in uniaxial compression (0.197) was almost twice larger than for oedometric compression (0.112). When compressing the sample inside the PTFE mould, the loss factor of the whole system is measured and the sample/mould contact surface thus has an impact on the damping properties.

In the upcoming section, damping measurements were however performed in an oedometer configuration as it is the only way to be able to characterize every type of samples, especially the pearlitic steel samples for which the deformation is mostly elastic.

### Influence of the manufacturing parameters on damping

For each sample, a stress-strain curve similar to the one presented in Figure 3.24 is obtained,

thus allowing us to follow the evolution of the loss factor during the compression. However, it should be noted that, since the contact surface between the PTFE mould and the sample changes during the mechanical test, values can only be compared for different types of materials (influence of the diameter and shape of the wire), for the same volume fraction, but the influence of the volume fraction itself can not be studied from this experiment.

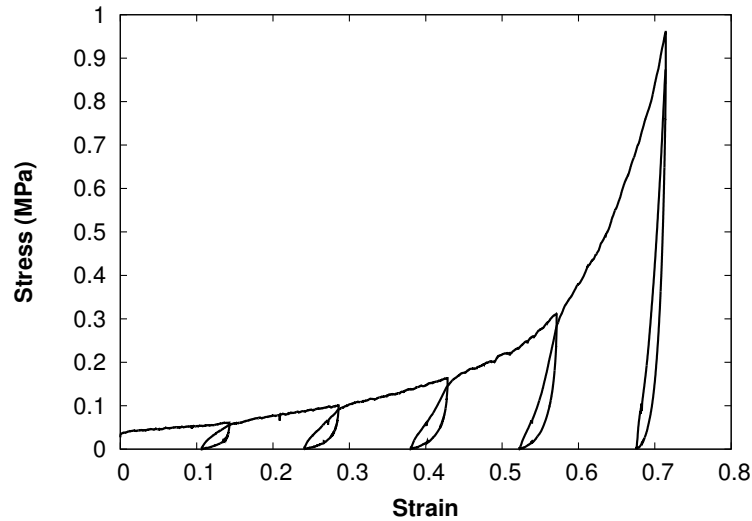


Figure 3.24: Typical stress-strain curve obtained for a 127  $\mu\text{m}$  stainless steel sample, including the unloading sequences.

As it was previously presented, samples with different initial wire shapes were compressed and loss factor could be measured for increasing volume fractions. Figure 3.25(a) shows the evolution of damping as a function of the relative density for 200  $\mu\text{m}$  stainless steel wire samples with all initial shapes presented in section 3.1.2.

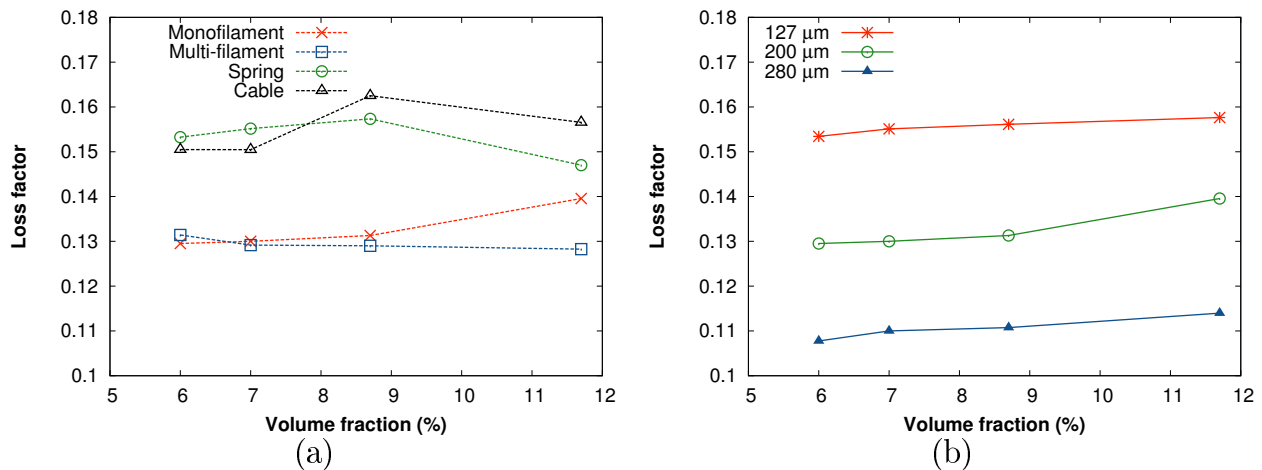


Figure 3.25: Evolution of the loss factor for 200  $\mu\text{m}$  stainless steel samples as a function of the wire initial shape (a) and of the wire diameter (b).

First, loss factor values oscillates between 0.1 and 0.2. This corresponds to high damping properties as it will later be discussed in more details. It is important to remember that damping in

entangled materials is thought to occur mostly through friction and should thus be closely related to the evolution of the number of contacts. Through the compression it was previously shown that the contact density was higher for “spring” samples. It can here be noticed that the loss factor is consistently higher than the straight monofilament. By contrast, the inverse effect can be seen for multi-filaments samples. The loss factor seems to be slightly lower, just as the number of contacts was shown to be inferior to the one of the reference monofilament sample. In the case of the cable structure, it should be mentioned that a new source of energy dispersion is introduced as friction between the wires constitutive of the cable also takes place in damping. Consequently, the corresponding loss factor is observed here to be noticeably higher.

For the same straight initial shape of the wire, the stress-strain data for the three stainless steel wires were analyzed and Figure 3.25 shows the evolution of the loss factor as a function of the diameter of the wire. During the compression test, damping seems to be significantly higher for a smaller wire diameter. As it was shown in section 3.2.3, the number of contacts decreases with the wire diameter and consequently, the energy dissipation decreases as well.

In order to confirm the tendencies that were observed, an experiment was designed where samples were prepared with the same height (10 mm) but different volume fractions and diameter of the wire, thus allowing to study the influence of the relative density on damping. Samples were then submitted to a cyclic load inside the PTFE mould and measurements were averaged over three different samples for each set of parameters (wire diameter and volume fraction).

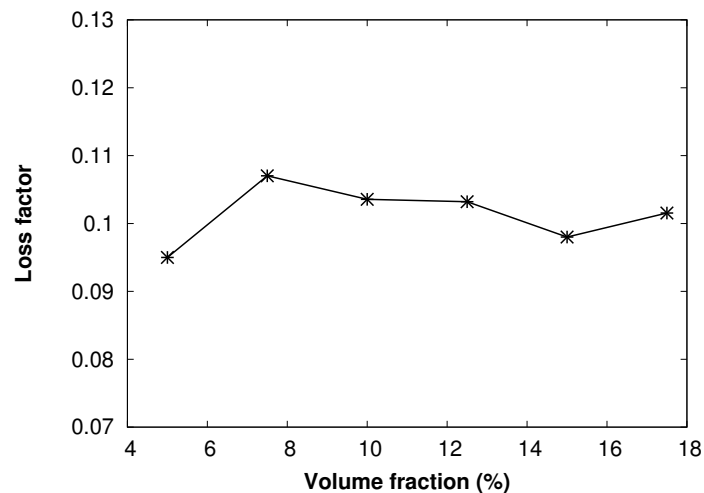


Figure 3.26: Evolution of the loss factor as a function of the volume fraction (200  $\mu\text{m}$  stainless steel wire).

We were finally able to characterize the damping behaviour as a function of the volume fraction and figure 3.26 shows the evolution of the loss factor as a function of the relative density for 200  $\mu\text{m}$  stainless steel samples. There appears to be no significant influence of the volume fraction on damping as values oscillate around 0.1 over the studied range.

Lastly, the influence of the yield strength of the wire was studied thanks to measurements performed on pearlitic steel samples, which can only be performed in a “contained” configuration as the deformation in this material is mostly elastic and that samples can not be taken out of the mould. For a 10% volume fraction, the loss factor was found to be around 0.19. Comparatively,

the value found for a stainless steel with an equivalent diameter was slightly lower than 0.11. This would indicate that, besides the energy dissipation at contact points, the material's properties can also influence the damping of the material and it would appear that a lower friction coefficient is obtained for harder material, thus resulting in more sliding at contact points.

In conclusion, it was possible to link the macroscopic damping behaviour of monofilament entangled materials to the evolution of a microstructural parameter (number of contacts). The influence of different manufacturing parameters could be studied from simple unloading cycles and the high energy absorption ability of this material was pointed out.

#### 3.3.3 Shear testing

As presented in section 0.2.2, this monofilament entangled material is investigated for its damping properties and could be used as a solution to the “connecting rod” specification. But in order to evaluate the ability of this material to act as a damper in the mass/spring system, the effective shear modulus of the material has to be evaluated. In order to obtain a meaningful result for this specific application, a shear test with a cylindrical revolution was designed. In the system presented in Chapter 1, the “spring” part is indeed deformed by shear between the central mass and the outer cylindrical rod.

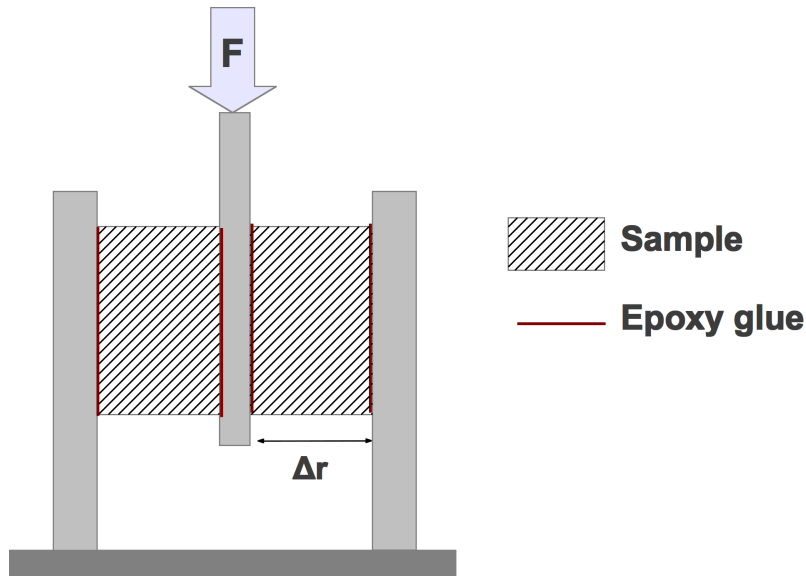


Figure 3.27: Schematic of the shear device used to evaluate the shear modulus of monofilament entangled materials.

The analysis presented in section 0.2.2 showed that, in order to fulfill the set of requirements, the material had to be chosen with a shear modulus as low as possible. If we consider that the shear modulus can be written as  $G = \frac{E}{2(1+\nu)}$  and that the Young's modulus  $E$  can be approached by the stiffness values that were previously measured, an approximate value of  $G$  can be obtained. It then appears that, considering that the stiffness increases with the volume fraction and the diameter of the wire, the shear modulus can be lowered by preparing an entanglement with a low relative density and using the smallest wire possible.

A cylindrical sample was thus prepared with a 5% volume fraction, using a 127  $\mu\text{m}$  stainless steel wire, in which a 3 mm steel rod was introduced and glued in the center. This sample was then glued inside a two part cylindrical mold with the typical 15 mm diameter. A bi-component epoxy glue was used. Figure 3.27 shows a schematic of the assembly, placed inside the compressive device shown in section 2.2.3.

The sample was then compressed with a  $1.10^{-4}$  strain rate and unloaded for increasing strains. The shear modulus of the assembly was evaluated by measuring the slope of the stress-strain curve at the very first instant of the unloading sequence. In such a configuration, the strain  $\epsilon$  was measured as  $\frac{\Delta z}{\Delta r}$ , where  $\Delta z$  is the applied displacement along the compression axis and  $\Delta r$  corresponds to the radial thickness of the sample as showed in Figure 3.27, and the stress  $\tau$  is defined as  $\frac{F}{S_{int}}$  where  $F$  is the axial force and  $S_{int}$  is the surface of the internal rod, to which a force is applied, in contact with the sample. Figure 3.28 shows the corresponding stress-strain curve as well as the evolution of the equivalent shear modulus with the strain.

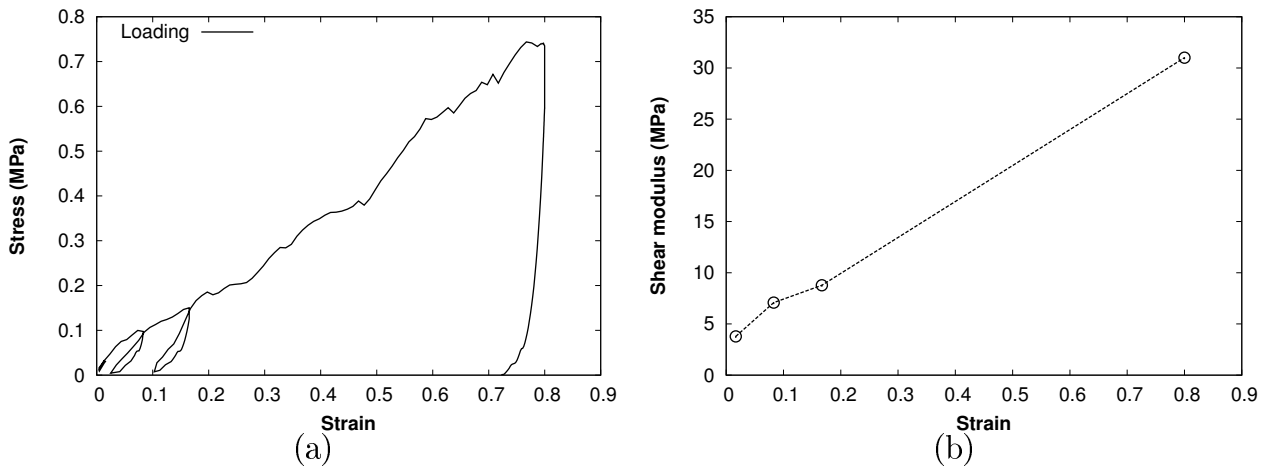


Figure 3.28: (a) : Stress-strain curve for a shear loading and (b) : evolution of the shear modulus with the strain.

Figure 3.28(a) shows the increasing mechanical response of the material with the strain and it can be observed that, just like in compression, the material presents an hysteresis when submitted to cyclic loads. This would very well meet the expectations of the “spring” material of the system presented in section 0.2.2. For a relatively low strain, a damping factor of approximately 0.09 was measured. This would indicate that this material is capable of energy absorption under shear loadings and that friction occurs at contact points.

For a sample with a 5 % volume fraction, a shear modulus of 3 MPa was measured for low strains, thus confirming the interest of this material for the “spring/mass” system. Eventhough a lower shear modulus was initially desired (lower than 1MPa) for this application, the combination of properties (relatively low modulus and high loss factor) exhibited by this material provides a promising alternate option. Moreover, the modulus seems to increase linearly with the strain as shown in Figure 3.28(b).

Using a dedicated shear mechanical device, the effective properties of this material were defined, thus allowing to have a better understanding of its behaviour under very specific solicitations. From this experiment, a relatively low shear modulus was found and the damping ability of the entanglement was confirmed. It was then decided to prepare a scaled experiment on the “connecting

rod” structure, using Monofilament Entangled Materials as a damping connector between the Inconel tube and the internal, vibrating, steel mass. The final aim of this analysis is to study the damping properties of the complete structure and it is a work in progress as absorption measurements are currently being performed on the system at ONERA Toulouse.

#### 3.3.4 Tensile test

Considering the unusual shape and structure of the material studied in this PhD, it was not possible to perform a classical tensile test. Thereby, a suitable setup was developed. First, 55 mm high cylindrical samples were prepared with a 5% volume fraction, using a 200 $\mu$ m stainless steel wire. Each extremity of the sample were then sealed inside specifically designed tension jaws, composed of a bath of Wood’s metal. This metal is a eutectic, fusible alloy with a low melting point of approximately 70°C, that could be melted down using a simple heat gun.

Around 1 cm on each side of the sample was preheated in order to obtain a good wettability of the stainless steel wire with the liquid melted alloy. While keeping the sample aligned with the tension jaws, the two ends of the sample were dipped into the liquid metal and the melted Wood’s metal was cooled down to a solid state, thus creating a fixed grip on the sample.

The tensile test was then carried out with a  $1.10^{-4}$  strain rate and unloading sequences were performed in order to study the energy absorption under tension. From this, a tensile stiffness could be measured using the initial slope at the very first instant of the unloading sequence.

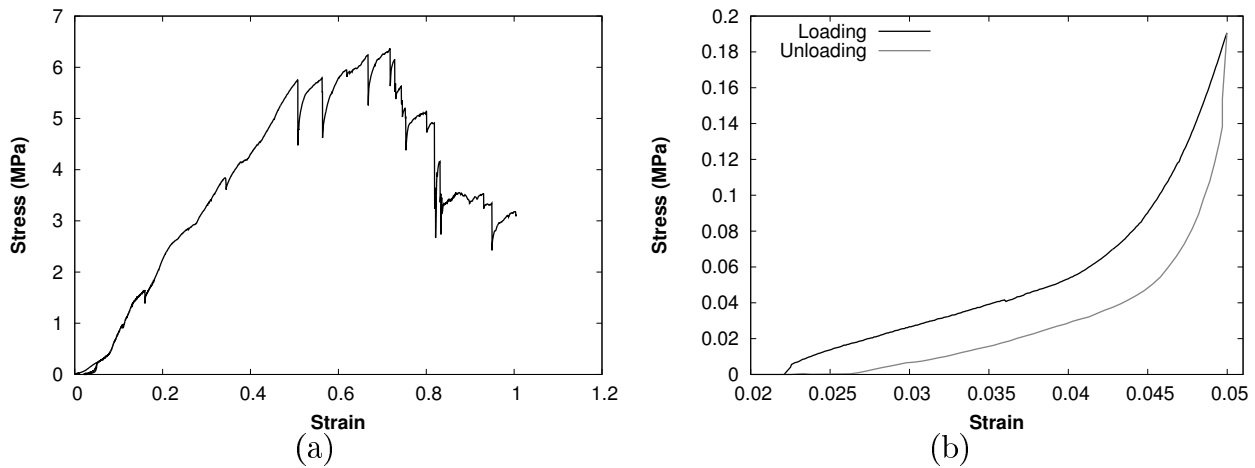


Figure 3.29: (a) : Stress-strain curve for a tensile loading and (b) : Stress-strain hysteretic behaviour in tension.

The tensile stress-strain curve presented in Figure 3.29(a) shows a very high ductility of the material in tension, as deformation up to almost 50% can be reached following a nearly linear evolution. A stiffness close to 40 MPa was measured at the very beginning of the tensile test ( $\approx$  5% volume fraction), which is in good agreement with the stiffness that was measured for the same material, in oedometric compression.

In a very similar way to what was observed in oedometric compression and uniaxial compression (or DMA), a hysteresis was obtained when under cyclic load. A loss factor could thus be measured

using the method presented in section 3.3.2. From the hysteresis shown in Figure 3.29(b) which corresponds to a volume fraction just below 5%, a loss factor of 0.1 was measured. Comparatively, a damping factor of 0.2 was obtained in uniaxial compression, thus indicating that contact points do not behave in the same way when under tension. It seems that contacts are getting undone and the energy absorption is thus lower.

### 3.3.5 Characterization of sintered materials

In order to create permanent cross links in the fiber network, “sintering” was performed using either a conventional or a SPS approach.

#### Single wire characterization

In order to better understand the mechanical behaviour of sintered entanglement, an equivalent heat treatment was performed on single wires thus allowing to have more information on the mechanical properties of the material after sintering. Wires were treated in a classical oven under an argon flux, to prevent the oxidation, at 1200°C for 2 hours. Since it was not possible to perform this heat treatment using the SPS approach, in which the actual temperature of the sample can not be precisely defined, an equivalent temperature was chosen.

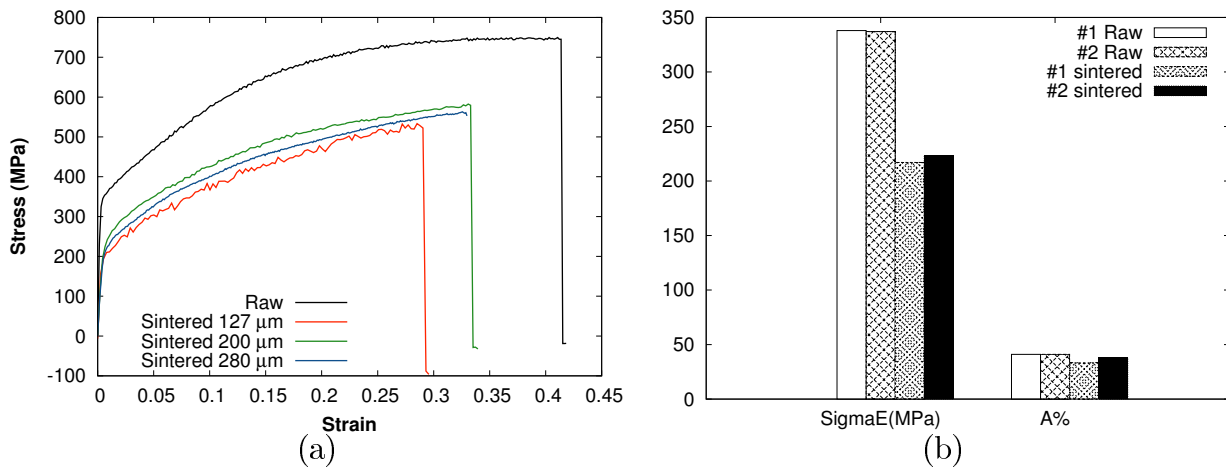


Figure 3.30: (a) : Tensile stress-strain curves for “raw” and “sintered” single wires and (b) : Summary of the mechanical properties of “raw” and “sintered” 200  $\mu\text{m}$  wires.

The wires were then placed inside a tensile device in order to determine their resulting mechanical properties. Wire ends were squeezed in between tensile grips dedicated to wire testing. Single non-treated wires were tested as well in order to verify the mechanical properties of the stainless steel and be able to compare to the final properties after treatment.

The corresponding stress-strain curves for stainless steel wires are shown in Figure 3.30(a). Both the elastic and the plastic domains could be observed and the yield strength and maximum elongation could be measured. Qualitatively, the mechanical properties of the wire after heat treatment were noticeably lower than the one of the “raw” wire, which is not surprising as the applied thermal treatment corresponds to a typical softening treatment for steels. The same behaviour was observed

for all other wire diameters.

The main characteristics of the mechanical behaviour of two  $200\mu\text{m}$  wires are regrouped in Figure 3.30(b). Results are presented for two identical wires for both the “raw” and the sintered cases.

The decrease in both the yield strength and the maximal elongation confirms the lower mechanical properties of the wire after sintering which will have to be taken into account when looking at the mechanical response of the sintered entanglement.

#### Spark Plasma Sintering

Using a  $280\mu\text{m}$  stainless steel wire, samples were prepared and sintered according to the SPS cycle defined in section 3.1.3. In order to have a first look at the structure of the material after heat treatment, samples were observed using Scanning Electron Microscopy. Since it is a 2D analysis and that the resolution of tomography scans were not good enough to be able to do it in three dimensions, only the surface of the samples could be observed. It was however possible to observe many different contact points in the material by tilting the sample around. The resulting images for sintering at  $950$  and  $1050^\circ\text{C}$  are presented in Figure 3.31.

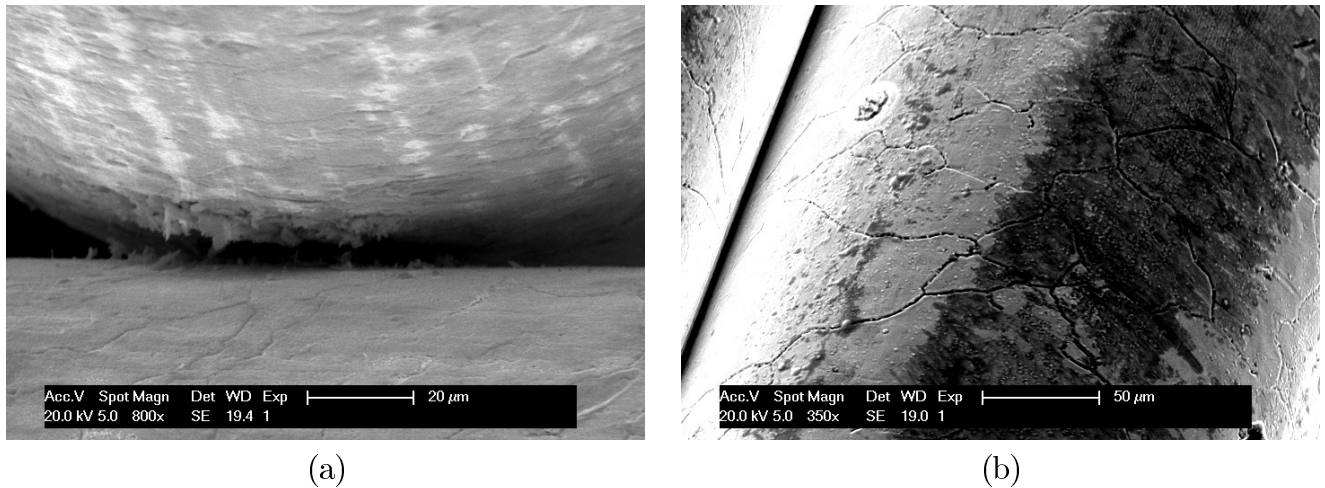


Figure 3.31: SEM observations of (a) a contact points and (b) a wire's surface after SPS sintering.

As shown in Figure 3.31(a), although the physical links between wires at the contact points could not be visualized, a preferential increase of the surface roughness around the contacts was observed, thus indicating that wires could be linked over a restricted area of contact between wires. The grooves that can be seen at the surface of the wire in Figure 3.31(b) are due to the high temperature modification of the grain boundary/gas tripple point.

As the SEM analysis could not ensure the creation of physical bridges after sintering, samples were tested under uniaxial compression in order to evaluate the evolution of the mechanical properties of the entanglement. Considering the small size of the samples, which could lead to heterogeneities (stronger “wall effect”), they were only studied for small strains, with a strain rate of  $1.10^{-4}$ .

Figure 3.32 gathers the corresponding compressive stress-strain curves. From the samples with a 20% volume fraction, the sintering step seems to increase greatly the stiffness of the material,



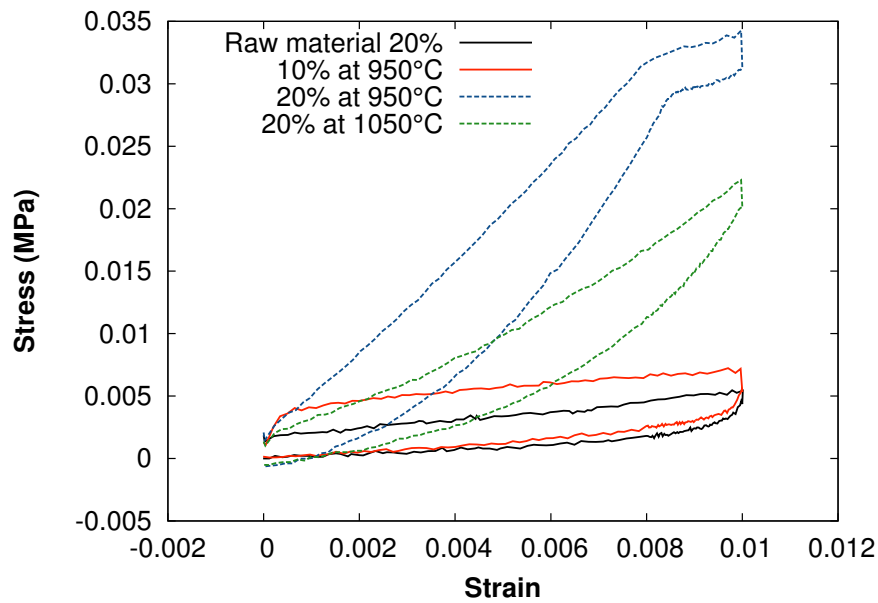


Figure 3.32: Stress-strain curves of samples after SPS sintering, submitted to a cyclic load in uniaxial compression.

compared to the “raw” material. Although it was showed that the heat treatment lowered the mechanical properties of the wire itself and that no physical bridges could be observed, the sintering step does make the material stiffer. This indicates that eventhough the fixed nodes could not be observed, wires were physically linked to some degree during sintering.

Although we could have expected an increasing stiffness with the temperature, it was observed for both volume fractions (10 and 20%), that a higher sintering temperature tends to lead to lower mechanical properties for the entanglement. Even though this observation can be due to the manual aspect of the sample preparation (reproducibility of the process), it could also indicate that an optimal temperature could be defined, which would depend on the accuracy of the temperature regulation (laser pyrometer). As it was shown that the mechanical properties of the wire decreased with the heat treatment, it is also possible that this softening becomes predominant at higher temperature, thus leading to a less stiff structure.

The strengthening of the structure could be observed for both studied volume fractions. Hence, the mechanical response of a sintered sample with a 10 % volume fraction was found to be close to the one of a “raw” 20% sample.

In conclusion, the stiffness of a metallic wire entanglement was greatly improved thanks to a fast, easy, Spark Plasma Sintering step. By playing with the sintering time and temperature, this process could be optimized further in order to obtain a given stiffness, thus allowing to answer to a large set of requirements.

### Conventionnal sintering

Samples (20 mm high and 12 mm in diameter) were prepared using a  $280\mu\text{m}$  stainless steel wire, placed inside a sealed quartz tube and then sintered according to the parameters presented in section 3.1.3.1. In a similar way to what was done for SPS sintered samples, an SEM analysis was

first performed in order to assess the state of the contact points in the entanglement.

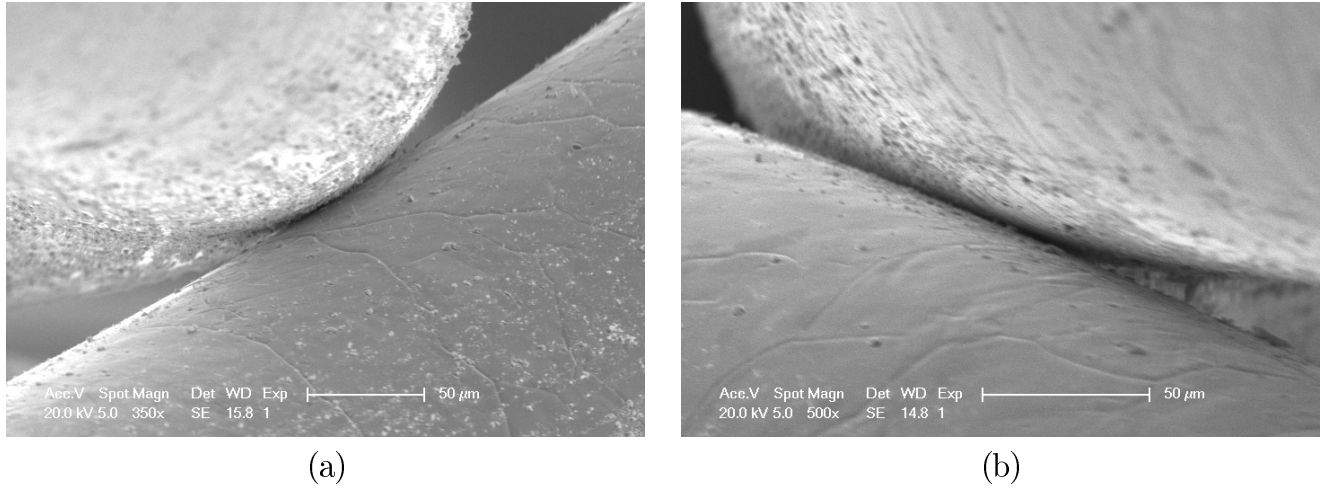


Figure 3.33: SEM observations of contact points after conventional sintering.

From the SEM images, no strong link between wires could be observed. Bridges could still exist but would be limited to a very small contact area at contact points and would not appear on the image. Figure 3.33 shows a close look at two different contact points where no physical link could be found after sintering. The grooves due to the high temperature modification of the grain boundary/gas tripple point can again be seen in these micrographs.

As the strengthening of the structure could not be confirmed by SEM observations, the sintered samples were then submitted to uniaxial compression with a  $1.10^{-4}$  strain rate. In order to study the influence of sintering on the evolution of the mechanical response of the material, an equivalent sample before sintering was also tested. Figure 3.34 shows the typical stress-strain behaviour of a sintered entanglement (3h at 1250°C) over a large strain range.

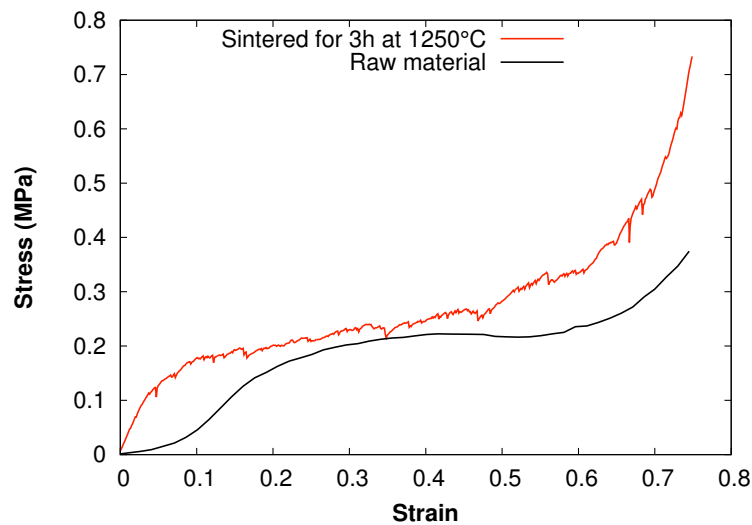


Figure 3.34: Complete stress-strain curve of a sample sintered for 3h at 1250°C (volume fraction : 7.5%).

The compressive mechanical behavior of this material, presented in Figure 3.34, exhibits a typical three stages evolution, comparable to the one of metallic foams. The first linear elastic stage corresponds to the first few percents of deformation. A stress plateau is then reached during which fixed nodes are broken. This plateau, contrarily to what can typically be observed for foams, is not flat as the stress keeps increasing slowly. As the material gets denser, links are broken but contacts remain, thus allowing a slower increase of the stress. Finally, densification occurs. When compared to an equivalent “raw” material, the sintered material mostly differs by its initial “elastic stage” in which fixed nodes are predominant, making the material stiffer. Once most contacts are broken, both materials exhibit a plateau in which new contacts are created but rearrangement is still possible. Finally, it was found that the sintering time and temperature had little to no influence on the mechanical properties of the sintered entanglement.

In order to be able to compare the two sintering techniques, samples with a volume fraction equivalent to the one of the samples that were studied in conventional sintering (7.5%) were prepared and submitted to the same SPS cycle that was previously used (10min at 1000°C). Figure 3.35 gathers the stress-strain curves of every sintered materials (conventional and SPS). The analysis was performed on relatively low strains as samples had different shapes depending on the sintering method (10 mm high samples when using SPS) and the general behaviour could thus be affected.

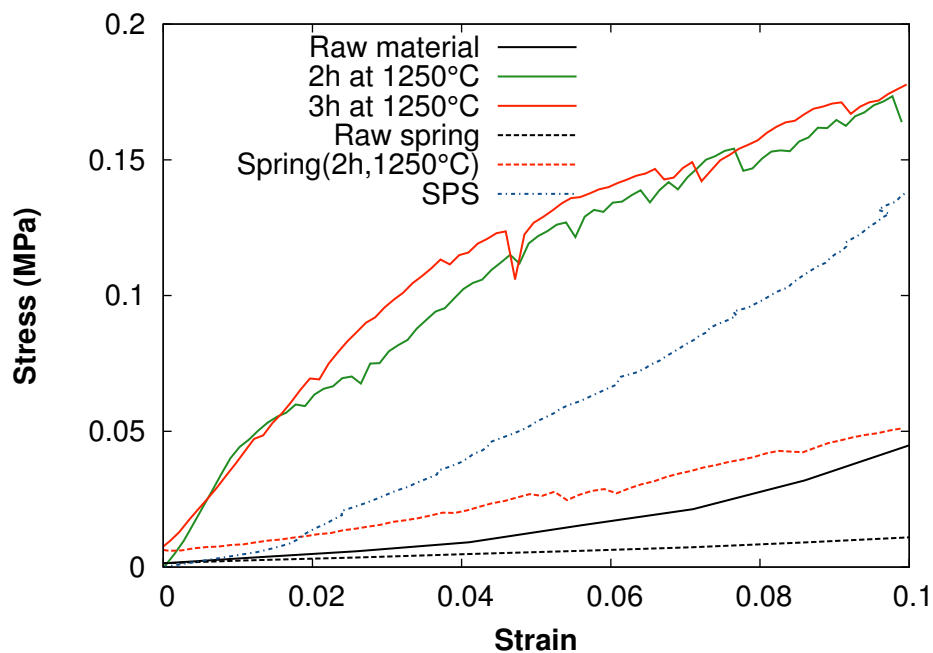


Figure 3.35: Uniaxial compressive stress-strain curves for samples with the same 7.5% volume fraction after either conventional or SPS sintering.

Firstly, the mechanical response of the material sintered for 2 or 3 hours (no influence of the sintering time) is much higher than the one of the “raw” material. Similarly to what was concluded for SPS sintered samples, this would tend to prove that, even though physical bridges could not be observed, fixed contacts were created even if limited to a small contact area. Moreover, the same effect, to some extent, can be seen on the mechanical properties of the sintered “spring” sample. As it was previously shown, the pre-deformation of the wire tends to lower the mechanical response of the entanglement. But when sintered, its properties are close to the one of a “raw” sample with a initially straight wire. However, the general shape of the stress-strain curve does not correspond to the typical

“three stages” evolution that was presented. The initial “linear elastic” increase of the stress can not be observed, thus indicating that the physical bridges are, in this case, not as strong. This can be linked to the better homogeneity of the sample, which could lead to a better density distribution of contact points, and thus to more punctual contacts.

Finally, while still higher than the one of the “raw” material, the mechanical response of the sample sintered using the SPS approach is twice lower than the one prepared using conventional sintering. Although this technique does not provide the same increase in stiffness as the conventional approach, it should be considered that it is also much faster (15 min) and could be improved by further optimization.

## 3.4 Dynamic Mechanical Analysis

In the previous section, the damping properties of Monofilament Entangled Materials were investigated using unloading sequences in monotonic oedometric compression. In order to obtain a better estimation of the ability of this material to absorb energy, measurements were performed dynamically in uniaxial compression with the help of S. Meille and P. Clement. In this configuration, there is thus no influence of the friction with the mold and the  $\tan\delta$  of the entanglement itself can be obtained.

Dynamic Mechanical Analysis (DMA) is a technique where a small deformation is applied to a sample in a cyclic manner. This allows to study the response of the materials to stress, frequency and other parameters. DMA works by applying a sinusoidal deformation to a sample of known geometry. It can be subjected to either a controlled stress or a controlled strain. For a known stress, the sample will then deform of a certain amount which is related to its stiffness.

Dynamic mechanical properties refer to the response of a material as it is subjected to a periodic deformation. These properties may be expressed in terms of stiffness and damping, reported as modulus and  $\tan \delta$ , of the studied material. For an applied stress varying sinusoidally with time, a perfectly viscoelastic material will also respond with a sinusoidal strain for low amplitudes of stress (see Figure 3.36(a)), out of phase with the stress applied by the phase angle  $\delta$ . In the particular case of the non-linear response of monofilament entangled materials, the output signal will not be perfectly sinusoidal and an hysteresis will be observed on the stress-strain plot (figure 3.36(b)).

Here, a sinusoidal strain is applied (in order to control the amplitude of the applied signal) in compression and the resulting force is acquired (see figure 3.36). The strain and dynamic stress can be written as  $\epsilon = \epsilon_0 \sin(\omega t)$  and  $\sigma = \sigma_0 \sin(\omega t + \delta)$ , where  $\omega$  is the angular frequency. Using this notation, it is then possible to express the modulus as an in-phase component, the storage modulus ( $E'$ ), and an out of phase component, the loss modulus ( $E''$ ) by noticing that :

$$\sigma = \sigma_0 \sin(\omega t) \cos\delta + \sigma_0 \cos(\omega t) \sin\delta \quad (3.11)$$

and thus, by dividing stress by strain to yield a modulus :

$$\sigma = \epsilon_0 E' \sin(\omega t) + \epsilon_0 E'' \cos(\omega t) \quad (3.12)$$

By combining equations 3.11 and 3.12, we obtain :

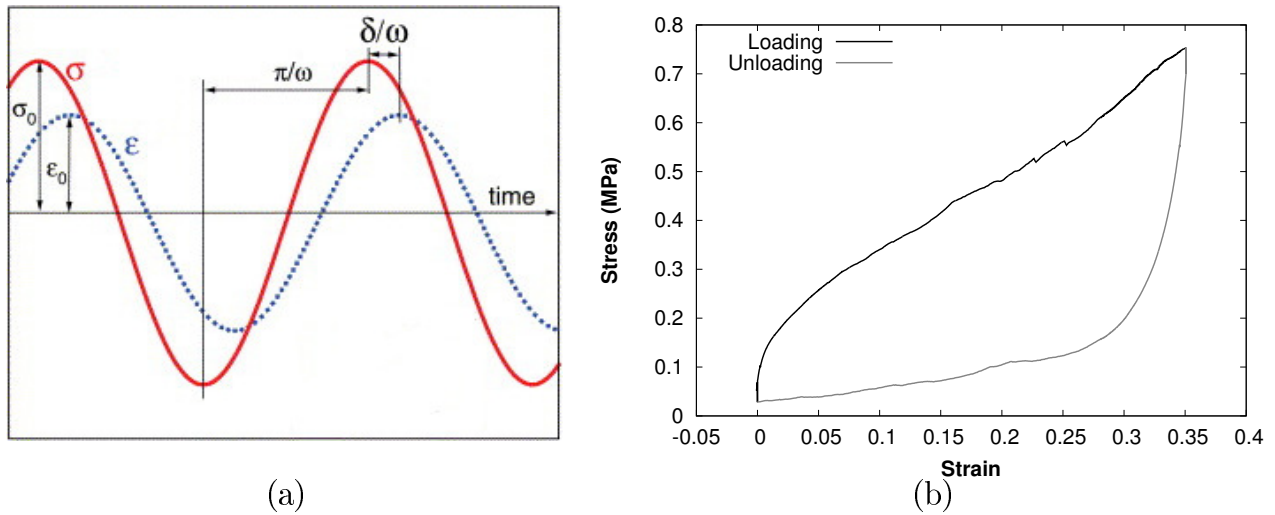


Figure 3.36: (a) : Schematic representation of the evolution of the strain and stress as a function of the time and definition of the phase angle  $\delta$  and (b) : Illustration of the hysteretic response of the material when under cyclic load.

$$E' = \frac{\sigma_0}{\epsilon_0} \cos \delta \text{ and } E'' = \frac{\sigma_0}{\epsilon_0} \sin \delta \quad (3.13)$$

Finally, the ratio of the loss modulus ( $E''$ ) over the storage modulus ( $E'$ ) is referred to as the  $\tan \delta$ , often called damping. Damping corresponds to the dissipation of energy in a material under cyclic load. It is an indicator of the capacity of the material to absorb energy and is reported as the tangent of the phase angle between the input and output signals.

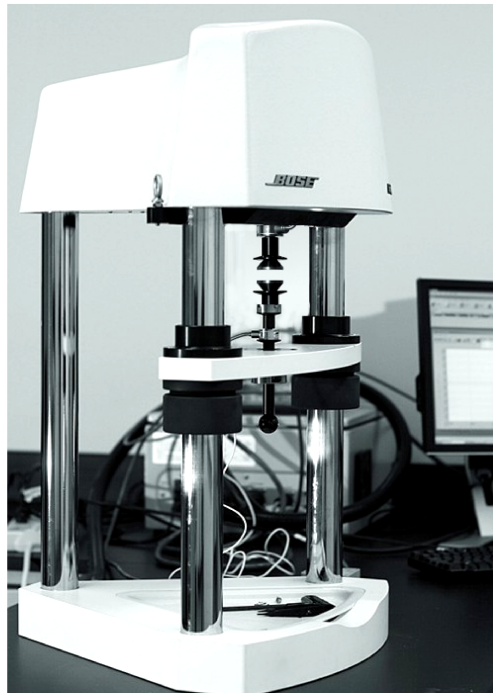


Figure 3.37: DMA testing device with compression plates.

A BOSE ElectroForce 3200 was used in this study (see Figure 3.37). It uses a moving-magnet linear motor, originally developed for an experimental loudspeaker, which provides an attractive alternative to traditional motion and force control because of its simple moving-magnet design. Moreover, it utilizes a friction-free motor suspension which allows for great precision, in particular for damping measurements. For each sample, the sinusoidal controller is accurately fitted so that the applied wave signal corresponds to the set parameters and that it is stable.

The samples were shaped inside the PTFE mould and taken out of it in order to place them in between the two compression plates. This procedure was selected in order to perform a measurement of the damping of the entanglement alone avoiding the effect of the mould. Since the measurements were not constrained (no cylindrical die), only the stainless steel wire samples were analyzed. In this particular case, a sinusoidal displacement, with an amplitude of 0.3 mm, was imposed on stainless steel samples. For each sample, a preload of 5N was applied in order to have a stable initial state and for each set of parameters (volume fraction, frequency), measurements were performed and averaged over 10 different samples.

#### Influence of the volume fraction

Following the preliminary results that were obtained from the hysteresis measurements, an equivalent analysis was performed using a DMA approach so as to also be able to compare values in and out of the PTFE mould. In order to study the influence of the volume fraction on the damping, samples with increasing relative densities (5, 7.5, 10, 12.5, 15 and 17.5%) were prepared using a 200  $\mu\text{m}$  stainless steel wire with a straight initial shape. Measurements were performed with a 1 Hz frequency. Figure 3.38 shows the evolution of the loss factor as a function of the volume fraction and for each point, an error bar is shown, corresponding to the scattering of the measurements for the same density value.

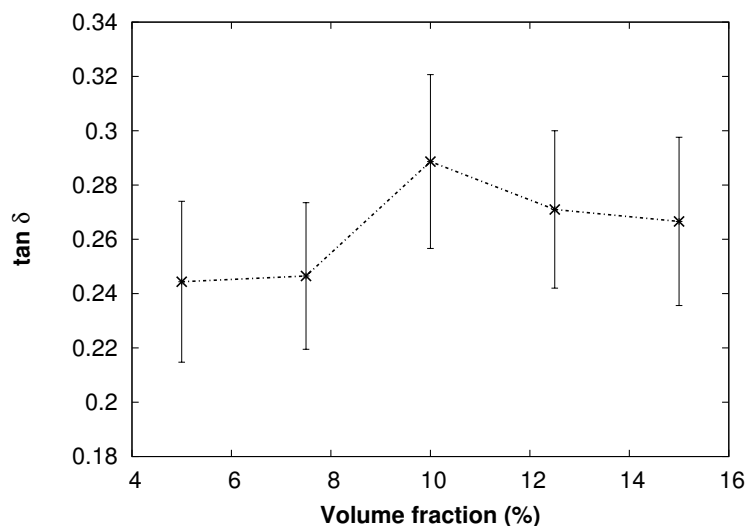


Figure 3.38: Evolution of the loss factor ( $\tan\delta$ ) as a function of the volume fraction.

First of all, the loss factor of this material seems to oscillate around a value of 0.27, which corresponds to a relatively high damping ability. It is also in good agreement with the value of 0.2 that was measured from the hysteresis under static uniaxial compression (as opposed to the dynamic analysis). Comparatively, the loss factor is around 0.5 for a polyurethane (highly absorbent polymer)

and around 0.01 for a metallic foam. Figure 3.39 shows an Ashby map of the loss factor as a function of the density and most materials with high damping appear to be polymers. This  $\tan\delta$  value is also more than twice higher than the average one found previously when cycling the material inside the cylindrical die. This illustrates very well the effect of friction between the sample and the PTFE mould.

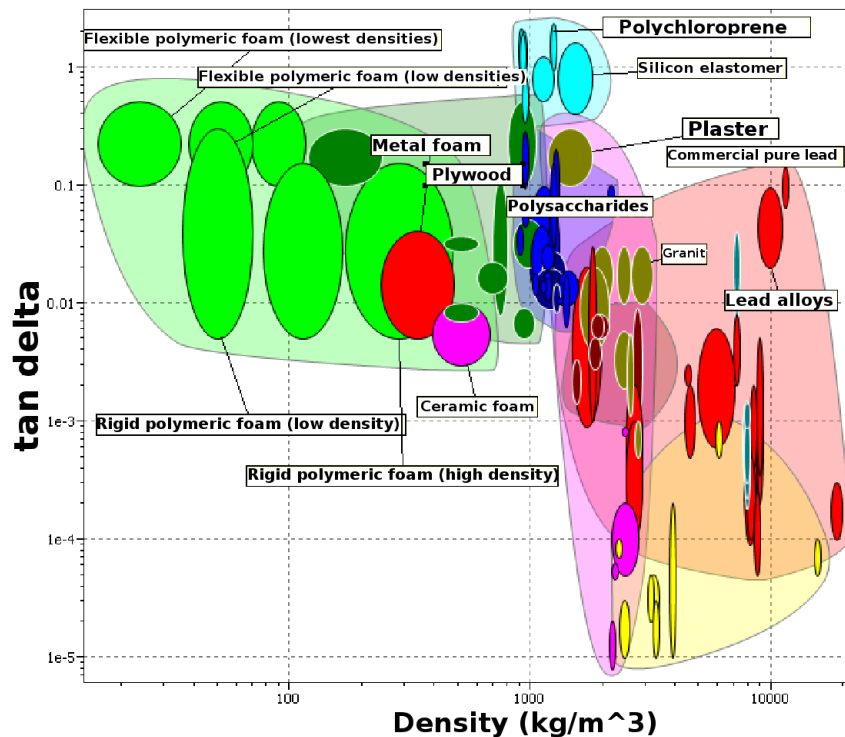


Figure 3.39: Ashby map of the loss factor as a function of the materials density, taken from the CES software [2].

As it was previously shown from the hysteresis analysis, the volume fraction does not have, over the studied range, a major influence on the damping of the material. However, from this more precise dynamic measurement, while taking into account the dispersion of the results, there seems to be an optimal value of the loss factor for volume fractions around 10%. First of all, it was shown from the mechanical analysis that the stiffness of the material increases greatly with the volume fraction, which could lead to a decrease of the damping factor. Meanwhile, the number of contacts increases as well, thus creating a stiffer entanglement with a higher contact density. Considering that in the particular case of entangled materials, the energy absorption is thought to occur mostly through friction at contact point between wire segments, the loss factor would then tend to increase. Consequently, there seems to be a compromise between the increase in stiffness and contact density which leads to a higher damping for volume fractions around 10 %.

### Influence of the frequency

Using a very similar approach, the influence of the frequency on damping was studied. It is worth mentioning that the dynamic analysis of “soft” materials (with relatively low mechanical properties) depends greatly on the stability of the input sinusoidal signal at high frequency. It was indeed soon noticed that in the case of monofilament entangled materials, the sinusoidal controller

could not provide a perfectly sinusoidal deformation for frequencies higher than 50 Hz, thus not allowing an accurate measurement of the loss factor. Taking that into account, a frequency sweep was performed on a 200  $\mu\text{m}$  stainless steel sample for increasing volume fractions (one sample for each : 6, 8.7, 11.7 and 17.5 %) up to 75 Hz.

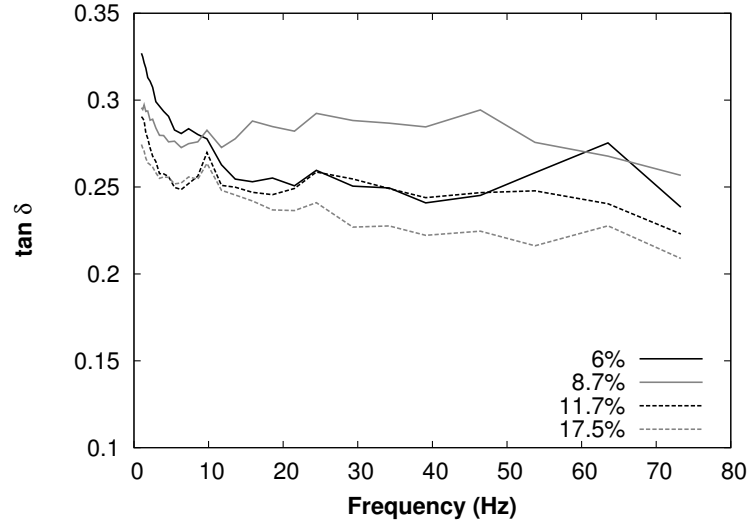


Figure 3.40: Evolution of the loss factor ( $\tan\delta$ ) as a function of the frequency and volume fraction.

Figure 3.40 shows the evolution of the loss factor of the material with the frequency for different relative densities. Taking into account that measurements were performed on only one sample for each volume fraction, no clear influence of the relative density can be observed with the frequency. However, on this set of samples, the same average value between 0.25 and 0.3 can be observed, thus confirming the high value of the damping factor.

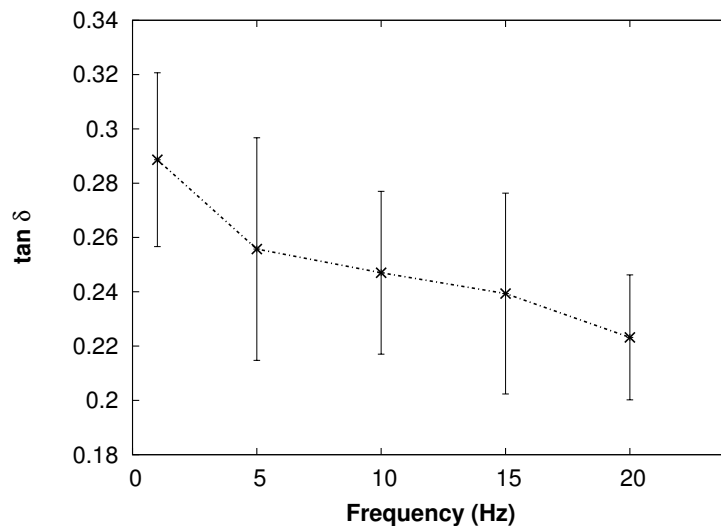


Figure 3.41: Evolution of the averaged loss factor ( $\tan\delta$ ) as a function of the frequency.

The loss factor does however seem to decrease with the frequency, even more so at low frequency (1-10Hz). Despite the technical limitation that was just exposed, the behaviour at higher frequencies



appears to be consistent. Since the biggest drop in damping was noticed at low frequency, a more precise analysis was performed on the same 200  $\mu\text{m}$  stainless steel sample with a 10 % volume fraction. For each frequency, the loss factor was averaged over 10 samples and Figure 3.41 shows its evolution with the frequency, taking into account the scattering of the measurements. As expected from the preliminary frequency sweep, damping decreases with the frequency which would indicate that the energy dissipation mechanisms, mostly friction, are more efficient at low frequency.

In conclusion, this material does exhibit high damping abilities. In uniaxial compression, a loss factor between 0.25 and 0.3 was measured and was found to be more or less influenced by the architectural parameters of the material. Damping was directly linked to the number of contacts and a dynamic analysis showed that a maximal energy absorption could be reached by playing with both the volume fraction and frequency.

### 3.5 Conclusion

From the microstructural analysis, it was shown that a better homogeneity of the material could be reached by pre-deforming the wire as a spring. The evolution of the number of contacts per unit volume was studied and compared to a model for entangled media. The initial shape of the wire was shown to influence the contact density and samples made out of short fibers were shown to fall closer to the theoretical value of the “tube” model. We were also able to link the local orientation state to the density distribution inside the sample.

The stiffness of this material in oedometric compression was shown to evolve with the yield strength and initial shape of the wire. Compromises between the number of contacts and the deformation state of the wire (pre-coiled wire) were found to influence the mechanical response of the entanglement. Its damping ability was also investigated and a Dynamic Mechanical Analysis underlined its great capacity to absorb energy, with a loss factor between 0.25 and 0.3. This damping coefficient was shown to decrease with the frequency and the diameter of the wire. A direct link between loss factor and number of contacts per unit volume was finally identified.

Figure 3.42 gathers on a Loss factor/Stiffness plot the data obtained in this study for different types of entangled materials with the same 10% volume fraction and for both oedometric compression and uniaxial compression (DMA values). By combining the different manufacturing parameters, the mechanical properties of an entanglement can be tailored to meet specific requirements over rather large ranges. Generally, the loss factor decreases with the stiffness of the material, with the exception of the pearlitic steel which, by changing the constitutive material's properties opens new avenues in terms of damping in oedometric conditions. The DMA values in uniaxial compression were naturally found to be significantly higher considering the important effect of friction with the cylindrical mould and to decrease with the frequency. The same tendencies remain however valid and an optimal value could be defined as a function of the volume fraction.

In parallel, the material was successfully strengthened by either a conventional or SPS sintering step. For conventional sintering, a typical three stage compressive behaviour, close to the one of a metallic foam, was observed. The SPS approach was shown to be slightly less effective in increasing the mechanical properties of the structure but also much faster than the conventional method. This resistive sintering technique seems to be an interesting, fast, solution to increase the stiffness of a

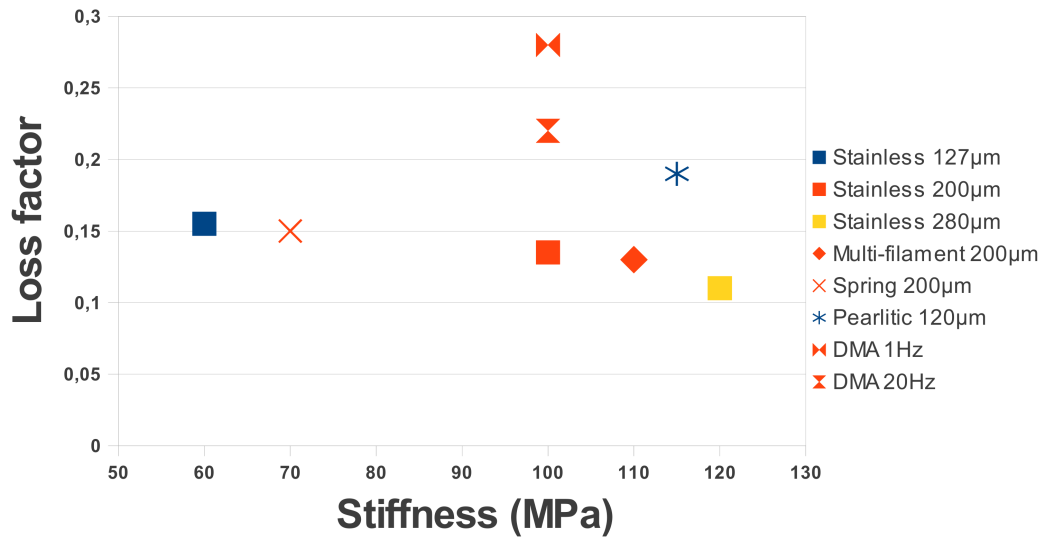


Figure 3.42: Evolution of the loss factor ( $\tan\delta$ ) as a function of the stiffness of the material (volume fraction : 10%).

given entanglement, thus allowing to easily tailor its properties.

Conclusively, it was shown that the properties of the material can be adjusted to given requirements by playing with manufacturing parameters such as the volume fraction, the initial shape of the wire or by adding a sintering step. Using a relatively simple process, samples can be prepared according to specific needs in terms of solicitation (shear, compression, damping) or density distribution (heterogeneity index).

## Chapter 4

# Discrete Element Method applied to the simulation monofilament entangled materials

*This chapter aims at describing the numerical approach that was developed in this PhD in order to model the compressive behaviour of Monofilament Entangled Materials, using a Discrete Element Method [63, 64]. It was inspired by the work of Rodney et al. [40] and is based on a discrete representation of the wire (spherical elements with the same diameter as the wire). Initial geometries were acquired either numerically through a random generation or from experimental 3D tomography data. This allowed to study the numerical behaviour of experimentally manufactured samples and to compare it to the experimental results precedently presented. Both a mechanical and a microstructural analysis were performed from the simulations.*

### Chapter's content

---

4.1	Numerical model . . . . .	101
4.1.1	Principle . . . . .	101
4.1.2	Generation of discrete numerical samples . . . . .	107
4.1.3	Solicitation : oedometric compression . . . . .	110
4.1.4	"Quench" relaxation . . . . .	111
4.1.5	Measurements . . . . .	112
4.2	Microstructural analysis . . . . .	113
4.2.1	Investigation of the random generation . . . . .	113
4.2.2	Comparison to the experimental data . . . . .	114
4.2.3	Influence of the volume fraction . . . . .	115
4.2.4	Deformation mechanisms and reorientation . . . . .	116
4.2.5	Number of contacts . . . . .	118
4.3	Mechanical analysis . . . . .	120
4.3.1	Random/experimental comparison . . . . .	120
4.3.2	Influence of the wire/wire friction coefficient . . . . .	121
4.3.3	Influence of the wire/wall friction coefficient . . . . .	123
4.3.4	Comparison to the experiment . . . . .	124

---

4.4	Conclusion . . . . .	124
-----	----------------------	-----

---

As introduced in Chapter 1, both analytical and numerical models of the compressive behaviour of entangled media can be found in the literature. However, it was shown in Chapter 2 that the specific case of Monofilament Entangled Materials does not exactly fit the hypothesis of the analytical “tube” model. Moreover, the existing numerical models call for rather long simulations and do not allow the analysis of “experimental” samples.

In this context, this study aims at reducing the computation time by using a classical molecular dynamics code running on parallel processors in order to model the compressive behaviour of Monofilament Entangled Materials. Our goal is to be able to model the properties of numerical samples acquired from experimental tomography data so as to allow a comparison between numerical and experimental results.

The principle of the numerical model developed in this PhD will first be introduced and will be followed by a description of the methods used in order to acquire discrete numerical samples (both randomly and from experimental data). Microstructural analysis techniques will then be presented before discussing the results of the simulations from both the morphological and mechanical analysis.

## 4.1 Numerical model

The modeling of entangled fibers was introduced by Rodney *et al.* [40] and continued in Barbier [36], as presented in Chapter 1.2.1.3. In each of these works, fibers are modeled by a succession of discrete elements using a in-house code. Although their work started with spherical elements, the authors turned to cylindrical elements in order to decrease the computation time. The aim of this study was to come back to a bead-like model, constituted of spherical element, using a well-established numerical open-source code (LAMMPS) in order to obtain faster simulations (parallelization of the algorithm).

A bead-like model was defined from a random numerical generation as well as from experimentally acquired 3D volumes, thus allowing to compare the numerical results to the experimental ones. As a sample is only constituted of a single wire, it is modeled as a continuous chain of spherical elements.

As it was previously shown that friction at the contact points plays an important role in the mechanical behaviour of the material, a frictional force, initially developed for granular media, was introduced in the model via Coulomb/Hertz interactions, thus allowing to accurately model both the compressive and hysteretic behaviour.

From the simulation, measurements, comparable to the experimental ones presented in Chapter 2 and 3, were performed in order to compare the compressive behaviour of the entanglement to the experiments.

### 4.1.1 Principle

In order to model the behaviour of entangled materials, the Discrete Elements Method has been focusing a lot of attention in the past few years. It is based on techniques adapted from molecular dynamics and is used to compute the stresses and displacement in a volume containing a large

number of particles. Fibers are modeled as discrete assemblies of spherical elements.

The mechanical behaviour of a fiber or wire is modeled by using a set of potentials between the constitutive elements of the wire. Two types of interactions can be differentiated : the global and local ones. The global interaction corresponds to the friction behaviour between two fibers whenever in contact, whereas the local interactions correspond to the links between successive elements which gives the chain both its tensile and flexural strength.

Similarly to what was developed in [36, 40], the system can be described by a potential energy, corresponding to the sum of three specific contributions.

$$\begin{aligned}
 E = & \sum_{\substack{(i,i+1) \\ \text{consecutive}}} \frac{K_b}{2} (r_i - r_0)^2 : + \sum_{\substack{(i-1,i,i+1) \\ \text{consecutive}}} \frac{K_a}{2} (\theta_i - \theta_0)^2 \\
 & + \sum_{\substack{(i,j) \text{ non} \\ \text{consecutive}}} E_{\text{friction}, r_{i,j}}
 \end{aligned} \tag{4.1}$$

The first term corresponds to the tensile strength of the chain which is modeled by a linear spring with a stiffness  $K_b$ . It is referred to as a “bond” between two successive spherical elements.  $r_i$  is the length of the considered bond and  $r_0$  is its equilibrium length. The same behaviour is observed in both tension and compression.

The second term models the flexural strength of the wire. It corresponds to an “angular” spring with a stiffness  $K_a$ .  $\theta_i$  is the angle defined by two consecutive bonds and  $\theta_0$  is the equilibrium angle of the spring. For initially straight fibers, it is set to  $\theta_0 = \pi$ .

Finally, the friction term only contributes to the energy of the system whenever the distance  $r_{i,j}$  between two non-consecutive elements is shorter than the diameter of the wire (contact point). It includes a repulsive potential which prevents two distinct elements from interpenetrating. The friction force will be described in more details in the following section.

### Tensile strength

The axial strength of the chain is given by a succession of linear springs linking each successive spherical element. Those local interactions give the chain both its tensile and compressive strength. Figure 4.1 shows a schematic representation of the resulting arrangement.

Both the diameter  $d$  and the distance between two successive elements  $r_0$  are defined in Figure 4.1. For each axial spring, such as the one shown in red in Figure 4.1, the force due to the deformation of the “bond” can be written as :

$$F = K_b(r_i - r_0) \tag{4.2}$$

The tensile behaviour of the chain can be fitted to the materials properties by adjusting the stiffness  $K_a$  of the springs. In pure tension, the first term of Equation 4.1 is the only contribution to the evolution of the potential energy. In the blue unit cell shown in Figure 4.1, the deformation can

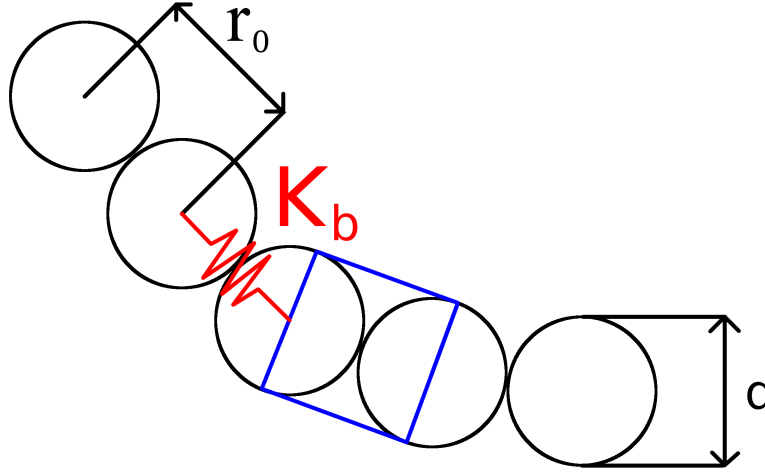


Figure 4.1: Schematic representation of the wire

be expressed as:

$$\varepsilon = \frac{r_i - r_0}{r_0} = \frac{\delta r}{r_0} \quad (4.3)$$

and the stress as :

$$\sigma = \frac{F}{S} = E\varepsilon \quad (4.4)$$

It can thus be determined that :

$$\frac{4F}{\pi d^2} = E \frac{\delta r}{r_0} \quad (4.5)$$

Consequently, we get, for the axial force :

$$F = \frac{E\pi d^2}{4r_0} \delta r \quad (4.6)$$

By combining equation 4.2 and equation 4.6, the stiffness of the spring can be identified as :

$$K_b = \frac{E\pi d^2}{4r_0} \quad (4.7)$$

The spring rate is then directly linked to the Young's modulus of the constitutive material and it was observed that, in a simple numerical tensile test, Hooke's law is verified. The elastic behaviour of the wire (Young's modulus = 200GPa) was thus accurately modeled.

### Flexural strength

In a similar manner, the flexural strength of the chain is modeled by an "angular" spring with a stiffness  $K_a$  and an equilibrium angle  $\theta_0 = \pi$ . Figure 4.2 shows the corresponding arrangement for two consecutive bonds forming an angle  $\theta_i$ .

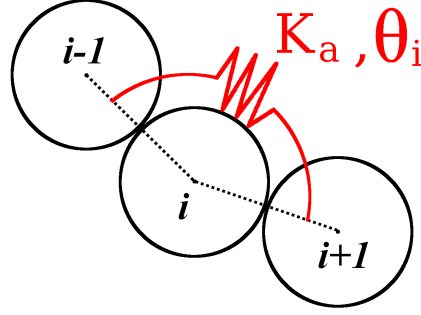


Figure 4.2: Angular spring between two consecutive bond between spherical elements along the wire.

For a given node  $i$ , the spring, shown in red in Figure 4.2, applies forces on both nodes  $i-1$  and  $i+1$ , perpendicularly to the segments between nodes. The intensity of the force can be written as:

$$F = \frac{K_a}{r_0}(\theta_i - \pi) \quad (4.8)$$

where  $r_0$  is the length between two consecutive nodes.

In order to fit the stiffness of the spring to the materials properties, the behaviour of a “discrete” cantilever beam, composed of  $N$  segments of length  $r_0$  was studied. As shown in Figure 4.3, it was fixed on one end and a vertical force was applied on the other end.

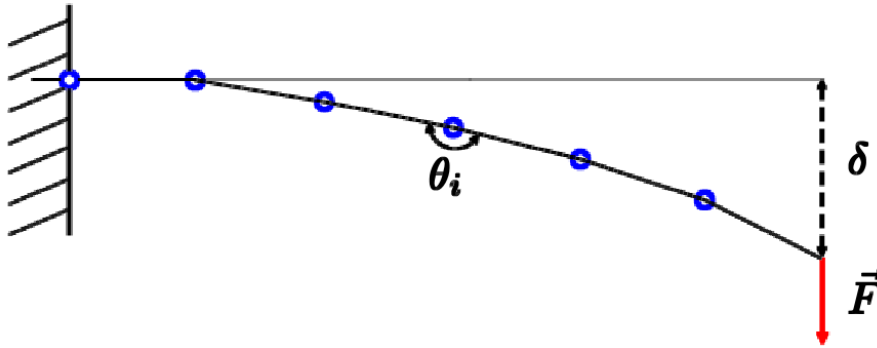


Figure 4.3: Schematic representation of a cantilever beam to which a vertical force  $F$  is applied. The beam is composed of  $N$  consecutive segments.

The deflection  $\delta$  can be defined as the sum of the vertical displacement  $x_i$  (see Equation 4.9) of each node, relative to its predecessor, which depends on the angle  $\theta_i$  of said node  $i$ .

$$x_i = r_0 \sin \left( \sum_1^i (\pi - \theta_i) \right) \quad (4.9)$$

In the case of small deformations,  $\sin(\pi - \theta_i) \approx (\pi - \theta_i)$  and it becomes :

$$x_i \approx r_0 \sum_1^i (\pi - \theta_i) \quad (4.10)$$



The deflection, for a single fiber, composed of  $(N - 1)$  elements, can thus be expressed as :

$$\delta = r_0 \sum_{i=1}^{N-1} (N - i)(\pi - \theta_i) \quad (4.11)$$

In this configuration, the contribution of tension and compression to the total potential energy is negligible and it thus corresponds to the sum of the bending energies to which the work of the force  $F$  is subtracted (see Equation 4.12).

$$E = \sum_{i=1}^{N-1} \left( \frac{1}{2} K_a (\theta_i - \pi)^2 \right) - F\delta \quad (4.12)$$

At equilibrium, the partial derivative of the potential energy with respect to each angle  $\theta_i$  is equal to zero and by combining Equation 4.11 and the derivative of Equation 4.12, we can obtain :

$$\frac{\partial E}{\partial \theta_i} = K_a (\theta_i - \pi) + Fr_0 (N - i) = 0 \quad (4.13)$$

$$\Leftrightarrow \pi - \theta_i = \frac{Fr_0}{K_a} (N - i) \quad (4.14)$$

The deflection can thus be written as :

$$\delta = \frac{r_0^2 F}{K_a} \sum_{i=1}^{N-1} (N - i)^2 \quad (4.15)$$

According to the sum of square's formula, which yields  $\sum_{k=1}^m k = \frac{m(m+1)(2m+1)}{6}$ , the deflection becomes :

$$\delta = \frac{r_0^2 F}{6K_a} N(N - 1)(2N - 1) \quad (4.16)$$

When considering the complete experimental sample, bending occurs between contact points and the mean length between contact  $\lambda$  was considered to be much larger than the diameter of the wire, thus implying that  $L \gg r_0$  (with  $L = N \cdot l_0$ ) and finally :

$$\delta = \frac{FL^3}{3K_a r_0} \left( 1 - \frac{r_0}{L} \right) \left( 1 - \frac{r_0}{2L} \right) \approx \frac{FL^3}{3K_a r_0} \quad (4.17)$$

According to the beam theory, the deflection of a cantilever to which an end force  $F$  is applied, can be calculated using :

$$\delta = \frac{FL^3}{3EI} \quad (4.18)$$

where  $E$  is the modulus of elasticity of the material,  $I$  is the area moment of inertia and  $L$  is the length of the beam. By identifying Equations 4.17 and 4.18, we obtain :

$$EI = K_a r_0 \quad (4.19)$$

The stiffness of the angular spring in the simulation was finally set to :

$$K_a = \frac{E\pi d^4}{64r_0} \quad (4.20)$$

A simulation of the deflection of a discrete cantilever beam was performed and it was shown to be in good agreement with the beam theory.

### Friction behaviour between two non-consecutive elements

Finally, repulsive pairwise interactions, combined to frictional forces, were defined between two atoms  $i$  and  $j$  whenever the distance  $r_{i,j}$  was smaller than the diameter of the wire (definition of a contact point). The overlap distance of the two spherical elements  $\delta$  is defined in Figure 4.4.

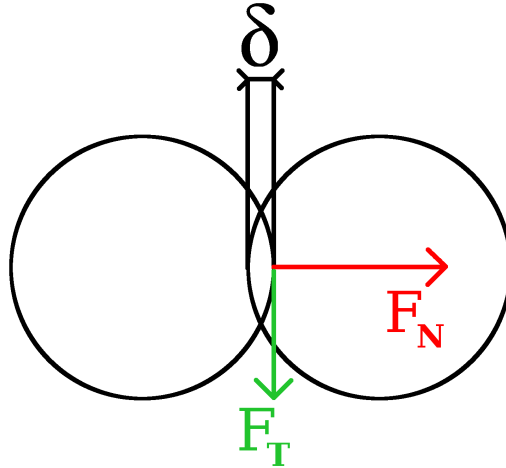


Figure 4.4: Two non-consecutive spherical elements with a radius  $R$  in contact. Illustration of the frictional normal  $F_N$  and tangential force  $F_t$  at the contact.

As described in [65–67], the following formula was used for the frictional force between two elements :

$$F_{hertz} = \frac{\sqrt{\delta d}}{2} [(k_n \delta \mathbf{n} - m_{eff} \gamma_n \mathbf{v}_n) - (k_t \mathbf{t} + m_{eff} \gamma_t \mathbf{v}_t)] \quad (4.21)$$

where  $\delta$  is the overlap distance between two elements (shown in figure 4.4),  $d$  is the diameter of the wire,  $k_n$  and  $k_t$  are the elastic constant for normal and tangential contact respectively,  $\gamma_n$  and  $\gamma_t$  are the viscoelastic damping constant for normal and tangential contact respectively,  $m_{eff} = M/2$  is the effective mass of two elements of mass  $M$ . Finally,  $\mathbf{n}$  and  $\mathbf{t}$  are the normal and tangential unit vector and  $\mathbf{v}_n$  and  $\mathbf{v}_t$  are the normal and tangential component of the relative velocity of the two elements in contact.

The first parenthesized term corresponds to the normal force, composed of a contact force and a damping force, and the second parenthesized term to the tangential force, composed of a shear force and a damping force. The shear force is a “history” effect that accounts for the tangential displacement between two elements for the duration of the time they are in contact.

The push-back force for two overlapping elements is proportional to the area of overlap and is thus a non-linear function of the overlap distance. As shown in [67]  $k_n$  and  $k_t$  can be set to values that correspond to the properties of the material being modeled by using the following formulas :

$$k_n = \frac{4G}{(3(1-\nu))} \text{ and } k_t = \frac{4G}{(2-\nu)} \quad (4.22)$$

Finally, a friction coefficient was defined and set to 0.5 for wire-wire contacts. A Coulomb criterion was used where the tangential force between two particles grows according to a tangential “spring and dash-pot” model until  $F_T = F_N * \mu_s$  and is then held constant until they lose contact.

#### 4.1.2 Generation of discrete numerical samples

In order to perform simulations of the mechanical and morphological behaviour of monofilament entangled materials, an initial sample geometry was necessary. It corresponds to a list elements which are indexed by their center points. The angular and axial linear springs were then defined by listing the elements constitutive of each interaction ((i,i+1) for a bond, (i-1,i,i+1) for an angle).

This numerical sample could be either generated randomly or acquired from tomography data, in order give a comparison of the results to the experimental investigations presented in Chapter 2 and 3.

#### Generation of a microstructure

Numerical samples were generated using a “random walk” algorithm within the boundaries of a cylindrical box which dimensions were defined as identical to the experimental ones. The length of the wire (number of elements) was defined accordingly to the distance between nodes ( $r_0 = d$ ) and to the aimed volume fraction : 5%.

The generation was first initialized by creating the two first elements of the wire. Using a random walk Monte Carlo method, the next element was placed according to the following conditions :

- $d_{i,i+1} = d$ , where  $d_{i,i+1}$  is the distance between two consecutive nodes and  $d$  is the diameter of the wire,
- the position (X,Y,Z) was contained inside the cylindrical box (radius : 15 mm, height : 35 mm),
- whenever the bending energy of the two consecutive segments ((i-1,i) and (i,i+1)), defined as  $E = K(\theta - \pi)^2$  (where K is the stiffness of the “angular” junction and  $\theta$  the angle), satisfied  $\exp\left(\frac{-E}{kT}\right) > r$  (where  $r$  is a random value between 0 and 1). This restriction results in a higher probability for the wire to be straight while allowing for angles close to 90° between two consecutive segments when necessary (perpendicular to the cylindrical wall, for example). After a few preliminary tries, a  $kT$  value was defined which allowed a fast enough iteration when perpendicular to the boundaries while preventing large angles between two consecutive segments.

A continuous, discrete, single wire was obtained but overlapping of elements was not yet taken into account. The system was thus relaxed using a “conjugate gradient” energy minimization algorithm, during which rearrangements occurred. Figure 4.5 shows the entanglement before minimization (a), which appears very “angular”, and after minimization (b). The initial sample configuration was finally obtained at that point.

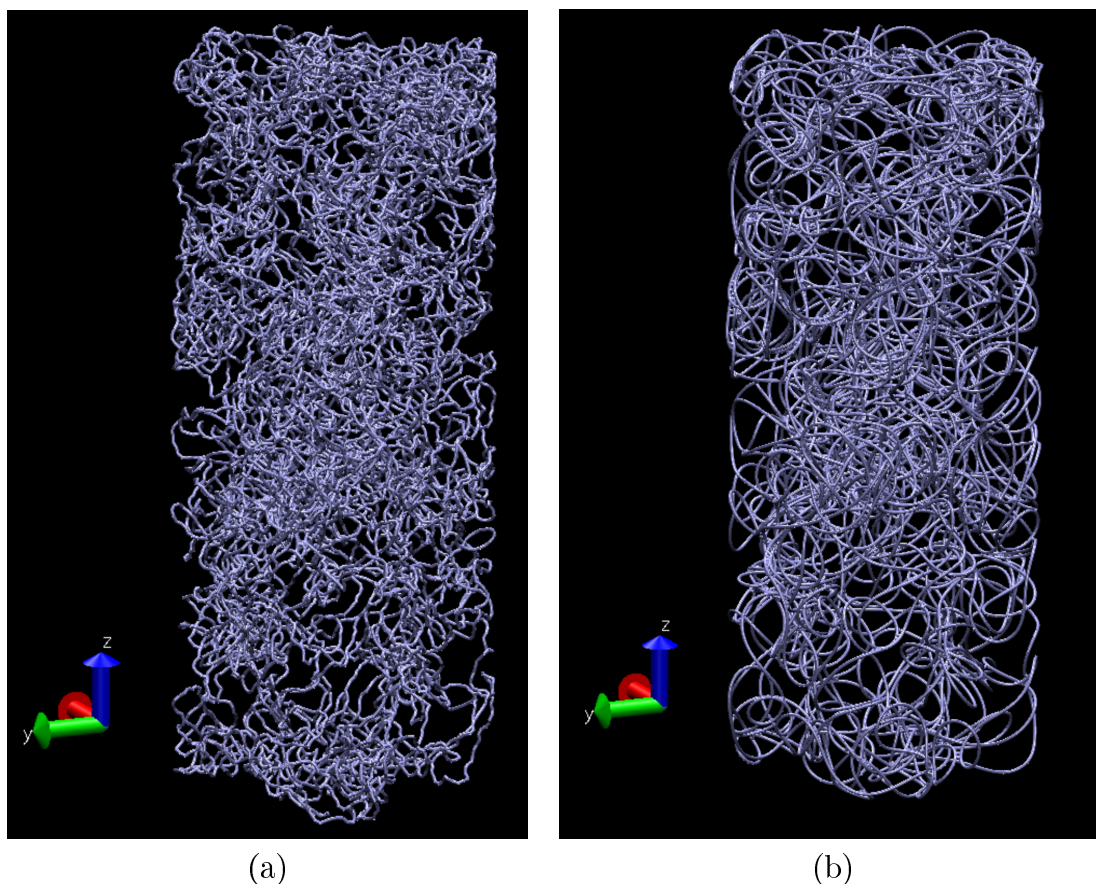


Figure 4.5: Numerically generated sample before (a) and after (b) minimization.

### Discretization from tomography data

Given the heterogeneous nature of monofilament entangled materials that was showed in Chapter 3, the results of the numerical simulation necessarily depends on the initial morphology of the entanglement, which is conditioned by the characteristic dimensions of the material (wire diameter/mold diameter ratio and height of the sample). So in order to be able to compare the experimental results to the modeled behaviour, our goal was to acquire a discrete geometry of the sample reproducing the experimental tomography data as closely as possible.

As mentioned in Chapter 2, the acquisition of a 3D volume in tomography results in a binary image where the wire is described by a set of white voxels. A typical image is composed of around 23 millions voxels. Firstly, the number of white voxels was reduced in order to limit the time of the discretization process. Erosion were applied to the 3D volume before down-scaling it with a 0.5 factor (each dimension was consequently divided by 2 so the total volume was divided by 8). The number of white pixels was thus reduced to around 1 million.

The discretization method was then performed by iteratively placing beads along the wire. To this end, the LAMMPS molecular dynamics code was used. First, an initial geometry was created by placing an element of type A for each white voxel. The position of these elements was fixed (no movement allowed) and it resulted in a 3D representation of the sample, composed of spherical elements. Figure 4.6 shows the corresponding structure over a small part of the wire.

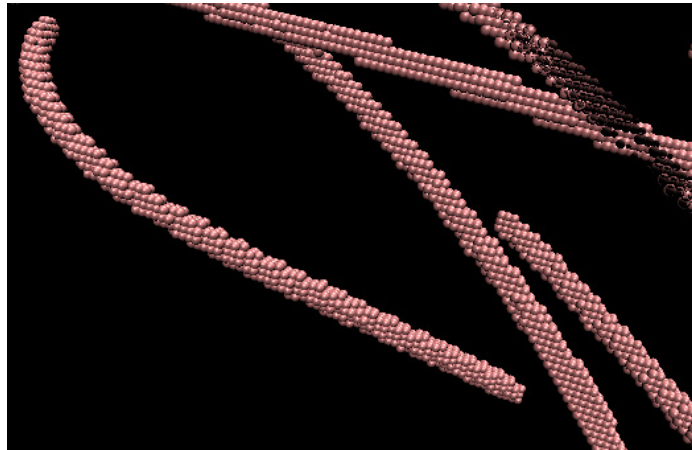


Figure 4.6: Sections of wire, acquired from tomography data , where each pixel was replaced by a spherical element.

The procedure was then initialized by placing, along the centerline of the wire, the first two type B elements of the final chain, which were fixed as well. Those type B elements, shown as red circles in Figure 4.7 were designed to be :

- attracted by the type A ones (shown as white squares in Figure 4.7,
- subjected to a pairwise interaction which is at equilibrium when two elements are distant by the diameter of the wire,
- linked by an axial linear spring (as described for the "tensile strength of the chain in the preceding section) in the case of two consecutive elements.

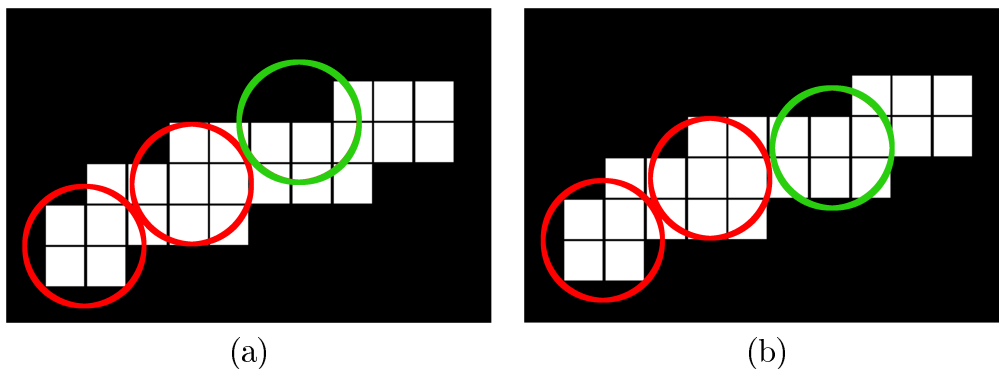


Figure 4.7: Schematic representation of the discretization process : in red, two initially placed type B elements and in green, the interpolated position of the new type B element before (a) and after minimization (b).

The position of each ensuing element was determined (as illustrated in Figure 4.7(a)) using a linear interpolation and it was then adjusted using a conjugate gradient minimization, thus placing it in the continuity of the wire (as shown in Figure 4.7(b)), according to the three conditions previously stated. From the two initial elements, this iterative process was performed in both directions until the



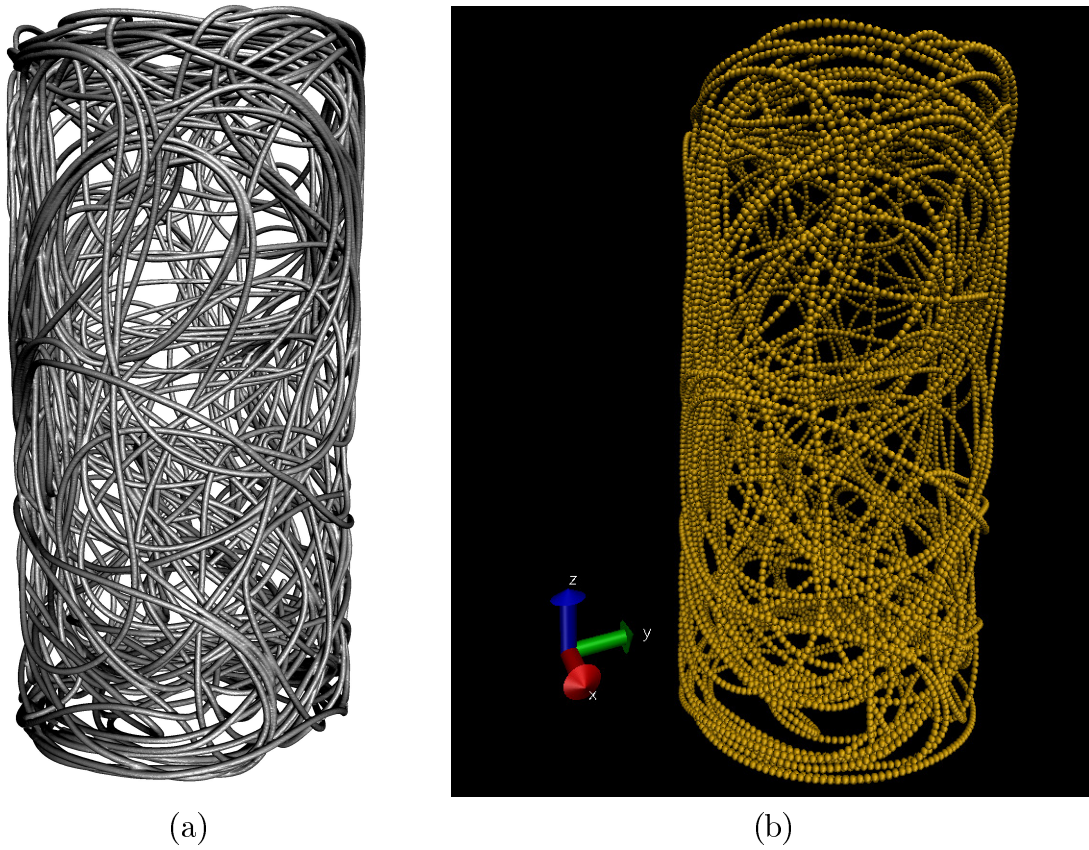


Figure 4.8: 3D representation of an experimental sample : (a) tomography data and (b) resulting discrete geometry.

ends of the wire were reached.

Figure 4.8 shows the result of this discretization on a  $280\ \mu\text{m}$  stainless steel wire sample. Considering the large number of elements used for this operation, the total calculation of such a configuration took about 2 weeks. Following this numerical process, an energy minimization was applied to the discrete geometry as the distance between two elements of a contact could be shorter than the actual diameter of the wire. The final initial geometry was finally obtained and samples could be compressed and compared to numerically generated samples.

#### 4.1.3 Solicitation : oedometric compression

In order to reproduce the experimental mechanical setup, numerical samples were placed inside a cylindrical mould which interacts with the elements of the wire in a similar way to what was previously presented for wire-wire contacts. The friction coefficient for wall-wire contacts was however set to 0.1, which corresponds to a PTFE-steel contact. Two pistons were created as well in order to be able to compress the samples. Figure 4.9 shows an example of a sample compressed within the die, between the two plates.

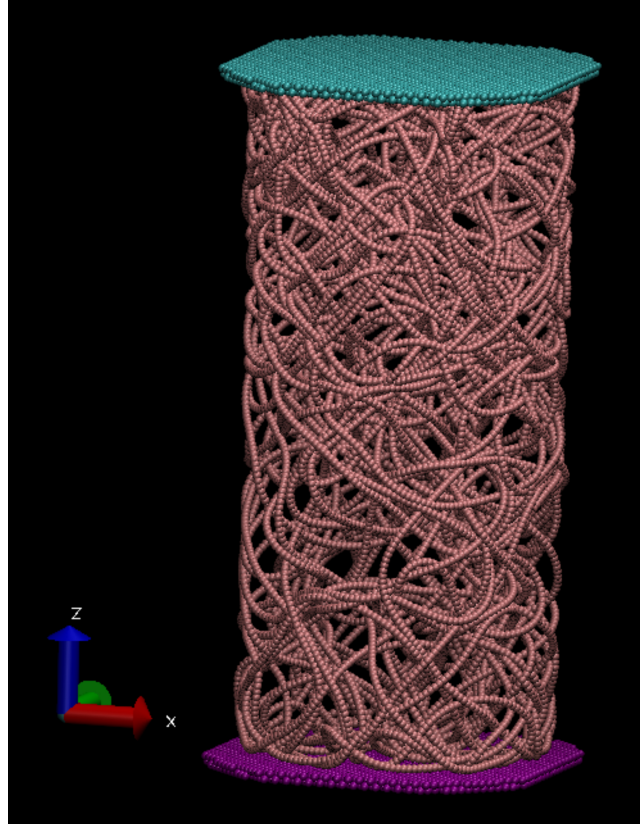


Figure 4.9: Numerical testing setup with a sample compressed between two plates (the containing cylindrical mould is not shown here).

The entanglement was then deformed by a small incremental displacement of one of the pistons, followed by a definition of the resulting equilibrium state using a "quench" numerical algorithm.

#### 4.1.4 "Quench" relaxation

After each incremental displacement of the piston, the system was relaxed for a few thousand timesteps until an equilibrium state was finally reached. At each step, elements were displaced by first evaluating all the forces that they were subjected to. The new position of each node was then defined using a Verlet algorithm (numerical method used to integrate Newton's equation of motion  $\mathbf{a} = \partial^2 \mathbf{r}(t) / \partial t^2 = \mathbf{f}(t) / m$ , where  $\mathbf{r}(t)$  is the position,  $\mathbf{f}(t)$  the sum of all forces on a node and  $m$  the "fictive" mass of this node).

The speed of a node at time  $t$  depends on its displacement over a  $\delta t$  time increment and is defined as :  $\mathbf{v}(t) = \frac{\mathbf{r}(t+\delta t) - \mathbf{r}(t-\delta t)}{2\delta t}$ . A "quench" condition was introduced in order to reach equilibrium. It corresponds to a reset of the kinetic energy of a node at the end of a timestep whenever the scalar product of the sum of forces and the speed is negative.

$$\text{if } \mathbf{f}(t) \cdot \mathbf{v}(t) < 0 \Rightarrow \mathbf{v}(t) = 0 \quad (4.23)$$

Using this "quenched" dynamic leads to a faster determination of the equilibrium state. Finally for each incremental deformation of the sample, this algorithm was used for as many timestep as necessary in order to reach a stable mechanical response. At each timestep, the resulting pressure of

the sample on the moving piston was calculated, which allowed for stress-strain curves to be plotted.

#### 4.1.5 Measurements

By recording the position of all elements during the simulation, data could be extracted in order to characterize the microstructural evolution of the numerical sample when compressed and to compare it to experimental results.

##### Density profiles

Much like it was previously described in Chapter 3, a radial density profile was acquired from the discrete representation of a sample by first calculating the distribution of the number of elements  $N_{element}(r)$  as a function of the radial position. The local density  $\rho(r)$ , at a distance  $r$  of the axis of the cylindrical sample, was then assessed by considering that every element accounts for a volume  $V_{element} = \frac{\pi d^2 r_0}{4}$ , where  $d$  is the diameter of the wire and  $r_0$  the distance between two consecutive elements. Finally, a local volume fraction  $\rho(r)$  was obtained by computing, for each class of the histogram, the following relation :

$$\rho(r) = \frac{N_{element}(r) \times V_{element}}{V_{class}(r)} \quad (4.24)$$

where  $V_{class}(r)$  is the total volume of the class located at a distance  $r$  from the axis.

Similarly, the density distribution along the compression axis ( $z$ ) was analyzed by computing a histogram of the number of elements  $N_{element}(z)$  as a function of the  $z$ -position. The local density  $\rho(z)$  was then defined as :

$$\rho(z) = \frac{N_{element}(z) \times V_{element}}{V_{class}(z)} \quad (4.25)$$

where  $V_{class}(z)$  is the total volume of the class located at a position  $z$  along the compression axis.

##### Local orientation

From the coordinates of each element, it was also possible to measure a local orientation of the wire to the compression axis ( $z$ ). An orientation vector was defined for each element  $i$  from the coordinates of elements  $i$  and  $i + 1$ .

$$\begin{cases} V_x(i) = X(i+1) - X(i) \\ V_y(i) = Y(i+1) - Y(i) \\ V_z(i) = Z(i+1) - Z(i) \end{cases}$$

and a local orientation could thus be written as :

$$\theta = \arccos \left( \frac{V_z(i)}{\sqrt{V_x(i)^2 + V_y(i)^2 + V_z(i)^2}} \right) \quad (4.26)$$

Finally, the orientation distribution from top to bottom of the sample was obtained by averaging the orientation angle for each  $z$ -position along the compression direction.



## Number of contacts

During the simulation, the positions of all elements were registered as a list of (X, Y, Z) coordinates. The number of contacts could thus be measured by analyzing the distances between elements. For each element along the wire, the number of "neighbors" located at a distance smaller than a threshold value, close to the diameter of the wire, was computed. Consequently, the total number of contacts between two particles could be followed throughout the compression.

This global measurement does not, however, correspond to the actual number of wire-wire contacts as one "longitudinal" contact can be composed of many touching elements. In order to obtain a more "quantitative" measurement, a contact was defined as a section of wire where elements have at least one neighbor and which is delimited by elements with no neighbors (as illustrated in figure 4.10).

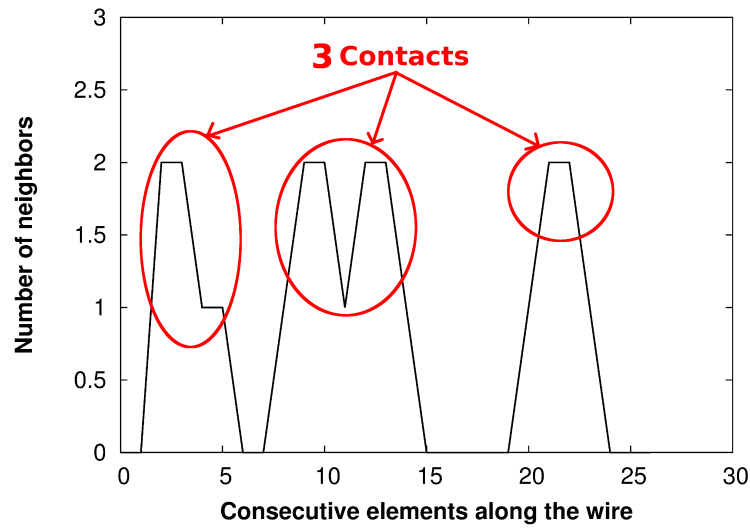


Figure 4.10: Evolution of the number of neighbors along the wire. Definition of a contact point.

A more accurate measurement of the number of contacts could thus be performed and compared to experimental results.

## 4.2 Microstructural analysis

Experimentally, it was previously shown that the mechanical behaviour of a Monofilament Entangled Material could be linked to its microstructural evolution. From a numerical point of view, as the model was developed with the same geometry as the experiment, it was possible to compare both the morphological and mechanical behaviour to what was concluded in previous chapters. The evolution of the entanglement's microstructure will here first be investigated.

### 4.2.1 Investigation of the random generation

Using the random walk algorithm previously introduced, samples with a 5% volume fraction were generated for different wire diameters, equivalent to the stainless steel wires used in the experiments.

Density profiles along the radial direction were plotted and results are shown in Figure 4.11.

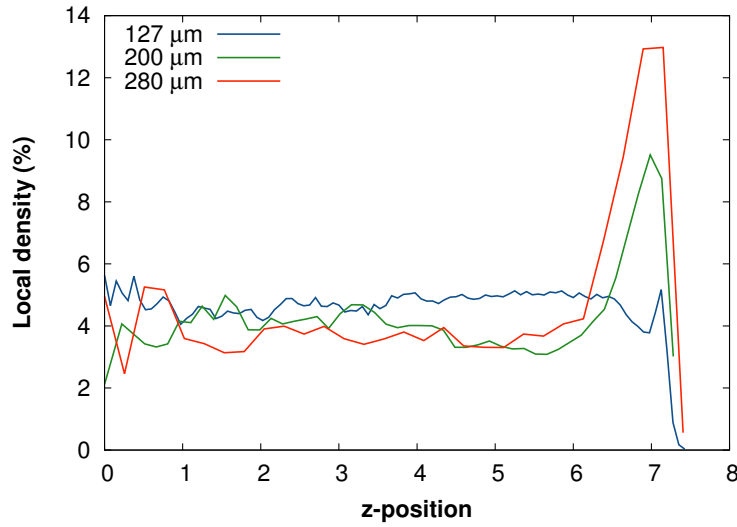


Figure 4.11: Influence of the diameter of the wire on the radial distribution for samples with a 5% volume fraction.

Firstly, a "noisy" distribution was observed due to the discrete nature of the entanglement (as opposed to the more continuous tomography data). It is even more pronounced in the center as the volume of the central bins of the histogram are much smaller than the ones on the outside. The distribution was shown to be rather homogeneous, regardless of the diameter. However, the "wall" effect, although less pronounced than for an equivalent experimental sample, seems to decrease with the diameter of the wire, which, considering that the "stiffness" of the chain, normalized by its diameter, during the generation was kept constant for all three wire diameters, is in agreement with the experimental observations.

The size ratio between the diameter of the wire and the size of the simulation box appears to have the same influence on the density distribution for the numerical generation as for the experimental sample preparation.

#### 4.2.2 Comparison to the experimental data

From the discretization process previously introduced, a discrete geometry of an actual experimental sample (280  $\mu\text{m}$  stainless steel wire, volume fraction : 5 %), which will be referred to as a "discrete experimental sample", was obtained and an equivalent density profile was calculated after minimization of the structure. Figure 4.12 shows the resulting comparison of both experimental and numerical profiles.

Eventhough some fluctuations, corresponding to the noise of the measurement, could be observed for the numerical profile, a very good agreement was observed between experiment and simulation. A few small differences could however be observed, such as the slightly lower density in the center of the sample and a steeper slope of the "wall effect" peak. The minimization that followed the discretization process did lead to a small evolution of the structure in order to reach an equilibrium

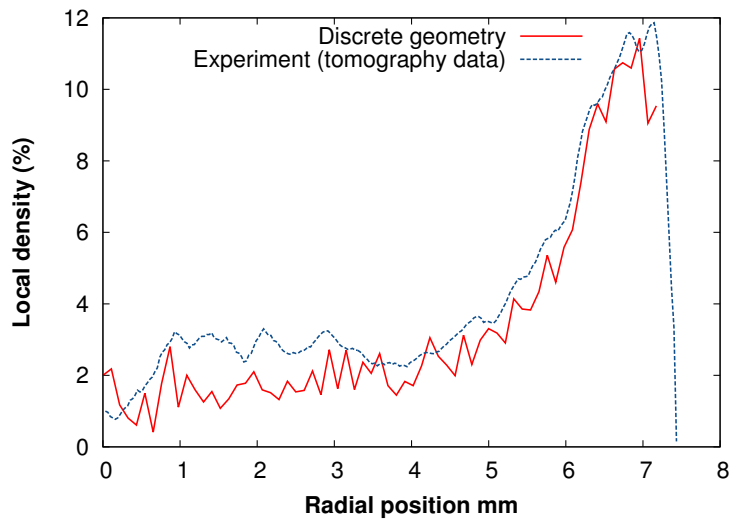


Figure 4.12: Experimental/numerical comparison of the radial density distribution of a 5%, 280  $\mu\text{m}$  stainless steel sample.

state.

### 4.2.3 Influence of the volume fraction

From the analysis of the tomography data, the shape of the radial density profile was shown to be independent of the volume fraction, thus indicating that there was no rearrangement along the radial direction but, as it will be discussed later, reorientation and local densification along the compression axis. By compressing the "discrete experimental sample", the evolution of the radial distribution during the simulation was finally studied.

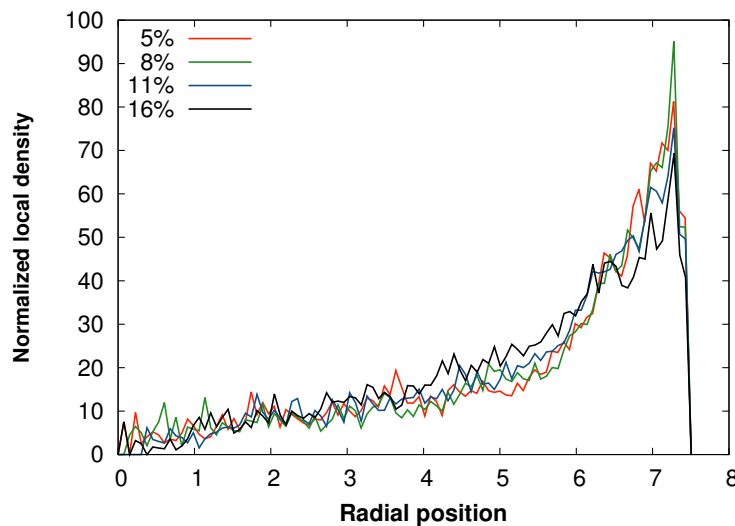


Figure 4.13: Influence of the volume fraction on the radial distribution for samples with a 280 $\mu\text{m}$  wire diameter, acquired from a simulation with a wire/wire friction coefficient of 0.4.

Figure 4.13 shows the evolution of the radial density profile with the volume fraction. The local density was normalized by the height of the sample in order to be able to compare profiles for different volume fractions.

Although a small shift of the normalized local density could be observed towards the center of the entanglement, the general shape of the distribution remained sensibly constant throughout the compression. Consequently and when compared to the experimental results, the microstructural evolution of the entanglement was accurately modeled in the simulation. Therefore, an analysis of the density and orientation distributions was performed in order to study the deformation mechanisms along the compression direction.

#### 4.2.4 Deformation mechanisms and reorientation

Similarly to what was done experimentally, simulations of the compressive behaviour of Monofilament Entangled Materials were performed for a "discrete experimental" sample using different wire/wire friction coefficient. At different stages of the simulation, data were acquired and analyzed, allowing to follow the evolution of both the density and orientation distributions along the compression direction as a function of the volume fraction.

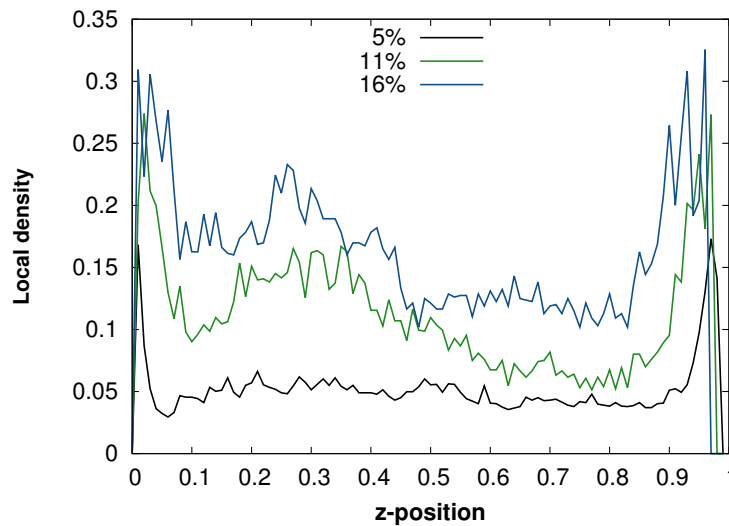


Figure 4.14: Evolution of the axial density profile with the volume fraction during the simulation for a 280 $\mu\text{m}$  stainless steel sample.

A strong correlation between local density and local orientation angle to the compression axis was found experimentally thus indicating that the entanglement gets denser by rearrangements and reorientations of the wire. Figure 4.14 shows the evolution of the density distribution along the compression axis as a function of the volume fraction.

Firstly, a higher density gradient can be observed on the side of the "moving" piston ( $z=0$ ), where densification primarily occurs. This behaviour is close to what can be observed in the densification of granular media and its evolution with the wire/wire friction coefficient will be discussed in more details later. For higher volume fraction, the densification is generalized to the entire sample and, more generally, a behaviour close to the localized "peak" densification that was described experimentally

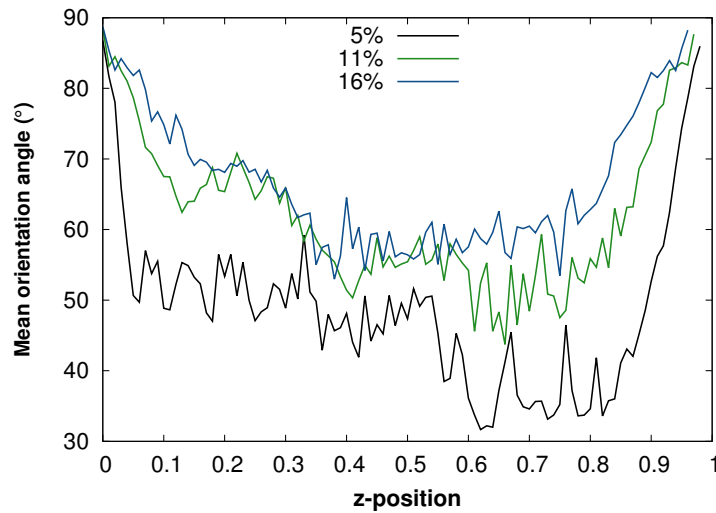


Figure 4.15: Evolution of the orientation profile with the volume fraction during the simulation, for a  $280\mu\text{m}$  stainless steel sample.

could also be observed.

In terms of orientation, as seen in Figure 4.15, the densification is associated with a reorientation of the wire perpendicular to the compression axis. The correlation between density and orientation is however less obvious than it was observed experimentally. The preferential deformation towards the moving side is consequently first accompanied by a strong reorientation of the wire, which, for higher volume fractions, remains constant and leads to global reorientations throughout the sample, thus confirming that the deformation tends to get more homogeneous for high densities.

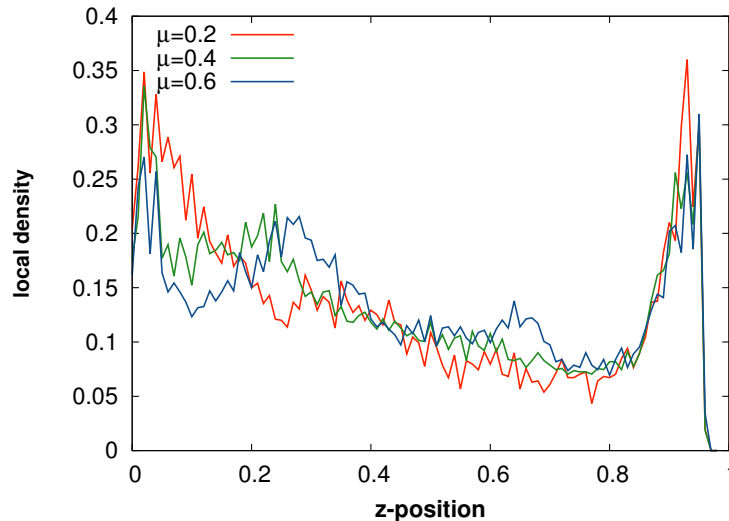


Figure 4.16: Evolution of the orientation profile with the volume fraction during the simulation, for a  $280\mu\text{m}$  stainless steel sample.

Finally, Figure 4.16 shows the influence of the wire/wire friction coefficient on the density distribution along the compression direction. For low friction coefficients, sliding at contact points occurs leading to rearrangements during the compression and thus to a localized densification close

to the applied deformation. In a way, it corresponds to a stage where the mechanical percolation is not fully reached for a given friction coefficient. However, for higher friction coefficients, preventing contacts from sliding, a more generalized densification could be observed throughout the sample.

A behaviour, typical of granular media, was observed when simulating the oedometric compression of an entanglement. As opposed to the generalized "peak" densification that was observed experimentally, simulations showed a more heterogeneous deformation which could indicate that friction is under-estimated in this model and that rearrangement along the compression axis is thus more predominant.

#### 4.2.5 Number of contacts

In parallel to the density analysis, the number of contacts was followed during the simulation. As it was presented in more details in Chapter 2, the "tube" model can be used in entangled materials in order to calculate a theoretical number of contacts. It will here be used with the parameters that were defined in Chapter 2 :  $f = 1.6$ , where  $f$  is a parameter describing the orientation distribution.

It should be reminded that the number of contacts per unit volume  $N_{cv}$  is defined as :

$$N_{cv} = \frac{16f}{\pi^2 d_f^3} \rho^2 \quad (4.27)$$

A global measurement was first performed without considering the refinement presented in section 4.1.5 and which will be discussed in more details later in this section. As a result, values presented here allow for a more qualitative analysis. Each compression state was analyzed using two different thresholds and the resulting number of contacts thus corresponds to an average value. Error bars are thus shown along with the values calculated from the model.

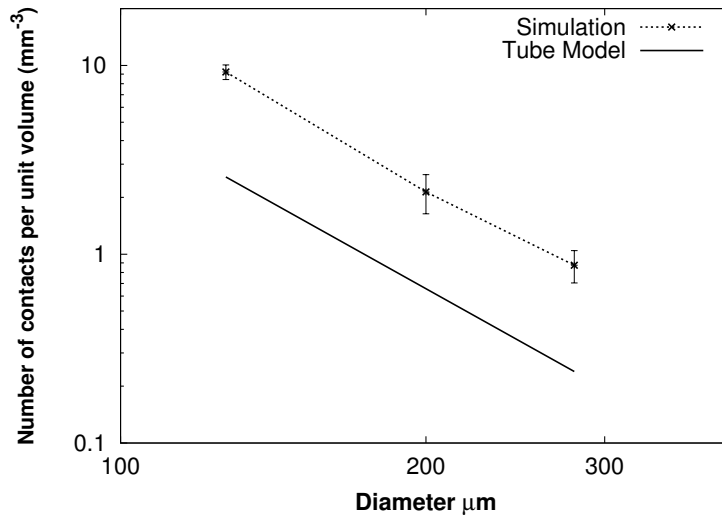


Figure 4.17: Evolution of the number of contacts per unit volume with the wire diameter for numerically generated samples with the same 6% volume fraction.

From the numerically generated samples, the number of contacts was measured for different wire diameters. Figure 4.17 shows the evolution of the number of contacts as a function of the diameter

of the wire  $d$ . The number of contacts per unit volumes was found to evolve as  $1/d^3$ , just as the model predicts. Finally, the morphological arrangements that were randomly generated correspond to typical fiber media and are thus expected to behave very similarly to experimental Monofilament Entangled samples.

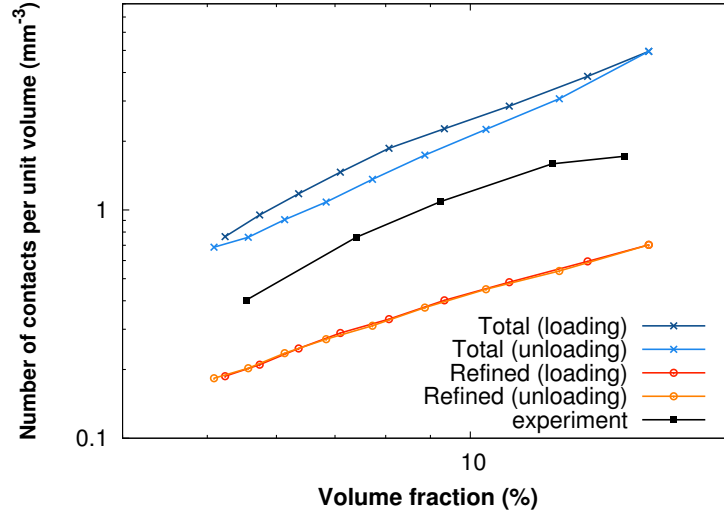


Figure 4.18: Evolution of the number of contacts per unit volume with the volume fraction for a “discrete experimental” sample with a  $280 \mu\text{m}$  wire diameter.

Figure 4.18 shows, in the case of the “discrete experimental” sample, the evolution of the number of contacts, registered during the numerical oedometric compression, as a function of the volume fraction. Both the total number of contacts between spherical elements and the refined contact points count are shown here. When compressed, contact points are created in the entanglement and the number of contacts increases at a rate close to what was observed experimentally. The total counts are obviously a lot higher than the experimental values as here, every contacts between two elements are considered and that a contact can be constituted of several touching elements. When refining the measurement using the process defined in section 4.1.5, a much lower contact density was obtained, even when compared to experimental data, while maintaining a typical increase as a function of the square of the volume fraction.

When unloading the sample, a faster decrease of the total number of contacts was observed, until the initial configuration was reached again, while the refined count showed a fully reversible process. Considering the purely elastic behaviour of the wire in this simulation, contacts are thus indeed broken at the same rate than during the compression but are limited to smaller contact surface.

Finally, the evolution of the number of contacts was investigated as a function of the wire/wire friction coefficient. Values between 0 and 1 were used and Figure 4.19 regroups the data acquired during the simulations.

For low friction coefficient, contacts do not transmit any forces and rearrangements thus occur, leading to the creation of new contacts. For increasing friction coefficients, the number of contacts was shown to decrease until a limit value was reached. The increase of the contact density with the volume fraction was also shown to be slightly slower for higher friction values. Rearrangements are made more difficult by the resistance of the contacts. It does not, however, imply a decrease

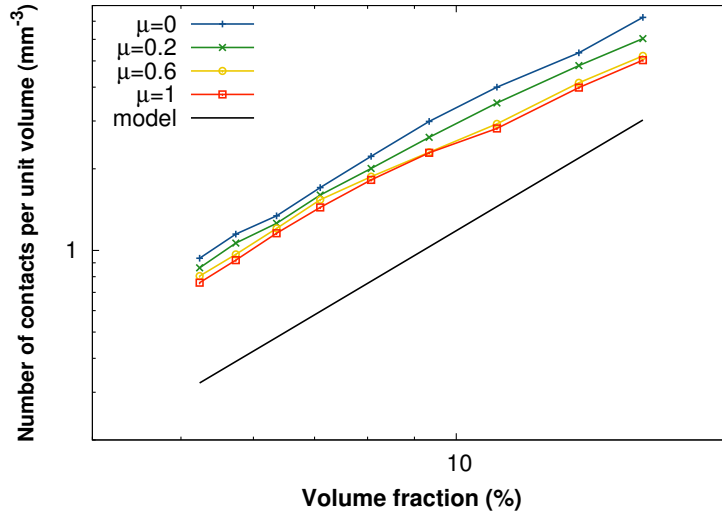


Figure 4.19: Evolution of the number of contacts per unit volume with the volume fraction for a “discrete experimental” sample with a  $280\ \mu\text{m}$  wire diameter and for different wire/wire friction coefficient.

of the mechanical response as contacts with friction are more resistant and thus transmit higher forces.

The microstructural evolution of the entanglement during the simulation was shown to be very similar to what could be observed experimentally. Although a heterogeneous deformation along the compression direction was noticed, which was shown to decrease with the wire/wire friction coefficient, the evolution of the number of contacts and density profiles were shown to be characteristic of the compression of entangled media. Consequently, one could predict a compressive mechanical behaviour typical of entangled media. Mechanical results from the simulations will thus be presented in the following section in order to verify that.

### 4.3 Mechanical analysis

During the simulation, the resulting pressure on the moving piston was registered, as well as the total deformation of the numerical sample. We were thus able to plot the evolution of the stress as a function of the volume fraction.

Numerical results will be compared to experimental data and the influence of a few parameters (friction, randomness) will be investigated.

#### 4.3.1 Random/experimental comparison

Simulations were performed using a 0.4 wire/wire friction coefficient and a 0.1 wire/wall friction coefficient for both a randomly generated sample and an experimentally acquired one. Much like the experimental “spring” sample, the generated structure was shown to be more homogeneously distributed with a lower local density at the contact with the mould. Unlike the plastically deformed stainless steel wire, the mechanical properties of the “random” wire were set, in the simulation, to



the elastic properties of a non-deformed steel.

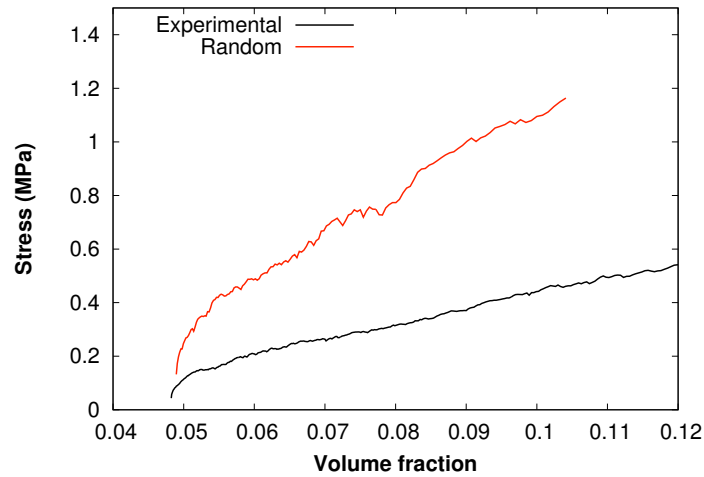


Figure 4.20: Comparison of the simulated stress/volume fraction behaviour of a randomly generated sample to an experimentally acquired one ( $\mu_{wire} = 0.4$  and  $\mu_{wall} = 0.1$ ).

A more homogeneous distribution resulted in a much higher mechanical response of the “random” sample when compared to an equivalent experimental one (see Figure 4.20). In the experimental samples prepared manually, localized heterogeneity such as lower density areas could lead to lower mechanical properties as the densification was shown to be concentrated in given zones of the entanglement.

Consequently, and in order to be able to compare the simulation’s results to the experimental data, most simulations were then performed on a “discrete experimental” sample. However, by lowering the flexural strength of the wire in the “random” simulation, a behaviour close to the one of an experimental “spring” sample could be obtained in the future.

#### 4.3.2 Influence of the wire/wire friction coefficient

The friction behaviour at wire/wire contact points was controlled by adjusting the corresponding friction coefficient to values between 0 (no friction) and 1. Considering the discrete geometry of the wire, the value entered in the model does not necessarily correspond to the actual experimental steel/steel friction coefficient. In parallel, a simulation was performed with additional fixed bonds at each contact points between two elements in the initial configuration in order to model an interaction with an initially infinite friction coefficient. This configuration comes close to what was obtained when sintering the material (creation of fixed contact points).

As shown in Figure 4.21, the mechanical response of the entanglement, composed of a “positioning” and a “densification” stage, can be greatly influenced by the friction behaviour at contact points. Without any friction, a low increase of the resulting stress on the moving piston could be observed, which is in accordance with the observations made previously on the strong rearrangements occurring in such a configuration. For increasing friction coefficients, the slope of the densification stage greatly increases as contacts are able to transmit higher forces. The final stress for  $\mu_{wire} = 1$  reaches values up to 10 times larger than with no friction.

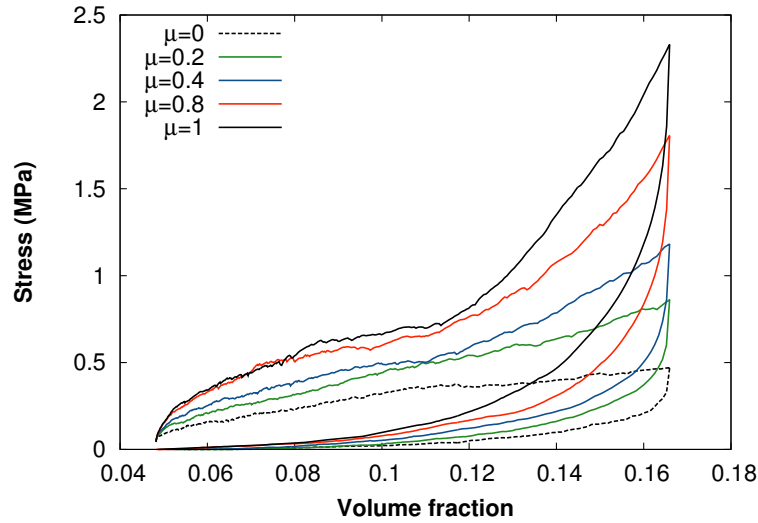


Figure 4.21: Evolution of the pressure on the moving piston as a function of the volume fraction for different wire/wire friction coefficient  $\mu_{wire}$  ( $\mu_{wall} = 0.1$ ).

Considering the purely elastic nature of this model and as it was introduced from the number of contacts analysis, a complete reversibility of the process could be observed when unloading the sample. As a result the hysteresis phenomenon, in the case of a stainless steel wire, is largely over-estimated and is thus closer to what was observed in the case of the high yield strength pearlitic steel.

Figure 4.22 presents the results of the simulation in which every initial contact points were fixed. The friction coefficient for newly created contacts was set to 0.4 and, similarly to the previous simulations,  $\mu_{wall} = 0.1$  was used.

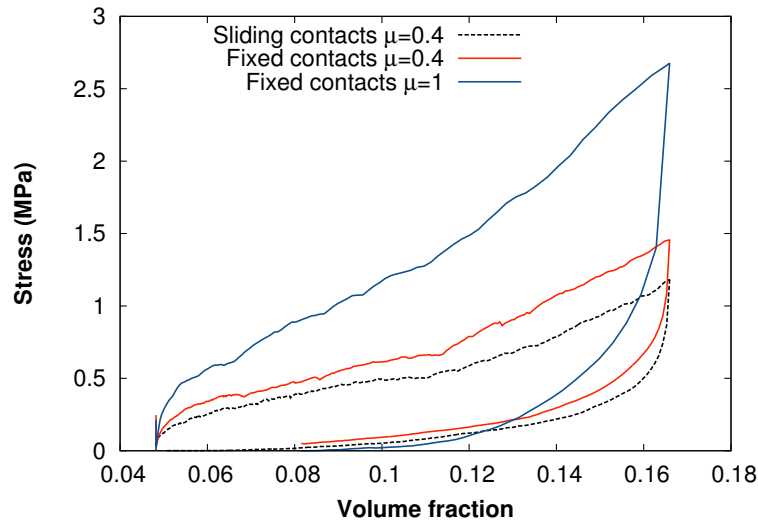


Figure 4.22: Evolution of the pressure on the moving piston as a function of the volume fraction for geometries with initially fixed or sliding contacts ( $\mu_{wall} = 0.1$ ).

In the case of a geometry with initially fixed contact points, a steeper mechanical response could be observed in the first instants of the simulation (see Figure 4.22), thus indicating that the structure

was successfully strengthened. More generally, the behaviour of both structures are very similar, with a consistently higher mechanical strength in the case of the fixed contacts. However it is worth mentioning that, although initial contacts were linked using “bond” interactions, the rotation of those links was not prevented. Rearrangements are thus still possible and a behaviour typical of sintered entangled media (elastic stage, plateau and densification) could not be observed.

For the same “sintered” geometry, simulations were performed for  $\mu_{\text{wire}} = 0.4$  and  $\mu_{\text{wire}} = 1$  and the mechanical response of the material was found to be greatly influenced by the creation of new contacts during the compression (see Figure 4.22). In this model, even though the initial contacts were physically bonded, the mechanical strength of the entanglement still results in the frictional behaviour at contact points.

### 4.3.3 Influence of the wire/wall friction coefficient

Similarly, simulations were performed for different values of the wire/wall friction coefficient while keeping the wire/wire friction coefficient constant ( $\mu_{\text{wall}} = 0.4$ ). In this model, the “wall” interaction is modeled by a finely defined assembly of elements, thus resulting in a relatively smooth surface (compared to the wire/wire contacts). Values between 0 and 0.3 were used and Figure 4.23 regroups the data acquired during the simulations.

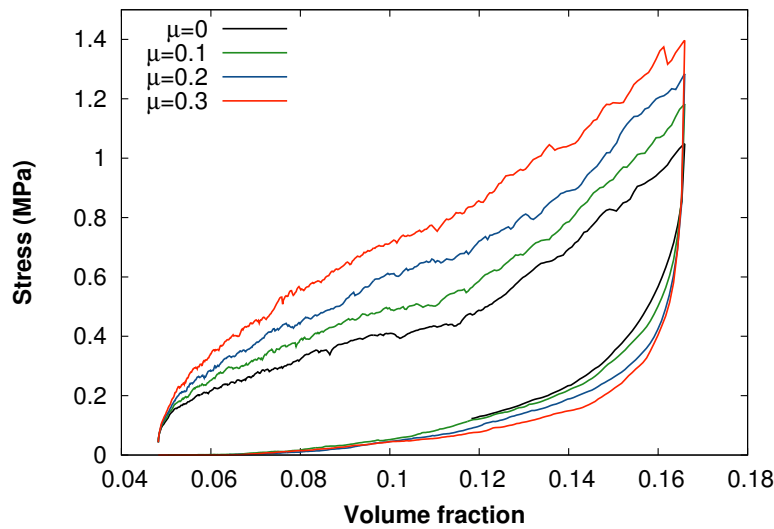


Figure 4.23: Evolution of the pressure on the moving piston as a function of the volume fraction for different wall/wire friction coefficient  $\mu_{\text{wall}}$  ( $\mu_{\text{wire}} = 0.4$ ).

For higher wire/wall friction coefficients, increased mechanical responses could be observed along with a slightly lower slope of the “densification” stage. The two stages are indeed more pronounced without friction and a more continuous evolution, closer to what was observed experimentally, was observed for higher friction values.

By increasing the wire/wall friction coefficient, a steeper behaviour was observed at the first instants of the discharge sequences. Due to higher frictional forces, the sample is indeed, in the simulation, more constrained inside the cylindrical mould, thus “simulating” a behaviour closer to the one observed experimentally for a plastically deformed stainless steel sample. The deformation

remains, however, completely reversible due to the elastic properties of the wire itself.

#### 4.3.4 Comparison to the experiment

From the previous analyses, both friction coefficients were adjusted in the simulation of a “discrete experimental” sample in order to fit the experimental results over the same volume fraction range.

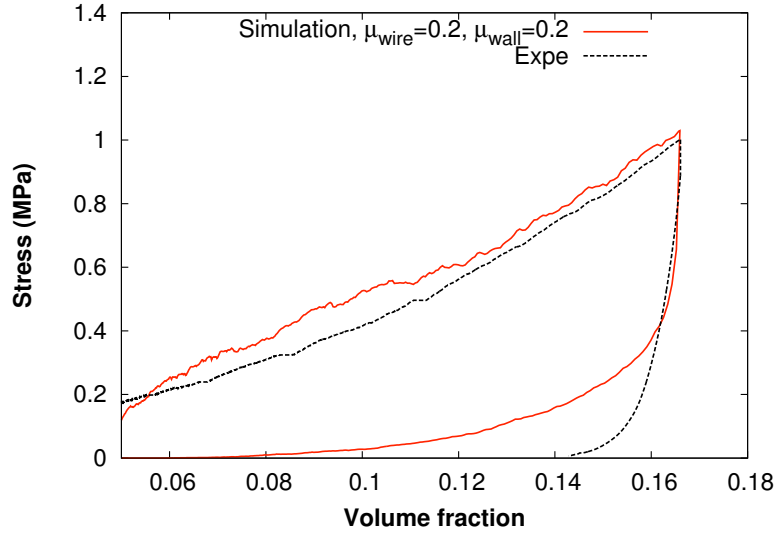


Figure 4.24: Comparison between experimental data and simulation for  $\mu_{wire} = 0.2$  and  $\mu_{wall} = 0.2$ .

Finally, the wire/wire friction coefficient was set to 0.2 in order to get a correct non-linear evolution of the stress and the wire/wall friction coefficient was also set to 0.2 so as to obtain the steepest unloading sequence, while staying in the right stress range. Figure 4.24 shows the resulting stress/volume fraction comparative plot of both experimental and numerical data.

A good general agreement could be obtained in these conditions although, due to the elastic properties of the wire, the remaining plastic deformation of the sample could not be observed. When unloading numerical samples, the stress decreases first rapidly, before slowly returning to its original state.

The compressive mechanical behaviour of monofilament entangled properties was modeled using a Discrete Element Method and results showed a good agreement with the experiment. Although this model only takes into account the elastic deformation of the wire, the non-linear evolution of the stress, as well as the unloading behaviour could be approached by adjusting the wire/wire and wire/wall friction coefficients.

## 4.4 Conclusion

A Discrete Element Method was used in order to model the oedometric compressive behaviour of entangled media, while taking into account the properties of the constitutive material as well as friction. The wire was defined as a succession of spherical elements and a “discretization” process

was developed in order to acquire numerical configurations from experimental tomography data.

A morphological analysis, equivalent to the one presented in Chapters 2 and 3 was performed and the numerical behaviour of the entanglement under compressive loadings was shown to be very similar to the experimental one in terms of both density and number of contacts measurements. The contact density was shown to decrease with friction and a fully reversible process was observed when unloading the sample.

From a mechanical point of view, although the wire/wire friction coefficient had more of an impact on the slope of the densification stage, the wire/wall friction coefficient was shown to influence the unloading behaviour. Finally, by adjusting the parameters of the model, the simulations resulted in a good fit between numerical and experimental results. A purely elastic model was here used and remaining plastic deformation that was observed experimentally could thus not be observed.



# Conclusion and prospects

The main goal of this PhD was to study the relationship between microstructure and mechanical properties of Monofilament Entangled Materials. A manufacturing process was first defined with a set of adjustable parameters such as the diameter or shape of the wire, or the elastic properties of the wire itself. In parallel, sintering techniques were adapted in order to be able to strengthen the entanglement by creating fixed nodes at the contact points.

Using in-situ experiments in X-ray tomography, the evolution of the microstructure of the material was followed. From the morphological measurements performed on the resulting 3D volumes and from the microstructural characterization, this material was shown to be very heterogeneous, with a strong “wall effect” (higher local density at the contact with the mold). A better homogeneity could be obtained by pre-deforming the wire as a spring. For all materials, an increase of the number of contacts, typical of entangled media, was observed and this critical parameter was shown to impact greatly the mechanical properties of the entanglement in terms of both damping and stiffness.

Using the characterization techniques developed in this PhD, a systematic analysis of different types of materials could be carried out using materials such as polymer wires or even a mixture of wires with different properties. In addition, a characterization of the electrical conductivity of the entanglement could provide useful information on both the microstructure (number of contact, percolation...) and the electrical properties of the entanglement.

The mechanical response of this material was studied under different type of loadings and it was shown to exhibit very high damping abilities, together with high ductility and a relatively good stiffness. Additional shear testings could be performed in order to investigate the influence of different manufacturing parameters on the shear modulus. From the different structures studied in this PhD, the loss factor was shown to decrease with the stiffness of the entanglement but by controlling the volume fraction, shape of the wire and degree of sintering, the properties of Monofilament Entangled Materials were able to be tailored to specific requirements. In this context, it was integrated in the “connecting rod” system and absorption measurements are currently being carried out. In-situ compressive and damping characterization in temperature (400-500°C) could also be performed in order to evaluate the properties of the material at high temperature.

An analytical model based on experimental measurements of the mean distance between contacts was adapted and fitted to experimental results and it enabled the validation of the equivalent orientation parameter  $f$ , specific to the geometry of the test. From the measurements of both the number of contacts and mean length between contacts for different types of structures, this model could be adapted in order to predict the properties of a given microstructure.

In parallel, a discrete element method was used to model the compressive behaviour of the structure. A bead-like model was defined from an experimentally acquired 3D volume and, based

on this discrete image of the sample, microstructural parameters were measured in order to study the deformation mechanisms in the simulation. Both the macroscopic and morphological behaviour of the entanglement in the simulation was shown to be in good agreement with experimental data. Finally, the plastic behaviour of the wire could, in the future, be implemented into the numerical model by, for example, changing the bending stiffness of the chain depending on its local deformation.

Stronger interactions could also be considered in “sintered geometries”, preventing any relative displacements or rotations of the contact points, and these structures could then be tested in uniaxial compression in order to compare their numerical behaviour to experimental results on sintered Monofilament Entangled Materials.

The discretization process developed in this PhD could finally be applied to different structures (wire shape and diameter) by acquiring high quality 3D volumes, required for a systematic, precise definition of a discrete geometry. Finally, the behaviour of these structures could then be modeled and compared to experimental data.



# Appendix A

## Industrial specifications

## Appendix B

# Materials selection and process : “materials selection” project

Over the course of the MANSART project, the specific “connection rod” application and its specifications were proposed as a case study for a “materials selection” class at INP Grenoble. The system, which was presented in more details in Chapter 0.2.2, was analyzed in order to determine the dimensions and properties of its different components.

The CES software was used in order to combine the different solicitations and to choose the best combination of materials. In the end, it was finally concluded that no bulk materials could answer to every requirements as the high temperature resistance was found to be incompatible with the required damping properties.

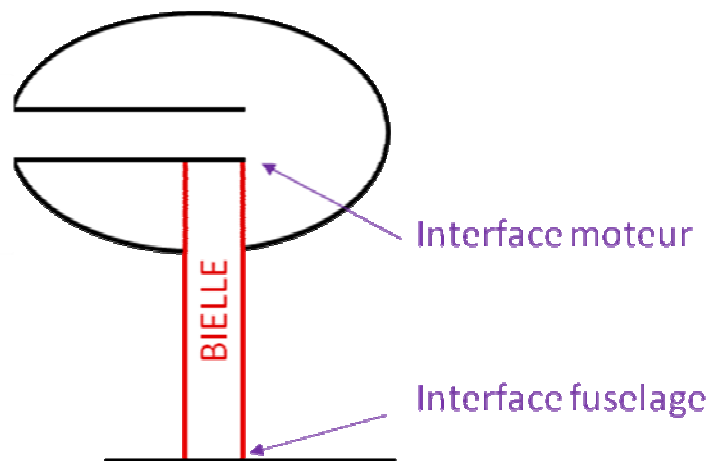
For demanding multi-functionnal applications, bulk materials are often unable to combine all specifications and in this context, “architected” materials recently appeared as a good, adjustable, solution to this type of problems.

## 2 Bielle d'attache

L'objectif du sujet « bielle d'attache » est de rechercher de nouveaux matériaux afin d'ajouter des fonctions à cette pièce. Bien que la fonction « tenue mécanique » doit être conservée, la fonction vibratoire est une fonction qu'il est nécessaire d'ajouter à l'ensemble afin d'améliorer son fonctionnement. Un autre objectif du projet est de minimiser la masse de la pièce

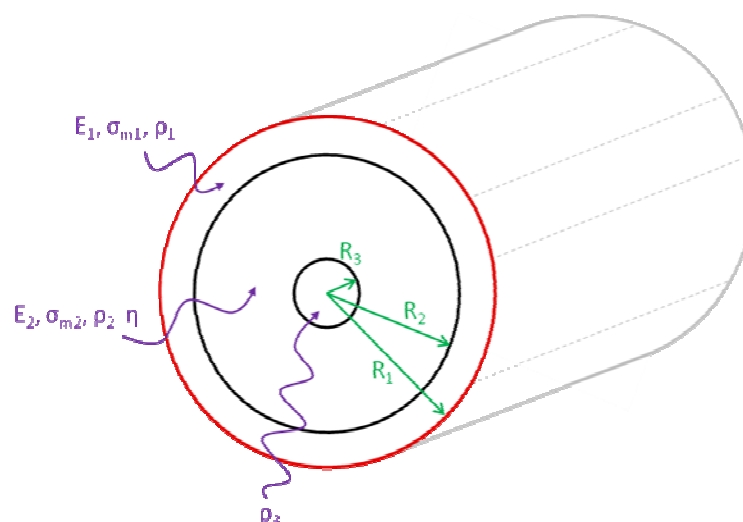
### 2.1 Description du sujet

L'étude va porter sur une bielle d'attache. Cette pièce a pour fonction de faire la liaison entre le fuselage et le moteur.



Le modèle de bielle d'attache actuellement utilisé dans le domaine aérospatiale est un tube creux, d'une épaisseur de 3-4 mm, fait d'Inconel 718, de type superalliage base nickel. Les caractéristiques et propriétés de l'inconel 718 sont présentées en annexe 1 p 23.

L'inconel 718 est capable de supporter les contraintes imposées sur la bielle. Cependant, il ne répond pas à la fonction « acoustique ». Pour cela, un matériau hybride est imaginé pour respecter toutes les fonctions.



### Explication de la nouvelle structure :

- Le matériau n°1, situé à l'extérieur du cylindre est constitué à l'origine de l'inconel 718 (alliage à base de nickel). Son but est d'effectuer la tenue mécanique entre le fuselage et le moteur. Dans notre étude, nous apporterons une solution de remplacement à l'inconel 718 afin de conserver ces propriétés mécaniques mais aussi d'alléger cette pièce.
- Le matériau 3, situé au centre du cylindre est une masselotte. Cette masselotte devra osciller aux pulsations émises par le moteur. Nous choisirons donc ce matériau en conséquence.
- Le matériau 2 est choisit pour transmettre les oscillations du moteur à la masselotte. Cependant, ces vibrations ne doivent pas être ressenties par les passagers. Les fréquences que nous ressentons devront donc être amorties. Pour cela, nous allons proposer un matériau 2 placé entre le matériau 1 et 3 afin d'amortir les vibrations de la masselotte.



Les matériaux 2 et 3 ne sont pas fixés aux interfaces comme le matériau 1. En effet, si le matériau 3 était fixé à l'extrémité du fuselage et du moteur, il transmettrait alors les vibrations du moteur à l'appareil. Dans un second temps, on cherche aussi à minimiser la masse de cet ensemble « matériau 2/matériau 3 » qui pourrait être considéré comme un ensemble « masse/ressort ».

La bielle d'attache est utilisée à de hautes températures. Faisant le lien entre le fuselage et le moteur, la bielle est logiquement soumise aux mêmes températures.

- Température à l'interface fuselage :  $\sim 100^{\circ}\text{C}$

{  $100^{\circ}\text{C}$

- Température à l'interface moteur 250°C => suivant l'état de refroidissement  
450°C

## 2.2 Choix du matériau 1

Le projet commence avec la recherche du matériau 1. Ce matériau est le plus simple puisque seules les contraintes « mécaniques » doivent être prise en compte. Le matériau 1 est un élément important de la structure. Il permet de maintenir la structure et de faire le lien entre le moteur et le fuselage.

### 2.2.1 Méthode de sélection

Afin de mener à bien la recherche du matériau 1, nous nous sommes d'abord appuyés sur le matériau actuellement utilisé : l'inconel 718 (voir annexes pour description).

En connaissant les sollicitations que subit le matériau, la recherche effectuée à l'aide du logiciel CES sera orientée de façon à obtenir des matériaux aux propriétés similaires ou supérieures à l'inconel.

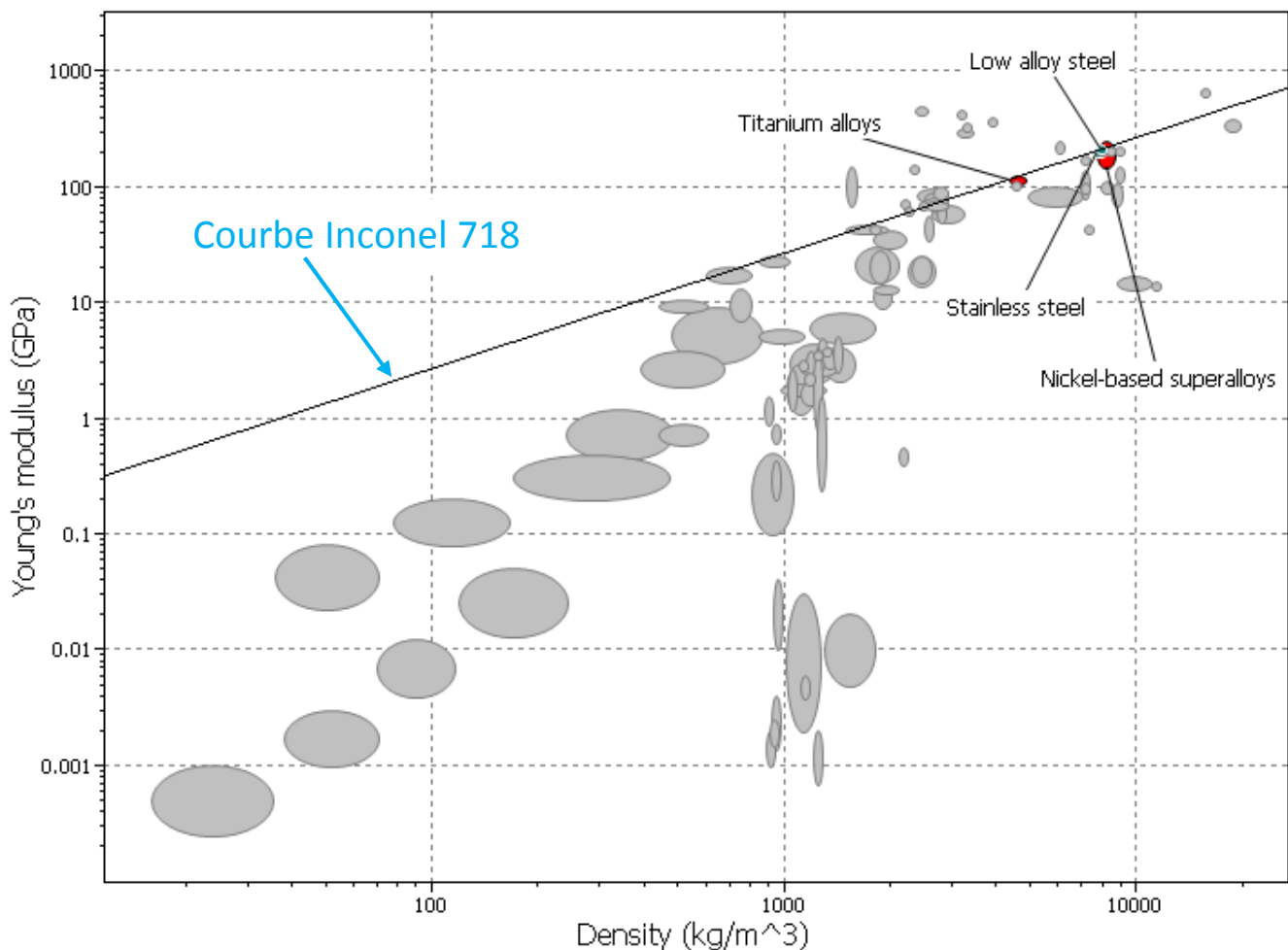
Les contraintes qui s'imposent sur ce matériau sont la résistance aux températures d'utilisations, à la compression et à la traction. La première limite imposée est donc la limite d'élasticité « yield strength » et la force en compression « compressive strength ».

<b>Yield strength (minimum)</b>	380 MPa
<b>Compressive strength (minimum)</b>	380 MPa

Ensuite viens s'ajouter les températures d'utilisation et la ténacité. La ténacité est une propriété importante à prendre en compte car elle permet d'éliminer les matériaux qui ne tiendraient pas les cycles de compression/traction tels que les céramiques.

<b>Température de service minimum</b>	- 50 °C
<b>Température de service maximum</b>	450 °C
<b>Ténacité</b>	20 MPa.m <sup><math>\frac{1}{2}</math></sup>

Une fois ces limites mises sur CES, le graphe « module d'Young en fonction de la densité » [ $E=f(\rho)$ ] est tracé (voir graphe ci-après). Une droite de pente 1 est tracée sur le graphe. Cette pente passe par les valeurs de l'inconel 718. Tout cela dans le but de choisir les matériaux les plus performants.



Les résultats obtenus par le graphe proposent quatre types de matériaux :

- **Acier faiblement allié** : « low alloy steel »
- **Superalliage base nickel** : « nickel-based superalloys »
- **Acier inoxydable** : « stainless steel »
- **Alliage de titane** : « titanium alloys »

Pour le choix du matériau 1, l'inconel 718 est désigné comme référence car les procédés de mise en forme en tube existent déjà. Le deuxième matériau choisi comme matériau 1 correspond à celui qui est le plus léger. Le matériau sera donc un alliage de titane.

Pour choisir un alliage de titane particulier, le site [matweb.com](http://matweb.com) est utilisé. Ce site internet permet de sélectionner un matériau précis dans une famille donnée. Les recherches effectuées sur les alliages de titane ont mené à l'alliage suivant : titanium alloy (Ti-15Mo-3Nb-3Al-0,2Si (fiche en annexe 2 p 24)

Une fois les matériaux 1 choisis, le calcul du rayon R2 est effectué afin que le tube extérieur

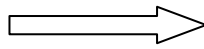
puisse supporter une traction de 130T.



### 2.2.2 Détermination du rayon R2

Le matériau 1 permet la jonction entre le moteur et le fuselage. Il doit donc avoir une résistance mécanique suffisante. Dans notre cas, une limite élastique est imposée. Notre cahier des charges nous indique une charge en traction de T=70 tonnes. Nous avons sélectionné dans la partie précédente deux matériaux : l'inconel 718 et un alliage de titane. Leurs limites élastiques  $\sigma$  sont respectivement 1040MPa et 1210MPa.

A l'aide de la formule :  $\sigma = \frac{T}{\pi \cdot (R_1^2 - R_2^2)}$ , il est possible de déterminer le rayon R2.



$$R_2 = \sqrt{R_1^2 - \frac{T}{\pi \cdot \sigma}}$$

Les résultats obtenus sont présentés dans le tableau suivant :

Matériau 1	Rayon 2 (mm)
Inconel 718	0,0455
Alliage de titane	0,046

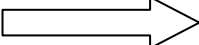
## 2.3 Choix du couple matériau 2/matériau 3

Après avoir sélectionné deux matériaux 1, la recherche va s'orienter vers les matériaux 2 et 3, puis vers le calcul du rayon R3. Les contraintes utilisées pour faire cette sélection avec le logiciel CES sont uniquement les conditions de température (100°C, 250°C, 450°C).

### 2.3.1 Méthode de sélection du matériau 2/matériau 3

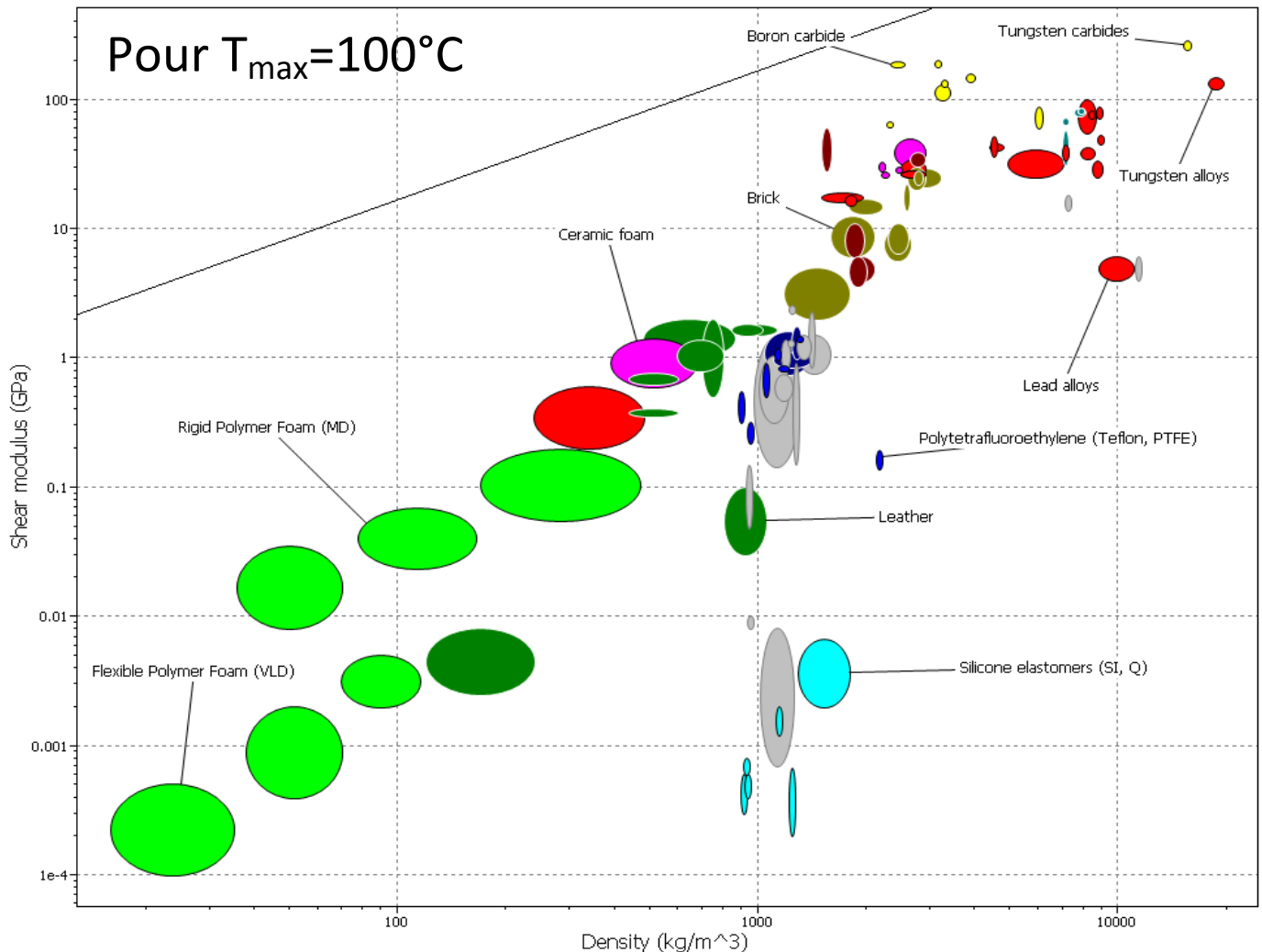
Dans un premier temps, la sélection des matériaux 2 et 3 commence avec la température de 100°C car c'est la limite de sélection qui donne le plus de solutions matériaux. Puis dans un second temps, la limite de sélection va être augmentée de 100°C à 250°C puis à 450°C. Seuls les matériaux qui se maintiennent à plus hautes températures seront gardés.

Il est important de considérer la contrainte vibratoire pour cette nouvelle recherche. En effet, la masselotte doit osciller afin d'amortir les pulsations que nous pouvons ressentir. Celles-ci sont situées à une fréquence de 15Hz.



$$\omega = 2\pi f = \sqrt{\frac{G_2 \cdot (R_2 - R_3)}{\pi \cdot (\rho_3) \cdot (R_3)^2 \cdot L}}$$

Nous disposons donc de deux inconnus : la masse volumique du matériau 3 ainsi que le module de cisaillement  $G$  du matériau 2. Sur le graphique CES suivant, nous avons tracés le module de cisaillement en fonction de la densité à 100°C.



Devant le nombre important de matériaux ressorti de la recherche, les matériaux vont être choisis dans différentes zones du graphique afin de pouvoir identifier par la suite quelles sont les zones favorables pour les matériaux 2 et 3. Le choix se fera selon les valeurs de  $R_3$  obtenues.

Les familles de matériaux choisis, de façon aléatoire pour  $T=100^{\circ}\text{C}$ , sont :

- Les mousses de polymère flexible
- Les élastomères de silicone
- Les mousses de polymère rigide
- PTFE
- Les mousses de céramique
- Les alliages de plomb
- Les alliages de tungstène
- Les carbures de bore

- **Les carbures de tungstène**

### 2.3.2 Détermination du rayon R3

Pour chaque famille de matériaux choisies, les valeurs de densité moyennes et de module de cisaillement « shear modulus » sont notées et répertoriés dans une feuille de calcul. Tout cela, dans le but de pouvoir calculer le rayon R3.

A l'aide du graphique obtenu par le logiciel CES, neuf familles de matériaux sont sélectionnés et placés dans le tableau suivant. Ce tableau regroupe le calcul du rayon R3, obtenu à l'aide de la contrainte d'absorption de la vibration pour une fréquence de 15Hz.

Rayon R3 (m)		Matériau 2	mousse de polymère flexible	élastomère de silicone	mousse de polymère rigide	téflon	mousse de céramique	alliage de plomb	alliage de tungstène	carbure de bore	carbure de tungstène
		G2 (Pa) →	300000	4300000	46300000	2E+08	2E+09	5E+09	1,34E+11	1,9E+11	2,63E+11
Matériau 3	$\rho_3$ (kg/m³) ↓										
mousse de polymère flexible	26		0,0425	0,0455	0,0455	0,0455	0,0455	0,0455	0,0455	0,0455	0,0455
mousse de polymère rigide	122		0,0355	0,0444	0,0454	0,0455	0,0455	0,0455	0,0455	0,0455	0,0455
mousse de céramique	531		0,0246	0,0414	0,0450	0,0454	0,0455	0,0455	0,0455	0,0455	0,0455
élastomère de silicone	1550		0,0169	0,0363	0,0442	0,0451	0,0455	0,0455	0,0455	0,0455	0,0455
téflon	2170		0,0148	0,0341	0,0438	0,0450	0,0455	0,0455	0,0455	0,0455	0,0455
carbure de bore	2450		0,0141	0,0332	0,0435	0,0449	0,0455	0,0455	0,0455	0,0455	0,0455
alliage de plomb	9925		0,0077	0,0226	0,0391	0,0433	0,0453	0,0454	0,0455	0,0455	0,0455
carbure de tungstène	15600		0,0062	0,0193	0,0367	0,0422	0,0452	0,0454	0,0455	0,0455	0,0455
alliage de tungstène	18700		0,0057	0,0180	0,0355	0,0416	0,0451	0,0453	0,0455	0,0455	0,0455

Légende :

	$R3 \geq 0,0455$
	$0,04 \leq R3 < 0,045$
	$0,035 \leq R3 < 0,04$
	$R3 < 0,035$

Pour de nombreuses familles de matériaux, le rayon R3 est trop élevé ( $R3 \geq 0,04$  m). Le rayon total de la bielle est de 0,05 m tandis que le rayon R2 est de 0,0455 m.

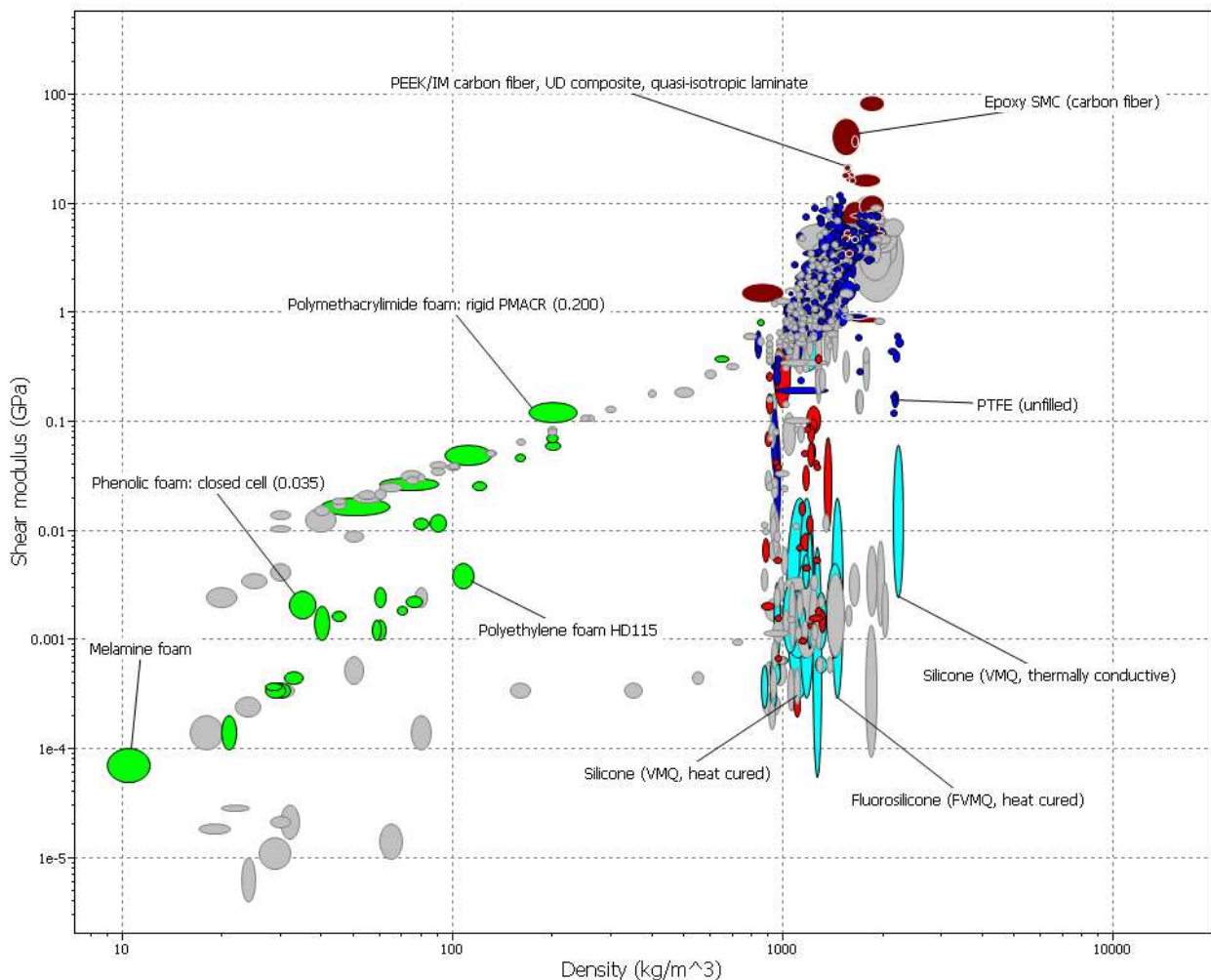
- Les solutions en violets sont donc impossibles, car cela signifierait qu'il n'y a pas de matériau 2.
- Les solutions en rouge sont aussi à écarter car elles ne donnent pas suffisamment d'épaisseur au matériau 2 pour lui permettre d'assurer correctement ses fonctions.
- Pour finir, les solutions en jaune sont jugées trop petites pour la mise en forme du matériau 2.
- Il reste donc que les solutions en bleu clair.

Les solutions matériaux convenables pour les matériaux 2 se situent autour de la famille des polymères tandis que pour les matériaux 3, les solutions se situent autour des familles qui possèdent une densité élevée.

### 2.3.3 Sélection approfondie du matériau 2

Après cette première phase de sélection, la suite va être d'affiner la recherche du matériau 2 en choisissant de se cibler sur les zones du graphique où le module de cisaillement  $G$  est faible, c'est-à-dire dans la zone des polymères. Le but étant de trouver des couples de matériaux encore plus intéressants.

Pour cela, une nouvelle sélection de matériaux sur le logiciel CES est effectuée. La recherche est faite uniquement avec la base de données des polymères. Les contraintes en températures sont identiques à la recherche précédente, c'est-à-dire  $T=100^{\circ}\text{C}$ .



D'après ce graphique (à T=100°C), de nombreuses familles de polymères sont présentes. Les silicones, les mousses de polymère, le PTFE sont toujours présents et il existe également les composites à matrice polymérique et à renfort fibre de verre ou de carbone.

Comme précédemment, des matériaux sont choisis aléatoirement. Les valeurs de densité et de module de cisaillement sont ensuite prises en compte pour calculer les rayons R3 correspondants.

Détermination R3 (m)		Matériau 2	mousse de mélanine	mousse de PP	silicone élastomère	mousse phénolique	silicone	Fluoro-silicone	silicone	PTFE
		G2 (Pa) →	75000	150000	500000	2200000	4000000	8000000	40000000	164000000
Matériau 3	$\rho_3$ (kg/m <sup>3</sup> ) ↓									
mousse de polymère flexible	26		0,0365	0,0455	0,0455	0,0455	0,0455	0,0455	0,0455	0,0455
mousse de polymère rigide	122		0,0253	0,0306	0,0385	0,0435	0,0443	0,0449	0,0454	0,0455
mousse de céramique	531		0,0149	0,0194	0,0286	0,0385	0,0411	0,0431	0,0450	0,0454
élastomère de silicone	1550		0,0095	0,0127	0,0204	0,0317	0,0358	0,0396	0,0440	0,0451
téflon	2170		0,0081	0,0110	0,0180	0,0292	0,0336	0,0379	0,0435	0,0450
carbure de bore	2450		0,0077	0,0105	0,0172	0,0282	0,0327	0,0372	0,0433	0,0449
alliage de plomb	9925		0,0040	0,0056	0,0096	0,0178	0,0220	0,0274	0,0384	0,0433
carbure de tungstène	15600		0,0032	0,0045	0,0079	0,0149	0,0188	0,0239	0,0358	0,0422
alliage de tungstène	18700		0,0030	0,0041	0,0072	0,0138	0,0175	0,0225	0,0346	0,0416

Légende :

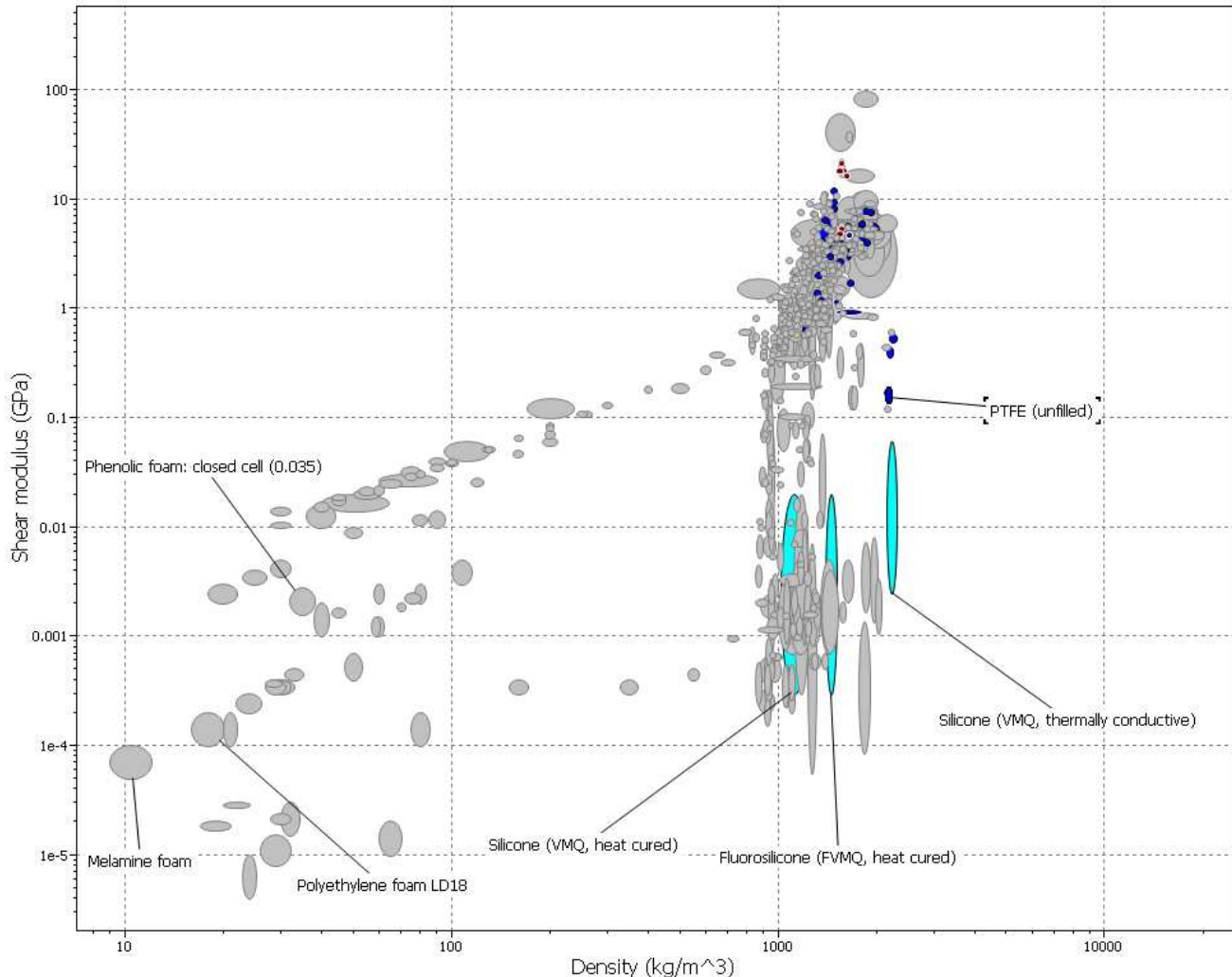
	R3 ≥ 0,0455
	0,04 ≤ R3 < 0,045
	0,035 ≤ R3 < 0,04
	R3 < 0,035
	Polymères résistants à 250°C

Les conclusions sont identiques à celles apportées au tableau précédent. Seuls les rayons R3 coloriés en bleu clair sont les rayons à prendre en compte. Les couples de matériaux correspondent donc aux matériaux 2 qui possèdent un module de cisaillement faible et aux matériaux 3 possédant une forte densité.

Cependant, les polymères sont sensibles à la température. Si à 100°C un grand nombre de polymères sont présents, à 250°C, le nombre de polymères diminue considérablement et

seuls les polymères fluorés ou les silicones sont capables de supporter de hautes températures.

Le graphique ci-dessous correspond à la sélection des polymères à 250°C. Ce graphique montre bien que les polymères résistants à hautes températures sont peu nombreux.



En conclusion, pour  $T=250^{\circ}\text{C}$ , le nombre de polymères résistant à cette température diminue considérablement. Il ne reste plus que quelques familles de polymères qui ont des propriétés mécaniques supérieures à tous les autres polymères afin de pouvoir tenir à hautes températures.

Pour  $T=450^{\circ}\text{C}$ , aucun polymère n'est suffisamment résistant pour tenir à ces températures élevées. Si la bielle est composée d'un polymère, il sera peut-être nécessaire d'introduire un système de refroidissement car au contact du moteur, la bielle risque d'être inutilisable.

Pour choisir le couple matériau2/matériau3, le calcul du rayon 3 ne suffit pas, il faut également prendre en compte la masse totale de la bielle. Puisque la réduction de la masse totale du système est l'un de nos objectifs.

## 2.4 Détermination de la masse totale

Afin d'effectuer notre choix final, nous allons utiliser le critère de la masse. En effet, l'objectif est de diminuer au maximum la masse malgré l'ajout de nouveaux matériaux.

Le critère masse doit être le plus faible possible :

$$\rho_1 \cdot (R_1^2 - R_2^2) + \rho_2 \cdot (R_2^2 - R_3^2) + \rho_3 \cdot R_3^2$$

### Données :

Matériau 1 = Inconel 718

Rayon 1 = 0,05 m

Matériau 2 = au choix

Rayon 2 = 0,045 m

Matériau 3 = au choix

Rayon 3 = au choix

Détermination M (kg)		Matériau 2	mousse de mélanine	mousse de PP	silicone élastomère	mousse phénolique	silicone	Fluoro-silicone	silicone	PTFE
		$\rho_2$ (kg/m <sup>3</sup> ) →	10,5	21	1100	35	2200	1450	2200	2200
Matériau 3	$\rho_3$ (kg/m <sup>3</sup> ) ↓									
mousse de polymère flexible	26		7,82	7,85	7,85	7,85	7,87	7,85	7,85	7,85
mousse de polymère rigide	122		7,94	8,03	9,56	8,25	8,77	8,44	8,34	8,30
mousse de céramique	531		8,03	8,25	11,72	9,51	11,54	10,58	10,32	10,19
élastomère de silicone	1550		8,08	8,37	13,15	11,24	15,91	14,67	14,97	14,83
téflon	2170		8,09	8,40	13,50	11,88	17,67	16,60	17,62	17,61
carbure de bore	2450		8,10	8,41	13,62	12,12	18,33	17,37	18,77	18,85
alliage de plomb	9925		8,13	8,50	14,53	14,74	25,98	28,29	42,75	49,56
carbure de tungstène	15600		8,14	8,52	14,71	15,47	28,10	32,03	55,42	70,19
alliage de tungstène	18700		8,14	8,53	14,77	15,73	28,87	33,48	61,13	80,64

### Légende :

	M ≥ 50
	25 ≤ M < 50
	15 ≤ M < 25
	M < 15
	Polymères résistants à 250°C
	Solutions matériaux écartées car R3 refusé



Ce tableau présente les masses totales obtenues selon le couple de matériau 2/3 considéré et pour un matériau 1 constitué d'inconel 718. Les mêmes calculs ont été effectués pour un matériau 1 constitué de l'alliage de titane et ont été présentés en annexe 3 p 25 afin d'alléger la rédaction et la compréhension.

Les solutions matériaux grisées sont des solutions qui ne peuvent pas être prises en compte car le rayon R3 correspondant est trop élevé. Par conséquent, ces solutions ne sont pas exploitables.

La bielle actuelle, constitué d'un tube creux en inconel 718, pèse aux alentours des 15kg. Si l'on veut alléger la structure, il sera donc préférable de privilégier les masses étant inférieures à cette valeur. Cela correspondant aux solutions coloriées en bleu clair.

Au vue des résultats, il existe un grand nombre de solutions apportant un allègement de la structure avec les propriétés nécessaires au bon fonctionnement de la bielle. Les polymères permettent d'apporter de la légèreté à l'ensemble tout en conservant une tenue mécanique jusqu'à 100°C.

Lorsque la limite de température monte à 250°C, les masses commencent à se disperser. Les polymères se maintenant à 250°C possèdent des masses deux fois plus importantes par rapport à celles des polymères présents pour 100°C (hormis la mousse phénolique).

## 2.5 Conclusion

Pour effectuer une sélection intéressante, il faut trouver un compromis entre la masse totale M et le rayon R3. Il faut choisir un matériau 2 possédant un faible module de cisaillement et un matériau 3 avec une forte densité.

L'étude effectuée avec l'inconel 718 (=matériau 1), nous donne un large choix de solutions matériaux pour les matériaux 2 et 3. Cependant, lorsque l'alliage de titane est considéré comme matériau 1, les masses totales calculées sont moins importantes que pour l'inconel 718. Utiliser un alliage de titane est donc une première solution pour alléger la bielle.

Le seul point négatif de la recherche est l'absence de solutions matériaux pour une température de 450°C. En effet, aucun polymère ne peut tenir à ces températures. Une modification de la structure (avec un circuit de refroidissement par exemple) pourrait être une solution à ce problème des hautes températures.

# Bibliography

- [1] M. Ashby and Y. Brechet, “Designing hybrid materials,” *Acta Materialia*, vol. 51-19, pp. 5801–5821, 2003.
- [2] U. Granta Design Limited, Cambridge, Ed., *Cambridge Engineering Selector*, 2001.
- [3] L. Zhang, J. M. Ferreira, S. Olheroc, L. Courtois, T. Zhang, E. Maire, and J. C. Rauhee, “Modeling the mechanical properties of optimally processed cordierite–mullite–alumina ceramic foams by x-ray computed tomography and finite element analysis,” *Acta Materialia*, vol. 60-10, pp. 4235–4246, 2012.
- [4] A. Fallet, P. Lhuissier, L. Salvo, and Y. Bréchet, “Mechanical behaviour of metallic hollow spheres foam,” *Advanced Engineering Materials*, vol. 10-9, pp. 858–862, 2008.
- [5] L. Mezeix, C. Bouvet, and D. Poquillon, “Porous materials made with entangled fibers network for an application as core material for sandwich structures.” Journée Nationale sur les Composites, May 2009.
- [6] D. Poquillon, B. Viguier, and E. Andrieu, “Compression de fibres enchevêtrées calibrées en nylon et aluminium. expériences et modélisations.” 18ème Congrès Français de Mécanique, August 2007.
- [7] A. Shahdin, L. Mezeix, C. Bouvet, J. Morlier, and Y. Gourinat, “Fabrication and mechanical testing of glass [U+FB01]ber entangled sandwich beams:a comparison with honeycomb and foam sandwich beams,” *Composite Structures*, vol. 90, pp. 404–412, 2009.
- [8] H. Wadley, N. Fleckb, and A. Evans, “Fabrication and structural performance of periodic cellular metal sandwich structures,” *Composites Science and Technology*, vol. 63, pp. 2331–2343, 2003.
- [9] Y. T. Zhu and W. R. Blumenthal, “Characterization of three dimensional fiber orientation in short-fiber composites,” in *TMS/ASM Materials Week*, 1995.
- [10] G. Zak, C. Park, and B. Benhabib, “Estimation of three-dimensional fibre-orientation distribution in short-fibre composites by a two-section method,” *Journal of Composite Materials*, vol. 35, pp. 316–339, 2001.
- [11] M. Idicula, S. Malhotra, K. Joseph, and S. Thomas, “Dynamic mechanical analysis of randomly oriented intimately mixed short banana/sisal hybrid fibre reinforced polyester composites,” *Composites Science and Technology*, vol. 65, p. 1077–1087, 2005.
- [12] J. Schofield, “Researches on wool felting,” *J. Textile Inst*, vol. 29, pp. 239–252, 1938.
- [13] D. Poquillon, B. Viguier, and E. Andrieu, “Experimental data about mechanical behaviour during compression tests for various matted fibres,” *Journal of Materials Science*, vol. 40, pp. 5963–5970, 2005.

- [14] D. Sedan, C. Pagnoux, A. Smith, and T. Chotard, "Propriétés mécaniques de matériaux enchevêtrés à base de fibre de chanvre et matrice cimentaire." 18ème Congrès Français de Mécanique, August 2007.
- [15] C. V. Wyk, "Note on the compressibility of wool," *J. Textile Inst.*, vol. 37, pp. 285–292, 1946.
- [16] M. Baudequin, G. Ryschenkow, and S. Roux, "Non-linear elastic behaviour of light fibrous materials," *Eur. Phys. J. B*, vol. 12, pp. 157–162, 1999.
- [17] J. Masse, L. Salvo, D. Rodney, Y. Bréchet, and O. Bouaziz, "Influence of relative density on the architecture and mechanical behaviour of a steel metallic wool," *Scripta Materialia*, vol. 54, pp. 1379–1383, 2006.
- [18] P. Latil, L. Orgeas, C. Geindreau, P. Dumont, and S. R. du Roscoat, "Towards the 3d in situ characterisation of deformation micro-mechanisms within a compressed bundle of fibres," *Composite Science and Technology*, vol. 71, pp. 480–488, 2011.
- [19] O. Guiraud, L. Orgeas, P. Dumont, and S. R. du Roscoat, "Microstructure and deformation micro-mechanisms of concentrated fibre bundle suspensions: an analysis combining x-ray microtomography and pull-out tests," *Journal of Rheology*, vol. 56, pp. 593–623, 2012.
- [20] L. Orgeas, P. Dumont, J. Vassal, O. Guiraud, V. Michaud, and D. Favier, "In-plane conduction of polymer composites plates reinforced with architected networks of copper fibres," *Journal of Materials Science*, vol. 47, pp. 2932–2942, 2012.
- [21] P. Dumont, S. L. Corre, L. Orgeas, and D. Favier, "A numerical analysis of the evolution of bundle orientation in concentrated fibre-bundle suspensions," *Journal of Non-Newtonian Fluid Mechanics*, vol. 160, pp. 76–92, 2009.
- [22] Q. Tan and G. He, "3d entangled wire reinforced metallic composites," *Materials Science and Engineering A*, vol. 546, pp. 233–238, 2012.
- [23] O. Bouaziz, J.-P. Masse, and Y. Brechet, "An analytical description of the mechanical hysteresis of entangled materials during loading-unloading in uniaxial compression," *Scripta Materialia*, vol. 64, pp. 107–109, 2011.
- [24] J. Dunlop, "Characterizing the compression properties of fibre masses," *J. Textile Inst.*, vol. 65, pp. 532–536, 1974.
- [25] —, "Acoustic emission from wool during compression," *J. Textile Inst.*, vol. 70, pp. 364–366, 1979.
- [26] —, "The dynamic bulk modulus of fibre masses," *J. Textile Inst.*, vol. 72, pp. 154–161, 1981.
- [27] —, "On the compression characteristics of fibre masses," *J. Textile Inst.*, vol. 74, pp. 92–97, 1983.
- [28] S. Toll, "Packing mechanics of fiber reinforcements," *Polymer Engineering and science*, vol. 38, pp. 1337–1350, 1998.
- [29] J. P. Masse, "Conception optimale de solutions multimatériaux multifonctionnelles : l'exemple des structures sandwichs à peaux en acier - choix des matériaux et développement de nouveaux matériaux de cœur," Ph.D. dissertation, INPG, 2009.

- 
- [30] S. Bergonnier, "Relations entre microstructure et propriétés mécaniques de matériaux enchevêtrés," Ph.D. dissertation, Université Paris VI, 2005.
- [31] P. Liu, G. He, and L. Wu, "Fabrication of sintered steel wire mesh and its compressive properties," *Materials Science and Engineering A*, vol. 489, pp. 21–28, 2008.
- [32] Q. Tan, P. Liu, C. Du, L. Wu, and G. He, "Mechanical behaviours of quasi-ordered entangled aluminium alloy wire material," *Materials Science and Engineering A*, vol. 527, pp. 38–44, 2009.
- [33] N. Pan, "A modified analysis on the microstructural characteristics of general fiber assemblies," *Textile Research Journal*, vol. 63, pp. 336–345, 1993.
- [34] T. Komori and M. Itoh, "A modified theory of fiber contacts in general fiber assemblies," *Textile Res. J.*, vol. 64, pp. 519–528, 1994.
- [35] N. Pan and R. Postle, "Strengths of twisted blend fibrous structures : Theoretical prediction of the hybrid effects," *Journal of Textile Institute*, vol. 86, pp. 559–580, 1995.
- [36] C. Barbier, "Modélisation numérique du comportement mécanique de systèmes enchevêtrés," Ph.D. dissertation, Institut polytechnique de Grenoble, 2008.
- [37] S. Toll, "Note: "on the tube model for fiber suspensions," *J. Rheol.*, vol. 37, pp. 123–125, 1993.
- [38] D. Durville, "Numerical simulation of entangled materials mechanical properties," *Journal of materials science*, vol. 40, pp. 5941–5948, 2005.
- [39] —, "Une approche pour la simulation numérique des milieux enchevêtrés et des structures tissées." 18ème Congrès Français de Mécanique, August 2007.
- [40] D. Rodney, M. Fivel, and R. Dendievel, "Discrete modeling of the mechanics of entangled materials," *Physical Review Letters*, vol. 95, p. 108004, 2005.
- [41] M. Bulacu, "Molecular dynamics studies of entangled polymer chains," Ph.D. dissertation, University of Groningen, The Netherlands, January 2008.
- [42] M. Allen and D. Tildesley, *Computer Simulations of Liquids*, Oxford, Ed. Clarendon Press, 1987.
- [43] S. Williams and A. Philipse, "Random packing of spheres and spherocylinders simulated by mechanical contraction," *Phys. Rev. E*, vol. 67, p. 051301, 2003.
- [44] C. Barbier, R. Dendievel, and D. Rodney, "Numerical study of 3d-compressions of entangled materials," *Computational Materials Science*, vol. 45, pp. 593–596, 2009.
- [45] —, "Role of friction in the mechanics of nonbonded fibrous materials," *Physical Review E*, vol. 80, pp. 016 115–1 – 016 115–5, 2009.
- [46] P. Liu, G. He, and L. Wu, "Uniaxial tensile stress-strain behaviour of entangled steel wire material," *Materials Science and Engineering A*, vol. 509, pp. 69–75, 2009.
- [47] —, "Impact behaviour of entangled steel wire material," *Materials characterization*, vol. 60, pp. 900–906, 2009.
-

- [48] —, “Structure deformation and failure of sintered steel wire mesh under torsion loading,” *Materials and Design*, vol. 30, pp. 2264–2268, 2009.
- [49] P. Ducheyne, E. Aernoudt, and P. D. Meester, “The mechanical behaviour of porous austenitic stainless steel fibre structures,” *Journal of materials science*, vol. 13, pp. 2650–2658, 1978.
- [50] G. He, P. Liu, and Q. Tan, “Porous titanium materials with entangled wire structure for load-bearing biomedical applications,” *Journal of the mechanical behaviour of biomedical materials*, vol. 5, pp. 16–31, 2012.
- [51] W. Zhou, Y. Tang, B. Liu, R. Song, L. Jiang, K. Hui, K. Hui, and H. Yao, “Compressive properties of porous metal fiber sintered sheet produced by solid-state sintering process,” *Materials and Design*, vol. 35, pp. 414–418, 2011.
- [52] M. Abramoff, P. Magalhaes, and S. Ram, “Image processing with imagej,” *Biophotonics International*, vol. 11-7, pp. 36–42, 2004.
- [53] C. Schneider, W. Rasband, and K. Eliceiri, “Nih image to imagej: 25 years of image analysis,” *Nature methods*, vol. 9, pp. 671–675, 2012.
- [54] J. Schindelin, I. Arganda-Carreras, E. Frise, V. Kaynig, M. Longair, T. Pietzsch, S. Preibisch, C. Rueden, S. Saalfeld, B. Schmid, J.-Y. Tinevez, D. J. White, V. Hartenstein, K. Eliceiri, P. Tomancak, and A. Cardone, “Fiji: an open-source platform for biological-image analysis,” *Nature Methods*, vol. 9-7, pp. 676–682, 2012.
- [55] M. Wilkinson and F. Schut, *Digital Image Analysis of Microbes: Imaging, Morphometry, Fluorometry and Motility Techniques and Applications*, J. Wiley and Sons, Eds., 1998.
- [56] W. E. Lorensen and H. E. Cline, “Marching cube: A high resolution 3d surface construction algorithm,” *Computer graphics*, vol. 21-4, pp. 163–169, 1987.
- [57] J. Buffieres, E. Maire, J. Adrien, J. Masse, and E. Boller, “In situ experiments with x ray tomography : An attractive tool for experimental mechanics,” *Experimental Mechanics*, vol. 50, pp. 289–305, 2010.
- [58] D. Fabregue, B. Mouawad, C. Buttay, M. S. Maher, A. Lamontagne, R. Forte, M. Perez, L. Courtois, C. Landron, E. Maire, and V. Massardier, “Elaboration of architected materials by spark plasma sintering,” *Materials Science Forum*, vol. 706-709, pp. 1885–1892, 2012.
- [59] J. B. Roerdink and A. Meijster, “The watershed transform: Definitions, algorithms and parallelization strategies,” *Fundamenta Informaticae*, vol. 41, pp. 187–228, 2001.
- [60] C. Eberhardt, A. Clarke, M. Vincent, T. Giroud, and S. Flouret, “Fibre-orientation measurements in short-glass-fibre composites ii : a quantitative error estimate of the 2d image analysis technique,” *Composites Science and Technology*, vol. 61, pp. 1961–1974, 2001.
- [61] E. Ungar and J. E.M. Kerwin, “Loss factors of viscoelastic systems in terms of energy concepts,” *Journal of the Acoustical Society of America*, vol. 34, p. 954, 1962.
- [62] M. Regelbrugge, “Smart structure and materials cls/asme,” in *Smart structures and materials applications : issues and case studies*, 1994.
- [63] C. L. Martin and D. Bouvard, “Study of the cold compaction of composite powders by the discrete element method,” *Acta Materialia*, vol. 51, pp. 373–386, 2003.

- [64] C. Martin, D. Bouvard, and S. Shima, “Study of particle rearrangement during powder compaction by the discrete element method,” *Journal of the Mechanics and Physics of Solids*, vol. 51, pp. 667–693, 2003.
- [65] N. V. Brilliantov, F. Spahn, J.-M. Hertzsch, and T. Pöschel, “Model for collisions in granular gases,” *Physical review E*, vol. 53, pp. 5382–5392, 1996.
- [66] L. E. Silbert, D. Ertas, G. S. Grest, T. C. Halsey, D. Levine, and S. J. Plimpton, “Granular flow down an inclined plane: Bagnold scaling and rheology,” *Phys. Rev. E*, vol. 64, p. 051302, 2001.
- [67] H. P. Zhang and H. A. Makse, “Jamming transition in emulsions and granular materials,” *Phys. Rev. E*, vol. 72, p. 011301, 2005.

## FOLIO ADMINISTRATIF

Thèse soutenue devant l'Institut National des Sciences Appliquées de Lyon

NOM: COURTOIS

DATE de SOUTENANCE: 13 decembre 2012

PRENOMS: Loïc, Jean, Raymond

TITRE: Monofilament entangled materials: relationship between microstructural properties and macroscopic behaviour

NATURE: Doctorat

N° D'ORDRE : 2012-ISAL-XXXX

ÉCOLE DOCTORALE: Matériaux de Lyon

SPECIALITÉ: Science des Matériaux

Cote B.I.U. - Lyon : T 50/210/19 / et bis

CLASSE:

RÉSUMÉ:

MOTS-CLÉS: monofilament, entangled, tomography, compression, damping, Discrete Element Method

LABORATOIRE DE RECHERCHE: Université de Lyon

MATEIS - UMR CNRS 5510 - INSA de Lyon

25 avenue Jean Capelle, 69621 Villeurbanne Cedex, France

DIRECTEUR DE THÈSE: Pr Michel PEREZ

DIRECTEUR DE THÈSE: Dr Eric MAIRE

PRÉSIDENT DU JURY: Pr John Hutchinson

COMPOSITION DU JURY: Olivier BOUAZIZ

John HUTCHINSON

Eric MAIRE

Patrick ONCK

Laurent ORGEAS

Michel PEREZ

